NASA/CR—2003–212397

The 2002 NASA Faculty Fellowship Program Research Reports

Program Co-Directors:
S.K. Nash-Stevenson, Marshall Space Flight Center, Marshall Space Flight Center, Alabama

C.L. Karr and L.M. Freeman, The University of Alabama, Tuscaloosa, Alabama

G. Karr, The University of Alabama in Huntsville, Huntsville, Alabama

J. Bland, Consultant,
Compiler and Editor
Marshall Space Flight Center, Marshall Space Flight Center, Alabama

Prepared for Marshall Space Flight Center
under Contract NAG8–1859

April 2003

The NASA STI Program Office…in Profile

Since its founding, NASA has been dedicated to the advancement of aeronautics and space science. The NASA Scientific and Technical Information (STI) Program Office plays a key part in helping NASA maintain this important role.

The NASA STI Program Office is operated by Langley Research Center, the lead center for NASA's scientific and technical information. The NASA STI Program Office provides access to the NASA STI Database, the largest collection of aeronautical and space science STI in the world. The Program Office is also NASA's institutional mechanism for disseminating the results of its research and development activities. These results are published by NASA in the NASA STI Report Series, which includes the following report types:

- TECHNICAL PUBLICATION. Reports of completed research or a major significant phase of research that present the results of NASA programs and include extensive data or theoretical analysis. Includes compilations of significant scientific and technical data and information deemed to be of continuing reference value. NASA's counterpart of peer-reviewed formal professional papers but has less stringent limitations on manuscript length and extent of graphic presentations.

- TECHNICAL MEMORANDUM. Scientific and technical findings that are preliminary or of specialized interest, e.g., quick release reports, working papers, and bibliographies that contain minimal annotation. Does not contain extensive analysis.

- CONTRACTOR REPORT. Scientific and technical findings by NASA-sponsored contractors and grantees.

- CONFERENCE PUBLICATION. Collected papers from scientific and technical conferences, symposia, seminars, or other meetings sponsored or cosponsored by NASA.

- SPECIAL PUBLICATION. Scientific, technical, or historical information from NASA programs, projects, and mission, often concerned with subjects having substantial public interest.

- TECHNICAL TRANSLATION. English-language translations of foreign scientific and technical material pertinent to NASA's mission.

Specialized services that complement the STI Program Office's diverse offerings include creating custom thesauri, building customized databases, organizing and publishing research results…even providing videos.

For more information about the NASA STI Program Office, see the following:

- Access the NASA STI Program Home Page at ***http://www.sti.nasa.gov***

- E-mail your question via the Internet to help@sti.nasa.gov

- Fax your question to the NASA Access Help Desk at (301) 621–0134

- Telephone the NASA Access Help Desk at (301) 621–0390

- Write to:
  NASA Access Help Desk
  NASA Center for AeroSpace Information
  7121 Standard Drive
  Hanover, MD 21076–1320
  (301)621–0390

NASA/CR—2003–212397

The 2002 NASA Faculty Fellowship Program Research Reports

Program Co-Directors:
S.K. Nash-Stevenson, Marshall Space Flight Center, Marshall Space Flight Center, Alabama

C.L. Karr and L.M. Freeman, The University of Alabama, Tuscaloosa, Alabama

G. Karr, The University of Alabama in Huntsville, Huntsville, Alabama

J. Bland, Consultant,
Compiler and Editor
Marshall Space Flight Center, Marshall Space Flight Center, Alabama

Prepared for Marshall Space Flight Center
under Contract NAG8–1859

National Aeronautics and
Space Administration

Marshall Space Flight Center • MSFC, Alabama 35812

April 2003

Available from:

NASA Center for AeroSpace Information
7121 Standard Drive
Hanover, MD 21076–1320
(301) 621–0390

National Technical Information Service
5285 Port Royal Road
Springfield, VA 22161
(703) 487–4650

INTRODUCTION

This is the administrative report for The 2002 NASA Faculty Fellowship Program held at the George C. Marshall Space Flight Center (MSFC) for the 38th consecutive year. The nominal starting and finishing dates for the 10-week program were May 28 through August 2, 2002. The program was sponsored by NASA Headquarters, Washington, DC, and operated under contract by The University of Alabama. In addition, promotion and applications are managed by the American Society for Engineering Education (ASEE) and assessment is completed by Universities Space Research Association (USRA). This program was one of ten such programs at nine NASA Centers sponsored and funded by NASA Headquarters. The basic objectives of the program are to:

- further the professional knowledge of qualified engineering and science faculty members
- stimulate an exchange of ideas between participants and NASA
- enrich and refresh the research and teaching activities at the participants' institutions
- contribute to the research objectives of the NASA Centers.

The major activities of the 2002 program were to:

- increase the quality and quantity of research collaborations between NASA and the academic community that contribute to NASA's research objectives
- provide research opportunities for college and university faculty that serve to enrich their knowledge base
- involve faculty in cutting-edge science and engineering challenges related to NASA's strategic enterprises while providing exposure to the methods and practices of real-world research
- enhance faculty pedagogy and facilitate interdisciplinary networking
- elevate the understanding of science, mathematics, and technology through outreach targeting K–12 students and teachers
- encourage collaborative research and technology transfer with other Government agencies and the private sector
- establish an effective education and outreach activity to foster greater awareness of this program.

Questions about any report should be addressed to Dr. Charles Karr, Department of Aerospace Engineering, The University of Alabama, Box 870280, Tuscaloosa, AL 35487–0280, e-mail: ckarr@coe.eng.ua.edu.

Table of Contents

System Identification of X-33 Neural Network
Shiv Aggarwal, Embry-Riddle Aeronautical University

Advanced Ceramic Technology for Space Applications at NASA MSFC
Mohammad Alim, Alabama A&M University

Developing a MATLAB-Based Tool for Visualization and Transformation
Blake Anderton, Lipscomb University

Subsurface Stress Fields in Single Crystal (Anisotropic) Contacts
Nagaraj Arakere, University of Florida

Our Space Future: A Challenge to the Conceptual Artist Concept Art for Presentation and Education
Mary C. Bangs, Empire State College

Identification and Characterization of Extremophile Microorganisms Significant to Astrobiology
Asim Bej, The University of Alabama at Birmingham

Mathematical Investigation of Gamma Ray and Neutron Absorption Grid Patterns for Homeland Defense-Related Fourier Imaging Systems
Dona Boccio, Queensborough Community College, The City University of New York

The Potential of Microwave Radiation for Processing Martian Soil
Walter Boles, Middle Tennessee State University

Fuzzy Logic Trajectory Design and Guidance for Terminal Area Energy Management
Brad Burchett, Rose-Hulman Institute of Technology

Development of a Tool for Dynamic Analysis of Momentum Exchange Electrodynamic Reboost Tethers
Stephen Canfield, Tennessee Technological University

Interfacial Reaction Studies Using ONIOM
Beatriz Cardelino, Spelman College

Enhancement and Extension of Porosity Model in the FDNS-500 Code to Provide Enhanced Simulations of Rocket Engine Components
Gary Cheng, The University of Alabama at Birmingham

Magnetized Target Fusion in Advanced Propulsion Research
Rashad Cylar, Alabama A&M University

Investigation of Friction Stir Welding of Al Metal Matrix Composite Materials
Ravinder Diwan, Southern University

An Improved RLV Stability Analysis Via a Continuation Approach
Mark Friedman, The University of Alabama in Huntsville

Partial Wave Analysis of Coupled Photonic Structures
Kirk Fuller, The University of Alabama in Huntsville

Adaptive Critic Neural Network-Based Terminal Area Energy Management and Approach and Landing Guidance
Katie Grantham, University of Missouri-Rolla

Magnetized Target Fusion Propulsion: Plasma Injectors for MTF Guns
Steven Griffin, The University of Memphis

Investigation of Methods for Supporting Tall, Slender Structures for Free-Free Modal Testing
Allen Fort Gwinn, Lipscomb University

Standards Advisor-Advanced Information Technology for Advanced Information Delivery
Scott Hawker, The University of Alabama

Creation and Implementation of a Workforce Development Pipeline Program at MSFC
Billy Hix, Motlow College

The Physics of Solar Sails
William Hollerman, University of Louisiana at Lafayette

Development of Low-Density Silica Particles for SHIVA
Njeri Karangu, Spelman College

Finite Element Modeling of a Cylindrical Contact Using Hertzian Assumptions
Erik Knudsen, University of Florida

Torque Limit for Bolted Joint For Composites: Experimentation
Kristian Kostreva, Embry-Riddle Aeronautical University

Parallel Information Processing (Image Transmission Via Fiber Bundle and Multimode Fiber)
Nickolai Kukhtarev, Alabama A&M University

The Land Use and Land Cover Dichotomy: A Comparison of Two Land Classification Systems in Support of Urban Earth Science Applications
William McAllister, Alabama A&M University

Concentration and Velocity Gradients in Fluidized Beds
Jim McClymer, The University of Maine

Development of Processing Parameters for Organic Binders Using Selective Laser Sintering
Amir Mobasher, Alabama A&M University

Fatigue and Fracture Analyses of Cracks in Ductile Materials
James Newman, Mississippi State University

Self-Consistent Large-Scale Magnetoshere-Ionosphere Coupling: Computational Aspects and Experiments
Tim Newman, The University of Alabama in Huntsville

Investigation of Structural Properties of Carbon-Epoxy Composites Using Embedded Fiber-Optic Bragg Gratings
Albert Osei, Oakwood College

Low-Energy Study of Gamma-Ray Bursts Having Spectral Line Features
Michael Pangia, Georgia College & State University

Metal Cutting Theory and Friction Stir Welding Tool Design
Lewis Payton, Auburn University

Using CASE to Exploit Process Modeling in Technology Transfer
Cheryl Renz-Olar, The University of Alabama in Huntsville

Independent Review of the Failure Modes of F-1 Engines and Propellant System
Paul Ray, The University of Alabama

NASA's Bioreactor: Growing Cells in a Simulated Microgravity Environment
Denise Richardson, Mississippi State University

Membrane-Based Gas Traps for Ammonia, Freon-21, and Water Systems to Simplify Ground Processing
Stephen Ritchie, The University of Alabama

Measuring Organizational Communication Health
Edward Rogers, The University of Alabama in Huntsville

Manufacturing Development for 100-kW Thermonuclear Simulator
Russell Rosmait, Pittsburg State University

Thermo-Mechanical Processing in Friction Stir Welds
Judy Schneider, Mississippi State University

Potential of Sintered Regolith Materials for Derivation of *In-Situ* Resource Utilization
Lois Schwarz, The University of Alabama in Huntsville

Preliminary Design, Feasibility and Cost Evaluation of 1- to 15-Kilometer Height Steel Towers
Ajay Shanker, University of Florida

Active and Passive Control of ISS Rack Shelf Vibrations
Steve Shepard, The University of Alabama

Comparative Study of Two Kinematics and Dynamics Analysis Tools for Multi-body Systems
Paul Shiue, Christian Brothers University

Probable Disastrous Consequences of Collision Between Unknown Small (100 m) Asteroids with Known (~1 km) Near Earth Orbiting (NEO) Asteroids
Larry Smalley, The University of Alabama in Huntsville

Lightning Location
Richard Solakiewicz, Chicago State University

A Computational Method for Determining the Equilibrium Composition and Product Temperature in a LH_2/LOX Combustor
Mehmet Sozen, Embry-Riddle Aeronautical University

Phase Retrieval Using a Genetic Algorithm on the Systematic Image-Based Optical Alignment Testbed
Jaime Taylor, Austin Peay State University

Using CASE to Adopt Organizational Learning at NASA
Gary Templeton, The University of Alabama in Huntsville

Impedance-Based Structural Health Monitoring for Composite Laminates at Cryogenic Environments
Kevin Tseng, Vanderbilt University

An Accident in History: *Challenger* in Perspective
Stephen Waring, The University of Alabama in Huntsville

Evaluation of Advanced Computing Techniques and Technologies: Reconfigurable Computing
Buren Wells, The University of Alabama in Huntsville

Torque Limit for Bolted Joint for Composites: TTTC Properties of Laminated Composites
Yi Zhao, Embry-Riddle Aeronautical University

REPORT DOCUMENTATION PAGE

Form Approved
OMB No. 0704-0188

Public reporting burden for this collection of information is estimated to average 1 hour per response, including the time for reviewing instructions, searching existing data sources, gathering and maintaining the data needed, and completing and reviewing the collection of information. Send comments regarding this burden estimate or any other aspect of this collection of information, including suggestions for reducing this burden, to Washington Headquarters Services, Directorate for Information Operation and Reports, 1215 Jefferson Davis Highway, Suite 1204, Arlington, VA 22202-4302, and to the Office of Management and Budget, Paperwork Reduction Project (0704-0188), Washington, DC 20503

1. AGENCY USE ONLY *(Leave Blank)*	2. REPORT DATE	3. REPORT TYPE AND DATES COVERED
	April 2003	Contractor Report (Final)

4. TITLE AND SUBTITLE

The 2002 NASA Faculty Fellowship Program Research Reports

5. FUNDING NUMBERS

NAG8–1859

6. AUTHORS

Program Co-Directors: S.K. Nash-Stevenson, C.L. Karr,* L.M. Freeman,* and G. Karr** (Program Co-Directors) J. Bland (Compiler and Editor)

7. PERFORMING ORGANIZATION NAMES(S) AND ADDRESS(ES)

The University of Alabama, Tuscaloosa, AL
The University of Alabama in Huntsville, Huntsville, AL

8. PERFORMING ORGANIZATION REPORT NUMBER

M–1074

9. SPONSORING/MONITORING AGENCY NAME(S) AND ADDRESS(ES)

National Aeronautics and Space Administration
Washington, DC 20546

10. SPONSORING/MONITORING AGENCY REPORT NUMBER

NASA/CR—2003–212397

11. SUPPLEMENTARY NOTES

*The University of Alabama, Tuscaloosa, AL
**The University of Alabama in Huntsville, Huntsville, AL
Prepared for Education Programs Department, Customer and Employee Relations Directorate

12a. DISTRIBUTION/AVAILABILITY STATEMENT

Unclassified-Unlimited
Subject Category 99
Standard Distribution

12b. DISTRIBUTION CODE

13. ABSTRACT *(Maximum 200 words)*

For the 38th consecutive year, a NASA Faculty Fellowship Program was conducted at Marshall Space Flight Center (MSFC). The program was conducted by The University of Alabama and MSFC May 28–August 2, 2002. Operated under the auspices of the American Society for Engineering Education, the MSFC program, as well as those at other NASA Centers, was sponsored by the University Affairs Office, NASA Headquarters, Washington, DC. The basic objectives of the program, which is in its 38th year of operation nationally, are to: (1) Further the professional knowledge of qualified engineering and science faculty members, (2) stimulate an exchange of ideas between participants and NASA, (3) enrich and refresh the research and teaching activities of the participants' institutions, and (4) contribute to the research objectives of the NASA Centers. The Faculty Fellows spent 10 weeks at MSFC engaged in a research project compatible with their interests and background and worked in collaboration with a NASA MSFC colleague. This CD is a compilation of Fellows' reports on their research during the summer of 2002.

14. SUBJECT TERMS

avionics; structures; mechanics; materials, processes, and manufacturing; flight projects; safety, reliability, and quality assurance; space science; optics; propulsion; vehicles development

15. NUMBER OF PAGES

291

16. PRICE CODE

17. SECURITY CLASSIFICATION OF REPORT	18. SECURITY CLASSIFICATION OF THIS PAGE	19. SECURITY CLASSIFICATION OF ABSTRACT	20. LIMITATION OF ABSTRACT
Unclassified	Unclassified	Unclassified	Unlimited

2002

NASA FACULTY FELLOWSHIP PROGRAM

MARSHALL SPACE FLIGHT CENTER
THE UNIVERSITY OF ALABAMA

SYSTEM IDENTIFICATION OF X33 USING NEURAL NETWORK

Prepared By:	Shiv Aggarwal
Academic Rank:	Professor
Institution and Department:	Embry Riddle Aero. University Department of Physical Sciences
NASA/MSFC Directorate:	Space Transportation
MSFC Colleagues:	Drs. John Hanson & Chong Lee

Introduction

Modern flight control research has improved spacecraft survivability as its goal. To this end we need to have a failure detection system on board. In case the spacecraft is performing imperfectly, reconfiguration of control is needed. For that purpose we need to have parameter identification of spacecraft dynamics.

Parameter identification of a system is called system identification. We treat the system as a black box which receives some inputs that lead to some outputs. The question is: what kind of parameters for a particular black box can correlate the observed inputs and outputs? Can these parameters help us to predict the outputs for a new given set of inputs? This is the basic problem of system identification.

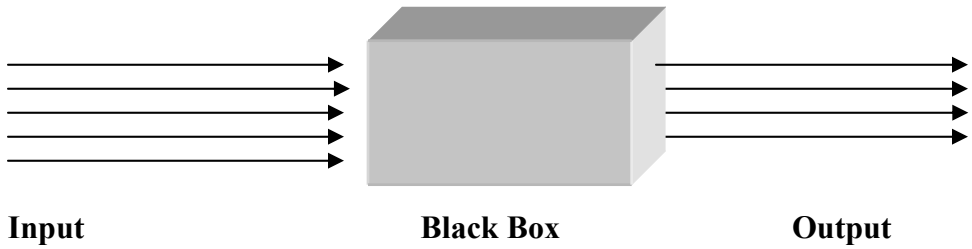

The X33 was supposed to have the onboard capability of evaluating the current performance and if needed to take the corrective measures to adapt to desired performance [3]. The X33 is comprised of both rocket and aircraft vehicle design characteristics and requires, in general, analytical methods for evaluating its flight performance [9].

Its flight consists of four phases: ascent, transition, entry and TAEM (Terminal Area Energy Management) [4]. It spends about 200 seconds in ascent phase, reaching an altitude of about 180,000 feet and a speed of about 10 to 15 Mach. During the transition phase which lasts only about 30 seconds, its altitude may increase to about 190,000 feet but its speed is reduced to about 9 Mach. At the beginning of this phase, the Main Engine is Cut Off (MECO) and the control is reconfigured with the help of aerosurfaces (four elevons, two flaps and two rudders) and reaction control system (RCS). The entry phase brings down the altitude of X33 to about 90,000 feet and its speed to about Mach 3. It spends about 250 seconds in this phase. Main engine is still cut off and the vehicle is controlled by complex maneuvers of aerosurfaces. The last phase TAEM lasts for about 450 seconds and the altitude and speed, both are reduced to zero.

The present attempt, as a start, focuses only on the entry phase. Since the main engine remains cut off in this phase, there is no thrust acting on the system. This considerably simplifies the equations of motion. We introduce another simplification by assuming the system to be linear after some non-linearities are removed analytically from our consideration. Under these assumptions, the problem could be solved by Classical Statistics by employing the least sum of squares approach. Instead we chose to use the Neural Network method. This method has many advantages. It is modern, more efficient, can be adapted to work even when the assumptions are diluted. In fact, Neural Networks try to model the human brain and are capable of pattern recognition.

Variables of the Project

In this section we will mention all the variables used in this project.

Input Variables

α, β, = vehicle angle of attack, vehicle angle of side slip (both measured in radians)
p, q, r = body axis roll rate, pitch rate and yaw rate (in radians per second)
M, A = Mach Number (dimensionless) and Altitude (in kilometers)
δts, δ_{ta}, δ_{fa} , δ_{rud} = symmetric trail deflection, asymmetric trail deflection, asymmetric flap deflection, rudder deflection (all in radians)

Output Variables

αd, βd, pd, qd, rd = time rate of change(d for dot) of associated variables (first two in rad/s, the last three in rad/s^2)

Other Variables

γ, μ = flight path angle, bank angle (about the velocity vector) (both in radians)
g_0, g_Y, g_L = gravitational acceleration in earth z-axis, Components of g_0 along the wind Y, and Z axis (all in ft/s^2). Also $g_Y = g_0 \cos\gamma \sin\mu$ and $g_L = g_0 \cos\gamma \cos\mu$
I_{ii}, I_{ij} = Vehicle body axes (moment, product) of inertia (in slug.ft^2) $\Gamma = I_{xx}.I_{zz} - I_{xz}^2$
V, m = Vehicle velocity (ft/s), Vehicle mass (slug)
Y, L = lateral force along the wind Y-axis, aerodynamic lift along negative wind Z-axis (in lb)
Lb, Mb, Nb = rolling, pitching and yawning moments (in ft-lb)

Equations of Motion

ANSI/AIAA recommended practice of using wind-axis force balances has been adopted. The angular equations of motion are resolved in body (not wind) axes system. The five equations of motion can be written in the matrix form OP = LP + NP where the actual output OP, linear part LP and nonlinear part NP are all 5 x 1 column matrices. Five elements of OP are the output variables αd, βd, pd, qd and rd. Five elements of LP are $-L/(mV \cos\beta) + g_L/(V \cos\beta)$, $Y/(mV) + g_Y/V$, $(I_{zz}.Lb + I_{xz}.Nb)/\Gamma$, Mb/I_{yy}, and $(I_{xz}.Lb + I_{xx}.Nb)/\Gamma$. Five elements of NP are $q - \tan\beta.(p \cos\alpha + r \sin\alpha)$, $p \sin\alpha - r \cos\alpha$, $I_{xz}.(I_{xx} - I_{yy} + I_{zz}).p.q/\Gamma + (Izz.(I_{yy} - I_{zz}) - I_{xz}^2).q.r/\Gamma$, $(I_{zz} - I_{xx}).p.r/I_{yy} + I_{xz}.(r^2 - p^2)/I_{yy}$, and $(I_{xx}.(I_{xx} - I_{yy}) + I_{zz}^2).p.q/\Gamma - I_{xz}.(I_{xx} - I_{yy} + I_{zz}).q.r/\Gamma$.

Methodology

Matrix NP basically arises because of the inertial cross couplings. Data (250 observations) was obtained from 6DOF (six degrees of freedom) MAVERIC (Marshall Aerospace Vehicle Representation In C) simulation from lift off to TAEM. NP was computed for each observation and then was subtracted from the corresponding output observations. Modified output OPM was given by OPM = OP – NP. This reduced the equations of motion to the matrix form OPM = LP.

Another assumption was made. We assumed LP = W*IP where W was the 12 x 5 weight (system identification) matrix and the input IP was the 12 x 1 input column matrix. This assumption is equivalent to saying that elements of OPM are the linear combinations of the elements of IP. The elements of matrix W were identified by training the neural network through the supervised learning. Five artificial neurons were used in the network, one for each output. Widrow-Hoff Delta learning rule was employed.

Results

All the 60 parameters of the problem (60 elements of W matrix) were successfully identified. The results were satisfactory, but not perfect. The imperfections are due to the nonlinearity in W because of the nonlinear dependence on β. Another source of imperfection is the time series nature of data which results in the multicollinearity problems. But both these problems are surmountable, given more time to analyze the problem.

Future Scope of the Project

The first next logical step would be to take care of some of the known weaknesses of the model, like a better treatment of the nonlinearities. Neural Network approach is an excellent tool for the purpose. On the mathematics side one may like to incorporate radial or Volterra orthogonal polynomials. The problem of multicollinearity introduced by the time series nature of the data may be handled by giving some weight to the past observations. The second step would be system identification in the ascent and transition phase of the flight. A last step might be to combine everything we have learnt in an attempt to automate the system.

Resources

This project required the use of many software tools. The main software chosen for the project were MATLAB [2],[10],[11] and NEURAL NETWORK TOOLBOX. MATLAB is software dealing with the manipulation of matrices and NEURAL NETWORK TOOLBOX deals with the methodologies of neural networks. A number of books from Redstone Scientific Information Center (RSIC) provide wealth of information related to the project [1],[3],[6],[7],[8].

Conclusion

The problem of System Identification can be perhaps adequately handled by using the presently available resources provided by MATHLAB and NEURAL NETWORK TOOLBOX.

Acknowledgements

The author would like to thank the entire team of engineers and scientists in the vehicle flight mechanics group of the Marshall Space Flight Center's Space Transportation Directorate.

Warren Adams provided the most needed computer hardware support. Bradley Burchett, Mehmet Sozen, and Ashok Batra were generous with their time in clarifying some of the subtleties of Computer Software. My MSFC colleagues Drs. John Hanson and Chong Lee were kind and amiable. They provided guidance without any reservations, whenever I needed.

References

[1] Cooper (1998). *Introduction to Partial Differential Equations with MATLAB,* Birkhauser

[2] Etter (1993), *Engineering Problem Solving with MATLAB*, Prentice Hall

[3] Hagan, Demuth & Beale (1996), *Neural Network Design,* PWS Publishing Company

[4] Hall C.E., Gallaher M.W., and Hendrix N.D. (1998). X33 Attitude Control System Design for Ascent, Transition, and Entry Flight Regimes, AIAA-98-4411 American Institute of Aeronautics and Astonautics, pp 1-10

[5] Hanson J.M. (2002). A plan for Advanced Guidance and Control Technology for 2nd generation Reusable Launch Vehicles AIAA Guidance, Navigation & Control Conference Proceedings pp 1-10

[6] Ogata (1994), *Designing Linear Control Systems with MATLAB,*Prentice Hall

[7] Ogata (1994), *Solving Control Engineering Problems with MATLAB*, Prentice Hall

[8] Tsoukalas & Uhrig (1997), *Fuzzy and Neural Approaches in Engineering*, John Wiley & Sons, Inc

[9] Ward D.G., Monaco J.F., and Bodson, M. (1998). Development and Flight Testing of a Parameter Identification Algorithm for Reconfigurable Control, Journal of Guidance, Control and Dynamics Vol. 21, No. 6, pp 948-956

[10] William Palm III (2001), *Introduction to MATLAB 6 for Engineers*, McGraw Hill

[11] Wilson & Turcotte (1997), *Advanced Mathematics and Mechanics Applications using MATLAB,* CRC Press

2002

NASA/ASEE SUMMER FACULTY FELLOWSHIP PROGRAM

MARSHALL SPACE FLIGHT CENTER
THE UNIVERSITY OF ALABAMA

ADVANCED CERAMIC TECHNOLOGY FOR SPACE APPLICATIONS AT NASA-MSFC

Prepared By:	Mohammad A. Alim, Ph.D.
Academic Rank:	Associate Professor
Institution and Department:	Alabama A & M University Department of Electrical Engineering P.O. Box 297, Normal, Alabama 35762
NASA/MSFC Directorate:	Engineering
MSFC Colleague:	Mr. Cydale C. Smith Materials Process and Manufacturing Department ED 34

Introduction

The ceramic processing technology using conventional methods is applied to the making of the state-of-the-art ceramics known as *smart ceramics* or *intelligent ceramics* or *electroceramics*.[1,2] The *sol-gel* and *wet chemical* processing routes are excluded in this investigation considering economic aspect and proportionate benefit of the resulting product. The use of ceramic ingredients in making coatings or devices employing vacuum coating unit is also excluded in this investigation. Based on the present information it is anticipated that the conventional processing methods provide identical performing ceramics when compared to that processed by the chemical routes. This is possible when sintering temperature, heating and cooling ramps, peak temperature (sintering temperature), soak-time (hold-time), etc. are considered as variable parameters. In addition, optional *calcination step* prior to the sintering operation remains as a vital variable parameter. These variable parameters constitute a *sintering profile* to obtain a sintered product. Also it is possible to obtain identical products for more than one sintering profile attributing to the *calcination step* in conjunction with the variables of the sintering profile. Overall, the state-of-the-art ceramic technology is evaluated for potential thermal and electrical insulation coatings, microelectronics and integrated circuits, discrete and integrated devices, etc. applications in the space program.

The ceramic systems are randomly oriented single/poly-phase polycrystalline semiconductors. These systems are based on oxides or non-oxides or some sort of hybrid composites comprising of both. Lightweight ceramic materials are continuously searched for variety space applications as sensors, microelectronic devices and circuits, insulators, coatings, radiation shielding, energy conversion, mechanical and structural support, etc. Utilizing traditional ceramic processing methods followed by sintering in conjunction with the calcining step is emphasized for better performing ceramic body. It is visualized that traditional ceramic processing methods are economic routes for making active stable devices, corrosion preventing coatings, non-degrading insulators and structures, etc. Therefore, smart ceramics imply effective ceramic bodies that are successfully used in the severe or the hostile application field without failure or having increased longevity.

Processing/Fabrication of Ceramics

The ceramic processing technique involves slurry and spray-dried granule preparation for conventional sintering using high temperature kiln. The *microwave sintering* and the *laser sintering* are not included in this investigation. The slurry preparation depends on the raw ingredients as the surface charges of the particles play an important role to constitute *zeta potential*. The zeta potential results from the lumped surface charges contributed by each particle from the dangling bonds. The nature of the charge density dictates the *p*H of the slurry and, thus, related to the zeta potential. In general, high zeta potential indicates *well-dispersed* slurry while low zeta potential indicates *weakly or strongly flocculated* slurry. In addition, agglomeration of the particles is also a severe issue caused by the van der Waals surface forces. Agglomerated powders do not fill the space efficiently. Both flocculation and agglomeration result in voids in the microstructure of the final product.

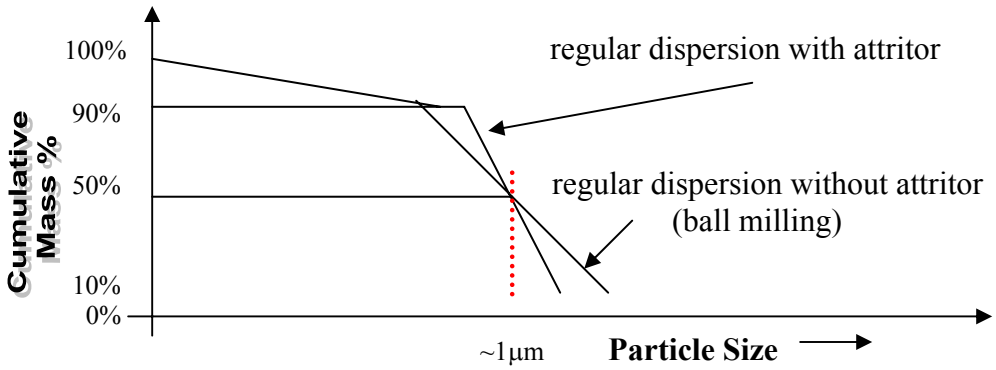

Figure 1: Particle size analysis of the powder.

The *p*H controlled *organic surfactants* are used as the dispersing agent to obtain better dispersion by removing flocculation and agglomeration. The organic binder is also used during the slurry preparation that also plays a role in achieving well-dispersed slurry possessing low viscosity of the non-Newtonian fluid. These organics are removed via the binder-burn-out operation prior to sintering. Again, the uniform particle size distribution plays vital role for the well-dispersed slurry. The particle size is measured at *50 cumulative mass percent* shown in Figure 1. The attritor milling system usually improves the distribution pattern of the particle size via narrowing down the broader distribution obtained by the conventional ball milling. After the slurry is prepared, granular powder is obtained via spray drying. The near loss-less condition for the amount of the granular spray-dried powder is achieved via the adjustment of the *orifice size* and *nozzle air pressure*. The granular powder, containing moisture, is used for pressing into desired geometry.

Effect of Sintering

The sintering operation can be initiated for both *calcined* and *non-calcined* processing routes. When the ingredients are calcined they need to be processed again by controlling the particle size for better dispersion and spray-drying operation. *The calcining operation allows forming single-phase or unified crystal structure* usually below 1000°C. It also allows better-dispersed slurry for certain multi-component ceramic systems. The multi-structure particles cause variation in the charge distribution without calcining operation affecting zeta potential. Thus, the calcining step is an additional operation depending on the type of the ingredients. The calcined phase may be treated as the single-phase like system or single-cation like dopant in the host material.

The sintering profile uses desired heating and cooling ramps with a soak-time (hold-time). *These ramps aid to develop desired electrical, mechanical, and structural characteristics*. Typical sintering profiles are depicted in Figure 2. More than one sintering profile can provide products possessing identical electrical, mechanical, and structural properties.[3,4] However, the degree of homogeneity in the operative electrical paths between the electrodes across the sample may vary. Each polycrystalline material exhibits *trapping effect* that can be minimized by adjusting the sintering profile. Each sintering profile may be replaced by another sintering profile via the manipulation of the heating and cooling curves or soak-time causing identical non-Debye response for the resulting products.

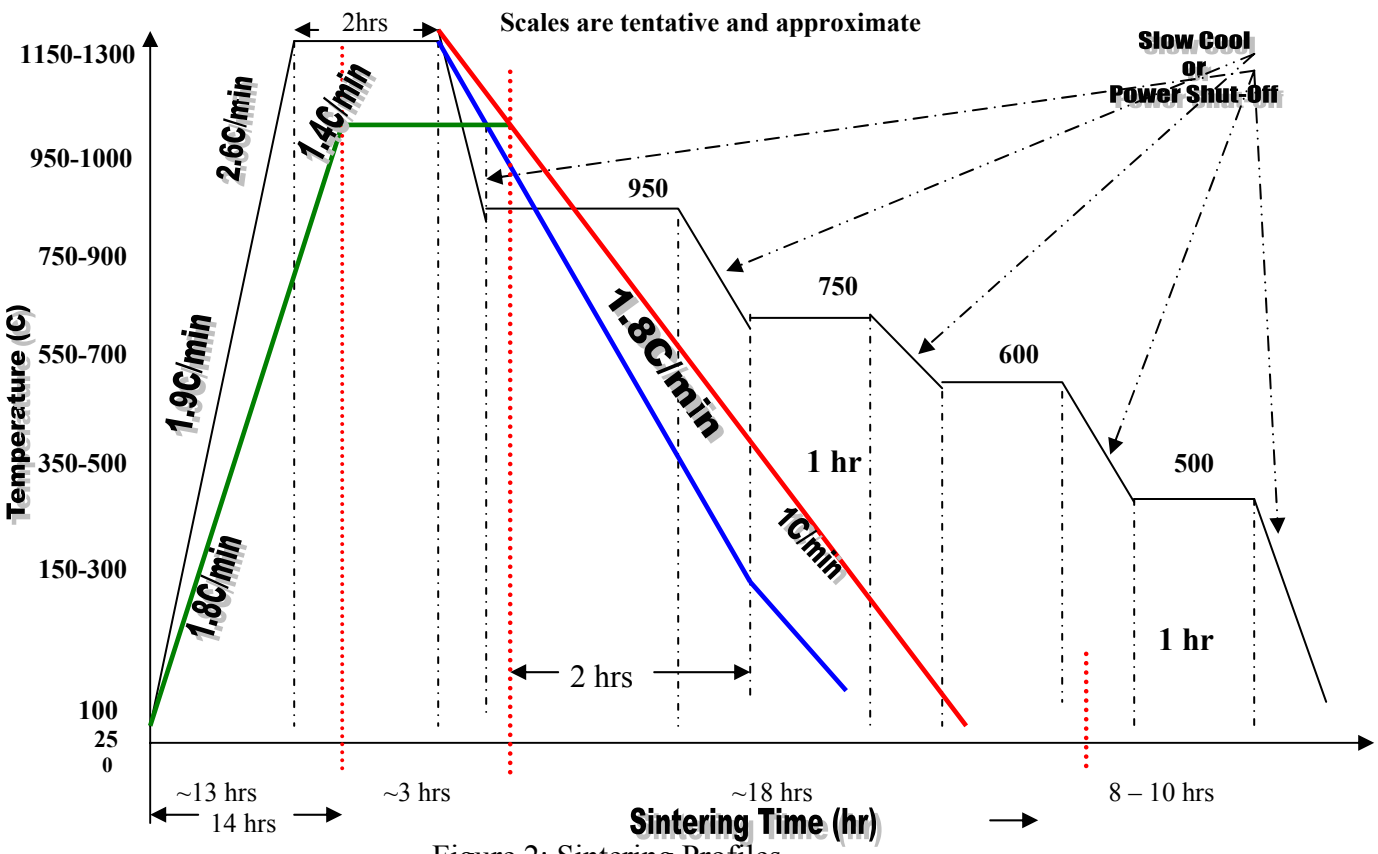

Figure 2: Sintering Profiles.

Sintering operation provides solid-state reaction process. Often causes liquid-phase sintering. Thus, sometimes the resulting shape of the products changes. Also liquid-phase sintering causes better compaction and densification of the sintered body possessing better grain-size. Usually multiple-phase microstructure results from multi-component starting recipe regardless of calcination. The soak-time usually causes the lattice sites adjusted and re-arranged with the doping process of the added cations.[3] The cooling ramp often can be exercised in various forms as the post-heat treatment or annealing of the material.

Figure 3 illustrates the effect of sintering temperature on grain size.[3] It also documents linear increase of grain size with increasing sintering temperature. The dotted and solid curves represent grain size distribution following attritor-milled particles and ball-milled particles, respectively. The distribution of grain size for the attritor-milled particles is narrow regardless of the sintering temperature. Thus, attritor-milled particles provide better microstructures with increased homogeneity via distribution of grain size.

Recommendation and Future Program

A number of oxides and non-oxides have been procured for making ceramic bodies for potential space applications. NASA – MSFC needs to set-up both calcining and sintering operations including sophisticated characterization tools/techniques.[1,4] The competitive state-of-the-art ceramic processing technology will be conducive to the desired goals.

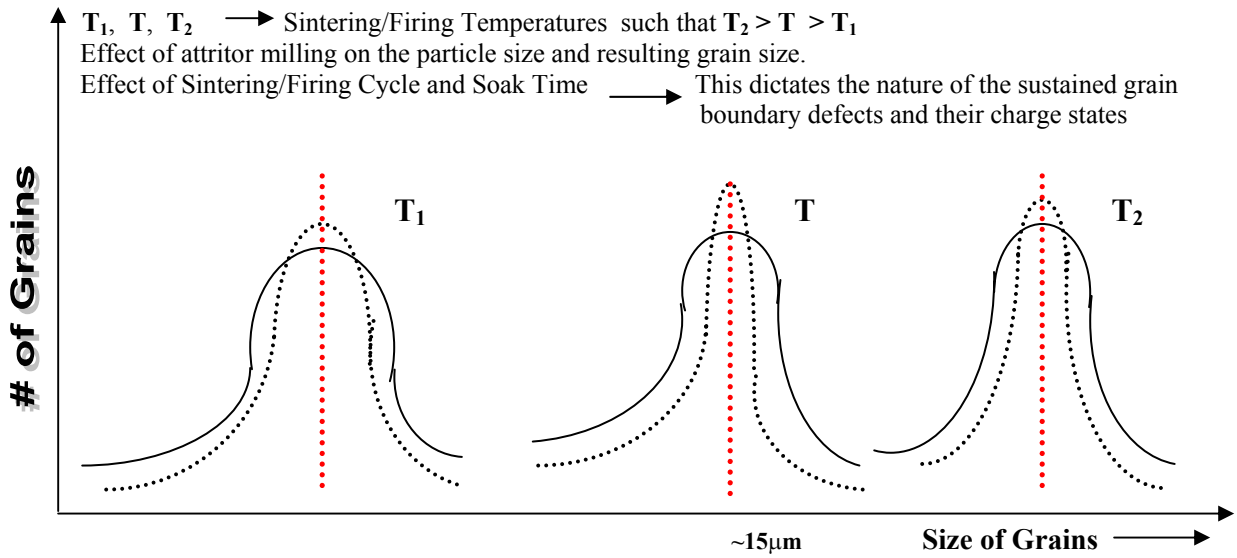

Figure 3: Effect of sintering temperature on grain size.

The existing kilns require precise controllers and real-time monitoring sintering profile (also calcination profile) including leak-less refractory materials. There are several in-house characterization tools such as SEM/EDXS, x-ray diffraction, vacuum coating unit, and etc. available for ceramic evaluation. However, addition of an Impedance Analyzer will be useful to complement information obtained via these characterization tools. Necessary information on the instrumentation such as MIC or Omega or Partlow temperature controllers, and the manufacturers of the kilns such as Harrop or Harper or Lindberg Blue M is provided to the NASA colleagues. In the near future additional Impedance Analyzer(s) may be needed to expand the frequency range data so that a broad window of interpretation becomes easy with better precision.

Acknowledgments

The author would like to thank NASA Summer Faculty Fellowship Program. Discussion with Mr. Cydale C. Smith including interactions with the summer co-op students in the ED34 laboratory is gratefully acknowledged.

References

[1] Alim, M. A. (1996), "Electrical Characterization of Engineering Materials," Active and Passive Electronic Components, Vol. 19, 139-169.
[2] Alim, M. A. (1996), "Phenomena Related To Concurrent Multiple Complex Plane Representations Of The Immittance Data," Materials Research Society Symposium Proceeding, Vol. 411, 113-125.
[3] Sletson, L.C., et al. (1988), "Influence of Sintering Temperature on Intrinsic Trapping in Zinc Oxide-Based Varistors," Journal of the American Ceramic Society, **71(11)**, 909-913 (1988).
[4] Alim, M. A. (1989), "Admittance-Frequency Response in Zinc Oxide Varistor Ceramics," Journal of the American Ceramic Society, Vol. 72(1), 28-32.

2002

NASA FACULTY FELLOWSHIP PROGRAM

MARSHALL SPACE FLIGHT CENTER
THE UNIVERSITY OF ALABAMA

DEVELOPING A MATLAB®-BASED TOOL FOR VISUALIZATION AND TRANSFORMATION

Prepared By:	Blake J. Anderton
Academic Rank:	Student (Undergraduate)
Institution and Department:	Lipscomb University Engineering Mechanics Department
NASA/MSFC Directorate:	Engineering
MSFC Colleague:	Ms. Kathy Kappus

Introduction

An important step in the structural design and development of spacecraft is the experimental identification of a structure's modal characteristics, such as its natural frequencies and modes of vibration. These characteristics are vital to developing a representative model of any given structure or analyzing the range of input frequencies that can be handled by a particular structure. When setting up such a representative model of a structure, careful measurements using precision equipment (such as accelerometers and instrumented hammers) must be made on many individual points of the structure in question. The coordinate location of each data point is used to construct a wireframe geometric model of the structure. Response measurements obtained from the accelerometers is used to generate the modal shapes of the particular structure. Graphically, this is displayed as a combination of the ways a structure will ideally respond to a specified force input.

Two types of models of the tested structure are often used in modal analysis: an analytic model showing expected behavior of the structure, and an experimental model showing measured results due to observed phenomena. To evaluate the results from the experimental model, a comparison of analytic and experimental results must be made between the two models. However, comparisons between these two models become difficult when the two coordinate orientations differ in a manner such that results are displayed in an unclear fashion. Such a problem proposes the need for a tool that not only communicates a graphical image of a structure's wireframe geometry based on various measurement locations (called *nodes*), but also allows for a type of transformation of the image's coordinate geometry so that a model's coordinate orientation is made to match the orientation of another model. Such a tool should also be designed so that it is able to construct coordinate geometry based on many different listings of node locations and is able to transform the wireframe coordinate orientation to match almost any possible orientation (i.e. it should not be a "problem specific" application) if it is to be of much value in modal analysis. Also, since universal files are used to store modal parameters and wireframe geometry, the tool must be able to read and extract information from universal files and use these files to exchange model data.

The purpose of this project is to develop such a tool as a computer graphical user interface (GUI) capable of performing the following tasks:

- Browsing for a particular universal file within the computer directory and displaying the name of this file to the screen.
- Plotting each of the nodes within the universal file in a useful, descriptive, and easily understood figure.
- Reading the node numbers from the selected file and listing these node numbers to the user for selection in an easily accessible format.
- Allowing for user selection of a new model orientation defined by three selected nodes.
- Allowing the user to specify a directory to which the transformed model's node locations will be saved, and saving the transformed node locations to the specified file.

Program Development

For this program, MATLAB 6.1 was chosen as the software most capable of generating the desired transformation results within a graphical user interface. A graphical user interface (GUI) is defined as a user interface built with graphical objects, such as buttons, text fields, sliders, and menus.

The programming process first began by sketching the most important attributes of the interface on paper to get an idea for what the finished program would resemble. Steps were taken to make sure every step necessary to achieving the project purpose were reflected in these design sketches. Using MATLAB 6.1's Graphical User Interface Development Environment (GUIDE) software, the following GUI figure was then designed as the program's graphical user interface.

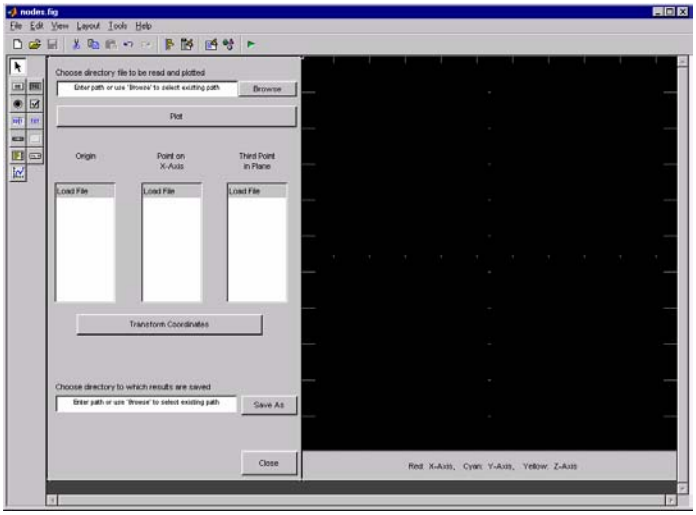

Figure 1: Layout of Program User Interface (using MATLAB 6.1 GUIDE)

As seen in Figure 1, the program was designed to be able to read a universal file, plot the unaltered geometry on the set of axes (in the darkened right half of the screen), extract and display a list of node numbers (in the three parallel, vertical listboxes), allow the user to select which three nodes constituted the transformation x-y plane by clicking nodes in the appropriate listboxes, transform the geometry to match the new x-y, and store the transformed geometry in a specified universal file.

One important note concerning the program coding between versions of MATLAB: while the code in the program was designed for use in MATLAB 6.1, it cannot be used in earlier versions of MATLAB (such as version 5.3). MATLAB's application m-files are designed to support a previous version's applications but will not support a later version's applications (i.e. code from version 6.1 will not run on version 5.3). The problems encountered when switching between different versions constituted much of the time used in program development (since the transformation code was developed using version 5.3).

Mathematical Theory

To show the mathematical basis for the nodal coordinate transformation, consider the figure below:

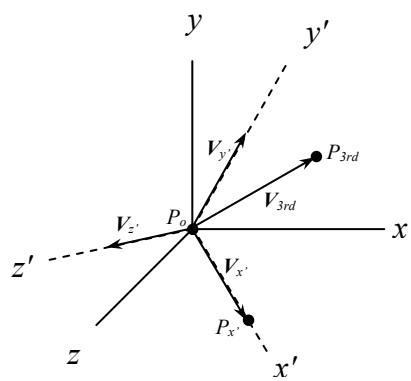

Figure 2: Example Coordinate transformation (from *xyz* to *x'y'z'* system)

Note that, unlike the above figure, the new origin does not have to have the same location as the original. The goal in transformation is to find matrix [*T*] that transforms coordinate locations defined by unit vectors in the *xyz* plane (denoted as [xyz]) to locations defined by unit vectors in the *x'y'z'* plane (denoted as [*x'y'z'*]). This is expressed as:

$$[T][xyz] = [x'y'z'] \qquad \textbf{(1)}$$

Note that unit vectors for the transformed plane are shown as $\boldsymbol{V}_{x'}$, $\boldsymbol{V}_{y'}$, and $\boldsymbol{V}_{z'}$. Finding [*T*] becomes much easier when unit vectors define point locations because the right hand side of the previous equation is simply the identity matrix (since each component has a magnitude of 1 in one of the three coordinate directions). The transformation matrix is then found as follows:

$$[T] = [xyz]^{-1} \qquad \textbf{(2)}$$

Also note that to find the unit vectors, the only points needed are the new origin P_o, a point $P_{x'}$ to define the *x'* axis, and a point P_{3rd} in the *x'-y'* plane. From these points, the vectors mentioned above can be found using cross products. The program is designed to give the user the option of choosing these three specific points from node locations.

Results

With the program appropriately designed coded to meet the previously stated objectives, testing was done using a number of sample models. This produced new ideas on program improvement and user accessibility. Features such as a black axes background and other details were added and error messages were designed to keep the user from making mistakes. Universal files with coordinates from the Italian heat exchanger tested by engineers from the Modal and Control Dynamics team at Marshall Space Flight Center were used in testing. The following figure

shows pictures of the program when first generating the plot (left) and after activating the transformation (right). Notice that the filename and filepath of the figure is displayed in both of the edit boxes (the features with white backgrounds on the left of the screen). This figure also shows that a top-front-side view is displayed along with an isometric view of the part's geometry.

Figure 3: Display of unaltered geometry (left) and transformed geometry.

Future Work and Applications for the Coordinate Transformer

The program successfully displays structure geometry and allows coordinate transformation along with an updated display of the transformed figure. The program also allows for rewriting data to stored universal files as well creating new universal files in which to store transformed (or untransformed) node coordinates. However, additional work can be done to make this program more applicable to modal analysis. A list of possible additional work to be done on the project is as follows:

- A feature showing the mode shapes can be added so that the analytical response of the structure in question can be observed directly from the universal file without having to transfer the file to another application in order to view mode shapes.
- A feature can be added to bring up a figure showing node numbers directly beside the nodes they represent.
- Other features such as right-click menus can allow for user display preferences.

References

[1] Ewins, D. J. (2000), *Modal Testing: Theory, Practice and Application, 2nd ed.*, Research Studies Press Ltd., pp. 1-23.

[2] *MATLAB® Online Help* (2002), "Using MATLAB: Creating Graphical User Interfaces", http://www.mathworks.com/access/helpdesk/help/techdoc/matlab.shtml

2002

NASA FACULTY FELLOWSHIP PROGRAM

MARSHALL SPACE FLIGHT CENTER
THE UNIVERSITY OF ALABAMA

SUBSURFACE STRESS FIELDS IN SINGLE CRYSTAL (ANISOTROPIC) CONTACTS

Prepared By:	Nagaraj K. Arakere
Academic Rank:	Associate Professor
Institution and Department:	University of Florida Mechanical & Aerospace Engineering Department
NASA/MSFC Directorate:	Engineering
MSFC Colleague:	Gregory R. Swanson

Introduction

Single crystal superalloy turbine blades used in high pressure turbomachinery are subject to conditions of high temperature, triaxial steady and fatigue stresses, fretting stresses in the blade attachment and damper contact locations, and exposure to high-pressure hydrogen. The blades are also subjected to extreme variations in temperature during start-up and shutdown transients. The most prevalent HCF failure modes observed in these blades during operation include crystallographic crack initiation/propagation on octahedral planes, and noncrystallographic initiation with crystallographic growth. Numerous cases of crack initiation and crack propagation at the blade leading edge tip, blade attachment regions, and damper contact locations have been documented. Understanding crack initiation/propagation under mixed-mode loading conditions is critical for establishing a systematic procedure for evaluating HCF life of single crystal turbine blades.

Techniques for evaluating two and three dimensional subsurface stress fields in anisotropic contacts are presented in this report. Figure 1 shows typical damper contact locations in a turbine blade. The subsurface stress results are used for evaluating contact fatigue life at damper contacts and dovetail attachment regions in single crystal nickel-base superalloy turbine blades.

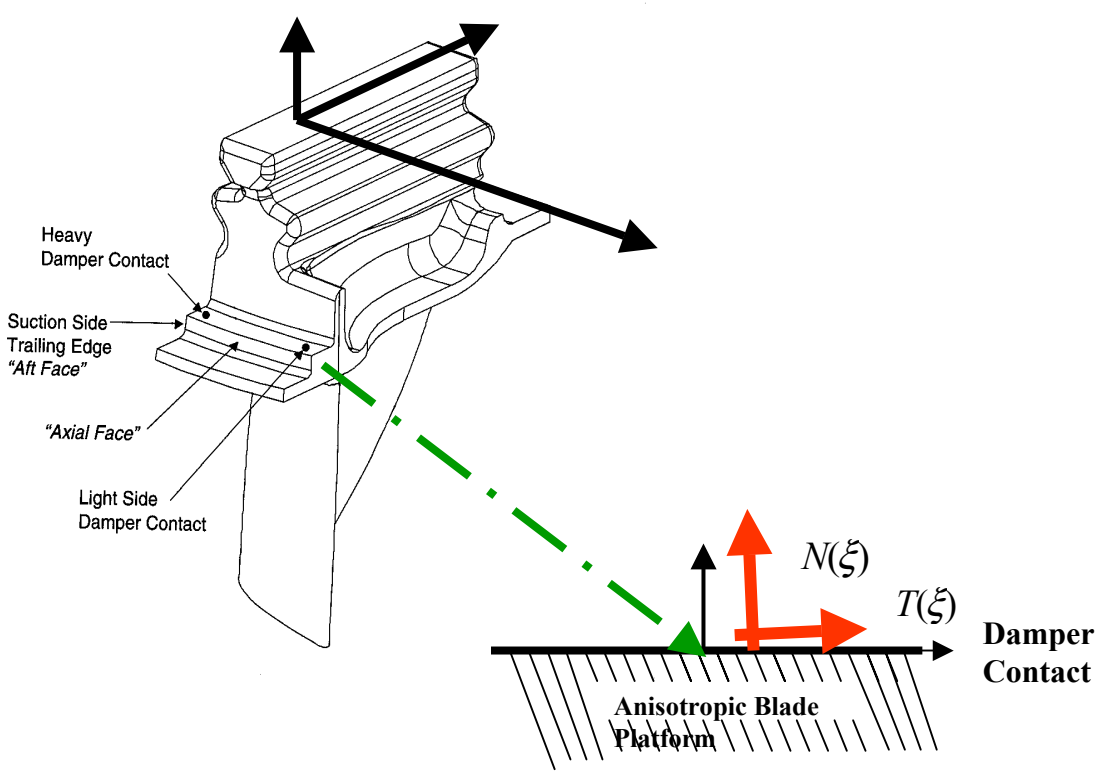

Figure 1: Damper contact locations on a typical turbine blade

Two-Dimensional Stress Distribution in an Anisotropic Elastic Half-Space

The damper contact regions shown in Figure 1 will be modeled as an elastic anisotropic half-space. This approximation is reasonable since Hertzian type contact stresses are confined to very small volumes in the vicinity of the contact. An analytical procedure will be presented for evaluating the subsurface stresses in the elastic half-space using a complex potential method outlined by Lekhnitskii [1]. Figure 2 shows the elastic half-space subjected to normal traction $N(\xi)$ and tangential traction $T(\xi)$ over the region –a to +a on the x-axis. The traction forces are independent of z, and functions of x and y only. The stresses are also functions of x and y only. Under the assumptions of generalized plane strain, the subsurface stresses due to the applied traction forces can be determined as outlined below.

The stress functions are given by

$$\phi_1'(z)+\phi_2'(z)+\lambda_3\phi_3'(z) = -\frac{1}{2\pi i}\int_{-a}^{+a}\frac{N(\xi)}{\xi - z}d\xi \tag{1}$$

$$\mu_1\phi_1'(z)+\mu_2\phi_2'(z)+\mu_3\lambda_3\phi_3'(z) = -\frac{1}{2\pi i}\int_{-a}^{+a}\frac{T(\xi)}{\xi - z}d\xi \tag{2}$$

$$\lambda_1\phi_1'(z)+\lambda_2\phi_2'(z)+\phi_3'(z) = 0 \tag{3}$$

The μ_i are the roots of the cylindrical characteristic equation, given by Eq. (4), and $z = x + \mu y$.

$$l_4(\mu).l_2(\mu) - l_3^2(\mu) = 0 \tag{4}$$

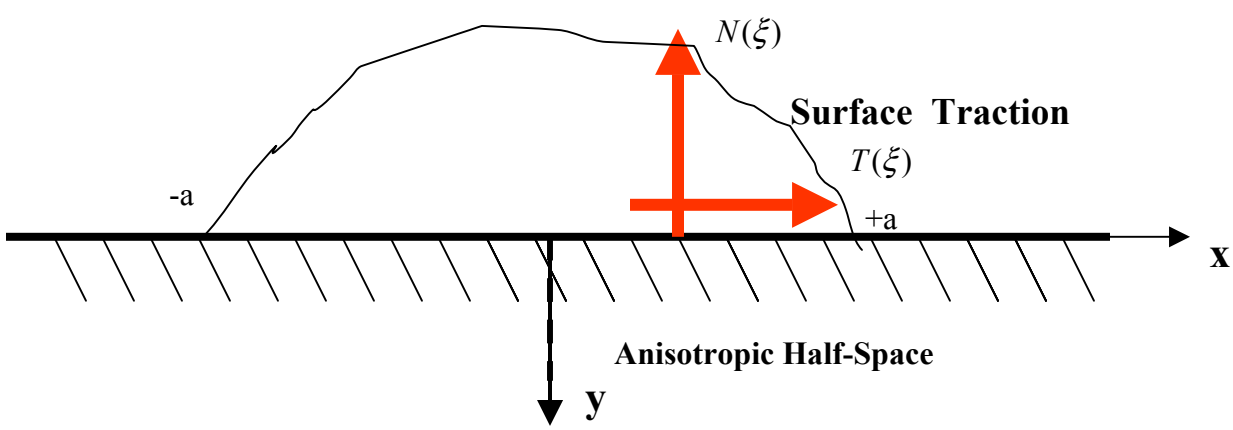

Figure 2: Anisotropic elastic half-space under generalized plane deformation subjected to normal and tangential traction forces.

$$l_2(\mu) = \beta_{55}\mu^2 - 2\beta_{45}\mu + \beta_{55}; \qquad l_3(\mu) = \beta_{15}\mu^3 - (\beta_{14} + \beta_{56})\mu^2 + (\beta_{25} + \beta_{46})\mu - \beta_{24}$$

$$l_4(\mu) = \beta_{11}\mu^4 - 2\beta_{16}\mu^3 + (2\beta_{12} + \beta_{66})\mu^2 - 2\beta_{26}\mu + \beta_{22}; \qquad \beta_{ij} = a_{ij} - \frac{a_{i3}.a_{j3}}{a_{33}} \tag{5}$$

$$\lambda_1 = -\frac{l_3(\mu_1)}{l_2(\mu_1)}, \quad \lambda_2 = -\frac{l_3(\mu_2)}{l_2(\mu_2)}, \quad \lambda_3 = -\frac{l_3(\mu_3)}{l_4(\mu_3)}$$

The matrix a_{ij} relates the strains to the stresses. The a_{ij} are functions of the crystal orientation. The stresses are then given by:

$$\sigma_x = 2\,\mathrm{Re}\left[\mu_1^2\phi_1'(z) + \mu_2^2\phi_2'(z) + \mu_3^2\lambda_3\phi_3'(z)\right]; \qquad \sigma_y = 2\,\mathrm{Re}\left[\phi_1'(z) + \phi_2'(z) + \lambda_3\phi_3'(z)\right]$$

$$\tau_{xy} = -2\,\mathrm{Re}\left[\mu_1\phi_1'(z) + \mu_2\phi_2'(z) + \mu_3\lambda_3\phi_3'(z)\right]; \qquad \tau_{xz} = 2\,\mathrm{Re}\left[\mu_1\lambda_1\phi_1'(z) + \mu_2\lambda_2\phi_2'(z) + \mu_3\phi_3'(z)\right]$$

$$\tau_{yz} = -2\,\mathrm{Re}\left[\lambda_1\phi_1'(z) + \lambda_2\phi_2'(z) + \phi_3'(z)\right] \tag{6}$$

$$\sigma_z = -\frac{1}{a_{33}}\left[a_{13}\sigma_x + a_{23}\sigma_y + a_{34}\tau_{yz} + a_{35}\tau_{xz} + a_{36}\tau_{xy}\right]; \qquad z_i = x + \mu_i y$$

The normal traction force $N(\xi)$ is given by the Hertzian cylindrical contact force as $N(\xi) = p_o\sqrt{1-\xi^2/a^2}$ and $T(\xi) = \mu_f p_o\sqrt{1-\xi^2/a^2}$, where p_o is the peak pressure and μ_f the coefficient of friction. The stress solution has been programmed in Mathcad and subsurface stresses computed for various crystal orientations. Figure 3 shows a representative half-space σ_y stress distribution for a = 0.01 inch, po = 260 ksi, and for the (x, y, z) axes parallel to the edges of the FCC crystal, i.e. x = <100>, y = <010> and z = <001>. The analytical solution shows good agreement with the finite element numerical solution.

Subsurface fretting fatigue cracks at the damper contacts caused by oscillatory tangential stresses, $T(\xi)$, is of much practical interest. Figure 4 shows the variation in resolved shear stress

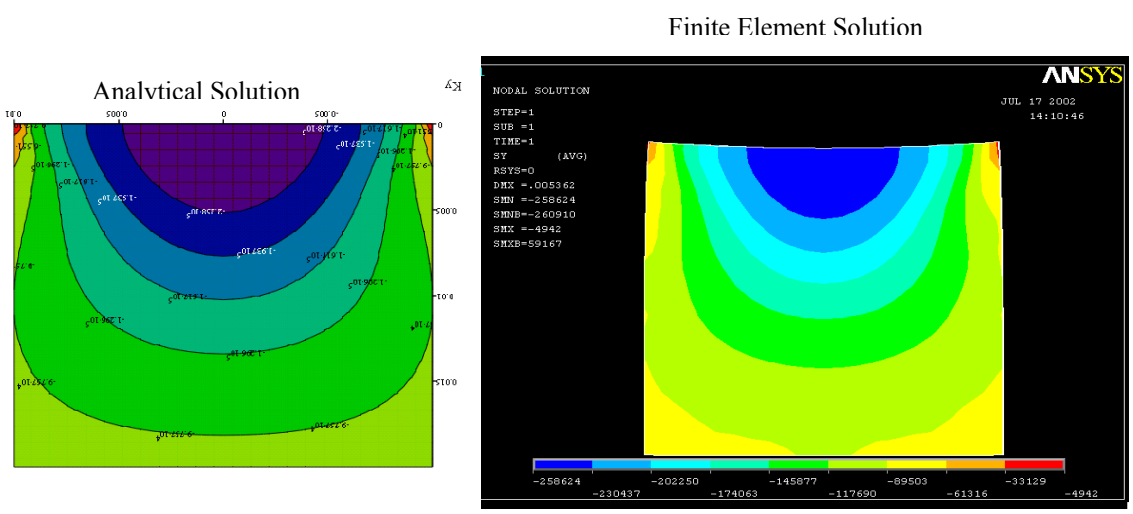

Figure 3: Stress (σ_y) contours using analytical solution and finite element (Ansys) solution

amplitude on the primary octahedral planes, as a function of secondary crystallographic orientation. It is seen that the highest resolved shear stress amplitude, $\Delta\tau_{rss}$, varies 32 percent as the secondary orientation varies from 0 to 90 deg. The secondary orientation of the blades is not controlled during the casting process and hence its variation can result in blade-to-blade variation in fatigue stresses ($\Delta\tau_{rss}$) at constant load, which is clearly undesirable from a design standpoint.

Conclusions

The two-dimensional analytical solution presented is an efficient and accurate method for obtaining contact stresses in anisotropic half-spaces. Finite element solution of contact problems is very tedious and requires highly refined meshes to obtain accurate stress solutions. Variation in secondary orientation between blades can result in large variation in fatigue life at damper contact locations.

Three-dimensional contact stress solutions for anisotropic half-spaces has also been obtained for elliptical contacts. Stress solutions have been obtained by linear superposition of a point-load solution outlined in Lekhnitskii [1]. The details of this solution could not be included in this report because of lack of space. Complete details of the 2D and 3D solutions will be documented in a future NASA Technical Publication.

Acknowledgements

The author would like to thank Gregory R. Swanson of the Marshall Space Flight Center's Engineering Directorate (ED22) for the summer program and also for supporting graduate student Erik Knudsen. Many thanks to Gilda Battista and Greg Duke at Sverdrup for numerous fruitful discussions, and for providing the finite element solutions to the contact problem.

References

[1] Lekhnitskii, S. G., "Theory of Elasticity of an Anisotropic Elastic Body," Holden Day, Inc. Publishers, San Francisco, 1963.

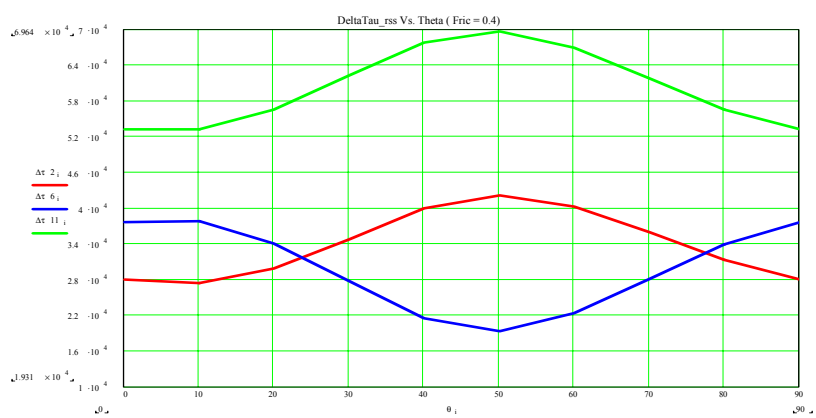

Figure 4: Effect of secondary orientation on resolved shear stress amplitude ($\Delta\tau_{rss}$)

2002

NASA FACULTY FELLOWSHIP PROGRAM

MARSHALL SPACE FLIGHT CENTER
THE UNIVERSITY OF ALABAMA

Our Space Future: A Challenge to the Conceptual Artist Concept Art for Presentation and Education

Prepared By :	Mary C Bangs
Academic Rank :	Tutor and Art Program Coordinator
Institution and Department :	Verizon / Corporate College Program Empire State College State University of New York
NASA / MSFC Directorate :	AD32A
MSFC Colleague :	Jack Hood Visual Information Specialist Graphics Coordinator

Introduction: Art and Human Culture

The history of visual representation is as old as the history of humankind. The Paleolithic drawings that are found in caves present our collective need for recording our dependence on the life-sustaining animal populations. Our wishes for their fertility (and for our own) comprise much of the art we find in these prehistoric drawings. As well, the cycles of the Moon are recorded in Paleolithic art—relating to women's estrus cycles that link the perpetuation of our species with the cosmos.

Art became our initial way of description and a way of envisioning our future goals. At the time when pictograms began to form humanity's first written languages, we also started to use art to invoke favorable forces and ward off devastation. Another important application of visual art became the conceptualization of tools, buildings and ideas that were impossible to describe by other means.

Humans have a historical tradition of considering visual images as vehicles to inspire us to pursue a different way of thinking through our ability of envisioning. Complex concepts can be described visually and have the ability to convey information on many different levels.
Conceptual art is a tool that can describe wide-ranging ideas from religious insights to currently unfeasible engineering projects and visionary dreams for humankind.

Some Preliminary Summer 2002 Applications of Conceptual Art to MSFC Programs

"Moonstruck Millie" was part of a project called "Rocket Racers," an animation project for NASA's Marshall Space Flight Center's web page. She was conceived as a vehicle to instruct children, age's kindergarten through fourth grade about the excitement and importance of space exploration. The other characters include "Rocket Rob", who will be one of the 6 or 7 characters comprising the ongoing instructional animated web site. "Moonstruck Millie" is portrayed as a young teenager who is interested in history and has the ability to move backwards and forwards in time, thereby enabling the her audience to meet historical figures involved with space travel.

I worked with Jack Hood, who had constructed an adolescent girl for another project. In my contribution to this project, I worked with him refining the figure and turning her into "Moonstruck Millie". In this effort, we applied the three-dimensional animation software program LightWave Modeler ™.

Art Contributions to an MSFC-Sponsored Workshop

The In-Space Manufacturing of Space Transportation Infrastructure Workshop was organized by Ann Trausch and supported by Gwen Artes and David Harris from Les Johnson's In-Space Propulsion Research group in the Space Transportation Directorate at MSFC. The workshop was scheduled for June 11-13, 2002 and held at the Huntsville Marriott. Various experts from

academia, government, and industry attended this workshop and presented their ideas on creating an expanded in-space infrastructure.

Ann Trausch and Gwen Artes requested that I sit in on various workshop discussion groups and sketch concept drawings of the following workshop themes: "Travel & Entertainment," "Research and Development in Space", "Space Manufacturing," "Solar System Exploration," and "Gateway Outposts." Other sketches to be worked on were included under the category titled "Legs." These include:
N-Integration, A-Ascent, O-Orbit, I-Interplanetary, Li-Libration Points, G-De-Integration.

The process of doing the drawings included researching existing NASA CAD-CAM constructions, engineering drawings and web searches for metaphoric material. Gwen Artes supplied the contact names of Debbie Soloman in MSFC graphics and Chieko Inman at the photo lab in the MSFC multi-media center. After meeting with them, Debbie Soloman at the photo lab burned a CD of images of next generation space transportation concepts. In preparation for my initial presentation, I incorporated these images with others from *NASA Tech Briefs* and *Innovation* magazines. Suggested websites for additional images included microgravity.nasa.gov, nasarp.msfc.nasa.gov and http://stin.nasa.gov. Other sources were brochures obtained during the NASA Summer Faculty Fellow tour of MSFC that included the Friction-Stir Welding Facility and the Thermal Spray Productivity Enhancement Complex.

The process of researching the images continued with further meetings where I would prepare drawings or research concepts and present them. Ideas would evolve as I met with Ann Trausch and we spoke of the goals of the workshop. The dialog continued to underscore the importance of Space Manufacturing and how it would enable us to achieve the "Stepping Stones" that would result in the ability to, "Go anywhere, anytime". Further discussion concluded that I work with both sketches and approved concept icons that would be collaged into my final drawings.

A Sampler of the Workshop Sketches

A total of 12 images were completed for the workshop proceedings volume. After scanning in or downloading imagery, collages were prepared and manipulated using the Adobe Photoshop ™ computer software package on a Macintosh G4 computer. Some of these are presented below.

Figure 1: Libration Points and Artificial Gravity Concept Vehicle

This collage, which includes a drawing, a CAD-CAM spacecraft concept, and Web-downloaded imagery, refers to the "gravity neutral" points between the Sun and the Earth. At the Libration points in the Earth-Sun system, solar and terrestrial gravity influences balance.

To present this concept, I drew an image of a scale with the Sun and Earth equally balanced. The other planets of the solar system are shown as they all have libration points in their relationship to the Sun. The constellation above the scale is "Libra," which symbolizes balance.

The "Artificial Gravity Concept Vehicle" collaged icon also includes the concept of balancing, at the center of it is a rotating centrifuge-like compartments that provides simulated gravity for the spacecraft's crew. Finally, a Web-downloaded cross section of DNA is between the Sun and Earth on the L1 Libration point as a reference to humankind's potential use of these concepts to spread life beyond the Earth.

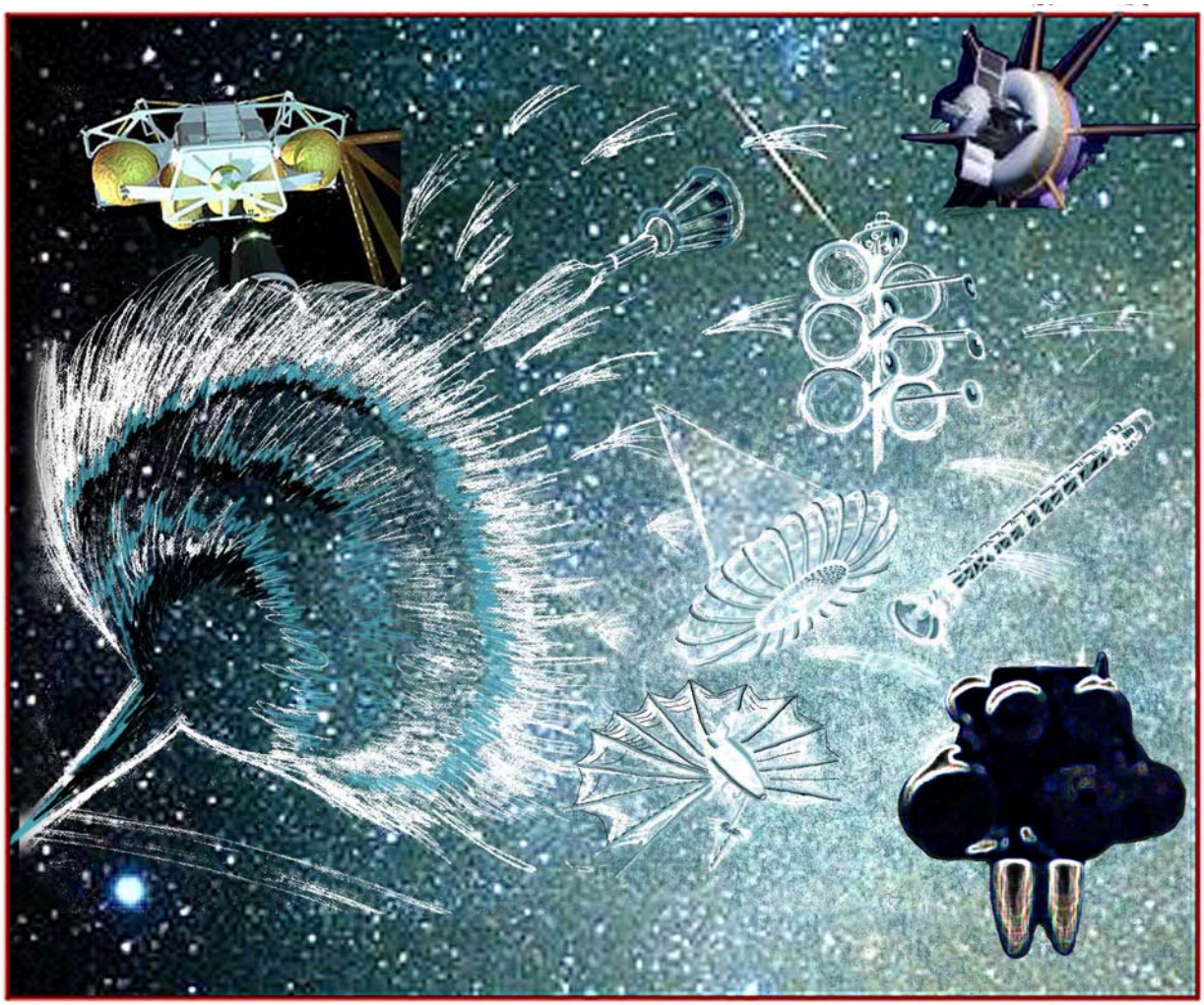

Figure 2 : De-Integration with Gateway, Mars Lander and Lunar Lander

This drawing/ collage features a cosmic flower that is spreading its seeds out to the cosmos. The collaged images feature a proposed Gateway architecture, the launch of a Mars Lander and a Lunar Lander. The line drawings feature an antimatter propulsion system, an advanced chemical propulsion system, a microwave lightcraft, a portion of a space solar-power station and a solar-electric propulsion concept. These concepts would enable humankind to manifest our destiny as Carl Sagan affirmed.

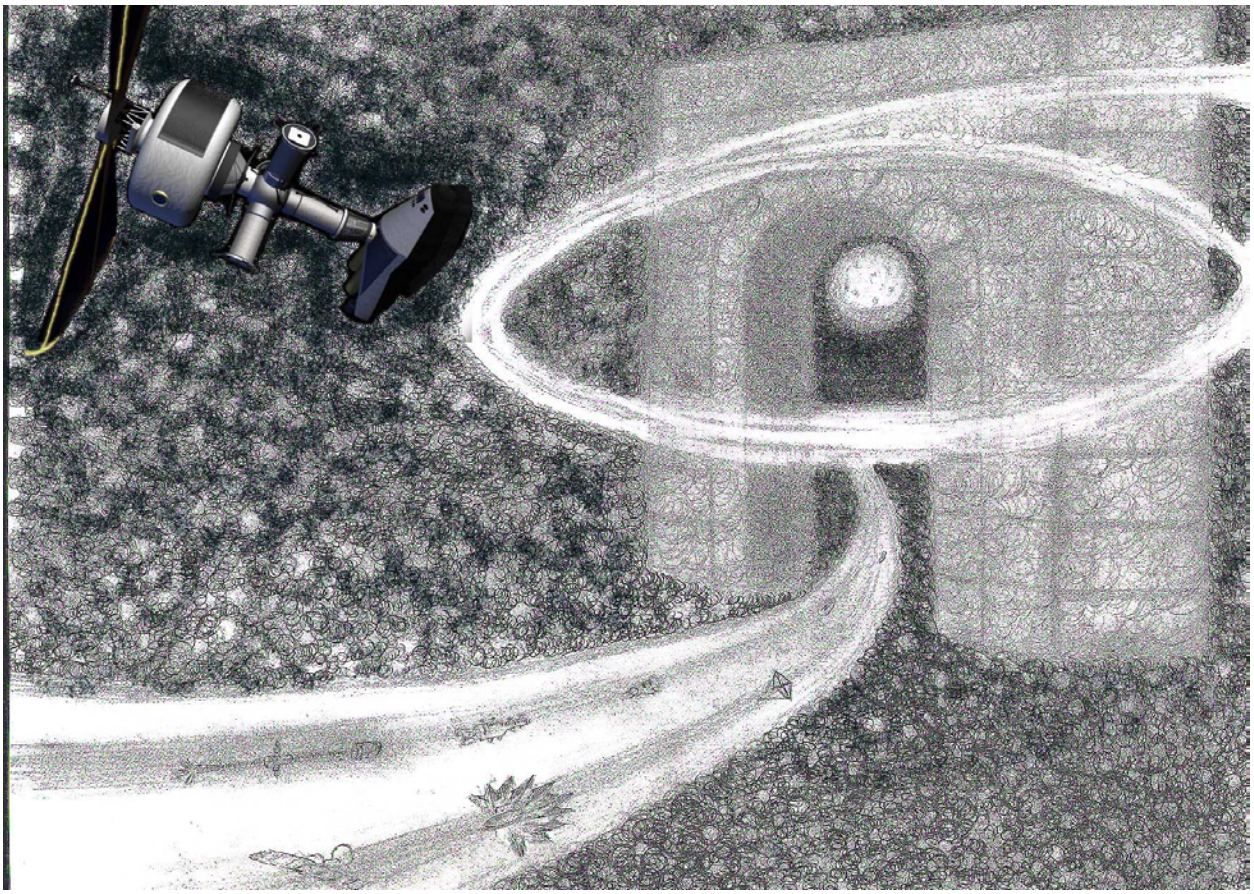

Figure 3. Gateway and Libration Highway with Tug

The Gateway is a phantom Roman arch that is positioned at the L1 Libration point where the cosmic highway encircles the Moon and then swings out to Mars and beyond. The vehicles that move along this highway include the solar-electric propulsion concept, a solar sail, and an artificial gravity concept vehicle among others too small to see clearly. Featured above is a CAD-CAM lunar tug.

Acknowledgements

The author would like to thank Jack Hood, Les Johnson, Ann Trausch, David Harris and Rodney Grubbs of MSFC, Gwen Artis of Gray Research, and the staff of the NASA MSFC Summer Faculty Program Office.

2002

NASA FACULTY FELLOWSHIP PROGRAM

MARSHALL SPACE FLIGHT CENTER
THE UNIVERSITY OF ALABAMA AT BIRMINGHAM

IDENTIFICATION AND CHARACTERIZATION OF EXTREMOPHILE MICROORGANISMS WITH SIGNIFICANCE TO ASTROBIOLOGY

Prepared by:	Asim K. Bej, Ph.D.
Academic Rank:	Associate Professor
Institution and Department:	University of Alabama at Birmingham Department of Biology
NASA/MSFC Directorate:	Space Science Directorate/SD50
MSFC Colleague:	Dr. Richard Hoover

Introduction

It is now well recognized that microorganisms thrive in extreme ecological conditions such as geothermal vents, polar region, acid and alkaline lakes, and the cold pressurized depth of the ocean floor of this planet. Morphological, physiological, biochemical and genetic adaptations to extreme environments by these extremophile microorganisms have generated immense interest amongst astrobiologists who increasingly believe in the existence of extraterrestrial life. The evidence collected by NASA's space probe Galileo suggested the presence of liquid water and volcanic activity on Mars and Jupiter's satellite Europa. Volcanic activity provides some of the heat necessary to keep the water on Europa from freezing that could provide important dissolved chemicals needed by living organisms. The possibility of the existence of hypersaline alkaline lakes and evaporites confined within closed volcanic basins and impact craters on Mars, and a layer of liquid water under the ice on Europa provide sufficient "raison d'être" to study microorganisms in similar extreme environments on Earth, which could provide us with a model that would help establish the existence of extraterrestrial life on other planetary bodies [4].

The objectives of the summer research project were as follows: (1) application of molecular approaches to help establish new species of extremophile microorganisms isolated from a hypersaline alkaline lake; and (2) identification of a major cold-shock gene (*cspA*) homolog from a psychrotolerant microorganism, PmagG1.

Objective 1: Application of molecular approaches to help establish new species of extremophile microorganisms isolated from a hypersaline alkaline lake.

Characterization of Spirochaeta americana str. ASpG1^T from soda Mono Lake. Some of the *Spirochaeta* are extremophiles and may serve as a model for the existence extraterrestrial life. *S. amaricana* ASpG1^T was isolated from black mud samples with strong odor of sulfur collected from Mono Lake in California by Richard Hoover.

Methods: Exponentially grown and stationary phase cultures of *S. amaricana* ASpG1^T were subjected to BacLight™ Live vs. Dead fluorescent stain (Molecular Probes, Inc.) and nucleic acid DAPI stain. The DAPI staining was was adopted from a previously described and examined under a *Leitz* Diaplan epifluoroscent microscope at a 1000x magnification.

Figure 1a. Soda Mono Lake in California with Tufa columns.

Results: The morphology of an exponentially grown culture of *S. americana* ASpG1^T exhibited typical spiral cells of 0.20-0.25 μm in diameter and 8-15 μm in length with rotating undulatory movement (Figure 2). The DAPI stained cells exhibited typical blue fluorescent color of the nucleic acids in the cells. Uniform blue color throughout the cell body suggests that unlike in other Gram-negative microorganisms the chromosomal DNA in *S. amaricana* ASpG1^T does not form a nucleoid structure (Figure 2). The stationary phase culture exhibited round irregular spheroplast cells possibly a mechanism to remain in "dormant" state (Figure 2).

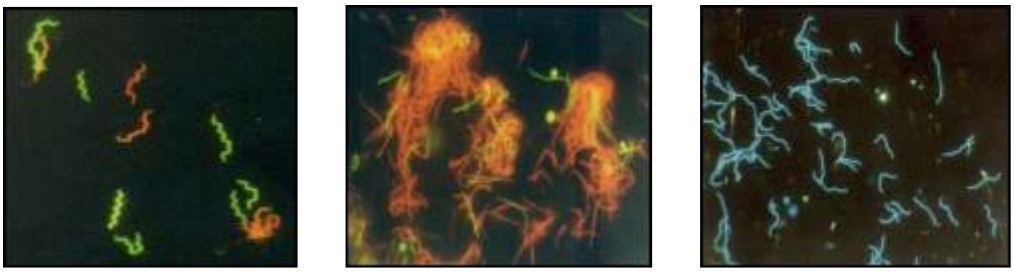

a. **b.** **c.**

Figure 2. BaLight™ and DAPI fluorescent stained *S. americana* ASpG1^T cells from (a) an exponentially grown culture with typical spiral morphologies and (b) a stationary phase culture with spheroplasts and aggregated cells. Green="live" cells; Red= "dead"cells; (c) DAPI fluorescent stained *S. americana* ASpG1^T cells with uniform blue color of the cell bodies.

Molecular Analyses: Phylogenetic analysis of *S. americana* ASpG1^T based on the 16S rDNA sequence exhibited 99.2% sequence homology with another haloalkaliphilic miroorganism, *Spirochaeta alkalica* Z-7491^T. However, the morphological, biochemical and total mol %GC content suggested that these two spirochetes are separate species. Therefore, it was necessary to conduct further experiments on the genome of these two microorganisms to firmly establish that *S. americana* ASpG1^T is a new species.

Methods: (i) Melting temperature (Tm): Melting temperatures (*Tm*) of total genomic DNA from *S. alkalica* Z-7491^T and *S. americana* ASpG1^T were determined by following the procedures described elsewhere [2,3]. Purified genomic DNA from *S. alkalica* Z-7491^T and *S. americana* ASpG1^T were subjected to sonication to generate DNA fragments between 400-800 bp. The sonicated DNA was treated with boiled RNase I and S1 nuclease [1]. The concentration and the purity of the DNA were determined using a spectrophotometer (Shimadzu UV-160). The denaturation process of the sonicated genomic DNA in 2x SSC was carried out in an uvonic cuvette placed in a spectrophotometer by increasing the temperature of the sample from 26 ºC to 100 ºC, and absorbance was recorded at 260 nm wavelengths. The melting temperature (*Tm*) was determined by calculating the temperature at which the hyperchromicity has reached half of the value obtained after completed melting.

(ii) DNA-DNA Hybridization: To determine the percent homology of genomic DNA between *S. alkalica* Z-7491^T and *S. americana* ASpG1^T, DNA-DNA hybridization was performed followed by DNA reassociation kinetics as described by DeLey *et al.* [2]. Sonicated genomic DNA (80 μg) from each of these microorganisms was added to 2x SSC and 25% formamide and then denatured by raising the temperature to 100°C and cooled to melting temperatures in the spectrophotometer. The samples were kept at melting temperature for 3 minutes and the optical density at 260 nm wavelengths was recorded at 5 seconds interval for a total of 20 minutes. The initial reassociation kinetics was determined by linear regression analysis. The percent homology of the DNA from these two microorganisms was calculated using the equation described by DeLay *et al.* [2]. All statistical analysis was performed using the Microsoft™ Excel software.

(iii) Genome size: The genome size of *S. americana* ASpG1^T was determined using the DNA-reassociation kinetics, following the Equation described by Gillis *et al.* [3], and by using the reported molecular weight of the genome of *S. alkalica* Z-7491^T.

Results: The *Tm* value of total fragmented genomic DNA of *S. americana* ASpG1^T was 68±2 ºC whereas it was 74±2 ºC for *S. alkalica* Z-7491^T. The regression analysis during the first 1.5 min of DNA reassociation kinetics for *S. americana* ASpG1^T exhibited a decrease of 0.03386±0.00074 (r^2=0.9937) OD units per min, whereas, *S. alkalica* Z-7491^T had a decrease of 0.03510±0.00049 (r^2=0.9974) OD units per min. The DNA from *S. americana* ASpG1^T and *S. alkalica* Z-7491^T strains in a mixture exhibited a decrease of 0.02563±0.00052 (r^2=0.9946) OD units per min. DNA-DNA hybridization established 48.7% homology between the genomes of *S. americana* ASpG1^T and *S. alkalica* Z-7491^T based on the reassociation kinetics and the equation described by Gillis *et al.* [3]. The genome size for *S. americana* ASpG1^T was 2.98x10^9 daltons. From this study, manuscript entitled "*Spirochaeta americana* sp. nov., a new halo-alkaliphilic, obligatory anaerobic spirochete isolated from soda Mono Lake in California" has been submitted to a peer reviewed journal for consideration for publication.

B. Characterization of Tindallia californiensis APO^T *from soda Mono Lake.*

This strictly anaerobic hyperalkaliphilic microorganism was isolated from black mud samples collected from soda Mono Lake in California by Richard Hoover and Elena Pikuta. Phylogenetic analysis based on the16S rDNA sequence exhibited 99.1% homology with *Tindallia magadii* Z-7934^T. Therefore, it was necessary to conduct additional genetic analysis to establish that in fact *T. californiensis* APO^T is a new species. The *Tm* values, DNA-DNA hybridization and genome size for these two species were conducted as described above. The *Tm* values for *T. californiensis* APO^T was 70°C±2°C and for *T. magadii* Z-7934^T was 63°C±2°C. DNA-DNA hybridization revealed that the homology between genomic DNA of these two species was 55%. Genome size for *T. californiensis* APO^T was 1.02x10^9 daltons and for *T. magadii* Z-7934^T was 1.15x10^9 daltons. Therefore, based on the genetic analysis along with the morphological and biochemical characteristics, it is determined that *Tindallia californiensis* APO^T is a new species. From this study, a manuscript entitled "*Tindallia californiensis* sp. nov., a new halo- alkaliphilic primary anaerobe, isolated from meromictic soda Mono Lake in California, and the correction of diagnosis for genus *Tindallia"* is currently being prepared.

.

Objective 2: Identification of a major cold-shock gene (cspA) homolog from a psychrotolerant microorganism, PmagG1.

The PmagG1 was isolated from guano of the Magellanic Penguine in Patagonia, South America by Richard Hoover. PmagG1 is a Gram-positive, anaerobic and phylogenetically closely related to *Lactosphera pasteurii* as determined based on the 16S rDNA sequence homologies (98%). DAPI fluorescent stain exhibited round cell morphologies in the form of clusters with a distinct nucleoid in each cell body (Figure 3). PmagG1 is a psychrotolerant bacterium with a growth temperature between 27°C and –5.5°C. To determine the genetic mechanism of cold tolerance, genomic DNA of PmagG1 was subjected to PCR amplification of the *cspA* gene that codes for the major cold shock protein in *E. coli*. PCR amplification resulted into a 210 bp amplicon (Figure 3). The *cspA* amplicon has been cloned onto a TOPO TA™ cloning vector (Invitrogen, Inc.) and nucleotide sequence is being performed. Further analysis of the *cspA* and its regulation at cold temperature may help understand underlying genetic and mechanisms of their tolerance and survival at cold temperatures for PmagG1.

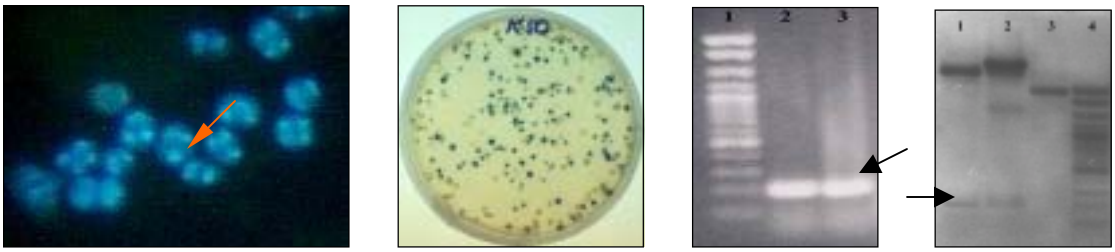

a. **b.** **c.** **d.**

Figure 3(a). DAPI-stained PmagG1 cells showing distinct chromosomes in nucleoid structures; (b) *E. coli* colonies with *cspA* clones (white); (c) Agarose gel electrophoresis showing the PCR amplified 210 bp *cspA* gene fragment from PmagG1 (Lane 2) and *E. coli* (Lane 3); lane 1, DNA size marker. (d). Agarose gel electrophoresis showing the *Eco*RI restriction endonuclease digested 210 bp fragment of the *cspA* gene fragments (arrows) from PmagG1 (Lane 1) and from *E. coli* (Lane 2); lane 3, undigested plasmid and lane 4, DNA size marker.

Discussion

The study of extremophile microorganisms is of particular interest to Astrobiology as extremophiles may provide models for extraterrestrial life. The haloalkaliphilic microbes in hypersaline soda alkaline lakes may represent possible analogs for microbial life that could have inhabited hypersaline alkaline lakes and evaporites confined within closed volcanic basins and impact craters of ancient Mars. Also, study of psychrotolerant and psychrophilic microorganisms in Antarctic ice and cryoconites provide model for the type of extraterrestrial life that may exist under the icy crust of Europa, polar ice caps in Mars and other frozen worlds of the Universe.

Acknowledgements

I would like to thank my NASA colleagues Dr. Richard Hoover and Dr. Elena Pikuta for their help and assistance. Also, thanks to NASA MSFC SFFP, Drs. Mike Freeman, Charles Karr and Jeanelle Bland for their support and providing me this opportunity to work at NASA.

References

[1] Ausubel, F.M., Brent, R., Kingston, R.E., Moore, D.D., Smith, J.G., Sideman, J.G., & Struhl, K. (eds) (1987), In *Current protocols in molecular biology*. New York: John Wiley & Sons, Inc., pp 2.10-2.11.

[2] De Ley, J., Cattoir, H., & Reynaerts, A. (1970), The quantitative measurement of DNA hybridization from renaturation rates. *Biochem* 12, 133-142.

[3] Gillis, M., De Lay, J., & De Cleene, M. (1970), The determination of molecular weight of bacterial genome DNA from renaturation rates. *Eur J Biochem* 12:143-153.

[4] Hoover R.B., Pikuta E.V., Marsic D., Ng J. (2002), Anaerobic psychrophiles from Alaska, Antarctica, and Patagonia: Implications to possible life on Mars and Europa, In *Instrument, methods, and Missions for Astrobiology IV* (R.B. Hoover, G.V. Levin, R.R. Paepe, A.Y. Rozanov editors), Proceedings of SPIE, 4495:313-324.

2002

NASA FACULTY FELLOWSHIP PROGRAM

MARSHALL SPACE FLIGHT CENTER
THE UNIVERSITY OF ALABAMA

MATHEMATICAL INVESTIGATION OF GAMMA RAY AND NEUTRON ABSORPTION GRID PATTERNS FOR HOMELAND DEFENSE RELATED FOURIER IMAGING SYSTEMS

Prepared By:	Dona Boccio
Academic Rank:	Professor
Institution and Department:	Queensborough Community College of the City University of New York Department of Mathematics and Computer Science
NASA/MSFC Directorate:	Flight Projects
MSFC Colleague:	Jonathan Campbell

Introduction

Terrorist suitcase nuclear devices typically using converted Soviet tactical nuclear warheads contain several kilograms of plutonium. This quantity of plutonium emits a significant number of gamma rays and neutrons as it undergoes radioactive decay.

These gamma rays and neutrons normally penetrate ordinary matter to a significant distance. Unfortunately this penetrating quality of the radiation makes imaging with classical optics impractical. However, this radiation signature emitted by the nuclear source may be sufficient to be imaged from low-flying aerial platforms carrying Fourier imaging systems.

The Fourier imaging system uses a pair of co-aligned absorption grids to measure a selected range of spatial frequencies from an object. These grids typically measure the spatial frequency in only one direction at a time. A grid pair that looks in all directions simultaneously would be an improvement over existing technology.

A number of grid pairs governed by various parameters were investigated to solve this problem. By examining numerous configurations, it became apparent that an appropriate spiral pattern could be made to work.

A set of equations was found to describe a grid pattern that produces straight fringes. Straight fringes represent a Fourier transform of a point source at infinity. An inverse Fourier transform of this fringe pattern would provide an accurate image (location and intensity) of a point source.

Methodology

Several types of spirals were investigated. The most basic type of spiral, the Spiral of Archimedes, has equation $r = a\theta$ for constant a. This is a special case of the Archimedean Spiral, $r = a\,\theta^{b}$ for constants a and b. Fermat's Spiral, $r = \theta^{1/2}$, is a special case of the Archimedean Spiral, with a = 1 and b = ½. Other types of spirals investigated were logarithmic spirals with $r = ae^{b\theta}$ for constants a and b, and $r = \ln \theta$.

In order to design a grid, a double spiral would need to be utilized. To create a double spiral, the equation and its negative were used. Figure 1a shows two spirals, $r = \theta^{1/2}$ and $r = -\theta^{1/2}$.
In Figure 1b, the area between the two spirals is filled in to indicate the material of the grid.

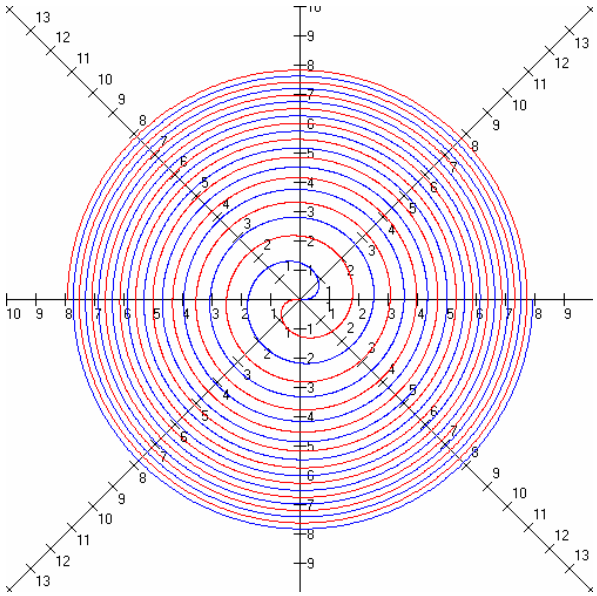

Figure 1a: Double Spiral

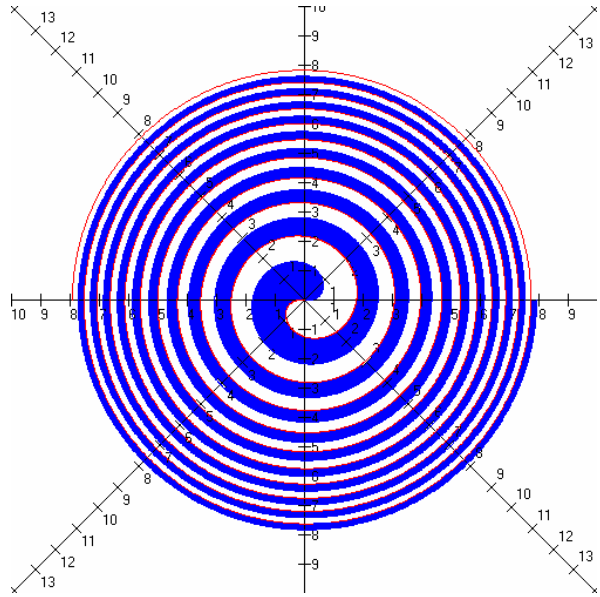

Figure 1b: Double Spiral

In order to show the pair of absorption grids to be used in the Fourier imaging system, it was necessary to represent a translation of the original curves. The equations were first converted from polar to rectangular coordinates using $x = r \cos \theta$ and $y = r \sin \theta$. $r = \theta^{1/2}$ becomes

$$x = t^{1/2} \cos t, \quad y = t^{1/2} \sin t \tag{1}$$

and $r = -\theta^{1/2}$ becomes

$$x = -t^{1/2} \cos t, \; y = -t^{1/2} \sin t \tag{2}$$

To produce a horizontal translation, $\pi/2$ was added in the x – direction, giving

$$x = \pi/2 + t^{1/2} \cos t, \quad y = t^{1/2} \sin t \tag{3}$$

$$x = \pi/2 - t^{1/2} \cos t, \quad y = - t^{1/2} \sin t \tag{4}$$

Graphs of the resulting equations are shown in Figure 2.

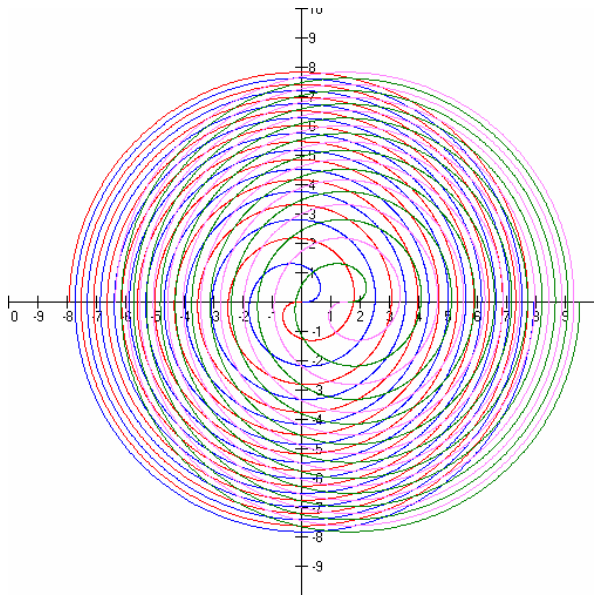

Figure 2: Equations (1), (2), (3), and (4)

In order to visualize the fringe pattern, the area between the spirals was again filled in (see Figure 3).

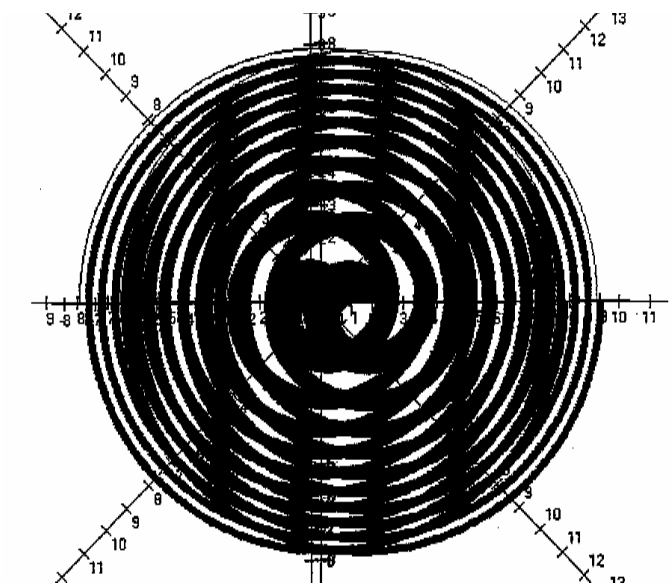

Figure 3: Equations (1), (2), (3), and (4)

Conclusion

A set of equations was found to describe a grid pattern that produces straight fringes. Straight fringes represent a Fourier transform of a point source at infinity. An inverse Fourier transform of this fringe pattern would provide an accurate image (location and intensity) of a point source. For an extended object, the resulting fringe pattern may be inversely Fourier transformed to provide an image. This image may be overlaid on a map to allow a precise location of the nuclear source.

References

[1] Lawrence, J. D. (1972), *A Catalog o f Special Plane Curves*, Dover Publications, pp. 184-190.

2002

NASA FACULTY FELLOWSHIP PROGRAM

MARSHALL SPACE FLIGHT CENTER
THE UNIVERSITY OF ALABAMA

THE POTENTIAL OF MICROWAVE RADIATION FOR PROCESSING MARTIAN SOIL

Prepared By:	Walter Boles
Academic Rank:	Professor
Institution and Department:	Middle Tennessee State University Department of Engineering Technology and Industrial Studies
NASA/MSFC Directorate:	Science
MSFC Colleague:	Dr. Benjamin Penn

Introduction

For extended or permanent stay operations on Mars, in situ resource utilization is necessary due to the high cost of space transportation. Using the soil and atmosphere of Mars for the extraction of important materials is essential. This work investigates the potential use of microwave radiation on a Martian soil analog to aid in beneficiation. The work is both exploratory and experimental. Results of experiments are presented and discussed.

Literature Review

Rao [5] reports the results of research using microwave heating of bauxite and hematite for the removal of iron. He observed formation of agglomerates, formation of metallic iron (longer heat – more iron), an increase in magnetic material from 0% to 29.5% by weight in the case of hematite, and from 22% to 75% in the case of bauxite (with coke as a reducing agent in both cases). The objective was to rid the ore of the contaminant iron. Rao looked for the chemical reaction as shown in Formula 1.

$$2Fe_2O_3 + 3C = 3CO_2 + 4Fe \qquad (1)$$

Kingman and Rowson of Birmingham University (UK) [3] report results of comparing microwave heating and conventional muffle furnace: "The results are very similar for both forms of heat treatment, showing that microwave energy produces the same overall structure changes, but in a more rapid time period." Similarly, Kingman, et al. [2] report the effect of microwave radiation upon a massive Norwegian ilmenite: "Short exposure to microwave radiation has been demonstrated to cause fractures within the ore matrix. Increased exposure to microwave radiation is shown to cause localised sample melting. The microwave treated samples have subsequently undergone a multi-stage magnetic separation process which produced concentrates of significantly higher grade and also better recovery of valuable mineral, when compared to those that are not treated."

Some authors such as Reid (http://home.c2i.net/metaphor/mypage.html) have looked at melting metals in a domestic microwave oven. Meek, et al. [4], describe potential benefits of using microwave radiation on lunar soils as energy efficient and discuss how selected frequencies may couple with specific bonds. They also experimented by melting ore and developing bricks. Tucker, et al., [6] describe a method of hydrogen recovery from extraterrestrial materials: "The use of microwave energy would offer a new, efficient method of heating lunar materials. Not only could extraterrestrial materials be heated with less energy than with conventional methods, but the heating would be accomplished in a controlled manner and in much less time than with a method such as solar heating."

Most of the work reviewed for this effort looks at the use of microwave energy in making bricks rather than beneficiating and extracting elements out of Lunar or Martian soils. It appears very little experimentation has been accomplished in beneficiation for the extraction of metals and other useful elements with microwave energy. No references were found that used microwave energy on JSC Mars-1 Martian soil simulant.

Objective

The objective of this research is to microwave a Martian soil Simulant, JSC Mars-1 [1], in a conventional microwave oven with graphite (carbon) as a reducing agent. This should result in

some of the iron oxide reacting as indicated in Formula 1, thereby, creating Fe that should be more easily removed by magnetic separation.

Estimating Carbon Content Required

For the reaction as depicted in Formula 1, each gram of Mars-1 requires about 0.0169 g of C, or 1.7% by weight. This may be theoretically accurate. However, there is a proximity issue. The carbon must be close to the iron oxide to react and the location of the iron oxide in the sample is not spatially homogenous. Therefore, it may take more than the amount indicated.

Procedure

A "hot spot" was located within the microwave (Sharp R-230BK, 700 W) using heat sensitive printer paper. All tests were run with an alumina thimble crucible placed on an alumina plate over the hot spot for 8 minutes. Preliminary efforts revealed significant blowout of material from the crucible anywhere from 10 to 50 seconds after starting the microwave. Shorter time to blowout was noted for higher carbon concentrations. It was initially believed this was due to the presence of water. However, even with samples dried at 150° C for 24 hours, blowout still occurred. This was assumed to be due to adsorbed water that doesn't evaporate until temperatures reach 350° C and is completely gone at 500°C. A sample was prepared and subjected to 500+° C for 3 hours. The sample was immediately heated in the microwave and blowout still occurred. This suggests that the reaction is not due to the presence of water.

Materials were stored in an oven at 60° C. After running preliminary samples a final group of samples was prepared with the carbon content increased from 2% to 10% in increments of 2%. No reaction was observed for the 2% sample. The sample was cool enough to touch by hand only after a minute or two of cooling. The 4% and 5% samples exhibited glowing red heat and slightly sintered in the center of the crucible. The 8% and 10% samples exhibited bright red to white heating and produced melted samples. Since blowout occurred in all samples, it is impossible to know the carbon content of the remaining portion.

In order to see if the grain size of the carbon had an effect on the blowout, a sample of carbon was crushed with a hammer to produce a coarse grain size. A soil-carbon sample was prepared with a carbon content of 10% coarse graphite. There was no visible reaction when irradiated in the microwave oven. There is obviously a critical relationship between grain size and carbon content. This may be due to smaller spaces between carbon particles in the small grain size portion, thus more easily allowing electrical arcing and resistive heating to occur.

Magnetic separation of the Mars-1 was accomplished using a vertical acrylic tube through a superconducting electromagnet set at 35 kilogauss. Approximately 35% of the sample was retained in the magnetic field within the tube and 65% passed through. Several samples were run on the magnetic and nonmagnetic portions. Visually, there was no difference in the heating of the magnetic portion at 6% carbon and the nonmagnetic portion at 12%. Both samples produced a completely melted bead. The magnetic portion appeared to produce less blowout of material. Time did not allow sample analysis prior to the deadline for this paper.

Discussion

Industrial extraction of iron is normally accomplished in a blast furnace where iron ore, rich in iron oxide, is heated to 1200° C to 1300° C with carbon as a reducing agent. The minimum

temperature required for the reaction in Formula 1 to take place is about 800° C. Depending upon the type of furnace, carbon may be used both as the reduction agent as well as burned to provide the heat required. When using microwave energy it is difficult to use carbon as a reactant and as a susceptor for microwave energy. The difficulty seems to be that at small concentrations or large grain size no reaction occurs and heating is limited to just over 100° C. At larger concentrations a very vigorous reaction occurs which sinters or melts the sample. From visual observation of color (almost white), the sample appears to reach well over 1000° C. The carbon either does not react at low concentrations or it reacts vigorously at higher concentrations. There seems to be little, if any, middle ground. Controlling heat using this method is likely to be a very difficult problem. Maintaining temperatures for periods of time longer than a few minutes is also difficult because the carbon is consumed. Thus, the original objective of transforming iron oxide into a more magnetically sensitive material in granular form was not accomplished.

Sample Analysis

Several melted samples were mounted and microprobe analysis performed. Perhaps the most interesting result is that iron elements seem to precipitate out and form tiny spheres of iron, iron phosphate, and iron silicide. Figure 1 (Left) shows an area of iron micro spheres surrounded by iron depleted glass melt. Figure 1 (Center) shows where iron micro spheres have apparently migrated to the perimeter of the melted bead. Figure 1 (Right) depicts a micro sphere at higher magnification. The darker shaded areas are predominately iron while the lighter shaded areas also include significant amounts of phosphorus. Other metals are sometimes included in the spheres such as titanium. Interestingly, iron phosphate and iron silicide do not occur naturally except in fulgurites (sandy soil melted by lighting). The larger spheres generally appear more at the edges and bottom of melted samples. It seems that the more vigorous the melt, the more spheres are formed and migrate to the edge and bottom of the melt. Perhaps gravitational pull helps the heavy spheres settle toward the bottom.

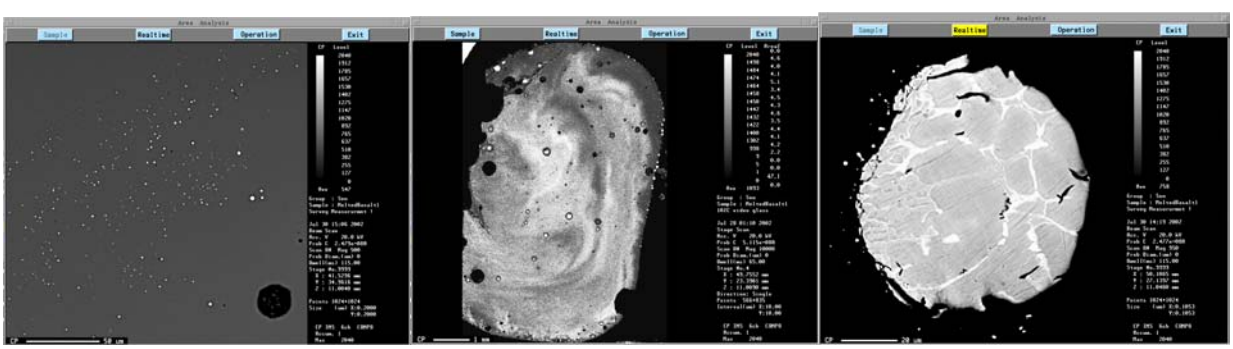

Figure 1. Microprobe Photos: Left—iron micro spheres within glass melt; Center—micro spheres at perimeter; Right—close-up view of micro sphere

Recommended areas for Further Study

- Heating mechanism: distributed susceptor material within non-susceptor matrix
    - Susceptor material, grain size, spacing, reactivity
    - Does susceptor material provide resistive heating through electrical circuits?
- Microwave radiation variables: frequency, focusing, power
- Controlling heat: producing a melt or heat below melt temperature

- What gas comes off early on?
- Is microwave irradiation an efficient energy delivery method in terrestrial steel making?
- Will iron form and settle to the bottom of the melt the way it does in steel making?
- Will a magnetic field aid in the collection of magnetic spheres (bottom, for example)?
- Will other chemical additives increase yield?

Conclusion

While this research is not conclusive, one can make the following comments regarding the potential benefits of microwave radiation for ISRU purposes:

- Microwave radiation with a susceptor material (carbon) will produce intense heat, produce a glassy melt material, and facilitate the formation of metallic micro spheres.
- Microwave equipment is typically low in mass, low in energy consumption, and simple
- Further research is required to determine the degree of purity obtainable whether by single batch operation or successive enrichment procedures.
- A robotic mission design is certainly feasible with existing technology.

This research effort was simple in concept. However, the results turned out to be very complex and created many questions and avenues for further research. The strikingly vigorous reactions obtained were quite unexpected. The concept of a fine-grained, distributed susceptor that may create electrical pathways for resistive heating is interesting per se. The potential of enhancing the yield by adding other chemicals and increasing reclaim efficiency with the use of a magnetic field during processing are also titillating. I wish to acknowledge the assistance of my NASA colleague, Ben Penn and URSA colleagues Laurent Sibille, Subhayu Sen, and Paul Carpenter.

References

[1] Allen, Carlton C.; Morris, Richard V.; Jager, Karen M.; Golden, D. C.; Lindstrom, David J.; Lindstrom, Marilyn M.; and Lockwood John P.; "Martian Regolith Simulant JSC Mars-1;" Lunar and Planetary Science XXIX, the Lunar and Planetary Institute, Houston, TX, 1998 http://www.lpi.usra.edu/meetings/LPSC98/pdf/1690.pdf

[2] Kingman, S. W., Corfield, G. M., and Rowson, N. A., "Effects of Microwave Radiation upon the Mineralogy and Magnetic Processing of a Massive Norwegian Ilmenite Ore," web page abstracts at http://www.bham.ac.uk/chemeng/minarticles.htm

[3] Kingman, S. W., and Rowson, N. A., "Microwave Treatment of Minerals—a Review," web page abstracts at http://www.bham.ac.uk/chemeng/minarticles.htm

[4] Meek, Thomas T; Vaniman, David T.; Cocks, Franklin H; and Wright, Robin A; "Microwave Processing of Lunar Materials: Potential Applications;" *Lunar Bases and Space Activities of the 21st Century*; The Lunar and Planetary Institute, Houston, TX, 1985, pp 479-486

[5] Rao, R. Bhima, "Novel Approach for the Beneficiation of Ferruginous Bauxite by Microwave Heating," *Minerals and Metallurgical Processing*, Vol. 13, No. 3, Transactions Vol. 300, August 1996, pp 103-106

[6] Tucker, D. S.; Vaniman, D. T.; Anderson, F. W.; Feber, R. C.; Frost, H. M.; Meek, T. T.; and Wallace, T. C.; Hydrogen Recovery From Extraterrestrial Materials Using Microwave Energy;" *Lunar Bases and Space Activities of the 21st Century*; The Lunar and Planetary Institute, Houston, TX, 1985, pp 583-590

2002

NASA FACULTY FELLOWSHIP PROGRAM

MARSHALL SPACE FLIGHT CENTER
THE UNIVERSITY OF ALABAMA

FUZZY LOGIC TRAJECTORY DESIGN AND GUIDANCE FOR TERMINAL AREA ENERGY MANAGEMENT

Prepared By:	Bradley Burchett
Academic Rank:	Assistant Professor
Institution and Department:	Rose-Hulman Institute of Technology Department of Mechanical Engineering
NASA/MSFC Directorate:	Space Transportation
MSFC Colleague:	Dr. John Hanson

Introduction

The second generation reusable launch vehicle will leverage many new technologies to make flight to low earth orbit safer and more cost effective. One important capability will be completely autonomous flight during reentry and landing, thus making it unnecessary to man the vehicle for cargo missions with stringent weight constraints. Implementation of sophisticated new guidance and control methods will enable the vehicle to return to earth under less than favorable conditions.

The return to earth consists of three phases--Entry, Terminal Area Energy Management (TAEM), and Approach and Landing. The Space Shuttle is programmed to fly all three phases of flight automatically, and under normal circumstances the astronaut-pilot takes manual control only during the Approach and Landing phase. The automatic control algorithms used in the Shuttle for TAEM and Approach and Landing have been developed over the past 30 years. They are computationally efficient, and based on careful study of the spacecraft's flight dynamics, and heuristic reasoning. The gliding return trajectory is planned prior to the mission, and only minor adjustments are made during flight for perturbations in the vehicle energy state.

With the advent of the X-33 and X-34 technology demonstration vehicles, several authors investigated implementing advanced control methods to provide autonomous real-time design of gliding return trajectories thus enhancing the ability of the vehicle to adjust to unusual energy states. [2-7] The bulk of work published to date deals primarily with the approach and landing phase of flight where changes in heading angle are small, and range to the runway is monotonically decreasing. These benign flight conditions allow for model simplification and fairly straightforward optimization. This project focuses on the TAEM phase of flight where mathematically precise methods have produced limited results. Fuzzy Logic methods are used to make onboard autonomous gliding return trajectory design robust to a wider energy envelope, and the possibility of control surface failures, thus increasing the flexibility of unmanned gliding recovery and landing.

Fuzzy Logic Trajectory Design and Guidance

Human beings perform a wide variety of complex tasks in every day life without precise mathematical calculations. One apt example is driving an automobile. The human operator readily adapts to different vehicles, and moves the controls to precisely navigate the vehicle without calculating steering angles, pedal pressures, etc. Fuzzy Logic methods provide a method to formalize proven human knowledge into an autonomous algorithm making it unnecessary for precise math models or dynamic inversion of a plant. [9] Fuzzy Logic control has been used in a wide array of applications including approach and landing control of a light aircraft [8]

A simplified dynamic model of a gliding aircraft can be found by treating the vehicle as a point mass, and applying the conservation of linear momentum. The resulting equations are lightly coupled and can be divided into three channels. Vehicle ground track is controlled primarily by bank angle ϕ, the altitude is controlled by normal acceleration N_Z, and the dynamic pressure $\bar{q} = 1/2\rho V^2$ is controlled by either changing the flight path angle γ, or changing the coefficient of drag C_D, by extending drag devices.

Next, each channel of the trajectory is constrained to a shape that intentionally limits the number of parameters needed to describe it. For example, we constrain the ground path to a minimum maneuver trajectory consisting of a shortest direction acquisition turn, a straight portion, and a base to final heading alignment turn (HAC). Each turn is designed as a circular arc. Finally, for each channel, important parameters defining the trajectory are determined through a Fuzzy Logic decision. The adjustable parameters in the horizontal channel are the heading alignment turn radius (YHAC), and position from the runway threshold (XHAC). The vertical trajectory is constrained by initial and final conditions. The spacecraft must reach the Auto-Land Interface (ALI) at approximately 10,000 ft above the runway, 20,000 ft from the runway threshold at a flight path angle depressed 30 degrees from horizontal. To maintain continuity through the trajectory, the vertical path is defined as a cubic polynomial which intersects the ALI at the appropriate altitude and slope. The coefficient on the quadratic term (CUBIC3) of this cubic is adjusted to provide a smooth path from the current state to ALI. We designed a two-input three-output fuzzy inference system to determine XHAC, YHAC, and CUBIC3 based on the spacecraft current energy state, and control surface health. The inputs are the quotient of energy over predicted downrange distance to ALI, and an integer denoting the degree of control surface health. This decision is based on twenty rules which essentially enlarge the turn radius for high energy states or poor maneuverability, or shorten the final approach length and lower the vertical path profile for lower energy states.

The bank guidance commands are generated by dividing the TAEM phase into four sub-phases, then applying rules appropriate to the variables of interest during each phase. The sub-phases are Acquisition, HAC Turn, and Pre-Final. This division is identical to Shuttle TAEM [10]. In acquisition phase, the spacecraft uses maximum available bank to turn in the shortest direction to point directly at the center of the HAC turn. Once the spacecraft is pointing at the center of the HAC turn, a set of 89 rules are used to intercept and fly the HAC. These rules are based on the author's own experience totaling more than 2000 hours of flight in military jet aircraft. For instance, many instrument approach procedures require the pilot to fly a circular arc around a VHF Omnidirectional Range with Distance Measuring Equipment. In order to fly such an arc, the pilot considers his distance from the station, and relative bearing and adjusts bank angle accordingly. [1] In the pre-final phase, bank is determined from a combination of distance from runway centerline and component of horizontal velocity orthogonal to runway centerline.

The normal acceleration guidance uses altitude error and vertical velocity error to generate commands up to ±1/2 g and restore the vehicle to the desired glidepath. During supersonic flight, the X-33 speed brake remains closed, and the normal acceleration guidance overrides flight path angle corrections as necessary to keep the dynamic pressure from exceeding nominal limits. During all phases of flight, the fuzzy guidance will generate a nose-down command if the dynamic pressure approaches the stall limit. For this work, we use the existing X-33 speed brake guidance

Results

The fuzzy inference systems described above were rapidly prototyped, tuned, and tested using Matlab and the Fuzzy Logic Toolbox. The simplified three degree of freedom dynamics described in the previous section were programmed in Matlab and served as a realistic model of

a reusable launch vehicle in the TAEM phase. After obtaining satisfactory results that demonstrated robustness to varying initial conditions and degrees of control surface health, we integrated our fuzzy systems with a high fidelity six degree of freedom simulation available at Marshall. Limited further tuning was required to replicate the results obtained in Matlab. A low pass filter was added to the bank commands to inhibit control saturation resulting in instability. Normal acceleration commands were multiplied by the reciprocal of the cosine of pitch angle

The ground track and bank angle of four high fidelity simulations are shown in Figure 1. The solid lines represent the trajectory with full flight control health. Dotted lines represent the trajectory when flight controls are degraded such that bank angle is limited to 36 degrees. The axes on the ground track plot do not have equal scaling so that differences are emphasized. Current entry guidance will provide a heading perturbation at TAEM interface of ±10 degrees. Note that we have varied the initial heading by ±30 degrees, thereby creating an energy initial state lower than nominal. All four cases reach a successful landing at 1500 to 2500 feet from the runway threshold.

One fascinating discovery is that the filters have complimentary effects although each channel was designed separately. For example, for a case with flight control limitations, and nominal initial energy, the trajectory designer will direct a wide radius HAC. The ground track predictor then computes a longer than normal ground track. Subsequently, the normal acceleration guidance keeps the flight path angle shallow during the acquisition phase of flight.

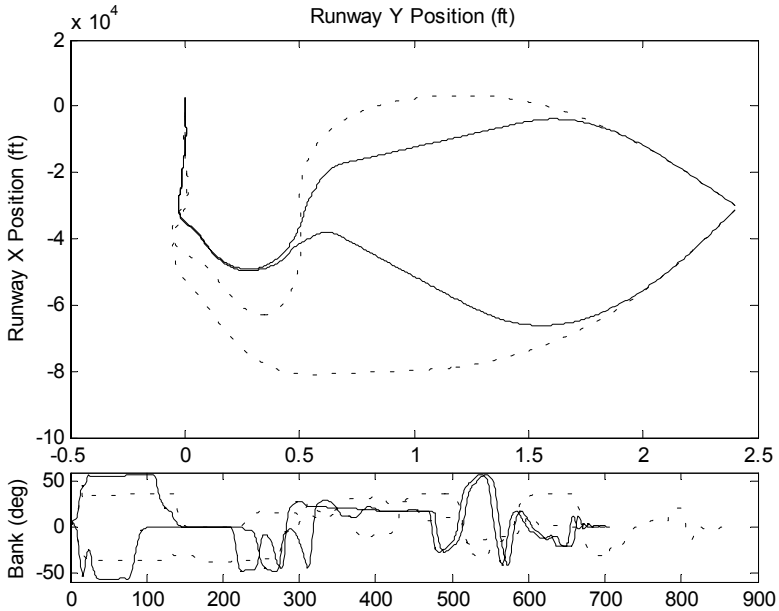

Figure 1: Vehicle Ground Track and Bank Angle Using Fuzzy Trajectory Design

This is then advantageous to the bank guidance since the spacecraft will reach subsonic flight sooner, and will thus be ready to intercept the HAC.

Conclusions

Fuzzy logic control is extremely powerful for control of complex systems without precise models. By applying the knowledge from Shuttle TAEM guidance and the author's own flight experience, we have developed an algorithm to design and fly gliding return trajectories for varying initial energy conditions and degrees of control surface integrity.

References

[1] Air Force Manual 11-217 Volume 1, *Instrument Flight Procedures,* 29 December 2000, http://afpubs.hq.af.mil

[2] Barton, G. H., (1999), "Autolanding Trajectory Design for the X-34," AIAA Atmospheric Flight Mechanics Conference and Exhibit, Portland, OR, AIAA Paper No. 99-4161, 1999.

[3] Barton, G. H., (2001), "New Methodologies for Assessing the Robustness of the X-34 Autolanding Trajectories," *Advances in the Astronautical Sciences,* Volume 107 Guidance and Control 2001, pp. 193-214.

[4] Girerd, A., Barton, G., (2000) "Next Generation Entry Guidance--Onboard Trajectory Generation for Unpowered Drop Tests," AIAA Guidance, Navigation, and Control Conference, Denver, CO, Paper No. 2000-3960, 2000.

[5] Girerd, A., "Onboard Trajectory Generation for the Unpowered Landing of Autonomous Reusable Launch Vehicles," S. M. Thesis, Massachusetts Institute of Technology / Charles Stark Draper Laboratory T-1390, 2001.

[6] Grantham, K. "Adaptive Critic Neural Network Based Terminal Area Energy Management / Entry Guidance," 41st AIAA Aerospace Sciences Meeting and Exhibit, Reno, NV, 2003.

[7] Grubler, A. C., "New Methodologies for Onboard Generation of Terminal Area Energy Management Trajectories for Autonomous Reusable Launch Vehicles," S. M. Thesis, Massachusetts Institute of Technology / Charles Stark Draper Laboratory T-1401, 2001.

[8] Larkin, L. I., "A Fuzzy Logic Controller for Aircraft Flight Control," *Industrial Applications of Fuzzy Control*, M. Sugeno, Ed., Elsevier Science Publishers, North-Holland, 1985, pp. 87-103.

[9] Lee, C. C., "Fuzzy Logic in Control Systems: Fuzzy Logic Controller--Part I," *IEEE Transactions on Systems, Man, and Cybernetics,* Vol. 20, No. 2, pp. 404-417.

[10] Moore, T. E. "Space Shuttle Entry Terminal Area Energy Management," NASA Technical Memorandum 104744, Lyndon B. Johnson Space Center, 1991.

2002

NASA FACULTY FELLOWSHIP PROGRAM

MARSHALL SPACE FLIGHT CENTER

THE UNIVERSITY OF ALABAMA

DEVELOPMENT OF A TOOL FOR DYNAMIC ANALYSIS OF MOMENTUM EXCHANGE ELECTRODYNAMIC REBOOST TETHERS

REPORT NOT AVAILABLE

Prepared By:

Stephen Canfield

Tennessee Technological University

2002

NASA/ASEE SUMMER FACULTY FELLOWSHIP PROGRAM

MARSHALL SPACE FLIGHT CENTER
THE UNIVERSITY OF ALABAMA

INTERFACIAL REACTION STUDIES USING ONIOM

Prepared By:	Beatriz H. Cardelino
Academic Rank:	Associate Professor
Institution and Department:	Spelman College Chemistry Department
NASA/MSFC Directorate:	Science and Engineering
MSFC Colleague:	Craig E. Moore

Introduction

Organometallic vapor phase epitaxy (OMVPE) is widely used in both scientific studies and industrial manufacturing of compound semiconductor devices and circuits. III-V compounds have been at the center of this development for many years. The nitrides, in particular, permit the extension of III-V optoelectronics and photonics to the blue and ultraviolet range of the electromagnetic spectrum[1]. There is growing interest in extending OMVPE to indium nitride (InN), which exhibit large thermal decomposition at their optimum growth temperature. To overcome decomposition of the deposited compound, the reaction must be conducted at high pressures. But high pressure OMVPE must be carried out at high flow velocity to keep the Grashof number (G_e) small compared to the square of the Reynolds number (R_e), to prevent onset of turbulence and thus non-uniform film growth. The G_e / R_e^2 ratio is proportional to $\mathbf{g}\left(\frac{\mathbf{P}}{\mathbf{u}}\right)^2$, where **g** is the gravity vector, **P** the standard pressure, and **u** the standard flow rate. On the ground, high pressure OMVPE must be carried out at a sufficiently high **u** to maintain a small ratio, which results in an inefficient growth rate. Alternatively, under conditions of reduced gravity, an increase in **P** could be coupled with a smaller **u** without an onset of turbulence. In order to extend OMVPE processing to elevated pressures, new reactor designs have been recently built to reach pressures as high as 100 atm. Epitaxy simulations that couple fluid dynamic equations with homogeneous and heterogeneous reactions have been helpful in both reactor and process design. At the present time, there is a need for obtaining input parameters for modeling these experiments under different conditions of pressure and gravity.

In this report, we focus on the calculations of the energetics and chemical kinetics of heterogeneous reactions for OMVPE. The work described in this report builds upon our own previous thermochemical[2] and chemical kinetics studies[3]. The first of these articles refers to the prediction of thermochemical properties, and the latter one deals with the prediction of rate constants for gaseous homolytic dissociation reactions.

The calculations of this investigation are at the microscopic level. The systems chosen consisted of a gallium nitride (GaN) substrate, and molecular nitrogen (N_2) and ammonia (NH_3) as adsorbants. The energetics for the adsorption and the adsorbant dissociation processes were estimated, and reaction rate constants for the dissociation reactions of free and adsorbed molecules were predicted. The energetics for substrate decomposition was also computed.

The GaN substrate mainly exists in three crystal structures: rocksalt, wurtzitic, and zincblende. At ambient conditions, the common structure is wurtzitic. The rocksalt structure can be induced at very high pressures. The zincblende structure can be obtained by epitaxy of GaN thin films on cubic structures such as Si, MgO and GaAs. So far, we have limited our calculations to zincblende crystals. In this structure, both atoms have a face-center cubic sub-lattice (see Figure 1a), offset along the diagonal of the cube by $^1/_4$ of the diagonal. A side view of a 3x3x1 unit-cell slab is shown in Figure 1b, where the terminal atoms at the top (red) are Ga atoms and at the bottom (blue) are N atoms. The

surface consists of parallel ridges and ditches. All non-terminal atoms form tetrahedral bonds. The terminal atoms have only one or two bonds, corresponding to an edge or the surface, respectively.

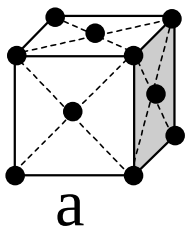

a)

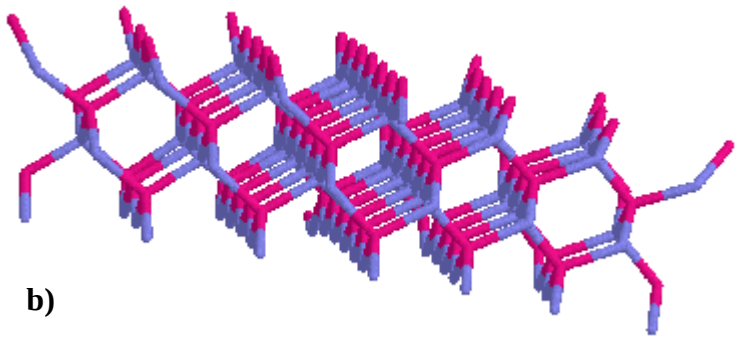

b)

Figure 1: a) Face-center cubic lattice. b) Zincblende slab seen from its narrow side

Method

The ONIOM[4] method, implemented in the Gaussian98 program[5], was used to perform the calculations. This approach has been selected since it allows dividing the system into two layers that can be treated at different levels of accuracy. The atoms of the substrate were modeled using molecular mechanics[6] with universal force fields[7], whereas the adsorbed molecules were approximated using quantum mechanics, based on density functional theory methods[8] with B3LYP functionals[9] and 6-311G(d,p) basis sets. Calculations for the substrate were performed in slabs of several unit cells in each direction. The N_2 and NH_3 adsorbates were attached to a central location at the Ga-lined surface.

Results

Selection of the surface size. In order to select an adequate surface size, the following properties were analyzed as a function of number of atoms: (a) lattice constant; (b) density; (c) Ga-N average bond distance; and (d) energy per Ga-N unit. The average Ga-N bond distance was calculated using only those N atoms that were tetrahedrally bonded to four Ga atoms; the average lattice constant was obtained using only atoms that had a coordination number of 12 with the same type of atoms; the density was based on the calculated lattice constant and the fact that a unit cell contains four Ga-N units. As an example, Figures 2a and 2b display the first two properties as a function of number of surface atoms. A compromise between property and number of atoms led us to select a 5 x 5 x 3 slab, which gave the values shown by the arrows. The experimentally determined lattice constant is 4.52 Å and the zincblende crystal has a density of 6.15 g cm^{-3}. The selected slab has a calculated average lattice constant of 4.44 ± 0.05 Å, a density of 6.37 ± 0.07 g cm^{-3}; and an average Ga-N bond distance of 1.92 ± 0.02 Å. The energy for N decomposition of the substrate was estimated to be 151 ± 14 kJ mol^{-1}.

Interaction of the surface with the adsorbates. As an example, Figure 3 shows the 5x5x3 unit-cell GaN substrate with an ammonia molecule (with light colors) adsorbed at

the Ga-lined surface. Lowest energy was obtained for an NH_3 molecule with its N atom sitting above a square of Ga atoms, 3.6 to 3.9 Å away.

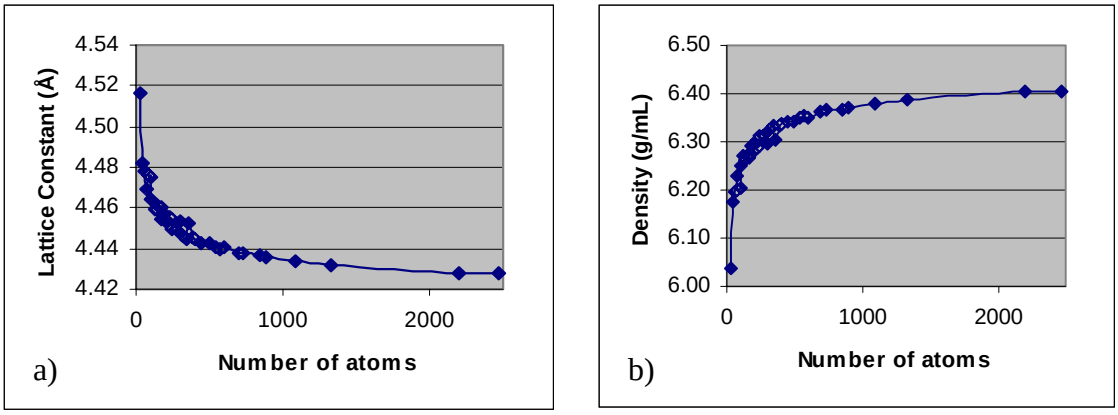

Figure 2: Properties of zincblende slabs as a function of number of atoms:
a) average lattice constant; b) density.

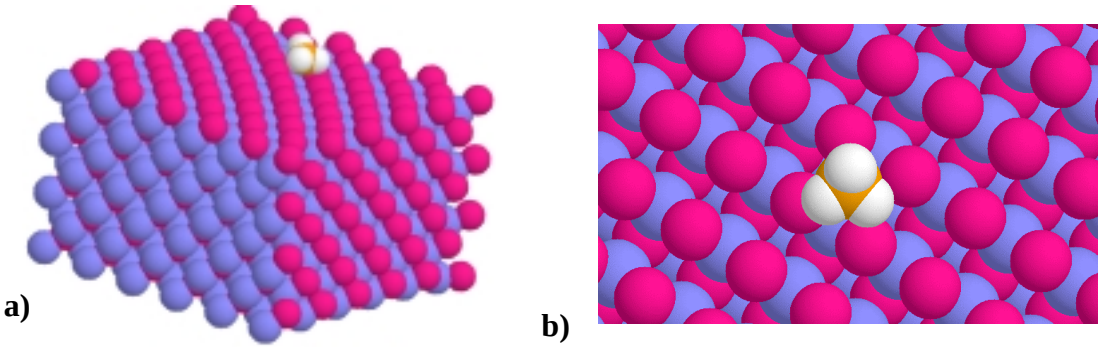

Figure 5: 5x5x3 unit-cell zincblende GaN substrate with an adsorbed NH_3 molecule.
a) complete substrate; b) enlarged view of adsorbate.

According to the calculations, NH_3, $^2NH_2$, ^3NH, and ^4N physisorb to the surface by 14, 12, 10, and 6 kJ mol^{-1}, respectively. Dissociation of a ^2H atom from the first three adsorbed species requires 470, 412 and 360 kJ mol^{-1}, respectively, similar to the free molecule. As a rough estimation, the H dissociation rate constants were calculated assuming that vibrational frequencies are inversely proportional to bond distance. The dissociation rate constants for adsorbed NH_3 between 700 and 1300 K were twice as large as for free NH_3.

N_2 is adsorbed almost parallel to the surface, with one N atom 3.60 Å above a Ga atom and the second N atom above a triangle determined by other three Ga atoms. Its binding energy is 12 kJ mol^{-1}. 942 and 947 kJ mol^{-1} are required to dissociate free N_2 and adsorbed N_2, respectively. (The experimental dissociation energy of N_2 at standard conditions is 949 kJ mol^{-1}.) The reaction rate constant for the dissociation of N_2 increases by a factor of two with adsorption, factor which decreases with increasing temperature.

Conclusions

Performing calculations at two different level of accuracy for interfacial reactions seems an adequate approach to study interfacial reactions. The calculated energies indicate that: (a) the chemisorption energy of N in the substrate is about 150 kJ mol^{-1}; (b) the five species considered (N_2, ^3N, NH_3, $^2NH_2$, and ^3NH) physisorb to the GaN substrate (by 12, 6, 14, 12 and 10 kJ mol^{-1}, respectively); (c) dissociation of N_2 into two ^4N atoms and of a ^2H atom from NH_3, $^2NH_2$ and ^3NH is endothermic; and (d) the above dissociations are a few kilojoules per mole lower for the free molecules than for the adsorbants. Roughly calculated rate constants indicate that: (a) dissociation of free N_2 is twice as fast as adsorbed N_2, and (b) dissociation of adsorbed NH_3 is twice as fast as free NH_3. The latter result would indicate that dissociation of NH_3 on a GaN substrate is kinetically driven.

Acknowledgments. The author would like to thank Drs. Craig E. Moore and Donald O. Frazier, from NASA-MSFC, for providing a stimulating working environment, as well as Drs. Klaus J. Bachmann, Nikolaus Dietz, and Carlos Cardelino, for many hours of fruitful discussions.

References

[1] Ambacher, O.; Brandt, M. S.; Dimitrov, R.; Metzger, T.; Stutzmann, M.; Fischer, R. A.; Miehr, A.; Bergmaier, A.; Dollinger; G.;J. Vacuum Science Technology B **1996**, *14*, 3532.
[2] Cardelino, B. H.; Moore, C. E.; Cardelino, C. A.; Frazier, D. O.; Bachmann, K. J.; J. Phys. Chem. A, **2001,** *105*, 849**.**.
[3] Cardelino, B. H.; Moore, C. E. ; Cardelino, C. A.; McCall, S. D.; Frazier, D. O.; Bachmann, K. J.; submitted June 2002 J. Phys.Chem.
[4] Dapprich, S.; Komaromi, I.; Byun, K. S.; Morokuma, K.; Frisch, M. J.; J.Molec.Structure (Theochem), **1999**, *461-462*, 1-21
[5] *Gaussian 98* (Revision A.11); M. J. Frisch, G. W. Trucks, H. B. Schlegel, G. E. Scuseria, M. A. Robb, J. R. Cheeseman, V. G. Zakrzewski, J. A. Montgomery, Jr., R. E. Stratmann, J. C. Burant, S. Dapprich, J. M. Millam, A. D. Daniels, K. N. Kudin, M. C. Strain, O. Farkas, J. Tomasi, V. Barone, M. Cossi, R. Cammi, B. Mennucci, C. Pomelli, C. Adamo, S. Clifford, J. Ochterski, G. A. Petersson, P. Y. Ayala, Q. Cui, K. Morokuma, P. Salvador, J. J. Dannenberg, D. K. Malick, A. D. Rabuck, K. Raghavachari, J. B. Foresman, J. Cioslowski, J. V. Ortiz, A. G. Baboul, B. B. Stefanov, G. Liu, A. Liashenko, P. Piskorz, I. Komaromi, R. Gomperts, R. L. Martin, D. J. Fox, T. Keith, M. A. Al-Laham, C. Y. Peng, A. Nanayakkara, M. Challacombe, P. M. W. Gill, B. Johnson, W. Chen, M. W. Wong, J. L. Andres, C. Gonzalez, M. Head-Gordon, E. S. Replogle, and J. A. Pople, Gaussian, Inc., Pittsburgh PA, **2001**.
[6] Allinger, N. L. J. Amer. Chem. Soc., **1977**, 99, 8127. Burkert, U.; Allinger, N. L.; "*Molecular Mechanics*", American Chemical Society: Washington, DC, **1982**.
[7] Rappe', A. K. ; Casewit, C. J.; Colwell, K. S.; Goddard III, W. A.; Skiff. W. M. J.Am. Chem. Soc, **1992**, *114*, 10024. Casewit, C. J.; Colwell, K. S.; Rappe', A. K. J.Am.Chem. Soc, **1992**, *114*, 10035. Casewit, C. J.; Colwell, K. S.; Rappe', A. K. J.Am.Chem. Soc, **1992**, *114*, 10046. Rappe', A. K.; Colwell, K. S.; Casewit, C. J. Inorg.Chem., **1993**, *32*, 3438.
[8] P. Hohenberg, W. Kohn; Phys. Rev. 136, B864, **1964**. Kohn, L. J. Sham; Phys. Rev. 140, A1133, **1965**.
[9] C. Lee, W. Yang, R. G. Parr; Phys. Rev. B37, 785, **1988**. A. D. Becke; Phys. Rev. A38, 3098, **1988**. B. Miehlich, A. Savin, H. Stoll, H. Preuss; Chem. Phys Lett. 157, 200, **1989**.

2002

NASA FACULTY FELLOWSHIP PROGRAM

MARSHALL SPACE FLIGHT CENTER
THE UNIVERSITY OF ALABAMA

ENHANCEMENT AND EXTENSION OF POROSITY MODEL IN THE FDNS-500 CODE TO PROVIDE ENHANCED SIMULATION OF ROCKET ENGINE COMPONENTS

Prepared By:	Gary Cheng
Academic Rank:	Assistant Professor
Institution and Department:	University of Alabama at Birmingham Department of Mechanical Engineering
NASA/MSFC Directorate:	Transportation
MSFC Colleagues:	Kevin Tucker, Jeff West, Roberto Garcia

Introduction

In the past, the design of rocket engines has primarily relied on the cold flow/hot fire test, and the empirical correlations developed based on the database from previous designs. However, it is very costly to fabricate and test various hardware designs during the design cycle, whereas the empirical model becomes unreliable in designing the advanced rocket engine where its operating conditions exceed the range of the database. The main goal of the 2nd Generation Reusable Launching Vehicle (GEN-II RLV) is to reduce the cost per payload and to extend the life of the hardware, which poses a great challenge to the rocket engine design. Hence, understanding the flow characteristics in each engine components is thus critical to the engine design. In the last few decades, the methodology of computational fluid dynamics (CFD) has been advanced to be a mature tool of analyzing various engine components. Therefore, it is important for the CFD design tool to be able to properly simulate the hot flow environment near the liquid injector, and thus to accurately predict the heat load to the injector faceplate. However, to date it is still not feasible to conduct CFD simulations of the detailed flowfield with very complicated geometries such as fluid flow and heat transfer in an injector assembly and through a porous plate, which requires gigantic computer memories and power to resolve the detailed geometry. The rigimesh (a sintered metal material), utilized to reduce the heat load to the faceplate, is one of the design concepts for the injector faceplate of the GEN-II RLV. In addition, the injector assembly is designed to distribute propellants into the combustion chamber of the liquid rocket engine. A porosity mode thus becomes a necessity for the CFD code in order to efficiently simulate the flow and heat transfer in these porous media, and maintain good accuracy in describing the flow fields. Currently, the FDNS (Finite Difference Navier-Stakes) code is one of the CFD codes which are most widely used by research engineers at NASA Marshall Space Flight Center (MSFC) to simulate various flow problems related to rocket engines. The objective of this research work during the 10-week summer faculty fellowship program was to 1) debug the framework of the porosity model in the current FDNS code, and 2) validate the porosity model by simulating flows through various porous media such as tube banks and porous plate.

Numerical Methodology

The framework of the FDNS code is an elliptic, finite difference Navier-Stokes flow solver[1-3], which employs a predictor plus multi-corrector pressure-based solution algorithm. Higher order upwind, total variation diminishing (TVD), or central difference schemes plus adaptive second-order and fourth-order dissipation terms are used to approximate the convection terms of the transport equations. Various matrix solvers, such as vectorized point implicit, conjugate gradient, and generalized minimal residual[4] (GMRES), are provided in the code such that users can select one for a given transport equation. Finite-rate and equilibrium chemistries were incorporated in the code to account for the effect of combustion. Since the FDNS flow solver is a structured code, multi-block, multi-zone options are included in the code so that problems with complex geometries can be analyzed efficiently. The governing equations in curvilinear coordinates solved in the code can be expressed in general form as

$$\frac{1}{J}\frac{\partial \rho q}{\partial t} = -\frac{\partial F_i}{\partial \xi_i} + S_q$$

where q stands for dependent variables (1, u, v, w, h, k, ε, and α_n which denote unity, velocities in the Cartesian x-, y-, z-direction, enthalpy, turbulence kinetic energy and dissipation rate, and species mass fractions respectively). ξ_i, t, and ρ are the curvilinear coordinates, time and fluid density. The numerical flux in the i-direction, F_i, consists of convective flux, Fc_i, and a viscous flux, Fv_i, i.e.

$$F_i = Fc_i + Fv_i \quad , \qquad Fc_i = \rho U_i q \quad , \qquad Fv_i = -\mu_e G_{ij} \frac{\partial q}{\partial \xi_i}$$

where U_i, G_{ij}, and J represent the transformed velocities, diffusion metrics, and Jacobian of the coordinate transformation, respectively. The source terms, S_q, of the continuity, x-, y-, z-momentums, energy, turbulent kinetic energy and dissipation rate, and species equations

Porosity Model

The porosity model is employed to account for the effects of area/volume blockage and drag force as well as heat source/sink due to the presence of the porous media without resolving the detailed geometry of tiny pores and solid objects. The implementation of the porosity into the CFD code is illustrated as follows. First, the volume porosity (γ_v defined as the ratio of the volume occupied by the fluid to the total volume), and the surface porosity (γ_i defined as the ratio of the surface area in the i-direction available for the flow passage to the corresponding total surface area in the same direction) are introduced into the governing equation and can be expressed as

$$\frac{\gamma_v}{J}\frac{\partial \rho q}{\partial t} = -\frac{\partial \gamma_i F_i}{\partial \xi_i} + \gamma_v S_q$$

Second, a distributed drag force, D, and a heat flux source/sink term, H, are added to the right hand side of the momentum equation and the energy equation, respectively, to account for the effect of resistance and heat transfer due to the presence of the porous media. These drag force and heat flux terms were modeled based on geometric parameters and the averaged velocity through the porous media. The drag force D is defined as

$$D = \tfrac{1}{2}\rho V_t^2 C_D A$$

where C_D is the local drag coefficient is a function of types of porous media, local flow speed and geometric parameter. For the flow through an inline or staggered tube bank, empirical correlations[5] in Tables 1 and 2, are incorporated into the code to compute the drag coefficient.

Table 1: Empirical correlations of the drag coefficient for the flow through in-line tube banks

Range	C_D
$10^2 < \mathrm{Re}_d < 4 \times 10^3$	$0.535 \exp(5.378\ \mathrm{Re}_d^{-0.345})$
$4 \times 10^3 < \mathrm{Re}_d < 6 \times 10^4$	$0.735 - 0.411 \times 10^{-6}\ \mathrm{Re}_d$
$6 \times 10^4 < \mathrm{Re}_d < 1 \times 10^6$	$0.621 + 0.169 \times 10^{-5}\ \mathrm{Re}_d - 11.343 \times 10^{-12}\ \mathrm{Re}_d^2 + 16.656 \times 10^{-18}\ \mathrm{Re}_d^3 - 7.377 \times 10^{-24}\ \mathrm{Re}_d^4$
$1 \times 10^6 < \mathrm{Re}_d$	0.2735

Table 2: Empirical correlations of the drag coefficient for flow through staggered tube banks	
Range	C_D
$10^2 < \mathrm{Re}_d < 4 \times 10^3$	$0.417 \exp(4.932\ \mathrm{Re}_d^{-0.296})$
$4 \times 10^3 < \mathrm{Re}_d < 6 \times 10^4$	$0.647 - 0.5 \times 10^{-6}\ \mathrm{Re}_d$
$6 \times 10^4 < \mathrm{Re}_d < 1 \times 10^6$	$0.618 + 0.491 \times 10^{-6}\ \mathrm{Re}_d - 6.303 \times 10^{-12}\ \mathrm{Re}_d^{\ 2} + 10.694 \times 10^{-18}\ \mathrm{Re}_d^{\ 3} - 5.2 \times 10^{-24}\ \mathrm{Re}_d^{\ 4}$
$1 \times 10^6 < \mathrm{Re}_d$	0.2735

Both the drag coefficient model for a perforated plate and the heat flux model are incorporated into the code. These models are detailed in the final report to NASA MSFC TD-64. Due to the space limitation of this report, these models will not be described here. Readers can refer to the final report to TD-64 for the detailed.

Numerical Results

Tube Banks

Three flow conditions (Re_d = 1000, 5000, and 10000) were simulated for the flow through both in-line and staggered tube banks with three different tube spacing ($a = S_1/d$ = 2, 1.5, and 1.25), where the tube has a diameter of 1 cm. Due to the space limitation of this report, only the result of the staggered tube bank flow is included here. The complete comparison and discussion are detailed in the final report to TD-64. The computational domain and definitions of key parameters are sketched as shown in Figure 1. The comparisons of the Euler number ($Eu = 2\Delta p / \rho u^2$) between the numerical results and the empirical data are plotted as shown in Figure 2. Though the pressure loss is shown to be dependent on the flow blockage; it does not demonstrate the similar trend for various Reynolds number. Later, it was found out the empirical correlation of drag coefficients has less dependence on the Reynolds number than the pressure drop data. Hence the empirical correlation of drag coefficients needs to be fine-tuned in the future to obtain the Reynolds number dependence.

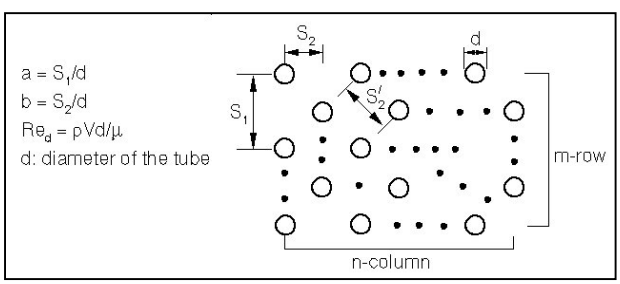

Figure 1: Definition of geometric parameters of the staggered tube bank

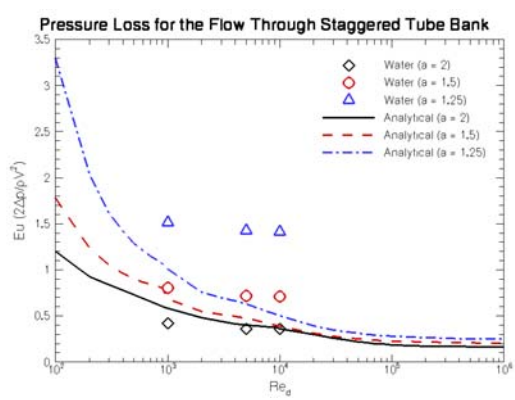

Figure 2: Pressure loss coefficient for the flow through staggered tube banks

Porous Plates

Numerical simulations were conducted for the flow through a 1”-thickness porous plate (pore diameter = 10 μm, volume porosity = 0.1) with various specific mass fluxes. The numerical result indicates the pressure loss predicted by the porosity model demonstrates a trend similar to the test data for various specific mass fluxes. Due to the proprietary of the test case as well as the space limitation of this report, the data comparison will not be presented here. If interested, readers can refer to the final report to NASA MSFC TD-64.

Conclusion

The framework of the porosity model in the FDNS-500 code has been verified. The numerical analyses of the tube bank flow demonstrate the qualitative trend of the pressure loss across the tube bank. However, more validations are needed to fine-tune the model to predict both qualitative and quantitative trends for various area porosities and Reynolds numbers. More validations are also needed for the porosity model of the perforated plate to examine the effect of different pore sizes and volume porosities. Due to the limitation of the time, only the empirical correlation for the drag force of the porosity model was verified. The empirical heat transfer correlation of the porosity model needs to be verified in the future.

Acknowledgements

The author would like to thank my colleagues of Applied Fluid Dynamics Analysis Group (TD64), Transportation Directorate, NASA Marshall Space Flight Center, for their support and valuable information, especially for Kevin Tucker, Jeff West, Marvin Rocker, Jeff Lin, and Roberto Garcia.

References

1. Chen, Y.S., Liu, J., “FDNS CFD Code Version 500-- Input Data Guide”, Engineering Sciences, Inc., Aug. 2000.

2. Chen, Y.S., "Compressible and Incompressible Flow Computations with a Pressure Based Method," AIAA Paper 89-0286, 1989.

3. Cheng, G.C., Chen, Y.S., and Wang, T.S., “Flow Distribution Within the SSME Main Injector Assembly Using Porosity Formulation,” AIAA Paper 95-0350, AIAA 33rd Aerospace Sciences Meeting and Exhibit, Jan. 9-12, 1995.

4. Saad, Y., and Schultz, M.H., SIAM Journal of Sci. Stat. Comput., Vol. 7, pp. 856-869, 1986.

5. Zukauskas, A., and Ulinskas, R., “Heat Transfer in Tube Banks in Crossflow,” Hemisphere Publishing Co., New York, 1988.

2002

NASA FACULTY FELLOWSHIP PROGRAM

MARSHALL SPACE FLIGHT CENTER
THE UNIVERSITY OF ALABAMA

MAGNATIZED TARGET FUSION IN ADVANCED PROPULSION RESEARCH

Prepared By:	Rashad Cylar
Academic Rank:	Undergraduate Student
Institution and Department:	Alabama A and M University Department of Engineering and Technology
NASA/MSFC Directorate:	Transportation
MSFC Colleague:	Steve Griffin Ph.D.

Figure 1: Proposed design for MTF Fusion Rocket

Introduction

The Magnetized Target Fusion (MTF) Propulsion lab at NASA Marshall Space Flight Center in Huntsville, Alabama has a program in place that has adopted to attempt to create a faster, lower cost and more reliable deep space transportation system. In this deep space travel the physics and development of high velocity plasma jets must be understood. The MTF Propulsion lab is also in attempt to open up the solar system for human exploration and commercial use.

Fusion, as compared to fission, is just the opposite. Fusion involves the light atomic nuclei combination to produce denser nuclei. In the process, the energy is created by destroying the mass according to the distinguished equation: $E = mc^2$. Fusion energy development is being pursued worldwide as a very sustainable form of energy that is environmentally friendly. For the purposes of space exploration fusion reactions considered include the isotopes of hydrogen-deuterium (D^2) and tritium (T^3).

Nuclei have an electrostatic repulsion between them and in order for the nuclei to fuse this repulsion must be overcome. One technique to bypass repulsion is to heat the nuclei to very high temperatures. The temperatures vary according to the type of reactions. For D-D reactions, one billion degrees Celsius is required, and for D-T reactions, one hundred million degrees is sufficient. There has to be energy input for useful output to be obtained form the fusion

To make fusion propulsion practical, the mass, the volume, and the cost of the equipment to produce the reactions (generally called the reactor) need to be reduced by an order of magnitude or two from the state-of-the-art fusion machines. Innovations in fusion schemes are therefore required, especially for obtaining thrust for propulsive applications. Magnetized target fusion (MTF) is one of the innovative fusion concepts that have emerged over the last several years. MSFC is working with Los Alamos National Laboratory and other research groups in studying the underlying principles involved in MTF.

Magnetized Target Fusion is an attempt to combine MCF (magnetic confinement fusion) for energy confinement and ICF (inertial confinement fusion) for efficient compression heating and wall free containment of the fusing plasma. It also seeks to combine the best features to these two main commonplace approaches to fusion. When plasma is magnetized a material wall implodes it to the required density and temperature. The use of gaseous linear as the imploding wall and the use of compact toroids as the target plasma. In the toroids there is a magnetic field that slows down the thermal loses from the target plasma to the imploding material wall. This

allows a relatively low implosion velocity, which is required while achieving near adiabatic compression. The correct imploding velocity can be reached by highly efficient electromagnetic acceleration techniques as compared to lasers, leading to low cost and low weight compact reactors.

The plasma jets will implode target plasma, which is created from merging compact toroids generated through theta pinch coils. Two conical theta pinches are used to generate and launch to compact toroids in the form of spheromaks into a rector chamber. The spheromaks contain fissionable materials. Magnetic fields are embedded in the spheromaks in force-free Woltjer-Wells-Taylors State of minimum energy, which has been proving to be stable in experimental cases. Depending on the relative orientation to their helicity, an FRC is formed or a larger spheromaks. An FRC is formed when the helicity is counter-aligned, in any other case a spheromak is formed. Since a spheromak is in a state of minimum energy, it is expected to be more stable theoretically. Both cases continue to be investigated.

Fusion Propulsion Unit

This MTF concept has very attractive features:

- The dense, hydrogenous liner is capable of converting greater than 97% of the neutron energy into charged particle energy.
- An attractively low-level fusion yield per pulse can be maintained (< 1 GJ), with a gain in excess of 70.
- The magnetic nozzle can operate as a magnetic flux compression generator to provide the necessary circulating power for continued operation, yet still maintain a high nozzle efficiency.
- The electrical energy from flux compression can recharge a capacitor bank or other energy storage without using a high voltage power supply.
- The electrical circuit is comprised mainly of inductors, capacitors and plasma guns, without any intermediate equipment, which allows a high rep-rate.
- All fusion related components are within the current state of the art for pulsed power technology.
- The scheme does not require any prefabricated target or liner hardware. All necessary fuel and liner material are introduced into the engine in a gaseous form and delivered to the fusion reaction region in a completely standoff manner.

–There are no classification issues.

The Plasma Feed Charge/Dump Box

One of the main project that I worked on this summer was the Plasma Feed Charge/Dump Box. The Marshall Gun is the name of the gun that is used to fire the plasma into one central location, which produces propulsive reaction. Within the makeup of the plasma gun and all of its components there consist a system which initiates the Marshall Guns known as the Charge/Dump box. The Charge/Dump box acts as the charge circuit as well as the power supply for the plasma gun. The charge initiates the gun and the dump performs as a safeing system for the end of each test firing. Any unused energy is dumped through a common centralized ground.

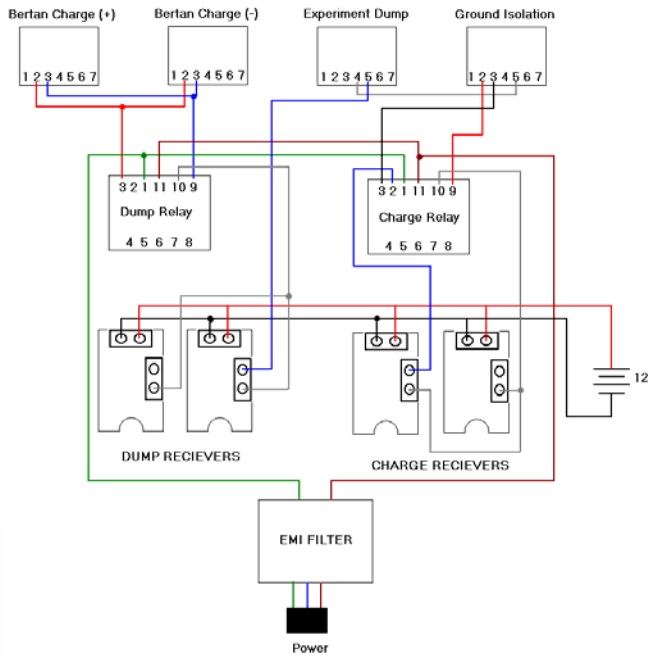

Figure 2: Relay Section of Box

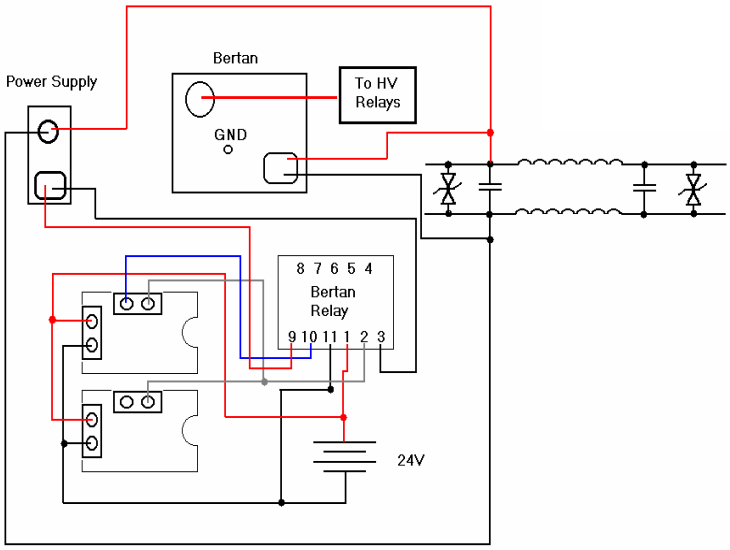

Figure 3: Bertan Section of Box

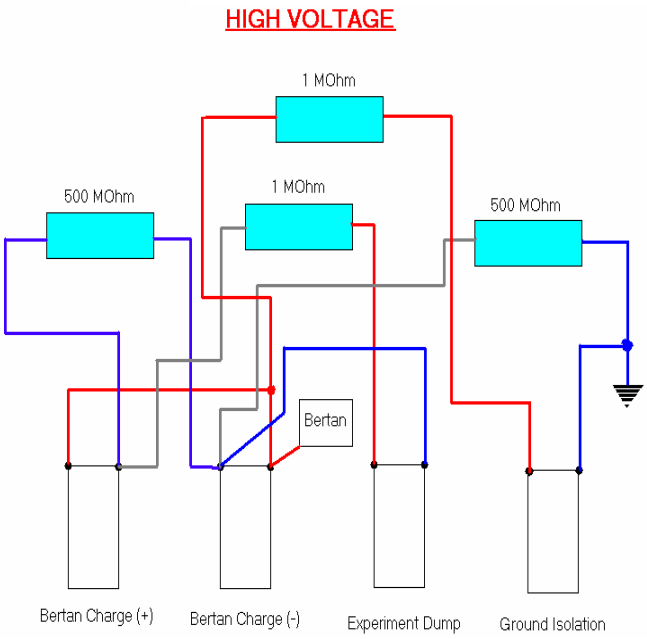

Figure 4: High Voltage Section of box

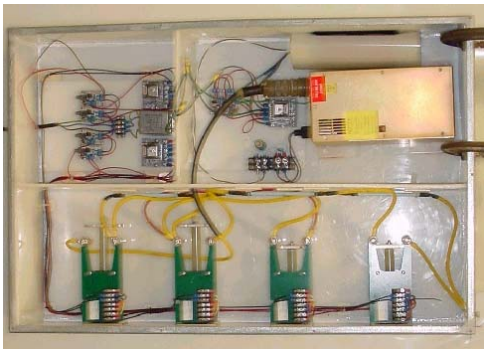

Figure 5: Actual Photo of Chare/Dump Box
Actual Size 3x4 Feet

Results

The construction of the Marshall Gun is still in the making and there has not been a firing of the Marshall Gun this summer. Previous tests were fired in the past three years, which has generated some interesting data. The Charge/Dump box has been armed and verified that it is in full working condition.

Future Applications for Magnetized Target Fusion

In the future, if a space vehicle is ever launched using Magnetized Target Fusion the charge dump box will play a major role in the vehicle's propulsion. The present construction of the Guns and Charge/Dump box is rather large and are strictly used for test purposes only. A more efficient and reliable construction will have to be made in order for the rocket to perform at the levels that MTF will produce.

Resources

The Plasma Feed Charge Dump box required the use of several materials found in the Electronics Lab located in Lab B. Some supplies not on hand had to be ordered. Jeff Richeson and Steve Griffin supervised the wiring of the dump box.

Conclusion

The NASA Summer Faculty Fellowship Program has been time well spent this summer. With this being my first summer with NASA, as well as my first internship as an undergraduate student, I have learned a lot and have grown to respect the work that is done at NASA's Marshall Space Flight Center.

Acknowledgements

I would like to thank all of Marshall Space flight Center's employees and contractors that I have worked with this summer. Special thanks to Propulsion Research Lab B and C for making this experience a good one.

References

[1] Clayton, P. R. (1992), *Introduction to Electromagnetic Compatibility*, John Wiley, pp. 242-279.

2002

NASA FACULTY FELLOWSHIP PROGRAM

MARSHALL SPACE FLIGHT CENTER
THE UNIVERSITY OF ALABAMA

INVESTIGATION OF FRICTION STIR WELDING OF Al METAL MATRIX COMPOSITE MATERIALS

Prepared By:	Ravinder M. Diwan, Ph.D.
Academic Rank:	Professor
Institution and Department:	Southern University Department of Mechanical Engineering Baton Rouge, LA 70813
NASA/MSFC Directorate:	Engineering
MSFC Colleague:	Dr. Sandeep Shah

Introduction

The innovative process of Friction Stir Welding (FSW) has generated tremendous interest since its inception about a decade or so ago since the first patent in 1991 by TWI of Cambridge, England. This interest has been seen in many recent international conferences and publications on the subject and relevant published literature [1-3]. Still the process needs both intensive basic study of deformation mechanisms during this FSW process and analysis and feasibility study to evaluate production methods that will yield high quality strong welds from the stirring action of the appropriate pin tool into the weld plate materials. Development of production processes is a complex task that involves effects of material thickness, materials weldability, pin tool design, pin height, and pin shoulder diameter and related control conditions. The frictional heating with rotational speeds of the pin tool as it plunges into the material and the ensuing plastic flow arising during the traverse of the welding faying surfaces provide the known special advantages of the FSW process in the area of this new advanced joining technology.

This research study will analyze the development of the FSW process in production of long welds of up to 4 foot length of functionally graded Al metal matrix materials (Al-MMC) materials. These materials possess high stiffness and other potential benefits for extreme conditions of space applications. The FSW process is now a reality and has been adopted by shipbuilding and marine industries and finds applications for aerospace applications. The present study should advance understanding in applications of the advanced Al-MMC materials. Developments of discontinuous reinforced Al-MMCs have found applications in space applications as seen in the special advantages of the solid state FSW process over conventional welding such as: the absence of a melt zone, reduced distortion, strong welds, no need for shielding gases, ease of automation and success seen in longitudinal butt welds and circumferential lap welds. Other industrial sectors can also realize benefits from this process. Development of the FSW process for Al-MMCs is relatively new and the process [4] promises advantages of no reaction and no need for joint preparation as mandated in conventional fusion welding. Microstructures should provide better evolution as no dendritic or inhomogeneous structures would result during the process. Some of the reported related work [5] has pointed out the difficulty in fusion welding of particulate reinforced MMCs where liquid Al will react with SiC to precipitate aluminum carbide (Al_4C_3). Advantages of the process are clearly seen and need to be realized in optimum processing conditions.

Al-MMCs, 4 in x 12 in plates of 0.25 in. (6.35mm) thickness, procured from MMCC, Inc. were butt welded using FSW process at MSFC NASA using prior set of operating conditions. These materials are of the same composition as studied in the previous analysis [6]. MSFC is developing the FSW process for several projects [7]. There is interest in advancing the FSW technology for production of long welds in Al-MMC materials and in comparison of the wear behavior of selected pin tool materials. Based on the pin tools behavior of the monolithic design and a two-piece pin tool design as utilized in the previous study, and wear characteristics encountered, in this study all welds were made using a modified design for a monolithic pin tool. ferro-tic, stellite, and tool steel T-15 pin tool materials were investigated for selected operating and material weld conditions. Details of welding history, pin tool wear performance and weld quality were investigated.

Weld quality was evaluated using radiography and standard metallography techniques. Mechanical behavior of these plate materials upon friction stir welding of these plates is to be analyzed with increasing volume fraction of ceramic particles in the composites. The weldability of the Al-MMC materials and the pin tool wear behavior is analyzed and reported in this work. Such studies are essential if Al-MMCs are to find their wide spread use in space applications.

Experimental Process Results

Al-MMC plates as procured from MMCC, Inc.,4 in x 12 in plates of 0.25 in. (6.35mm) thickness with 40 vol. % SiC and 55 vol. % SiC, (17μ+3μ), 3 DP +sintered + 0.25 in. layer with ceramic edge of 5%, 20% and 30% Al_2O_3 saffil edges were friction stir welded to study the weldability and pin tool wear behavior. The five categories of Al-MMC materials that are investigated in this study included:

Category 1-40% SiC bulk, 0.25" 5% saffil Al_2O_3 layer at plate edges

Category 1-40% SiC bulk, 0.25" 20% saffil Al_2O_3 layer at plate edges

Category 1-40% SiC bulk, 0.25" 30% saffil Al_2O_3 layer at plate edges

Category 4-40% SiC bulk and at plate edges

Category 5-55% SiC bulk and at plate edges.

In the earlier FSW studies the two piece ferro-tic pin tool shoulder had indicated fracture in some of the welding, and one of the goals of the present study has been to investigate the behavior of the new monolithic design of the pin tool materials for the five selected categories of the Al-MMC materials. The study included analysis of 3 different monolithic pin tools namely, of ferro-tic, stellite and T-15 tool steel, F 1-4, S 1-4, and T 1-4 pin tools.

The FSW process in this research work was performed using the MSFC vertical weld tool friction stir weld system in the Productivity Enhancement Complex. The welds of up to 4 foot length were produced in selected process conditions. All welds were single pass butt welded in comparative similar conditions. The study included the pin tool characterization prior to and post welding under similar FSW process conditions. All pin tools had the same standard design for comparison purposes. The welding operating conditions were selected similar to as in prior studies. A typical horizontal travel speed of about 3 inches per minute, a plunge depth of about 0.01 inch and a rotating spindle speed of about 650 rpm was considered appropriate from these studies.

In initial welds, the welding was done in a satisfactory manner using T-1 pin tool from category 1 to 4 MMC materials. However in welding of the category 4 MMC material with no saffil edges and 40 vol. % SiC material welding, the pin tool had been heavily worn out and threads were mostly gone. In the next category 5 MMC plates with no saffil edges and 55 vol. % SiC material weld, the welding was carried out with S-1 pin tool. However, this weld could not be completed, and the plates cracked into pieces at about 3-3/8 inch location into the weld. Category 5 MMC material indicated difficulties in welding of these plates and appears to be unweldable. All the other four category materials were then subsequently utilized in the FSW study of long welds up to 4 foot length. The test welds and the material weldability were evaluated further with radiographic inspection, and macroevaluations and microscopic examinations.

In production of the long MMC welds, plates from each category 1 to 4 MMC materials were utilized. The selected category plates were stacked in sequence on each other along the short edges and tack welded. Two sets of 4 tack welded plates were then used for producing 4 foot long welds that were butt joint and tack welded along the length at the beginning, end and selected locations for stability and keeping a straight edge during welding. These first 4 foot long welds were completed using ferro-tic and T 15 tool steel pin tool materials in similar process conditions. In the welding of category 4 material with 40% SiC edge and no saffil, the pin tool broke during welding at about 1-1/3 foot location indicating difficulty in long welds for this material. Welded panel photos were taken and radiography was performed for weldability evaluations.

The evaluation of the Stellite pin tools was performed by welding of the remainder plates of the materials in category 1, 3, and 4 that were available for this study. With the remaining MMC plates, for this evaluation, 3 foot long welds were completed using similar previous process conditions. The Stellite pin tools S-2, S-3 and S-4 were evaluated in this part of the study. .

From the weld panels after completing the first 4 foot long welds of category 1 to 4 MMC materials, these welds were then cut out and these plates were then used to re weld using outside second edges. There was ,however, difficulty in cutting of the first weld of category 4 materials, and for this only two foot long weld was produced. Evaluation of ferro-tic and tool steel pin tools was carried out in this analysis. Based on evaluation of the processing of the first 4 foot long welds, and to reduce any distortion on welding at the junctions in long welds, tack welds along the short edges in these second 4 foot long welds were done across the two sides in stacking the plates to nearly cover the width of the two plates along their short edges. These second weld panels were earmarked for further evaluation of weld properties at room temperature and cryogenic temperatures and any joint efficiency and related studies. All welding history data and process results for the above 3 foot and 4 foot long welds are available and submitted separately. All weld panels were photographed after the FSW process and evaluated by radiography. The wear of the ferro-tic, stellite and T 15 tool steel pin tools was evaluated using micrometer, and profile measurements and details of measurements are provided separately.

Large optical macroscans of the FSW weld regions of selected specimens showed a typical weld and stir zone structure as seen in a typical onion type structure in the center enclosed by the surrounding HAZ, and the unaffected parent metal structure. The composite base plate with saffil edges have the structure gradient and interactions of the Al_2O_3 and the SiC particulates in category 1-3 materials, and the variation of SiC particulates in the materials with out the saffil edges. The Al_2O_3 particles appear as lighter elongated particles and the SiC as the angular, darker particulates in the FSW weld microstrutures.

FSW in welding panels of functionally graded Al-MMC materials of categories 1-4 has been accomplished for up to 4 foot length welds using selected ferro-tic, stellite and T 15 tool steel pin tools. Category 5 material due to 55 vol% SiC reinforcement was unweldable. In some cases lack of consolidation and possible worm holes are seen and quality improvements in such cases can be made based on data generated and welding experience in these cases. Material push through can be seen in some cases due to soft saffil edges, and for this a backing plate has then been used to avoid any effect on the anvil material. In some cases, flash has been accumulated possibly due

to too hot a weld. In these productions of long welds, the pin tool history has indicated that T 15 tool steel pins provided larger cumulative weld lengths of up to about 72 inches, and the ferro-tic pin tools provided cumulative weld lengths of about 54 inches in producing 4 foot long welds. The stellite pin tools provided cumulative weld lengths of about 36 inches in producing 3 foot long welds. Continuing mechanical property evaluations are to be carried out of the second 4 foot long welds. The welded plate specimens and all weld data are available to further fine tune the processing conditions for producing long welds.

Summary

The selected FSW weld evaluations of up to 4 foot long welds have analyzed the behavior of ferro-tic, stellite and tool steel pin tool materials for welding of functionally graded Al-MMC materials. Category 1-4 MMC materials are weldable using the FSW process. The weld defects could be reduced further upon optimization of weld parameters. However, in producing long welds it is seen that a related problem is seen in the alignment of the plates and distortion that affects the weld quality. Having long plates will remove this issue arising from having small size plates. In the previous study and from the current work, it is seen that monolithic pin tools have fared better than the two piece pin tool shoulder assembly used in prior studies. Ferro-tic, stellite and T 15 tool steel all appear to be suitable for welding of Al-MMCs. The pin tool life and wear is seen to be dependent on the volume % reinforcement. The FSW process using the monolithic design pin tool holds good promise for welding and development of MMC materials.

Acknowledgments

The author expresses his appreciation and thanks to Dr. Sandeep Shah, MSFC Research Colleague for his enthusiastic support and in continuation of this research work. Special thanks are also expressed to several associated personnel; Mr. Robert Carter for FSW work, Dr. Arthur Nunes and Mr. Jeff Ding for discussions related to prior FSW work, Mr. Robert Bond for tensile testing of MMC plates and heat treatment, Dr. Ron Beshears for radiographic work, and to Mr. Greg Steele, Mr. Mike Gant and Mr. Greg Jerman for performing metallography related work.

References

[1] TWI, Proceedings of the 1st Friction Stir Welding Symposium, Thousand Oaks, CA, 1999.
[2] TWI, Proceedings of the 2nd Friction Stir Welding Symposium, Gothenburg, Sweden, 2000.
[3] TWI, Proceedings of the 3rd Friction Stir Welding Symposium, Kobe, Japan, Sep. 2001.
[4] Stellwag Jr. W.L. and Lienert, T. J., "Friction Stir Welding of Aluminum Metal-Matrix Composites", AEROMAT Conference, June2001.
[5] Lee, J.A., Carter, R.W. and Ding, J: Friction Stir Welding for Aluminum Metal Matrix Composites (MMC's), NASA/TM – 1999-209876.
[6] R.M. Diwan, "Investigation of Friction Stir Welding and Laser Engineered Net Shaping of Metal Matrix Composite Materials", NASA SFFP Report 2001.
[7] B.N. Bhat, R.W. Carter, R.J. Ding, K.G. Lawless, A.V. Nunes, C.K. Russell and S.R. Shah., "Friction Stir Welding Development at NASA" - Friction Stir Welding and Processing, edited by K.V. Jata, M.W. Mahoney, R.S. Mishra, S.I. Semiatin, and D.P. Field, TMS (The Minerals, Metals & Materials Society), 2001.

2002

NASA SUMMER FACULTY FELLOWSHIP PROGRAM

MARSHALL SPACE FLIGHT CENTER
THE UNIVERSITY OF ALABAMA

AN IMPROVED RLV STABILITY ANALYSIS VIA A CONTINUATION APPROACH

Prepared By	Mark Friedman
Academic Rank	Professor
Institution and Department	University of Alabama in Huntsville Department of Mathematical Sciences
NASA/MSFC	Transportation
MSFC Colleague:	Mark Jackson

Introduction.

The Continuation of Invariant Subspaces (CIS) algorithm [1] and [2] produces a smooth orthogonal similarity transformation to block triangular form of $A(s)$.

- Smooth dependence on s: h_i decreases if $\mathcal{R}(s)$ changes fast, h_i increases if $\mathcal{R}(s)$ changes slowly.
- Works if $\Sigma_1(s)$ and $\Sigma_2(s)$ do not come close.

1. Want to detect *bifurcations*: $\lambda(s)$ crosses $\operatorname{Re}\lambda = 0$.
2. Want to ensure: only $\lambda(s) \in \Sigma_1(s)$ can bifurcate.

- *An application:* stability analysis of a simulation model of the reusable launch vehicle X-33. *Problem*: choosing the points in flight that capture critical events affecting stability and performance.

Background.

Theorem 1 *Given $A \in C^1([0,1],\ \mathbb{R}^{n\times n})$ with:*

$$\Sigma(s) = \Sigma_1(s) \cup \Sigma_2(s), \quad \Sigma_1(s) \cap \Sigma_2(s) = \emptyset, \tag{1}$$

$\mathcal{R}(s) \equiv \mathcal{R}(\Sigma_1(s))$, $\dim(\mathcal{R}) = m > 0$;

(i) *There exist smooth T and Q, Q orthogonal:*

$$Q^T(s)A(s)Q(s) := T(s) = \begin{bmatrix} T_{11}(s) & T_{12}(s) \\ 0 & T_{22}(s) \end{bmatrix}, \tag{2}$$

$Q = [Q_1\ Q_2]$, $\mathcal{R} = \operatorname{span}(Q_1)$, $\mathcal{R}^\perp = \operatorname{span}(Q_2)$.

(ii) *Let*

$$\widehat{T} = \begin{bmatrix} \widehat{T}_{11} & \widehat{T}_{12} \\ E_{21} & \widehat{T}_{22} \end{bmatrix} := Q^T(0)A(h)Q(0), \tag{3}$$

$Y \in \mathbb{R}^{(n-m)\times m}$ solve algebraic Riccati equation

$$F(Y) := \widehat{T}_{22}Y - Y\widehat{T}_{11} + E_{21} - Y\widehat{T}_{12}Y = 0. \tag{4}$$

Then $Q(h)$ and $T(h)$ in (2) are given by

$$\begin{aligned} Q_1(h) &= (Q_1(0) + Q_2(0)Y)(I + Y^TY)^{-1/2}, \\ Q_2(h) &= (Q_2(0) - Q_1(0)Y^T)(I + YY^T)^{-1/2}, \end{aligned} \tag{5}$$

$$T(h) = \begin{bmatrix} T_{11}(h) & T_{12}(h) \\ 0 & T_{22}(h) \end{bmatrix} := Q^T(h)A(h)Q(h). \tag{6}$$

(iii) *Let Y_0 solve the Sylvester equation*

$$T_{22}(0)Y_0 - Y_0T_{11}(0) = -E_{21}, \tag{7}$$

and let h be so small that

$$\tilde{\kappa}(\widehat{T}) := \frac{\|\widehat{T}_{12}\|_F \|F(Y_0)\|_F}{\mathrm{sep}^2(\widehat{T}_{11} + \widehat{T}_{12}Y_0,\ \widehat{T}_{22} - Y_0\widehat{T}_{12})} < \frac{1}{4}. \tag{8}$$

Then (4) has unique solution Y and Newton method with initial guess Y_0 converges for $\tilde{\kappa}(\widehat{T}) < 1/12$.■

Here $\mathrm{sep}(A, B)$ is the smallest singular value of the Sylvester operator:

$$\mathrm{sep}(A, B) = \inf_{X \neq 0} \frac{\|AX - XB\|}{\|X\|}.$$

$\mathrm{sep}(A, B) = 0$ if and only if A and B have a common eigenvalue. It is small if there exists a small perturbation of either A or B that makes them have a common eigenvalue.

A practical CIS algorithm.

Replace the assumption (1) by

$$\Sigma_1(s) \equiv \{(\lambda_i(s))_{i=1}^m\}, \quad \Sigma_2(s) \equiv \left\{(\lambda_i(s))_{i=m+1}^n\right\},$$
$$\mathrm{Re}\,\lambda_1 \geq \ldots \geq \mathrm{Re}\,\lambda_{m_u} \geq 0 > \mathrm{Re}\,\lambda_{m_u+1} \geq \ldots \geq \mathrm{Re}\,\lambda_m,$$
$$\mathrm{Re}\,\lambda_m > \mathrm{Re}\,\lambda_{m+1} \geq \ldots \geq \mathrm{Re}\,\lambda_n,$$
$$m_s(s) \equiv m(s) - m_u(s) \geq m_s^{ref} > 0,$$

m, m_u, m_s vary; m_s^{ref} fixed, typically, $2 \leq m_s^{ref} \leq 4$.

- Algorithm, one step: given $Q(s)$, find $Q(s+h)$:
  - Can we actually compute $Q(s+h)$?
  - Once $Q(s+h)$ is computed, is it acceptable or it has to be modified (how?)?

1. Newton iteration for (4) fails to converge with $h_{\min}$.
   (a) Generically (Beyn et. al. 2000): real λ_m, λ_{m+1} coalesce and become a complex conjugate pair.
   (b) Move λ_{m+1} to $\Sigma_1(s)$ if $m_s \leq m_s^{ref}$, and λ_m to $\Sigma_2(s)$ if $m_s > m_s^{ref}$. Recompute $Q(s)$ by (2).

2. Newton iteration for (4) converges.
   (a) Test for an *overlap*

$$\psi_1 := \begin{cases} 0, & \mathrm{Re}\,\lambda_m > \mathrm{Re}\,\lambda_{m+1} \text{ (no overlap)}, \\ 1, & \mathrm{Re}\,\lambda_m < \mathrm{Re}\,\lambda_{m+1} \text{ (overlap)}. \end{cases}$$

   If $\psi_1 = 1$, decrease h to ensure that *overlap* is only in one real eigenvalue or in one complex conjugate eigenpair.

(b) Test for a *bifurcation*

$$\psi_2 := \begin{cases} 0, & m_u(s) = m_u(s+h) \text{ (no bifurcation)}, \\ 1, & m_u(s) \neq m_u(s+h) \text{ (bifurcation)}. \end{cases}$$

If $\psi_2 = 1$, update m, m_u, and m_s.

(c) If $\psi_1 = \psi_2 = 1$, decrease h, if allowed, else *fail*.

(d) If $\psi_1 = \psi_2 = 0$, accept the point $Q(s+h)$.

(e) If $\psi_1 = 0$ & $\psi_2 = 1$, adapt m, m_u, and m_s, if needed, and then recompute $Q(s+h)$ by (2).

(f) If $\psi_1 = 1$ & $\psi_2 = 0$, adapt m, m_u, and m_s by swapping or moving some eigenvalues between Σ_1 and Σ_2 (depending on whether $m_s \leq m_s^{ref}$ or $m_s > m_s^{ref}$, and whether the eigenvalues in question are real or complex conjugate eigenpair(s)) and then recompute $Q(s+h)$ by (2).

Stability analysis of the X-33.

- A co-operative agreement between NASA and Lockheed Martin resulted in development of single stage to orbit reusable launch vehicle called the X-33.
- Simulation model of X-33 includes the 6 degree-of-freedom equations of motion and the engine, aerodynamic, sensor, actuator, wind disturbance, mass property, guidance and control system models.
- Flight control of the X-33 vehicle during assent mode involves attitude maneuvers through a wide range of flight conditions. The vehicle dynamics are rapidly changing in time and changing nonlinearly with respect to propellant usage, aerodynamics, engine thrust, control surface usage, and control command generation.
- Stability analysis during powered operation: linearizing the system at various operating points along its flight trajectory. It is not unusual for the system to be unstable (real part of eigenvalue is positive) for a portion of ascent flight; however, due to the high velocity nature of rocket flight, this instability might not adversely affect system performance because this phase of flight is passed so quickly.
- A problem in stability analysis: choosing the points in flight to capture all events that affect stability and performance of the vehicle.

Discussion.

Continuation/Bifurcation Analysis Future Work.

- Test approach with a sample RLV concept design.
  - Perform the bifurcation and stability analysis for models like X-33 and identify regions that need more analysis.

- Compare the computational results with experiments.

- Develop a method that relates migration of eigenvalues into the right half-plane to elements of A-matrix and parameters in the nonlinear system of equations.

- Develop an efficient method to determine effects of parameters variations on magnitude of eigenvalue λ_1 with the largest real part. Idea (λ_1 real), $A(s)q_1(s) = \lambda_1(s)q_1(s)$. From Eq. (2) with $m = 1$
$$\lambda_1(s) = q_1^{\mathrm{T}}(s)A(s)q_1(s). \tag{9}$$
Hence the CIS algorithm produces $\lambda_1(s)$ as a *smooth function of parameters*. Hence can use minimization methods for $-\lambda_1(s)$ for smooth functions to determine $\max \lambda_1(s)$ rather than more expensive Monte Carlo.

- Addressing the issue of nonnormality. Recent results show that in the case of nonormal matrices (when the set of the eigenvectors does not form an orthogonal set) eigenvalues may not be a relevant tool to study stability. And one instead should use pseudospectra. Our preliminary results show that A-matrices can be highly nonnormal. This issue has to be investigated further.

Benefits of Continuation/Bifurcation Analysis Approach.

Continuation/bifurcation analysis addresses NASA's needs to reduce vehicle development cost and improve safety by aiding in the development of a more robust vehicle.

- *Need to develop safer vehicles*: identifying problematic operating conditions that would have been missed by a conventional stability analysis.

- *Need to reduce cost*: possibly reducing the time spent in sensitivity analyses. If this method of analysis can identify key parameters that affect vehicle stability, then a sensitivity analysis can focus on just these parameters, reducing number of iterations needed.

Acknowledgements.

The author wishes to thank the NASA/Marshall Space Flight Center TD55/Vehicle Control Systems group: Mark Jackson and Charles Hall for their help in formulating the problem and Steve Ryan, Kerry Funston, and Don Krupp for helpful discussions.

References.

[1] J.W Demmel, L. Dieci and M.J. Friedman, Computing connecting orbits via an improved algorithm for continuing invariant subspaces, *SIAM J. Sci. Comput.*, **22**, No. 1 (2001), 81–94.

[2] L.Dieci and M.J. Friedman, Continuation of Invariant Subspaces, *Numer. Lin. Alg. Appl.* **8** (2001), 317-327.

2002

NASA FACULTY FELLOWSHIP PROGRAM

MARSHALL SPACE FLIGHT CENTER

THE UNIVERSITY OF ALABAMA IN HUNTSVILLE

PARTIAL WAVE ANALYSIS OF COUPLED PHOTONIC STRUCTURES

REPORT NOT AVAILABLE

Prepared By:	Kirk A. Fuller
Academic Rank:	Research Scientist
Institution and Department:	The University of Alabama in Huntsville Earth System Science Center
NASA/MSFC Directorate:	Biological and Physical Sciences
MSFC Colleague:	Dr. David D. Smith

2002

NASA FACULTY FELLOWSHIP PROGRAM

MARSHALL SPACE FLIGHT CENTER
THE UNIVERSITY OF ALABAMA

ADAPTIVE CRITIC NEURAL NETWORK BASED TERMINAL AREA ENERGY MANAGEMENT AND APPROACH AND LANDING GUIDANCE

Prepared By:	Katie Grantham
Academic Rank:	Masters Student
Institution and Department:	University of Missouri-Rolla Department of Aerospace Engineering
NASA/MFSC Directorate:	Space Transportation
MSFC Colleague:	Dr. John Hanson

Introduction

Reusable Launch Vehicles (RLVs) have different mission requirements than the Space Shuttle, which is used for benchmark guidance design. Therefore, alternative Terminal Area Energy Management (TAEM) and Approach and Landing (A/L) Guidance schemes can be examined in the interest of cost reduction. A neural network based solution for a finite horizon trajectory optimization problem is presented in this paper. In this approach the optimal trajectory of the vehicle is produced by adaptive critic based neural networks, which were trained off-line to maintain a gradual glideslope.

Problem Formulation and Solution Development

The point mass equations of motions over a flat Earth are used as the model for the trajectory propagation dynamics. The final time for a TAEM & A/L trajectory varies for each set of initial conditions. Therefore it is more beneficial to use an independent variable whose final value is invariant. Also, the independent variable must be monotonically increasing or decreasing. This led to the reformulation of the vehicle dynamics with altitude as an independent variable. This procedure is shown in Equation 1, where the ith state equation, dX_i/dx, where X_i represents the ith state has the following form, f_i is the right hand side of the equations of motion and τ represents time. This procedure reduces the order of the vehicle system to five because the state variable x is represented as the independent variable [5]. The current TAEM and A/L guidance

$$\frac{\partial X_i}{\partial x} = \frac{\partial X_i}{\partial \tau}\frac{\partial \tau}{\partial x} = \frac{f_i}{V \sin\gamma} \tag{1}$$

is divided into flight phases. Those flight phases are Acquisition, Heading Alignment Cone (HAC), Pre-Final, and A/L. The cost function for the trajectory generation, as shown in Equation 2, was selected to minimize the controlled parameters, δC_L and $\delta\sigma$, to operate the system near

$$\begin{aligned} J &= \tfrac{1}{2}\int_{h+H}^{h} \delta C_L^{\,2} + \delta\sigma^2 dh \\ C_L &= C_{L_{ss}} + \delta C_L \\ \sigma &= \sigma_{ss} + \delta\sigma \end{aligned} \tag{2}$$

steady state, δC_{Lss} and $\delta\sigma_{ss}$, during each flight phase. Each flight phase has different goals to accomplish; therefore, an optimal trajectory is one in which each trajectory phase was optimized according to its goal. To accomplish this the selected steady state values of the controls vary for the different trajectory phases. Table 1 shows the various steady state values for each flight phase considered in this formulation [6]. Also, since the flight phases are defined by altitude ranges the cost function transitions are simple to implement [7].

Table 1: Cost Function Parameters				
	Acquisition	**HAC**	**Pre-Final**	**A/L**
C_{Lss}	$f(\dot{\gamma}=0)$			
σ_{ss}	$f(\dot{\psi}-\dot{\psi}_{des})$ $\dot{\psi}_{des}=\frac{V_{horizontal}}{TurnRadius}$		$f(\dot{\psi}=0)$	
	$TR=RF+R_1\psi+R_2\psi^2$	$TR=\frac{V_{horizontal}V}{g\tan\sigma}$		
Terminal Constraints	$states_f=states_{HACi}$	$states_f=states_{p\text{-}fi}$	$\psi_f=0$ $states_f=states_{A/Li}$	$\psi_f=0$ $V_f\sin\gamma_f=-2$ $h_f=x_f=y_f=0$

Neural Network Solution Development

An action network and a critic network comprise the adaptive-critic neural network structure. The action network behaves as a controller while the critic network behaves as a supervisory network, which criticizes, or evaluates, the outputs of the action network [3]. The system model is used with the cost function to find an optimal control, u, such that the cost function is minimized. The optimal control problem can be formulated in terms of Hamiltonian [2]. The propagation equations for the Lagrange multipliers, co-states, are subjected to the boundary condition and used along with the system model and the control equations derived from the optimality condition to generate the optimal control for the system. The neural network method of solution development is shown in Figure (1). In this figure the outputs of the "CRITIC"

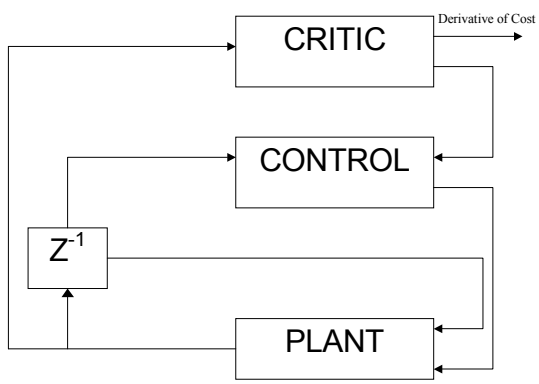

Figure 1: Neural Network Solution Development

block are the co-states the output of the "CONTROL" block is obtained through the optimality condition, and finally the "PLANT" block represents the system model [1]. The solution of finite-horizon problems with neural networks evolves in two stages: the synthesis of the last network and the propagation of the remaining networks [4].

Synthesis of Last Network

The synthesis of the last network is shown in Figure 2 and described below.

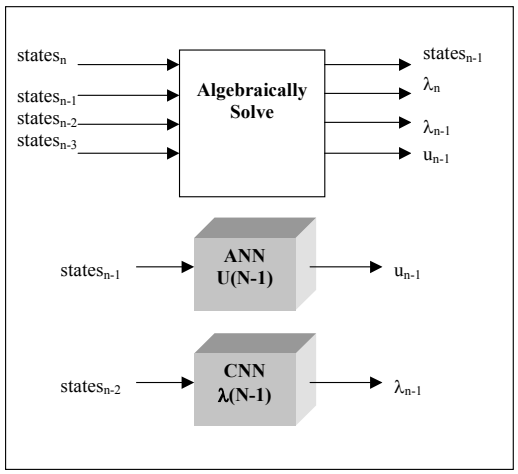

Figure 2: Synthesis of Last Network

1. Generate various random values of states$_{N-1}$, states$_{N-2}$, states$_{N-3}$ and calculate λ_N, λ_{N-1}, u_{n-1}, the co-states and optimal control respectively, by solving the discrete algebraic propagation and optimality equations.

2. Train two neural networks, the action network (ANN) and the critic network (CNN). The ANN inputs values of states$_{N-1}$ and outputs u_{N-1},. The CNN also inputs states$_{N-2}$ and it outputs λ_{N-1}.

Synthesis of Remaining Networks

The process of forming the other networks is described below and shown in Figure 3.

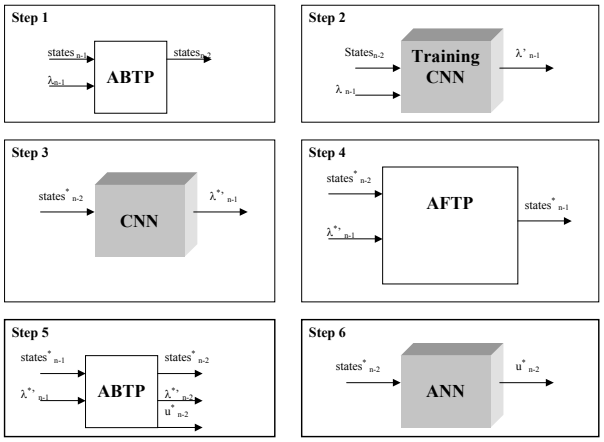

Figure 3: Synthesis of Remaining Networks

1. Algebraically back propagate the trajectory (ABTP) with the states$_{N-1}$ and λ_{N-1} to get the corresponding states$_{N-1}$.

2. Train the CNN with the $states_{N-2}$ and the corresponding λ_{N-1}.

3. Expand $states_{N-2}$ and use the CNN to obtain the corresponding λ_{N-1}.

4. Algebraically forward propagate the trajectory (AFTP) with the expanded $states_{N-2}$ and the corresponding λ_{N-1} to obtain the corresponding $states_{N-1}$.

5. ABTP with the new $states_{N-1}$ to obtain $states_{N-2}$, λ_{N-2}, and u_{N-2}.

6. Train an ANN with the $states_{N-2}$ as input and u_{N-2} as output.

Results

The neural network synthesis as described above was used to generate TAEM and A/L trajectories. The trajectories generated used down range as an independent variable, rather than altitude, as discussed earlier so that the results can first be validated with an existing result. The performance of the neural network generated trajectories is obtained by assuming any state variable value, within the trained scope, and using the appropriate δC_L, lift coefficient correction factor during simulations to generate the trajectories. The down range history from –1000 m of

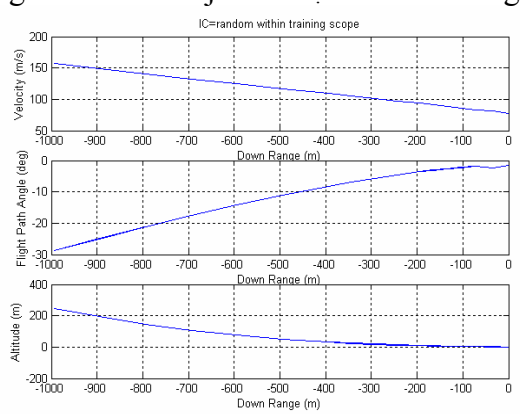

Figure 4: Down Range Neural Network Trajectory Histories

the velocity, the flight path angle, and the altitude for various initial conditions are shown in Figure 4. The ranges of these initial conditions are provided in Table 2. These results were

Table 2: Initial Condition Ranges (from –1000 m Down Range)

	Maximum	Minimum
Velocity (m/s)	157	156
Flight Path Angle (deg)	-28.8	-29.7
Altitude (m)	248	241

generated without the use of the CNN as an expander of initial conditions. This was done so that this trajectory set could be compared to an existing trajectory to determine its validity. Figure 5 demonstrates that from –1000 meters before the runway the RLV can meet the final constraints, x_f=0, and $V_f \sin\gamma_f$=-2 m/s for any initial condition within the predefined range. The down range history of lift coefficient, C_L, which is used as the guidance control variable is displayed in.

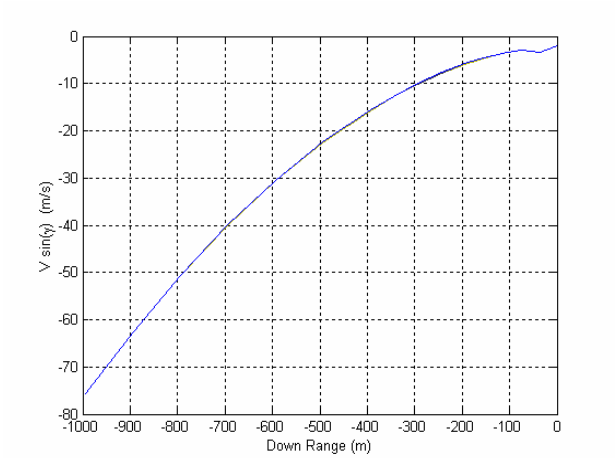

Figure 5: Satisfaction of Final Constraints

Figure 6 along with the down range history of the lift coefficient components. From this figure it is determined that the commanded lift coefficient values are within an acceptable range for a RLV

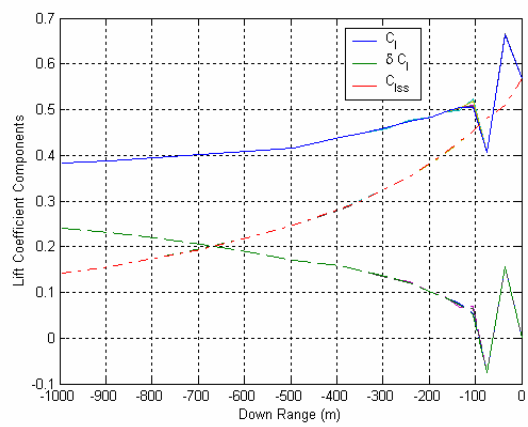

Figure 6: Control History

Future Work

Once the trajectory comparison has been completed, the CNN expansion, as described in Section 3.2 will be applied. After its successful application, the study will transition into the use of altitude as the independent variable and the 6-degrees of freedom trajectory synthesis will commence. This study will continue until the TAEM interface is reached with the neural network synthesis. The final results of this study will produce a larger range of initial conditions, which like trajectories shown in Figure 5, will meet the predetermined final constraints. Finally the neural network guidance will be implemented into Marshall Aerospace VEhicle Representation In C (MAVERIC) for a final validation on the X-33 aircraft simulation.

Conclusion

A neural network approach to developing optimal TAEM trajectories has been presented in this study. This approach solves a nonlinear guidance problem without linearizing the model. The results of the future work will demonstrate the powerful capability of adaptive critic based neural networks to solve this class of problems.

Acknowledgements
The author would like to thank the NASA Faculty Fellowship program and John Hanson for the opportunity to do research at the Marshall Space Flight Center. Also, Warren Adams, Greg Dukeman, and Jim McCarter for their help with MAVERIC. As well as S.N. Balakrishnan for his wonderful performance as an academic advisor.

References

[1] Balakrishnan, S. N. and Biega, V., "Adaptive Critic Based Neural Networks for Aircraft Optimal Control", Journal of Guidance, Control, and Dynamics. Vol. 19, No .4, July-Aug, 1999, pp893-898.

[2]Bryson, A. E. and Ho, Y. C., *Applied Optimal Control*, Halsted Press, 1975.

[3] Hagan, M.T., Demuth, H.B. and Beale, M., "Neural Network Design". PWS Publishing Company, Boston, 1996,(pp1-1).

[4] Han, Dongchen and Balakrishnan,S.N., "Adaptive Critic-Based Neural Networks for Agile Missile Control", Journal of Guidance, Control, and Dynamics, Vol. 25, No.2, March-April, 2002,pp404-407.

[5] Lu, Ping, Shen, Zuojun, Dukeman, Greg A., Hanson, John, M., "Entry Guidance by Trajectory Regulation", *Proceedings of AIAA Guidance, Navigation, and Control Conference*, Denver, CO, August 14-17, 2000.

[6] Moore, Thomas, "Space Shuttle Entry Terminal Area Energy Management", NASA Technical Memorandum 104744, November 1991.

[7] Olson, Lee, "Flight Systems Design and Analysis, Terminal Area Energy Management and Approach/Landing Guidance and Control", Presentation, X-33, Day 3, FA, July 1996, pp250-276.

2002

NASA/ASEE SUMMER FACULTY FELLOWSHIP PROGRAM

MARSHALL SPACE FLIGHT CENTER
THE UNIVERSITY OF ALABAMA

MAGNETIZED TARGET FUSION PROPULSION: PLASMA INJECTORS FOR MTF GUNS

Prepared By:	Steven T. Griffin
Academic Rank:	Associate Professor
Institution and Department:	The University of Memphis Electrical and Computer Engineering Department
NASA/MSFC Directorate:	Transportation
MSFC Colleague:	Dr. Francis Thio

Introduction - MTF: Plasma Injector

To achieve increased payload size and decreased trip time for interplanetary travel, a low mass, high specific impulse, high thrust propulsion system is required. This suggests the need for research into fusion as a source of power and high temperature plasma. The plasma would be deflected by magnetic fields to provide thrust. Magnetized Target Fusion (MTF) research consists of several related investigations into these topics. These include the orientation and timing of the plasma guns and the convergence and interface development of the "pusher" plasma. Computer simulations of the gun as it relates to plasma initiation and repeatability are under investigation. One of the items under development is the plasma injector. This is a surface breakdown driven plasma generator designed to function at very low pressures. The performance, operating conditions and limitations of these injectors need to be determined.

Plasma Injector and Plasma Gun Initiation

The basic plasma gun is a cylindrically symmetric coaxial line. An inner conductor is charged positive by several kilovolts with respect to the outer conductor. The injection of plasma initiates a vacuum arc breakdown between the anode and cathode. The resulting high current flow through a low inductance circuit produces a strong magnetic field circulating around the central anode. The Lorentz Force on the arc produces acceleration down the tube towards the gun muzzle. Rapid heating of the ion and neutral population ahead of the plasma produces a hypersonic shock wave out the gun. This wave collects and pushes the background gas out the muzzle. The basic gun configuration has been tested and verified.

A significant factor in the performance of the proposed multi-gun configuration is the consistency and reliability of the arc initiation in the breech of the plasma gun. Variable delays in plasma formation in the gun breech could result in timing problems in the multi-gun configurations. In particular the firing jitter of a plasma gun needs, at a minimum, to be known and repeatable. In turn, the plasma formation time in the gun breech needs to be controlled and is heavily dependent on the behavior of the plasma injection system during the surface breakdown.

In a normal field initiated surface breakdown, the process is started by field electron emission at the triple point between dielectric, cathode metal and vacuum. The electrons are accelerated by the anode-to-cathode applied field and attracted back to the surface by imbedded charge. Secondary electron emission produces additional electrons and embedded positive charges causing an avalanche to the anode. Devolved or decomposition gas from the surface is impacted producing mobile ions that migrate towards the cathode. The redistribution of space charge reinforces the triple point electron emission [3]. In low impedance systems, large currents may flow. This constricts the conduction path in the gas and along the dielectric. The result is "tracking" - the creation of a depressed trace where dielectric material has been preferentially removed to provide gas for the constricted discharge / arc. Frequently these tracks exhibit deposits of the non-volatile components of the dielectric after the surface breakdown has been externally interrupted.

In this system Vacuum UltraViolet (VUV) and charge generated in and near the surface of the dielectric initiates the process. This process is not as well characterized, developed or documented [4]. As a result research is required for the MTF guns.

To further the gun development, an experiment was planned to characterize the behavior of the plasma injectors. Of particular interest was the plasma temperature and density as a function of plasma injector parameters. Consistent performance of the plasma guns depends in part on the characteristics of the plasma injected into the breach from the plasma injectors. It also depends on the time delay and stability of the plasma injectors. Though a total investigation of this is beyond the scope of a ten-week program, instrument design and construction was completed and preliminary data was obtained. A description of the apparatus, a sample of the results and implications are detailed below. Further detail will be published under separate cover.

Experimental Apparatus

The experimental apparatus is shown in figure one. An existing vacuum system based on a turbomolecular pump was tested and demonstrated a base pressure of 0.7×10^{-6} Torr. A platform was introduced to the system. The initial version of the plasma injector was mounted to the platform. The injector contains a 50 nF capacitor in a coaxial configuration. One terminal of the capacitor is connected to the inner pin of the plasma injector. The other end of the capacitor is connected to a coaxial outer sheath. This sheath encloses the capacitor providing the return current path. The plasma-generating portion of the injector consists of a brass inner pin and outer shield held in a coaxial configuration by an insulator. The injector resembles a cut coaxial cable except the inner pin stops short of the outer jacket by about 0.25 inches. The insulator is cut in a conical shape - gradually slopping from the inner pin to outer sheath. The resulting structure is a negatively sloped cone whose surface breakdown characteristics have been described previously [4]. The unique aspect of this implementation is that the cone has been reversed so that the vacuum is inside rather than outside as shown in Latham [4]. This was an expediency of design and should not significantly impact its surface breakdown behavior under vacuum. [5,6] Teflon and polyethylene were the dielectric materials chosen to insulate the injectors and two injectors were built.

A RF shielded charge-dump system was built. This allowed the charging of the 50 nF capacitor through an electrically insulated wire. The charge-dump system used four HV relays, a 40kV Bertan High Voltage (HV) supply, assorted control relays and fiber optics communication components. In addition a test system was constructed from a HV choke and power supply. The temporary test system was used to prove the basic plasma injector design. A fiber optics based control system was developed for use in a pre-existing RF shielded control room.

Under normal operation the plasma injector capacitor is charged to 5-8 kV and the charging supply disconnected HV relays. In the temporary design test configuration a 660 nH high voltage inductor is used to isolate the HV supply during discharge. Either way, the capacitor is charged to its operating voltage and a surface break down initiated by a HV spark. The carbon spark is generated from two closely spaced wires impregnated with graphite**.** This assembly is positioned even with the top of the outer brass shell and approximately $^{3}/4$ of a cm. from the end

of the injector. An inductively generated HV pulse produces a spark. This initiates a surface breakdown along the dielectric.

As shown in figure one an experimental apparatus was built around this core device**.** A 0.75 meter spectrograph with three gratings (600, 1200, 2400 l/mm) on a rotating turret was joined to a 512 x 512 Charge Coupled Device (CCD) array**.** The CCD array and spectrograph are both computer controlled. The CCD array can be gated or operated as a fixed array. The light collection optics for the spectrograph is mounted on a Newport Research Corporation (NRC) rail. A pair of mirrors was mounted with four degrees of freedom. This allows the spectrograph field-of-view to be directed to any location with respect to the plasma injector nozzle. A $f^{\#}$ 9.7 condensing lens focuses the light from a collimated field-of-view onto the slits of the $f^{\#}$ 9.7 spectrograph. A 10x beam expander reduces the diameter of the spectrograph field-of-view to 1/10 of the setting of an aperture stop iris. Thus the location, orientation and diameter of the field-of-view of the spectrograph can be controlled. Location can be varied over the entire observation window and is repeatable to ± 0.1 mm. Orientation is repeatable to ± 100 micro-radians. Diameter is variable form 2.54 mm to 100 microns. Removal of a couple of optical posts converts the optics to an imaging type collection system.

In addition an optical fiber with a numerical aperture of 0.5 was used to collect spatially and temporally integrated spectra over the visible band. The fiber is routed to the Radio Frequency (RF) shielded control room into a separate spectrograph with CCD array. This second system is also under computer control and is used for wavelength survey and species identification. It was 0 extensively calibrated and verified last year. Though it has a specified 3 Δ resolution, sub-pixel resolution has been previously demonstrated. Wavelength accuracy was previously demonstrated to be less than 1 Δ .

All instrumentation and vacuum system components are isolated from building power by battery powered Un-interruptible Power Supply (UPS). RF and HV protection was provided to all instruments via mylar sheets and Kapton tape insulation, grounded metal RF shields and air gaps. Insulation tests were conducted in the vacuum chamber to verify HV integrity. Optical alignments were verified and triggering and control circuits tested. Wavelength calibration of the 0.75 meter spectrograph was accomplished using a set of hollow cathode spectroscopic standards.

Results, Post Processing and Discussion

Data sets were taken with the apparatus. These results will be reported under other cover. As an example of a raw data set, consider figure two below. It originated from a calibration run. The curve in figure two was signal processed and converted through MathCAD and Roper Scientific software but has not been digital signal processed to extract the desired parameters. In this figure there are ten discernable spectral lines attributable to neon. Several exhibit asymmetrical inhomogeneous broadening, possibly due to the relatively high percentage of isotopic contamination in natural neon. The large line at the right appears to be associated with neon at 3520.47 A. To obtain the desired plasma information a set of eight MathCAD programs were written to redistribute any error in the ten identified lines, compensate for baseline, extract this line [3520] from the spectra, convert from wavelength to frequency, remove system resolution

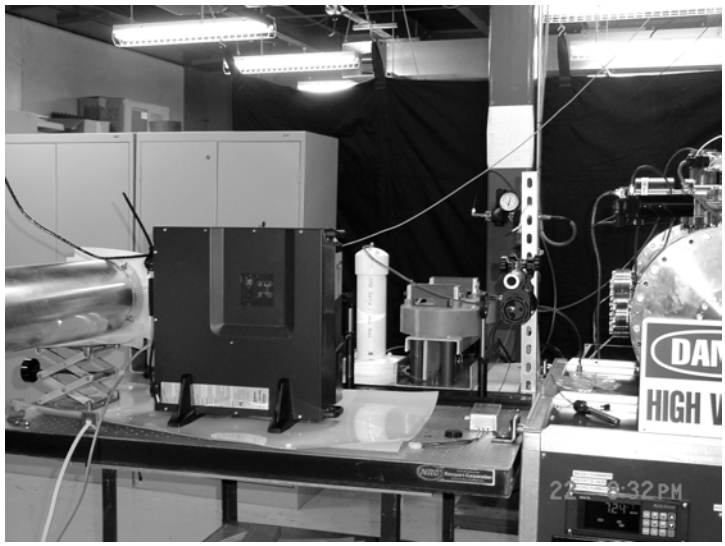

Fig. 1: Experimental apparatus

(partially), identify and de-convolve the Voight profile into the Lorentzian and Gaussian forms, and identify the widths associated with these. Most programs were fairly straightforward. The system resolution removal used standard techniques, based on a detailed optical analysis of the system, to generate a theoretical description of the optical transfer function (OTF) [1]. It was then removed from the data. The last two programs used an algorithm based on the transform of the magnitude of the spectral line. It was shown by closed form analytical development that the Lorentzian and Gaussian forms were separatably related to the slope and curvature of the result. Actual implementation developed some problems caused by the limited sampling capability of the CCD array available in ,conjunction with the dispersion capabilities of the spectrograph. These were overcome by a DSP scheme though they could also be addressed by the use of 2k, 4k or larger linear CCD arrays. The resulting software was verified by processing the output below which originated from a previously characterized and documented lamp and by multiple test runs on software generated lines.

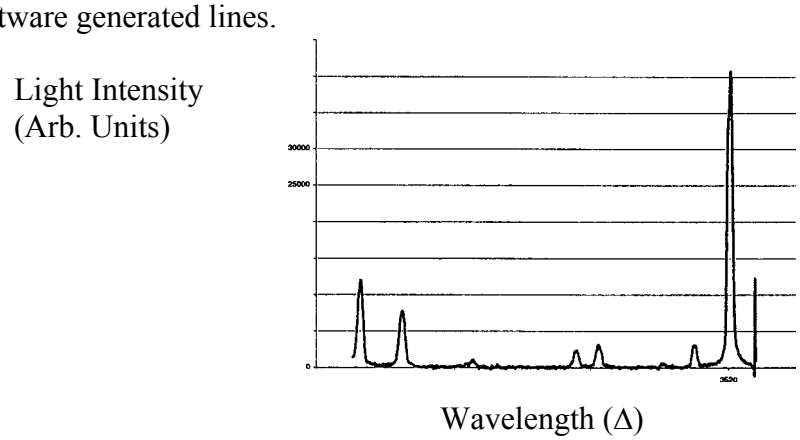

Fig. 2: Intensity versus Wavelength

In addition, initial firings of the Teflon plasma injector provided several important results. Several different states were observed for the injectors. These included a glow discharge like diffuse emission, an intermediate constricted, but still diffuse emission and a highly intense, low volumetric, arc like emission. Which occurred depended on charging voltage, background pressure, igniter placement, etc. With each optical emission, chamber ion gauge pressure was observed to jump from half of an order of magnitude to significantly more than an order of magnitude. Pressure jumps to a little below 10^{-5} Torr were observed in some cases. The time constant associated with its subsequent decay was consistent with gas evolution rather than electrical phenomena. Given a background pressure in the low to medium 10^{-7} Torr, it seems likely that the dielectric decomposition products dominate the plasma during the injection. The injector is currently producing an intense and pronounced optical plume. The initial test is considered a success and no further igniter modifications will be implemented at this time.

Some limitations were noted in the charging voltage. An initial charge voltage ceiling around 7500 volts was observed due to field initiated surface breakdown. After several shots, this voltage ceiling gradually lowered and filaments were observed in the dielectric. Some observers indicated the presence of carbon on the traces. After a few conditioning shots the ceiling was restored. The formation of the traces and/or carbon appears related to the type and intensity of the breakdown. These in turn appear related to the breakdown conditions.

Conclusions and Subsequent Work

Several conclusions can be drawn from the results to date.

(1) The injector demonstrates glow, abnormal glow and arc like behavior depending on a number of parameters.

(2) There is a maximum voltage to which the injector can be charged before field initiated self breakdown occurs. This breakdown depends on injector history.

(3) The current igniter placement appears a good choice for initial work.

(4) The surface breakdown in the current injector design provides significant plasma injection. It is likely that no additional gas source will be required.

(5) Spectroscopic analysis using old techniques and modern computers is able to provide density and temperature information for this application [2].

It is recommended that subsequent work emphasize the characterization of the plasma injector. The intention is to develop a set of parameters to guarantee consistent injection performance. For example, depending whether the injector generates a glow, abnormal glow or arc, the plasma injected may be very different in its composition and produce a different initiation sequence in the main gun. With six injectors per gun and multiple guns, it is advantageous to establish a stable parametric space and develop experience diagnosing behavior for a single injector.

Acknowledgements

The author would like to thank Francis Thio, Tom Markusic, Jim Martin, Mike Lee, James W. Smith, Jeff Richeson, Rashad Cylar, Willie Griffin, John Martin, Doug Davenport, Roger Harper, Jason Cassibry, Chris Dobson, Richard Eskridge, Adam Martin, Jeanelle Bland, Susan Dunnavant, Tammy Barcala and Chuck Karr for their assistance during the summer.

References

Complete list available upon request.

[1] Gaskill, J.D., (1978), *Linear Systems, Fourier Transforms, and Optics,* John Wiley and Sons, New York, pp. 449 - 515.

[2] Huddlestone, R.H. (1965), *Plasma Diagnostic Techniques,* Academic Press, New York, pp. 460-464.

[3] Kirkici, H., (1997), "Optical Emission Characteristics of Polycrystalline Diamond during Surface Flashover in Vacuum", IEEE Transactions on Dielectrics and Electrical Insulation, Vol.4, No. 6, pp.822 - 826.

[4] Latham, R.V., (1995), *High Voltage Vacuum Insulation: Basic Concepts and Technological Practice,* Academic Press, New York, pp. 299 - 401.

[5] Sudarshan, T.S. and Li, C.R., (1997), "Dielectric Surface Flashover in Vacuum Experimental Design Issues", IEEE Transactions on Dielectrics and Electrical Insulation, Vol. 4, No. 5, pp. 657-662.

[6] Wetzer, J.M., (1997), "Vacuum Insulator Flashover Mechanisms, Diagnostics and Design Implications", IEEE Transactions on Dielectrics and Electrical Insulation, Vol. 4, No. 4, pp. 349-357.

2002

NASA FACULTY FELLOWSHIP PROGRAM

MARSHALL SPACE FLIGHT CENTER

THE UNIVERSITY OF ALABAMA

INVESTIGATION OF METHODS FOR SUPPORTING TALL SLENDER STRUCTURES FOR FREE-FREE MODAL TESTING

REPORT NOT AVAILABLE

Prepared By:	A. Fort Gwinn, Jr.
Academic Rank:	Associate Professor
Institution and Department:	Lipscomb University Engineering Mechanics Department
NASA/MSFC Directorate:	Engineering
MSFC Colleague:	Ms. Kathy Kappus

2002

NASA FACULTY FELLOWSHIP PROGRAM

MARSHALL SPACE FLIGHT CENTER
THE UNIVERSITY OF ALABAMA

STANDARDS ADVISOR – ADVANCED INFORMATION TECHNOLOGY FOR ADVANCED INFORMATION DELIVERY

Prepared By:	J. Scott Hawker
Academic Rank:	Assistant Professor
Institution and Department:	University of Alabama Department of Computer Science
NASA/MSFC Directorate:	Engineering
MSFC Colleague:	Paul Gill

Introduction

Developers of space systems must deal with an increasing amount of information in responding to extensive requirements and standards from numerous sources. Accessing these requirements and standards, understanding them, comparing them, negotiating them and responding to them is often an overwhelming task. There are resources to aid the space systems developer, such as lessons learned and best practices. Again, though, accessing, understanding, and using this information is often more difficult than helpful.

This results in space systems that

- Do not meet all their requirements,
- Do not incorporate prior engineering experience,
- Cost more to develop,
- Take longer to develop.

The NASA Technical Standards Program (NTSP) web site at http://standards.nasa.gov has made significant improvements in making standards, lessons learned, and related material available to space systems developers agency-wide. The Standards Advisor was conceived to take the next steps beyond the current product, continuing to apply evolving information technology that continues to improve information delivery to space systems developers. This report describes the features of the Standards Advisor and suggests a technical approach to its development.

Product Overview

Figure 1 illustrates the concept for the Standards Advisor.

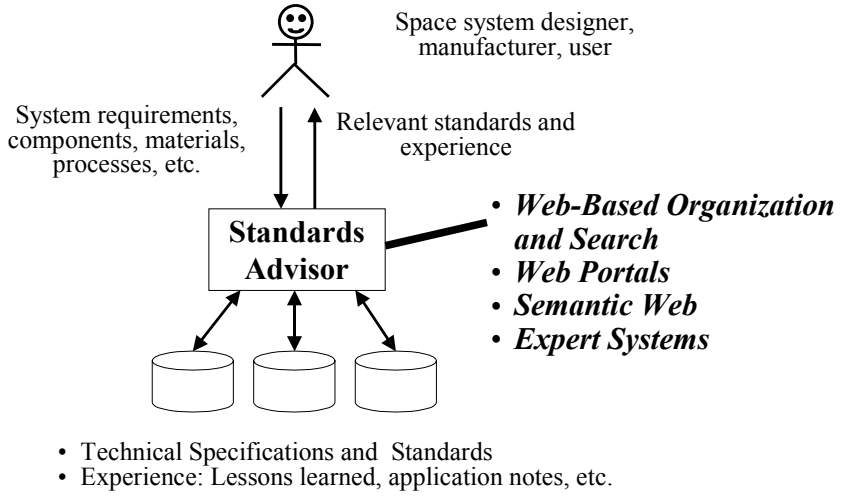

Figure 1: Standards Advisor Concept.

The current standards product provides keyword-based search of extensive standards and experiences databases, as well as organization of documents using various categorizations. The Standards Advisor will extend this capability in three areas:

- **Group/Project-Specific Web Portals.** These portals will provide the specific standards and other documents the group uses for their work, directly in the context of their work.
- **Advanced Document Search and Organization.** Newly available web search technology allows "fuzzy" word search, automatic concept/summary extraction, automatic document categorization, and search of the content of documents not stored in HTML (web text) format.
- **Knowledge Capture, Query, and Reasoning.** Augment the documents with additional data, using the language of the space system developer, capturing information about the meaning and content of the document. This will provide a more natural organization of and access to relevant documents. It will also enable software applications that reason about the documents in the context of the user's needs.

Technical Approach

This section suggests candidate technical approaches to provide the product features.

Web Portal

The primary issue in linking standards documents to web portals is passing user login credentials to 3rd-party servers of documents.

Figure 2 illustrates an approach to resolve this. An intermediate server script running on the NASA web server can front-end the document access, and a client-side script can pass user information as part of the document request.

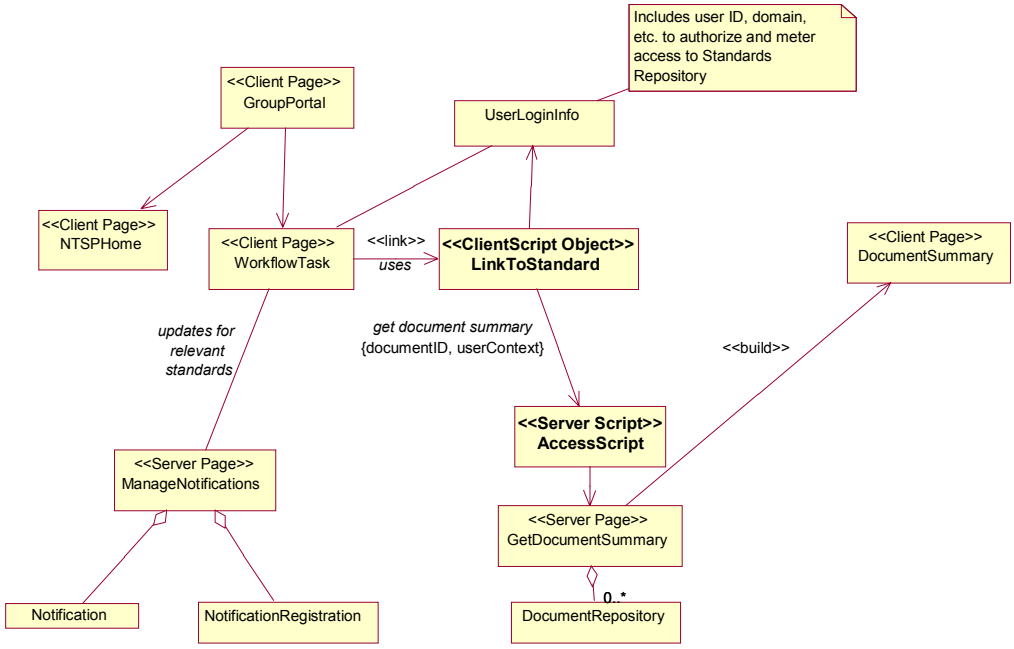

Figure 2: Using an intermediate server script.

Advanced Document Search and Organization

Products from a number of commercial vendors, such as Verity (www.verity.com), Google (www.google.com), and Inktomi (www.inktomi.com), all provide web site developers with tools to embed their search technology into intranets, allowing the Standards Advisor to use existing search technology to crawl, index, access, and display a diversity of data, including HTML and XML pages, application-specific document types (Word, Acrobat, etc.), and ODBC-compliant databases.

To crawl and index a web site or other repository, a crawler must have authority to do so. The crawler must be allowed through firewalls, and Robot META tags and robots.txt settings should be appropriate. Figure 3 illustrates a concept to crawl the sites and databases that get linked to standards documents. This would give the space systems developer a more complete view of standards in context.

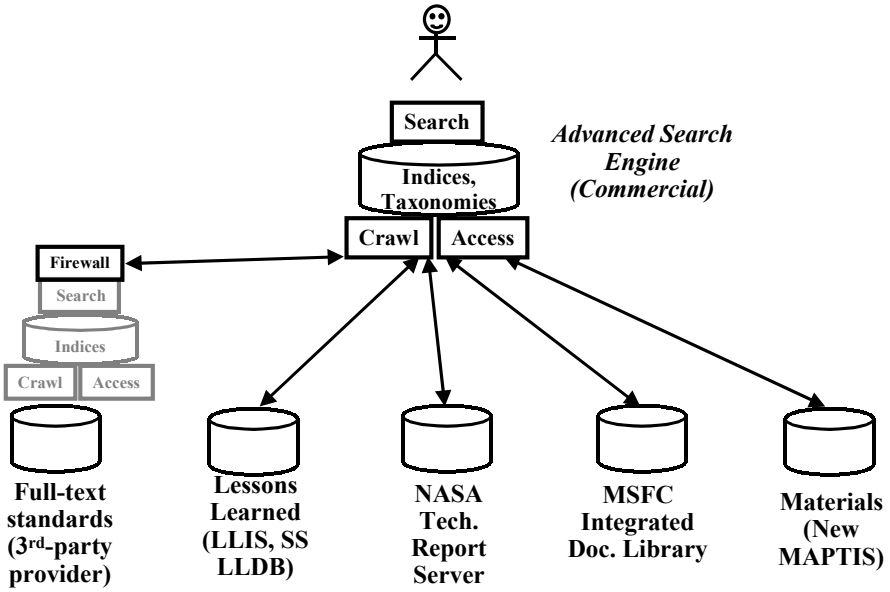

Figure 3: Advanced search across related databases.

Knowledge Capture, Query, and Reasoning

The dominant use of the web is, currently, to exchange and present documents for humans to view. More recently, the web has also become a means of data exchange and integration between software applications. Evolving standards for web services and metadata technologies are allowing web site and web application developers to use the web as a distributed computing environment, application database, and a knowledge base, as well as a document repository for humans. These technologies, collectively called the semantic web, provide an infrastructure to capture the meaning and intent of documents and related information, and to manipulate these to provide better information delivery for space systems developers.

As Figure 4 shows, the semantic web technologies enable capture of increasingly rich layers of data and knowledge, which, in turn, enable increasingly sophisticated processing and reasoning to support end users.

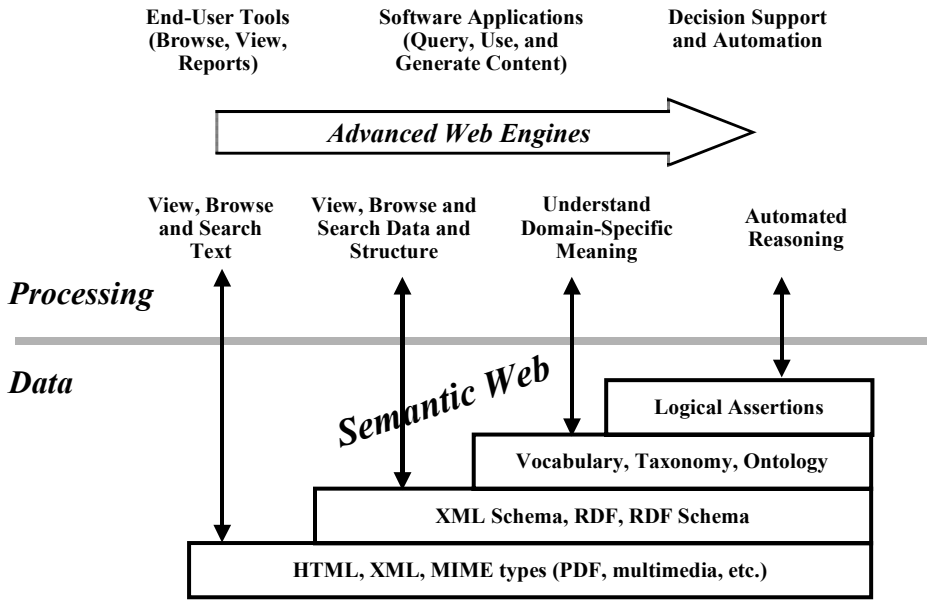

Figure 4: Increasing layers of metadata enable increasingly sophisticated functionality.

There are risks associated with using a technology as abstract and new as that of the semantic web. Users will now have to understand the basics of a new technology, and document developers will now have to create new information: ontologies and metadata.

Recommended steps

The next steps use prototypes to explore the possibilities in each area. Example steps include

- Prototype 1
  - Develop a "Smart Standards" portal for a selected NASA MSFC Engineering Directorate Group or manufacturing group
- Prototype 2
  - Implement an advanced search across the 3rd-party provider of full-text standards
  - Develop a strategy for integrated search across standards, lessons learned, etc.
  - Develop the requirements for and evaluate commercial search engine products
- Prototype 3
  - Use an advanced search engine to extract candidate metadata from focused collections of existing documents – begin to identify taxonomies and vocabularies
  - Build on existing ontologies to create a top-level standards ontology and taxonomy
  - Work with Topic and Discipline Working Groups to develop discipline-specific ontology and taxonomy
  - Add metadata to existing and new documents
  - Exploit the metadata (new search techniques, agents, expert systems, etc.)
  - Provide tools to develop and maintain ontologies and metadata

There are integration and overlap opportunities in related application areas such as workflow management, knowledge management, document management, product data management, and data warehouses.

2002

NASA FACULTY FELLOWSHIP PROGRAM

MARSHALL SPACE FLIGHT CENTER
THE UNIVERSITY OF ALABAMA

CREATION AND IMPLEMENTATION OF A WORKFORCE DEVELOPMENT PIPELINE PROGRAM AT MSFC

Prepared by:	Billy Hix
Academic Rank:	Professor
Institution and Department:	Motlow College Business Information Systems
NASA/MSFC Directorate:	Education
MSFC Colleague:	Mr. Jim Pruitt

Introduction

Within the context of NASA's Education Programs, this Workforce Development Pipeline guide describes the goals and objectives of MSFC's Workforce Development Pipeline Program as well as the principles and strategies for guiding implementation. It is designed to support the initiatives described in the *NASA Implementation Plan for Education, 1999-2003* (EP-1998-12-383-HQ) and represents the vision of the members of the Education Programs office at MSFC.

This document:

- Outlines NASA's Contribution to National Priorities
- Sets the context for the Workforce Development Pipeline Program.
- Describes Workforce Development Pipeline Program Strategies
- Articulates the Workforce Development Pipeline Program Goals and Aims
- List the actions to build a unified approach
- Outlines the Workforce Development Pipeline Programs guiding Principles
- The results of implementation

NASA's Contribution to National Priorities in Education

Since the creation of the National Aeronautics and Space Administration (NASA), chartered by the Space Act of 1958 (as amended), NASA has been committed to education. That commitment continues to the present, and occupies a significant place in the *NASA Strategic Plan*. NASA's contribution to education is based on the Agency's inspiring mission, specialized workforce, close working relationship with the research and development community, and unique world-class facilities. Based on these unique attributes, NASA has created a comprehensive Education Program containing a portfolio of activities directed toward education at all levels to inspire the next generation as only NASA can.

The outcomes of NASA's activities contribute to the achievement of the Nation's science and technology goals and priorities, including educational excellence.

NASA Educational Excellence Outcome

We involve the educational community in our endeavors to inspire America's students, create learning opportunities, and enlighten inquisitive minds.

Using this outcome as guidance for NASA's Education Program, the NASA Education Program Mission Statement is, "NASA uses its unique resources to support Educational Excellence for all as only NASA can."

It is within this context that the Workforce Development Pipeline Program has developed its Education Strategy. Just as the US Department of Education has established as it mission that "No Student will be Left Behind", NASA will take the program one step further and state that in addition, we want "No promising student in science and engineering left behind".

MSFC Workforce Development Pipeline Program Organizational Strategies

Program Goal and Aims

The goal of the MSFC Workforce Development Pipeline Program is to develop a highly skilled and competitive workforce for the 21st century by encouraging and involving young scholars to consider careers in technical and high skills areas.

The Workforce Development Pipeline Program aims to:

- To encourage and inspire students starting at an early age to continue their studies in math, science and technology.
- To foster an interest among students to pursue technical jobs and to track these students in a system that continually provides opportunities to students as they progress in their education.
- Produce a customer base that can support NASA's goals and objectives as well as those of our nation as a whole.

A new Unified Approach to the Workforce Development Pipeline Program

A unified approach will help coordinate the efforts of several programs at MSFC thereby minimizing redundancy and maximizing impact. Most importantly, it will cause all programs to find ways of sharing data benefiting the students in the different programs. Using this approach, the Workforce Development Pipeline Program will build upon existing resources; determine methods to better showcase our programs; examine and implement methods to share knowledge and data about each program; and to start the process of determining the ROI (Return on Investment) on individual programs. By using this approach, this will allow the program to achieve high quality results that make immediate impacts on students with little additional expense. Being focused on the integrated long-term professional development of students is a new approach within NASA. This will cause systemic change in the way that we view all of our programs.

Our focus will change from implementing and conducting a program to being able to articulate very specific long-term goals and success measures in the areas that fall under the Development Pipeline Program. This program will also address the national educational goals of supplying a skill workforce to NASA and to American industry.

Building a Unified Approach

Actions

- Develop a charter for the Workforce Development Pipeline Program
- Implement an HRIC (Human Resource Investment Council)
- Examine preliminary methods to share data between programs
- Conduct quarterly meetings of the HRIC

Implementing a Unified Approach

Actions

- Create an internal survey to determine the needs of the future workforce
- Determine how best to market all of the programs involved in workforce development in one central "one-stop" location for the customer
- Showcase one of the programs involved in Workforce Development at each of the quarterly workforce development meetings
- Select one program to start the process of ROI (Return on Investment)
- Provide an informational seminar to inform the staffs of all participating departments on the programs offered by the Workforce Development Program.
- Assess programs to determine if their content would be appropriate for e-learning for greater outreach of students.
- Utilize the ERC network to inform educators about the Workforce Development Pipeline programs and e-learning opportunities.
- Understand the existing educational programs that address needs used in the Workforce Development Pipeline Program.
- Identify any mis-match between workforce needs and educational opportunities.
- Create an information network or system to share data about programs and the customers that use them between managers of the workforce development program.
- Understand the workforce needs of NASA in the upcoming years.
- Develop new models for training or educational programs and remove ineffective programs based on current and future workforce needs at MSFC.
- Engage educators in helping identify specific needs in their curriculum that can be addressed by our Workforce Development Pipeline Program
- Evaluate the effectiveness of how the curriculum and customer information is passed onto the next higher-level program. Programs must share data and modify content of the program to make the program into the goals of the Workforce Development Pipeline Program.

- Be opportunistic by presenting information at professional educator conferences and in school systems.
- Create an internal and external survey of employment needs to match with workforce development programs.

Program Assessment

External and internal assessment efforts ensure the quality of the program, locate areas of needed improvement, and guide the efforts to achieve goals. Internal assessment should assess the effectiveness of the committee and the programs that fall under the Workforce Development program. It is important to involve the individuals that are managing the program in this process. This assessment should help guide program planning and should ensure that workforce development programs are effective, that they change with the needs of the target audiences, and they achieve a high impact for the investment.

Integrating actions benefit teamwork within all of the programs involved in the Workforce Development Pipeline Program by providing coherent support for educational excellence. This will reduce duplication of effort among our people, improve quality and ease of availability for our customers, promote cost effectiveness, and enhance better outreach of our current programs. This innovative approach taken by MSFC will assist in supporting the role of education in NASA's Strategic plan and play a vital part in developing the workforce of the 21st century.

Actions:

- Select one program to start the long-term process of ROI.
- Create an internal/external panel of experts to review and comment on the Workforce Development Pipeline Program
- Collect and analyze Edcats and other data
- As the Workforce Development Pipeline Program matures, data should be tracked on former Workforce Development Pipeline Program students who enter the NASA Workforce. A questionnaire should be created and would be completed by the workforce member at the point of hiring and at the first year anniversary. This questionnaire should help create a list of best practices and further refine the programs offered in the Workforce Development Pipeline Program and assist in helping NASA improve its hiring practices. In addition, all students completing any college level program should be required to answer questions at their "exit interview" to capture feedback on their plans for future employment. Attention should be given to the reasons why they would or would not chose employment at NASA.

2002

NASA FACULTY FELLOWSHIP PROGRAM

MARSHALL SPACE FLIGHT CENTER
THE UNIVERSITY OF ALABAMA

THE PHYSICS OF SOLAR SAILS

Prepared By:	William Andrew Hollerman
Academic Rank:	Assistant Professor
Institution and Department:	University of Louisiana at Lafayette Department of Physics
NASA/MSFC Directorate:	Engineering
MSFC Colleague:	Dr. David Edwards

Introduction

The concept of using photon pressure for propulsion has been considered since Tsiolkovsky in 1921 [1-7]. In fact, Tsiolkovsky and Tsander wrote of "using tremendous mirrors of very thin sheets" and "using the pressure of sunlight to attain cosmic velocities" in 1924 [1-4]. The term "solar sailing" was coined in the late 1950s and was popularized by Arthur C. Clarke in the short story *Sunjammer* (*The Wind From the Sun*) in May 1964 [5]. The National Aeronautics and Space Administration (NASA) used sailing techniques to extend the operational life of the Mariner 10 spacecraft in 1974-1975. A problem in the control system was causing Mariner 10 to go off course. By controlling the attitude of Mariner 10 and the angle of the solar power panels relative to the Sun, ground controllers were able to correct the problem without using precious fuel [4, 6, 7].

Once thought to be difficult or impossible, solar sailing has come out of science fiction and into the realm of possibility. Any spacecraft using this method would need to deploy a thin sail that could be as large as many kilometers in extent. Candidate sail materials should be: 1) strong, 2) ultra-lightweight (density of a few g/m^2), 3) able to be folded or crushed until deployed, 4) subject to minimal sagging or stretching, and 5) resistant to ionizing radiation, such as galactic and solar particles (electrons and protons), x-rays, ultraviolet light, and magnetically trapped charged particles. Solar sails must be resistant to each of these types of radiation [8].

Theoretical Considerations

Since photons are electromagnetic quanta, they have associated electric and magnetic fields [4, 7, 9]. For distances larger than several solar radii, an electromagnetic plane wave can be used to approximate the interaction of photons with a sail. Assume a sail is positioned in relation to the Sun as shown in Figure 1.

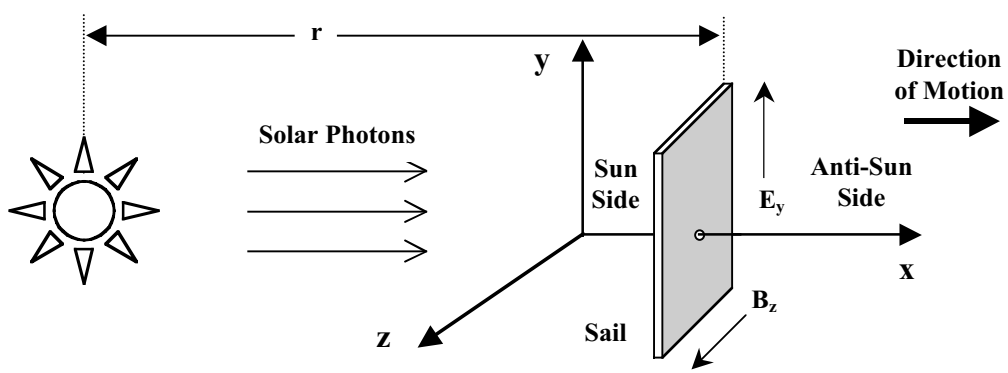

Figure 1: Solar Sail Model

In this model, the sail is positioned at a distance r from the Sun. Photon pressure will cause the sail to move along the +x axis. Using a plane wave solution for photons in a vacuum, the electric and magnetic fields will be in phase along the +y and +z axes respectively. Both the fields will be perpendicular to the direction of photon motion. The main components of the electric (E_y) and magnetic fields (B_z) can be written as

$$E_y = E_0 \sin\left[\omega\left(t - \tfrac{x}{c}\right)\right] \tag{1a}$$

$$B_z = \tfrac{E_0}{c} \sin\left[\omega\left(t - \tfrac{x}{c}\right)\right]. \tag{1b}$$

The E_0 parameter is the constant value of the electric field (N/C), ω is the angular frequency (rad/s), t is elapsed time (s), x is the displacement along the axis (m), and c is the speed of light in a vacuum. These equations assume the incident solar photons are monochromatic, which allows the quantity (E_0/c) in (1b) to be equal to the constant value of the magnetic field (B_0), which is in tesla (T).

The flux vector (**S**) transported by the fields is equal to

$$\mathbf{S} = \varepsilon_0 c^2 \left(\mathbf{E} \times \mathbf{B}\right), \tag{2}$$

where ε_0 is the permittivity of free space, **E** is the electric field vector, and **B** is the magnetic field vector. All vector quantities are shown in bold font. The flux is also known mathematically as the Poynting vector and can be calculated using (1a), (1b), and (2) as

$$\mathbf{S} = \varepsilon_0 c^2 \begin{vmatrix} \mathbf{i} & \mathbf{j} & \mathbf{k} \\ 0 & E_y & 0 \\ 0 & 0 & B_z \end{vmatrix} = \varepsilon_0 c^2 E_y B_z \mathbf{i} \;=\; \varepsilon_0 c^2 E_y \sin^2\left[\omega\left(t - \tfrac{x}{c}\right)\right] \mathbf{i}. \tag{3}$$

Obviously the flux vector and the solar photons are both moving in the +x direction. The average of the Poynting vector in the +x direction over one period (τ) is known as the intensity (I_x), and can be calculated as

$$I_x = \tfrac{1}{\tau} \int_0^{\tau} S\,dt = \frac{\varepsilon_0 c E_0^2}{2}. \tag{4}$$

Intensity has the same units as flux, namely watts per square meter (W/m^2). The stored energy density (U) in the fields for the solar sail is

$$U = \tfrac{1}{2}\left[\varepsilon_0 \mathbf{E}^2 + \tfrac{1}{\mu_0}\mathbf{B}^2\right] = \varepsilon_0 \mathbf{E}^2 = \varepsilon_0 E_0^2 \sin^2\left[\omega\left(t - \tfrac{x}{c}\right)\right], \tag{5}$$

where μ_0 is equal to the permeability of free space. The square notation is shorthand for the vector dot product. The quantity U has the units of joules per cubic meter (J/m^3), which is analogous to pressure (N/m^2 or Pa). The average pressure (p) on the solar sail due to photon bombardment is equal to the average energy density over one period, as shown by

$$p = \langle U \rangle = \tfrac{1}{\tau} \int_0^{\tau} U\,dt = \frac{\varepsilon_0 E_0^2}{2}. \tag{6}$$

Dividing both sides of (4) by the speed of light and equating the result to (6), gives a expression for p, shown as

$$p = \frac{\varepsilon_0 E_0^2}{2} = \frac{I_x}{c}. \tag{7}$$

Equation (7) assumes the sail material totally absorbs the incident solar photons. If the sail has a constant reflectivity (R), the total pressure (p_t) on the sail is

$$p_t = (1+R)\frac{I_x}{c}. \tag{8}$$

Momentum imparted to the sail by the reflecting photons introduces the extra term in (8). The R parameter is a constant for a given sail material and is a fraction between zero and one.
The light intensity (I_x) shown in (4) is an experimentally determined constant. Since the sail distance r is large compared to the solar radius, the intensity will fall off with the inverse square of the separation distance, and be equal to

$$I_x = \frac{3.83 \text{x} 10^{26}}{4\pi r^2}. \tag{9}$$

The constant in the numerator is the luminosity in watts at the surface of the Sun. At 1 AU, I_x reduces to the familiar vacuum solar constant of 1,368 W/m^2. Substituting (9) into (8) gives the result for total pressure of

$$p_t = \frac{(1+R)}{r^2}\frac{3.83 \text{ x } 10^{26}}{4\pi \text{ c}} = 1.02 \text{ x } 10^{17}\frac{(1+R)}{r^2}. \tag{10}$$

Equation (10) can be simplified to

$$p_t = 4.56 \text{ x } 10^{-6}\frac{(1+R)}{r_{AU}^2}, \tag{11}$$

where r_{AU} is equal to the distance to the sun in AU and p_t is in N/m^2. Using (11), a perfectly reflective solar sail (R = 1) at a distance of 1 AU from the Sun experiences a light pressure of 9.1 μN/m^2.

It is often wrongly stated that particle pressure from the "solar wind" powers sail spacecraft. Solar wind is composed of low-density protons and electrons moving at high velocity. The pressure due to the solar wind (p_w) is on the order of

$$p_w \sim m_p \rho_w v^2, \tag{12}$$

where m_p is the mass of the proton (kg), ρ_w is the particle density, and v is the velocity [4]. Near the Earth, a solar wind density of 6 x 10^6 m^{-3} at a velocity of 4 x 10^5 m/s gives a particle pressure of about 1 nN/m^2, which is more than three orders of magnitude smaller than the equivalent photon pressure [4, 10, 11].

Sail Materials

Physical characteristics for several candidate solar sail materials can be found in Table 1. These materials shown in Table 1 were selected due to their relevance to the application, availability, and manufacturability. These sails each have a density of a few grams per square meter.

Table 1: Tested Solar Sail Material Properties

Sample Description	Base Polymer	Base Thickness (µm)	Front Coating		Back Coating	
			Thickness (nm)	Element	Thickness (nm)	Element
Aluminized Mylar	Mylar	3.0	50	Al	50	Al
Aluminized Mylar With Chromium	Mylar	0.9	50	Al	20	Cr
Aluminized Kapton	Kapton	8.0	30	Al	30	Al
Aluminized CP1	CP1	3.0	50	Al	None	

The back surface of one mylar sample was coated with 20 nm of chromium. Chromium was selected because it has a higher emissivity than aluminum and radiates heat more efficiently. The selected aluminized mylar uses stock that contained Kevlar threads to serve as a rip-stop mechanism. These threads were positioned 25 mm (1 inch) apart. The aluminized Colorless Polyamide 1 (CP1) is a moisture resistant polymer that can be stored for long periods of time without significant property degradation. The aluminized CP1 sample did not have a metal coating on the back surface. Kapton maintains it properties at extreme temperatures. Mylar, Kapton, and Kevlar are trademarks of E. I. duPont de Nemours and Company. CP1 is a registered trademark of SRS Technologies.

MSFC Sail Research

The Environmental Effects Group (ED31) at the National Aeronautics and Space Administration's Marshall Space Flight Center (MSFC) maintains world-class facilities to simulate the effects of radiation on an assortment of space-qualified materials. Starting in 2001, ED31 began a comprehensive program to characterize the radiation survivability of candidate solar sail materials. Results from this research indicate that degradation in mechanical properties was observed after radiation exposure [12]. The data reinforces the fact that the thermo-optical properties do not significantly degrade. From this preliminary data, it appears the space environment will not significantly affect the propulsion performance of the sail. Electron exposure measurements are underway and will continue for the rest of 2002. Results from the electron measurements will be presented at the International Solar Energy Conference in Hawaii in March 2003. Proton and ultraviolet irradiation measurements will be completed in the future.

Acknowledgements

The author would like to thank Dr. David Edwards and the entire ED31 team at MSFC for their help and support during my stay in 2002. I appreciate the support and kindness of the entire team. I would like to continue this relationship in the future.

References

[1] Tsander, F.A. (1969), "From a Scientific Heritage", Translation, pp. 1-92, NASA TT F-541, National Aeronautics and Space Administration, Washington, DC.

[2] Blagonravov, A.A., Editor (1968), "K.E. Tsiolkovsky Selected Works", Translation by G. Yankovsky, pp. 140-163, Mir Publishers, Moscow, USSR.

[3] Tsander, F.A. (1964), "The Use of Light Pressure for Flight in Interplanetary Space, Problems of Flight by Jet Propulsion", L.K. Korneev, Editor, pp. 303-321, Israel Program for Scientific Translations, Jerusalem, Israel.

[4] McInnes, C.R. (1999), "Solar Sailing: Technology, Dynamics and Mission Applications", pp. 1-50, Praxis Publishing, Chichester, United Kingdom.

[5] Clarke, A.C. (1990), "The Wind From the Sun", A.C. Clarke, Editor, "Project Solar Sail", pp.9-31, Penguin Books, New York, NY.

[6] Souza, D.M. (1994), "Space Sailing", pp. 1-63, Lerner Publications Company, Minneapolis, MN.

[7] Turcotte, D.L. (1965), "Space Propulsion", pp. 108-125, Blaisdell Publishing Company, New York, NY.

[8] Evans, S.W., Editor, "Natural Environment Near the Sun/Earth-Moon L2 Liberation Point", Next Generation Space Telescope Program, NASA Marshall Space Flight Center, MSFC, AL, http://sail.msfc.nasa.gov/nse/sgst.html.

[9] Griffiths, D.J. (1989), "Introduction to Electrodynamics, Second Edition", pp. 304-360, Prentice-Hall, Incorporated, Upper Saddle River, NJ.

[10] "NASA Marshall Space Flight Center Solar Wind", NASA Marshall Space Flight Center, MSFC, AL, http://science.msfc.nasa.gov/ssl/pad/solar/sun_wind.htm/.

[11] "Science news and information about the Sun-Earth space environment", http://www.spaceweather.com/.

[12] Edwards, D., Hubbs, W., Stanaland, T., Hollerman, A., and Altstatt, R. (2002), "Characterization of Space Environmental Effects on Candidate Solar Sail Material", Proceedings, 47th International Symposium on Optical Science and Technology, Seattle, WA.

2002

NASA FACULTY FELLOWSHIP PROGRAM

MARSHALL SPACE FLIGHT CENTER
THE UNIVERSITY OF ALABAMA

Development of Low-Density Silica Particles for SHIVA

Prepared by:	Njeri T. Karangu
Academic Rank:	Assistant Professor
Institution and Department:	Spelman College Chemistry Department
NASA/MSFC Directorate:	Science
MSFC Colleague:	Dr. David Smith

Introduction

The objective of this work is the syntheses of low-density spherical silica particles, which will be used to further enhance our knowledge of the fundamental physics of the particle movements in fluids. The equations describing the particle/fluid motions have being under development and investigation over the last 100 years, yet the complete solution to this equation remained elusive, yielding only approximations and numerical solutions. Recently however, the first analytical solution to the general equation was produced by the joint efforts of NASA and NRA (Coimbra and Rangel, 1998). These particles will be used as a part of the various studies conducted to support SHIVA (Spaceflight Holography Investigation in Virtual Apparatus), the flight experiment proposed to validate this new analytical solution to the Stokes equation. The SHIVA project is designed to investigate the movement of particles in fluid and to understand and quantify the phenomena of microgravity, as well as allow the expansion of the limits associated with this analytical solution (Trolinger, J. D. 2001). The experiment proposes to use state-of-the-art holography, to precisely record the position of the particle and to allow the electronic downloading of these holograms, so that they are available on earth in real time.

Grounds experiments, utilizing tethered 2mm-diameter polypropylene particles in Krytox fluid, have being conducted and they have proven that the particle can be located with a precision sufficient to measure the effect of the history term (Trolinger, Espernace, Rangel, Coimbra et. el). Tethering the particle, allows the simulation of microgravity, however tethering the particle, produced added forces, which served to further complicate the equation. To make measurements of more general cases that cannot exist on the ground, particles with different densities are needed for the space experiment. Specifically three classes of particles are needed. Heavy particles with densities higher than the fluid, which would lag behind the fluid, particles with similar density as the fluid, which would move with the fluid, and light particles with densities less than the fluid, which would lead the fluid.

Our laboratory was charged with synthesizing the light spherical particles. This article discusses the synthesis, drying, sputtering and properties of these particles. Ideally the density of the fluid that is used in the experiment should be ten times more than the density of the particles. The fluid utilized in the experiment, Krytox, a perfluorinated polyether fluid, has an average density of 2g/cc, consequently, we would like to synthesize particles with an average density less than 0.2 g/cc. Since aerogels are highly porous, lightweight materials, with density as low as 0.003 g/cc (Physical Properties of Silica Aerogels) we decided to synthesize silica microspheres aerogels with diameters ranging from 0.5 mm to 4 mm. Aerogels are synthesized using sol-gel techniques, followed by supercritical solvent extraction, which leaves the original gel structure virtually intact.

Aerogels are open-cell polymers with pores less than 50 nanometers in diameter, as shown in figure 1. They are made by the reaction of the appropriate monomer, via the sol-gel polymerization technique, scheme 1. The monomers, which are suspended in solution, react with each other to form a sol, followed by cross-linking, which forms the sol-gel. The final aerogel is produced by carefully drying, so that the final structure does not collapse. In the case of silica aerogels, the monomeric units usually utilized are either tetramethyl orthosilicate (TMOS), Si(OCH3)4) or tetraethyl orthosilicate (TEOS, $Si(OCH_2CH_3)_4$). This is a multiple step

process involving the initial hydrolysis, where by the metal alkoxide reacts with water to form metal hydroxide (M-OH), followed by condensation, where two metal hydroxides (M-OH + HO-M) combine to give a metal oxide species (M-O-M.)

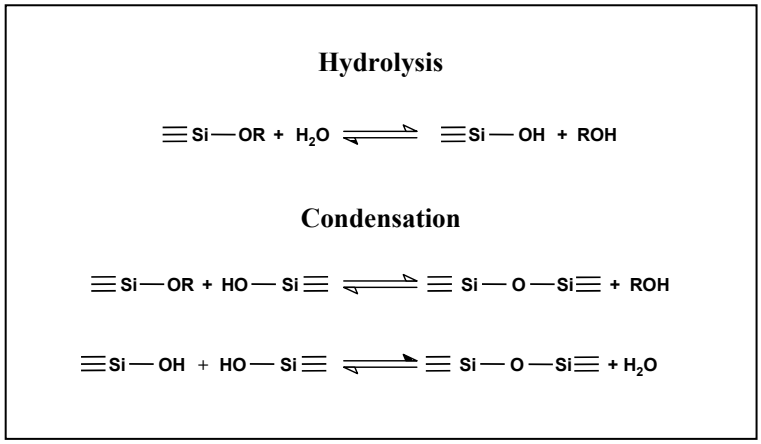

Scheme 1. Silica Sol-gel Formation.

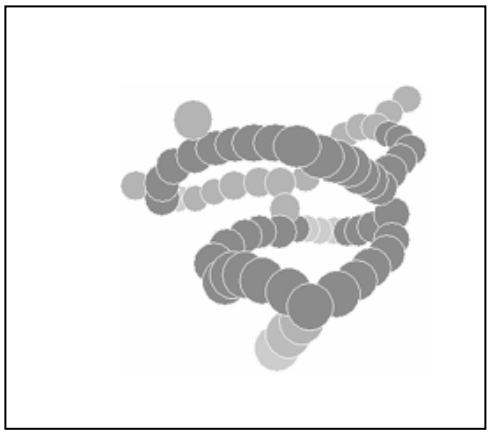

Figure 1. Aerogels open-cell

Methodology and Discussion

The aim of the research is to synthesize low-density spherical silica aerogels ranging in diameter from 0.5 to 4 mm. Once the particles are dried, via supercritical drying, they are then sputtered with gold. The sputtering serves to prevent silica pores from absorbing moisture and or other liquids, such as the Kyrtox fluid, which in turn would increase the density of the particles. The hydrolysis and polycondensation of silicates, such as tetramethyl orthosilicate (TMOS), using the sol-gel methods have been used to produce controlled monodisperse silica spheres in the micron size range (Stober, 1968). However, we wanted to make larger particles in the millimeter size range, so we modified this process.

The sol-gel process that we used consisted of the four steps (scheme 2). In the first step, we prepared a homogeneous solution, by dissolving the TMOS into deionized water. The amount of TMOS used ranged from 5 % - 25% (v/v). (It should be noted that the final density of the particles is controlled by the total amount of TMOS used.) We found out that it is very important to make sure that the initial solution was homogeneous and thus we stirred the solution for 90 minutes before proceeding to the next step. The second step involved converting the homogeneous solution into a sol. This was done via an inverse emulsion process. The homogeneous TMOS/water solution was pipetted into a mineral oil/pentane solvent mixture and then stirred until the delicate gel had formed. The size of the microspheres could be controlled by the amount of mineral oil added into the pentane, the string speed and the percent TMOS utilized. For smaller size spheres, more mineral oil was added, faster stirring speeds employed, and less TMOS used, as shown in table 1. Aging and soaking is the combined third step. In aging, the sols are reinforced and strengthened. This was accomplished by placing the delicate spheres into H_2O/EtOH solvent (1:1 v/v) for 48 hours. Soaking the particles in pure EtOH, is critical, because it serves to remove all the water in the alcogel's pores, and replaces it with ethanol. Any water left in the gel is not removed by the supercritical drying, and leads to opaque

and dense aerogel. Soaking the gels in pure EtOH and constantly replacing the bath EtOH, with new anhydrous EtOH, accomplished this step. The fourth and final step consists of the supercritical drying of the gels, which serve to remove all liquid within the gels, leaving only the solid linked silica networks. CO_2/EtOH solvent exchange, followed supercritical venting of CO_2 is the process employed in this step. The process is conducted in an autoclave.

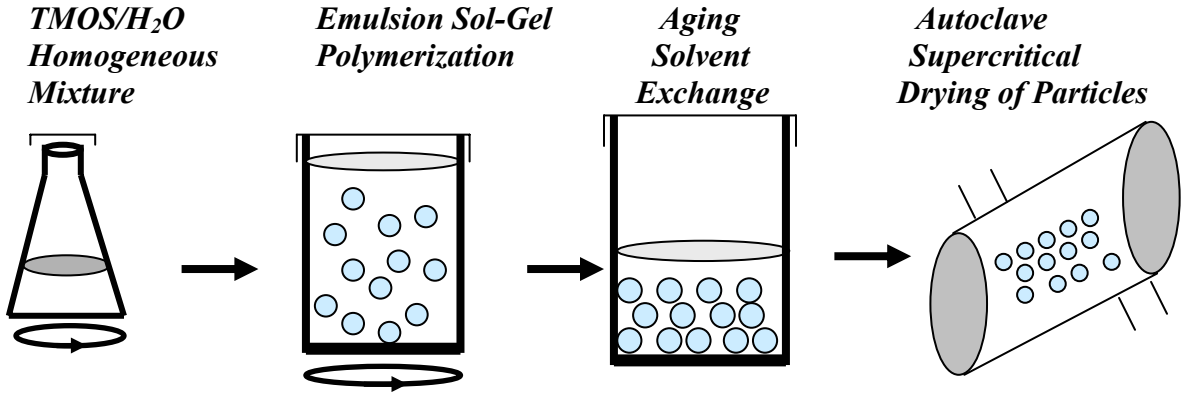

Scheme 2. The Four-Step Process of producing Spherical Silica Aerogels

Once the particles are dried, they are then sputtered with gold. The first trial, the particles were sputtered for 200 sec, however, the resulting particles were purple, indicating that there was a very thin layer of gold on the particles. The second time, the particles were sputtered for a 1000sec, and the resulting particles were golden. Figure 2, depicts wet alcogel, dried aerogels, 200-secs gold sputtered particles and 1000-secs gold sputtered particles.

Wet-gel particles, in ethanol

Supercritically dried particle

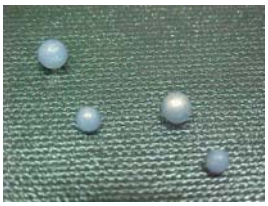

Purple Particles: 200-sec-gold sputtered

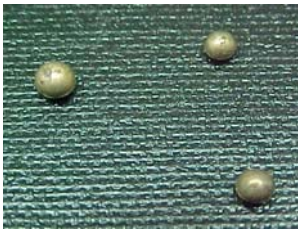

Gold Particles:1000-sec-gold sputtered

Figure 2. Spherical Silica Particles made from 25% TMOS

Particle Properties

Density

The particle's density was calculated as follows:

The total mass of three gold particles, made from the 25% TMOS, was found to be 0.0315 g
Average mass was 0.0105 g
The average diameter of gold particles, was found to be 3.0 mm
Average radius = 1.5 mm = 0.15 cm
Volume = $4/3\pi r^3$ = 0.01413 cm^3
Density = 0.743 g/cc
The resulting density was 3 times less than the density of Krytox. This particles were made using 25 % TMOS. Ideally we would like the particle density to be 0.2g/cc. So we decided to try and make some particles using 20 % TMOS, then reducing the amount of TMOS until we get a density that closely match what we are looking for. However, the following calculations show that the density of 20% TMOS particles would closely match the density that we are aiming for;
Final Volume Fraction (f) of SiO_2 = % TMOS (V/V) * .395
For Example: 20 % TMOS
1-p = (.2)(.395) = 7.9 % SiO_2 ; Gel porosity is p = 92.1 %
ρ(aerogel) = $\rho(SiO_2)$ (1-p) + ρ (Air) p = (2.2) (0.079) + (0) (.921) = 0.174 g/cc
However, we have assumed that we have complete conversion and that there is no shrinkage during the drying process:
Now, Assume 10% Shrinkage
$\rho_{shrinkage} = \rho$ (aerogel) /.9 = 0.193 ~ 0.2 g/cc.

Lyophobic Particles

The terms lyophilic (liquid-loving) and lyophobic (liquid-hating) are frequently used to describe the tendency of a surface or functional group to become wetted or solvated. If the solvent used is water, then the terms hydrophilic and hydrophobic are used. Since it is paramount to make sure that the particles are both hydrophobic and lyophobic, we tested the wetterability of both the aerogels and the gold-sputtered aerogels. Initially when the uncoated particles are placed in 10 ml of water, in a graduated cylinder, they float. However, in a few seconds, they fall to the bottom, indicating that water wets the silica particles and then the particles absorb water into the empty pores. This indicates that the surface groups of these particles are predominately silanol, Si-OH. On the other hand, both the purple particles and the gold particles float in the water, even after 5 minutes, indicating that gold converts the hydrophilic surface into a hydrophobic one.

Experimental Procedure

Silica alcogel was prepared from tetramethyl orthosilicate (TMOS, Aldrich 98 %) using a two-step process. Dissolving the appropriate amount of TMOS in water and stirring the sample for

90 minutes prepared a homogeneous TMOS sample, first step. The TMOS ranged from 5 % to 25 % (v/v) in de-ionized water. In the second, step, mineral oil and pentane were added into a 1,000 ml, glass long beaker equipped with a magnetic stir. The reaction was allowed to react, while stirring, until the gel-like particles had formed. The amount of time allowed for the second step, depends upon the % TMOS, as shown in table1. The mineral/oil pentane was decanted carefully, and the gelled particles were washed several times with H_2O and then with H_2O/ EtOH (1:1 v/v). Solvent exchange was conducted for two days, with pure anhydrous EtOH being added every 12 hours.

Sample Preparation of 25 % TMOS

2.5 ml of 98 % TMOS was added into 7.5 ml of de-ionized water and stirred for 90 minutes. 600 ml of pure mineral oil was added into a 1,000-ml long-glass beaker, equipped with a magnetic stir. 300 ml of pentane was added. The two solvents formed two layers, but after thorough stirring, a homogenous mixture was obtained. 9 ml of the 25 % TMOS was pipetted into the mixture, while stirring, and the reaction was allowed to react for 2 hours. The mineral oil/pentane was decanted and the gelled particles were washed five times with de-ionized with H_2O and three times with then with H_2O/ EtOH (1:1 v/v) mixture. Finally the particles were aged in a glass beaker for 48 hours in a water/ethanol (50/50 v/v) mixture. Then, the water/ethanol was decanted and the anhydrous ethanol was added to the particles. Every 12 hours, the ethanol was decanted and pure anhydrous ethanol was added. The solvent exchange was conducted for 48 hrs.

Results and Discussions

Low-density spherical silica particles, were prepared via sol-gel routes in which tetramethyl orthosilicate, TMOS, was hydrolyzed and condensed forming a gel, which was aged, dried under supercritical conditions and subsequently sputtered with gold. The density of the particles ranged from 0. to 0.74 g/cc depending on the amount of TMOS used in the reaction. The higher the % TMOS utilized, the higher the density, as illustrated in table 2. The gelation time, also depended on the % TMOS used in the reaction, the higher the % TMOS utilized, the less time it took to form the gel, table 2. The size of the particles depended on the amount of mineral oil used in the reaction, and the % TMOS used. The greater the quantity of mineral oil utilized, the smaller the particles. The higher the % TMOS utilized the larger the particle size. Particles with TMOS less than 10 % formed gels that were too soft. When these gels were dried, they collapsed. Particles made from the 15% TMOS constantly had bubbles in the gels, so these gels were not dried. Consequently, the densities from these particles were not determined.

Table 1. Particle Gelation Time and Density of Particles

% TMOS	Reaction Time (h)	Mineral oil: Pentane Ratio	Density (g/c)	Average Diameter Size
25	2	2 :1 (Speed = 5)	0.74 (3 particles)	3.0 mm
20	3.25	2 :1	0.28 (8 particles)	2.9 mm
15	4.0	2 :1		
10	6	2 :1		
5	22.5	2 :1		
25	3	3:1 (Speed = 7)	0.37 (8 particles)	1.5 mm

Conclusions

Low-density spherical silica particles were prepared, via an inversion emulsion polymerization process, utilizing mineral oil/pentane mixture as the reaction media, and water/TMOS homogeneous mixture as the emulsion. This four-step process involved an initial formation of a TMOS/H_2O homogeneous mixture, followed by the emulsion sol-gel formation of the particles. The amount of time required for the gelation depended upon the % TMOS, low % TMOS utilized, longer gelation times. Aging and soaking, whereby the sols are reinforces, strengthened, and all water in the alcogel is replaced by ethanol, was the combined third step. The final step was the supercritical drying of the particles, which was performed in an autoclave, utilizing carbon dioxide as the supercritical solvent. The particles were then sputtered with gold, converting them from hydrophilic to hydrophobic. This step serves to prevent the silica particles from absorbing any moisture or fluid into the pores. The density of the particles, which was controlled by the amount of TMOS utilized in the reaction, ranged from 0.74 g/cc to 0.15 g/cc.

Acknowledgments

The author would like to thank the entire team of the SHIVA project. David Smith, for your support, training and creating an opportunity for me to be here this summer, I am truly indebted to you. To Laurent Sibille and Curtis Banks, thank you very much for your help with the drying and sputtering of the particles, respectively. To Bill Witherow, thank your for the pictures. To Steve Paley, Don Frazier and Ben Penn, thank you for the advice. To Kirk Fuller, Amanda Gates, Wendy Patterson, thank you for your support. To Willie Love, Shelia Nash-Stevenson, Melanie Bodiford, Bill Patterson and Ron Young thank you for the funding.

Future Work

During the course of the research, it was noted that it is very important to make the particles spherical. However, we were not able to control the particles shape, hence, it would be ideal, for lab to determine the reaction conditions which would provide, a good control for the particles shape. Futhermore, the lab should make particles from 12.5 and 17.5 % and determine if these particles have a density less than 0.2 g/cc.

References

Coimbra, C.F.M., and Rangel R.H. "General Solutions to the Particle Momentum Equation in Unsteady Stokes Flow. "J. Fluid Mech., (1998)

Trolinger, J.D, PI., SCIENCE REQUIREMENTS DOCUMENT: *DRAFT* , SHIVA *(Spaceflight Holography Investigation in a Virtual Apparatus),* 18 September 2001

Trolinger, J.D, Esperance, D. L**.,** Rangel R.H, Coimbra, C.F.M, Witherow, W., Rogers, J., and Ravindra, L., Small Particle Response to Fluid Motion Using Tethered Particles to Simulate Microgravity.

Stober. W. Fink, A., and Bohn, E. "Controlled Growth of Monodisperse Silica Spheres in the Micron Size Range," J. Colloid Interface Sci., 26, 62-69 (1968).

Physical Properties of Silica Aerogels, http://eande.lbl.gov/ECS/aerogels/saprops.htm

2002

NASA FACULTY FELLOWSHIP PROGRAM

MARSHALL SPACE FLIGHT CENTER

THE UNIVERSITY OF ALABAMA

FINITE ELEMENT MODELING OF A CYLINDRICAL CONTACT USING HERTZIAN ASSUMPTIONS

Prepared By: Erik Knudsen

Academic Rank: Graduate Student

Institution and Department: University of Florida, Mechanical Engineering Department

NASA/MSFC Directorate: Strength Analysis Group

MSFC Colleague: Dr. Greg Swanson

Introduction

The turbine blades in the high-pressure fuel turbopump/alternate turbopump (HPFTP/AT) are subjected to hot gases rapidly flowing around them. This flow excites vibrations in the blades. Naturally, one has to worry about resonance, so a damping device was added to dissipate some energy from the system.

The foundation is now laid for a very complex problem. The damper is in contact with the blade, so now there are contact stresses (both normal and tangential) to contend with. Since these stresses can be very high, it is not all that difficult to yield the material. Friction is another non-linearity and the blade is made out of a Nickel-based single-crystal superalloy that is orthotropic.

A few approaches exist to solve such a problem and computer models, using contact elements, have been built with friction, plasticity, etc. These models are quite cumbersome and require many hours to solve just one load case and material orientation.

A simpler approach is required. Ideally, the model should be simplified so the analysis can be conducted faster. When working with contact problems determining the contact patch and the stresses in the material are the main concerns. Closed-form solutions for non-conforming bodies, developed by Hertz, made out of isotropic materials are readily available. More involved solutions for 3-D cases using different materials are also available. The question is this: can Hertzian[1] solutions be applied, or superimposed, to more complicated problems-like those involving anisotropic materials? That is the point of the investigation here. If these results agree with the more complicated computer models, then the analytical solutions can be used in lieu of the numerical solutions that take a very long time to process. As time goes on, the analytical solution will eventually have to include things like friction and plasticity. The models in this report use no contact elements and are essentially an applied load problem using Hertzian assumptions to determine the contact patch dimensions.

Finite Element Model and Formulation

Figures 1-2: From left to right; Finite Element Model and close-up of the fine mesh region

The figure above shows the small portion of the blade that would be touching the damper. Eight node brick elements comprised the dense region of the finite element model (FEM). The dimensions of each brick are 0.001 in x 0.001 in x 0.005 in. Very fine meshes are needed because of the applied load for this problem. A very large gradient is present, even over a thousandth of an inch. The applied load was determined by Hertz. It takes the form of a parabola and is applied along the surface of the model.

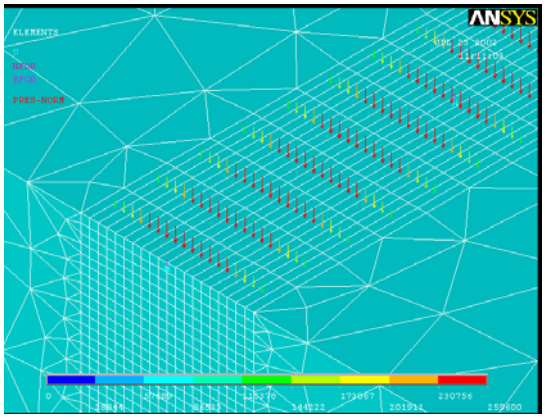

Figure 3: Parabolic Load Distribution

The colored arrows are the pressure applied to that particular surface element. Notice how the applied pressure (psi) starts at 0, but rapidly increases to over 100,000 psi in a just a few thousandths of an inch.

The model was constrained so no translation could take place in the direction of the applied load (Global Y-direction). A few other nodes were also constrained in the other two principal directions (X and Z) to provide stability. With the correct load, material

properties (single-crystal Nickel-based super alloy), geometry, and constraints in place the stresses were obtained using the ANSYS Finite Element software.

Results and Discussion

Single-crystal superalloys are not isotropic. The relative location of the crystal lattice (atomic structure) of the steel plays a vital role in the behavior of the material. Two sets of results are presented below, case 0^2 and case 33. In case 0, the crystal lattice coordinate system is parallel to the global material coordinate system. With case 33, the lattice is offset by a certain degree relative to the global coordinate system.

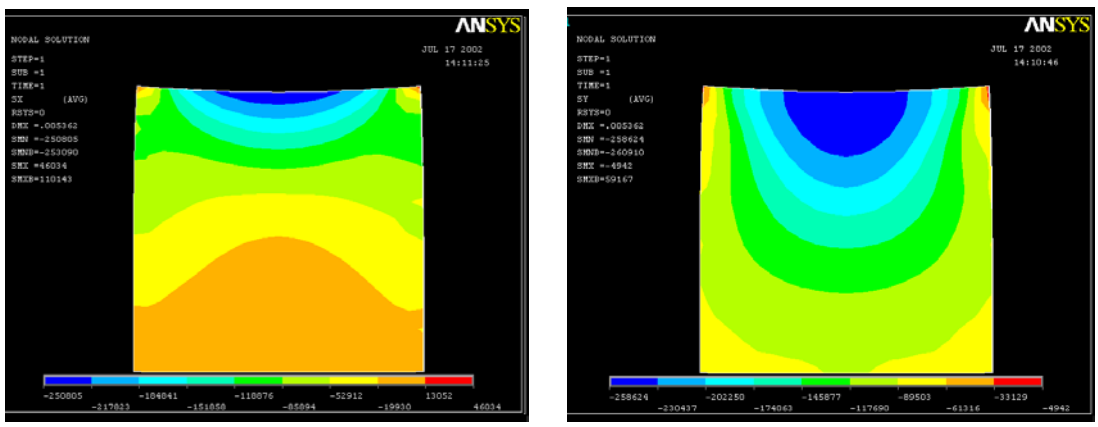

Figures 4-5: From left to right; contour plots (σ_x and σ_y) for case0

The stresses for case 0 (and for all other contour plots using this orientation) are symmetric. The above contour plot is the portion of the FEM that only contains the contact region. Outside of that region the stresses are uniform, which follows the predictions and analysis by Hertz. It was his contention that as one looks outside the contact zone, the stresses eventually become uniform. Thus, the primary area of interest is where the contact patch is and a few mills into the substrate (depth of the material).

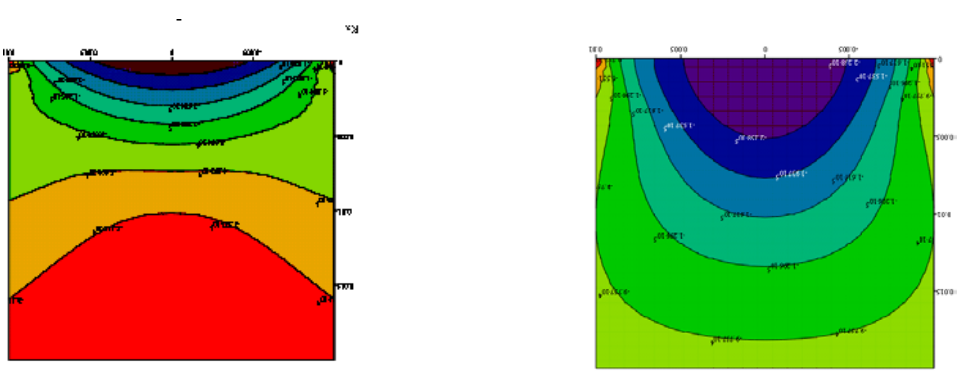

Figures 6-7: From left to right; contour plots from the analytical solution (σ_x and σ_y) for case 0

Nagaraj Arakere and Gilda Battista formulated an analytical solution, as this model was being developed, that complements the FEM. Note that in the above figure, the stresses are symmetrical just as the FEM contour plots are.

Looking at case 33, a case where the crystal orientation is now off-set by a certain degree, the contour plots are no longer symmetric, but the plots taken from the closed-form solution and the FEM look very much alike.

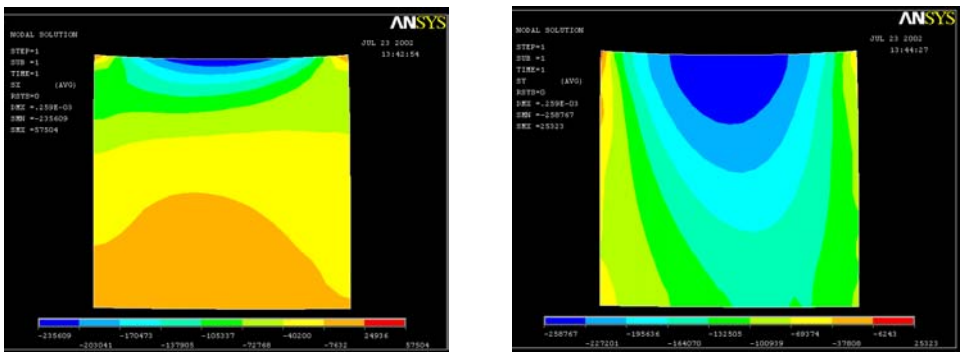

Figures 8-9: From left to right; case 33 contour plots (σ_x and σ_y)

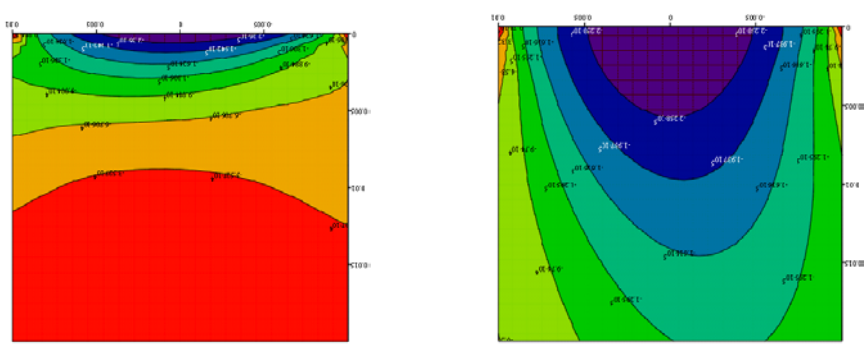

Figures 10-11: From left to right; case 33 contour plots (σ_x and σ_y) from the analytical solution

Conclusion

From looking at the above two cases, the FEM and the closed form solution seem to agree rather well. The next step is to add the tangential load with friction and also try to compare those results with an analytical solution. Hopefully the results will agree and then the analytical solution can be used exclusively to solve this problem since it will be much faster than the large FEMs.

References

1. Johnson, K.L.: *Contact Mechanics*, Cambridge University Press, 1985.
2. Arakere, N.K.; Swanson, G.R.: "Effect of Crystal Orientation on Analysis of Single-Crystal, Nickel-Based Turbine Superalloys," NASA Technical Report 2000-210074, February, 2000.

2002

NASA FAULTY FELLOWSHIP PROGRAM

MARSHALL SPACE FLIGHT CENTER
THE UNIVERSITY OF ALABAMA

TORQUE LIMIT FOR BOLTED JOINT FOR COMPOSITES
PART B
EXPERIMENTATION

Prepared By:	Kristian M. Kostreva
Academic Rank:	Graduate Student
Institution and Department:	Embry-Riddle Aeronautical University Department of Aerospace Engineering
NASA/MSFC Directorate:	ED 23
MSFC Colleague:	Frank Thomas

Introduction

Today, aerospace quality composite parts are generally made from either a unidirectional tape or a fabric prepreg form depending on the application. The matrix material, typically epoxy because of it dimensional stability, is preimpregnated onto the fibers to ensure uniform distribution. Both of these composite forms are finding themselves used in applications where a joint is required. Two widely used joint methods are the classic mechanically fastened joint, and the contemporary bonded joint; however, the mechanically fastened joint is most commonly used by design engineers.

A major portion of the research up-to-date about bolted composite joints has dealt with the in-plane static load capacity [2]. This work has helped to spawn standards dealing with filled-hole static joint strength. Other research [3,6] has clearly shown that the clamp-up load in the mechanical fastener significantly affects the joint strength in a beneficial manner by reducing the bearing strength dependence of the composite laminate. One author reported a maximum increase in joint strength of 28% [3]. This finding has helped to improve the reliability and efficiency of the joint in a composite structure.

Hence, the question that many design engineers ask is how much clamp-up load, applied via fastener torque, to specify in this joint. The current practice at MSFC is based on neither analytical techniques nor experimental results for composites. Instead, designers utilize conservative adjustments from the standard MSFC-STD-486B [7]. They use half of the experimentally determined torque value for any given bolt size when designing a composite joint [8]. This practice does not account for possible failure of the joint because of fastener preload.

Speaking with regards to material properties, composites are known to be notoriously poor performers in a state of pure compression. Lack of a fundamental knowledge base concerning the mechanical behavior of fiber-reinforced composites under through-the-thickness compression (TTTC) is responsible. After an extensive literature survey, it has been concluded that very little research has been done up-to-date regarding through-the-thickness (TTT) composite properties and nothing was found regarding TTTC; therefore, an experimental approach was needed to investigate the behavior of a composite single-lap joint.

This work involved development of a recommendation to determine the torque limit in a composite single-lap joint using the guidelines outlined by NASA/MSFC 486B. The graphite/epoxy laminates were configured according to MIL-HDBK-17B [5] and three different through-hole diameters were examined. Acoustic emission (AE) nondestructive testing was employed to supplement the data from the standard 486B test.

Acoustic Emission

The textbook definition of acoustic emission is a transient elastic wave generated by the rapid release of energy from localized source within a material. AE is a passive, nondestructive technique requiring the structure or specimen to be under load in order to generate the failure mechanisms that produce the elastic waves. Piezoelectric sensors attached to the surface detect the stress waves that propagate throughout the material and output a voltage signal. A

preamplifier is used to boost the voltage signal to a usable level, and a band-pass filter is used to remove unwanted noise. The voltage signal is then fed to a data acquisition system that extracts information about the signal and generates AE quantification parameters.

When stressed, the graphite/epoxy composite material emits acoustic emission from the various failure mechanisms occurring within the material. As noted by Awerbuch, the complexity of failure in composite materials is due to the multiplicity of possible modes of failure. In this project, it is not the intent to be able to discern the different composite failure mechanisms by the measured AE parameters [4], but to clearly detect joint failure and relate that to either the composite or the mechanical fastener. By superimposing the standard torque-tension data with the AE data, a clear picture to the failure mechanism(s) in the simulated joint should emerge.

Experimentation

A single-lap joint made from IM7/8552 prepreg material was chosen for testing. The fiber configuration of the plates was $(n(0, \pm 45, 90))_s$, where n = 3, 4, 5. Nominal cure thickness for each of these laminates was 0.132, 0.176, 0.220, respectively, and surface finish was smooth on both sides. A diamond tipped drill was used to drill the through holes in the coupons. Three different bolt sizes for each plate thickness were intended for investigation: 0.125", 0.250", and 0.500"; however, after initial testing it was determined to use only the largest two bolts. The designations of the bolts were NAS1958C-32 (0.5") and NAS1954C-32 (0.25") with corresponding self-locking threaded nuts. The washers used were NAS1587-8 and NAS1587-4, respectively. There were only two joint configurations tested in the four tests performed due to time constraints, both bolt sizes on the $(3(0, \pm 45, 90))_s$ laminates. Seen in Figure 1 and 2 is the test fixture according to the standard 486B.

The AE system used was comprised of a R15 transducer (seen in Figures 1 and 2 coupled to the composite with hot glue) whose signal was amplified with a PAC 2/4/6 preamplifier set to 40dB of gain. The test data presented herein were gathered with the PAC DSP-32 and MISTRAS software with all measurable time-domain parameters recorded. AE system settings included: preamp gain, 40 dB; system gain, 20 dB; threshold, 50 dB; peak definition time, 50 μs; hit definition time, 100 μs; and hit lockout time, 300 μs. An attenuation check with a mechanical pencil on the composite laminate showed no significant loss of signal.

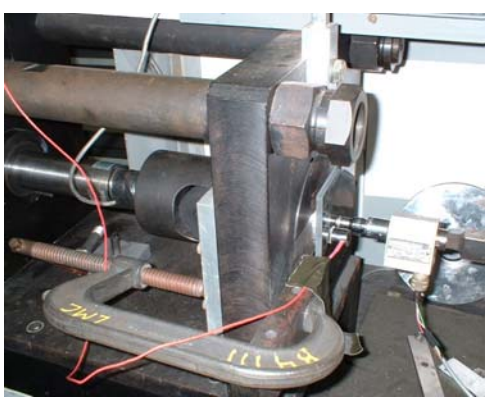

Figure 1: Test Fixture

Figure 2: Close-up of Coupon

Discussion of Results

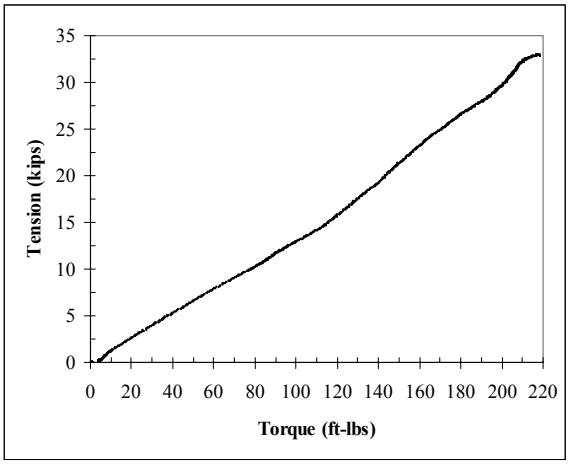

Figure 3: 0.5 inch Bolt T-T Data

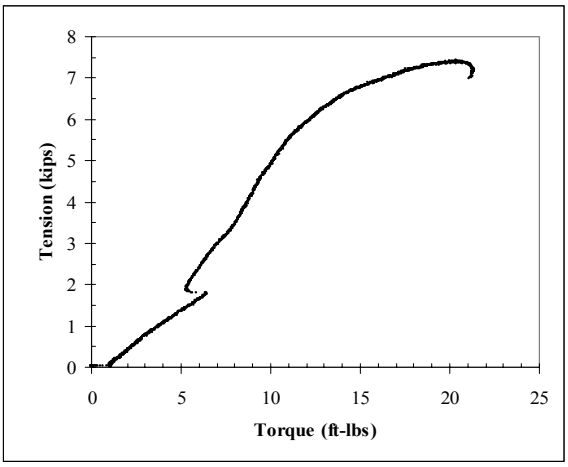

Figure 4: 0.25 inch Bolt T-T Data

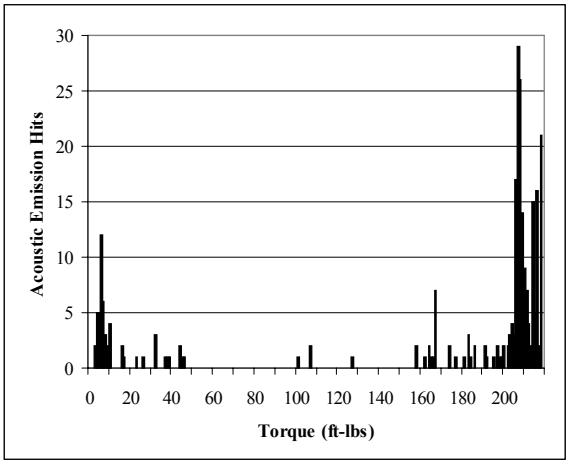

Figure 5: 0.5 inch Bolt AE Data

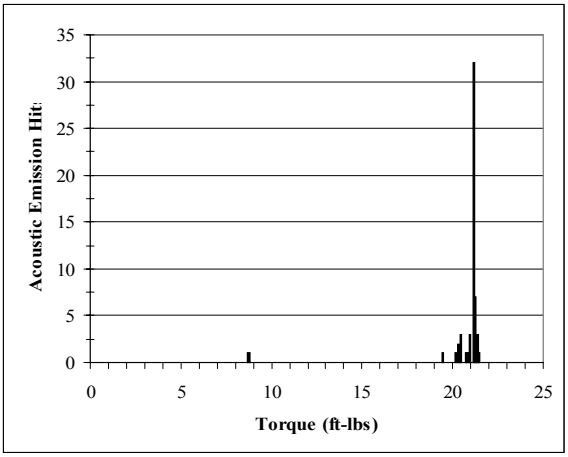

Figure 6: 0.25 inch Bolt AE Data

The torque-tension data produced from the tests (Figures 3 and 4) were typical of those seen in a 486B test. The anomaly at 6.5 ft-lbs in Figure 4 is attributed to slack in the test fixture during loading. In all the tests performed, the threads of the bolt failure first, which the AE data confirmed. This can be seen by comparing the AE activity level at a given torque load to the torque tension curve. Figure 5 shows some ambiguous signals at the beginning of the test. The recorded signals did not originate from a source dislocation, rather these signal were generated from unwanted friction as the washer spun against the composite plate during torque-up. Using calcium grease in the washer/composite, the washer/nut and the nut-thread/bolt-thread interfaces solved this problem. Figure 6 shows the AE data taken from the 0.25 inch bolt test with the calcium grease. Compared to Figure 4, it is clear that the failure of the bolt was identified by the exponentially increasing AE activity as the torque-tension curve kneeled over (the same can be said about Figure 3 and 5). Inspection of the composite plates at the test showed no obvious signs of failure or damage while the bolt threads were completely stripped.

Conclusions and Recommendations

The results of the tests showed that the composite plates under investigation did not fail before the bolt; hence, the current practice of reducing the fastener preload specified by 486B is a very conservative approach when using IM7/8552 in a single-lap joint. Weight savings in a composite joint using any of the bolts tested and the tested fiber configuration might be achieved by increasing the torque load to 486B standards. This will result in a joint with fewer fasteners will maintaining the same joint strength. Also, once it was shown that the 0.5 inch bolt cold not fail the plates is was assumed that the 0.125 inch bolts would not generate a large enough tensile load to cause failure either and consequentially these test were not performed. However, it is important to remember that composites come in many different configurations and this means experimenting with different materials and fastener types, such as the countersunk fasteners used on the graphite/epoxy shuttle nose cone.

Acknowledgements

The investigator would like to thank Yi Zhao, Frank Thomas, and Sidney Rowe for the opportunity to join the Summer Faculty Fellowship Program and ED23 to perform this work. The investigator would also like to thank the following individuals and groups for their support: Karen Stevens and ED03, Paul McConnaughey and ED20, Pete Rodriguez and David Shular of TD20, Wayne Gamwell and ED33, Bill McMahan, Brett Smith, Tom Delay of ED34. .

References

1. Awerbuch, J., *Acoustic Emission During Damage Progression in Composites*, Presented in the PAC school of Acoustic Emission, Princeton, NJ, May 2, 1985.
2. Hart-Smith, L. J., "Bolted Joints in Graphite-Epoxy Composites," NASA CR-144899 (June 1976).
3. Horn, W. J., and Schmitt, R. R., "Influence of Clamp-up Force on the Strength of Bolted Composite Joints," *AIAA Journal*, Vol. 32, No. 3, 1993, pp. 665-667.
4. Kostreva, K. M., and Hill, E. v. K., "Classification of Acoustic Emission Data from Graphite/Epoxy Failure Mechanisms Using Neural Networks," Proceedings of the Fourth International Conference on Nonlinear Problems in Aviation and Aerospace, Melbourne, FL, 2002.
5. MIL-HDBK-17B, "Polymer Matrix Composites," *Guidelines*, Vol. 1.
6. Sun, H. -T., Chang, F. -K., and Qing, X., "The Response of Composite Joints with Bolt-Clamping Loads, Part II: Model Verification," *Journal of Composite Materials*, Vol. 36, No. 1, 2002, pp. 69-92.
7. Torque Limits for Standard, Threaded Fasteners, MSFC-STD-486B, November 1992.
8. Y. Zhao, D. Ford, and S. Richardson, "Torque Limit for Fasteners in Composites," Technical Report, NASA/MSFC/ED23, August 2001.

2002

NASA FACULTY FELLOWSHIP PROGRAM

MARSHALL SPACE FLIGHT CENTER
THE UNIVERSITY OF ALABAMA

PARALLEL INFORMATION PROCESSING
(IMAGE TRANSMISSION VIA FIBER BUNDLE AND MULTIMODE FIBER)

Prepared By:	Nicholai Kukhtarev
Academic Rank:	Research Professor
Institution and Department:	Physics Department Alabama A&M University
NASA/MSFC Directorate:	SD72
MSFC Colleagues:	Dr. Ruth Jones Joseph Grant

Introduction

Growing demand for visual, user-friendly representation of information inspires search for the new methods of image transmission. Currently used in-series (sequential) methods of information processing are inherently slow and are designed mainly for transmission of one or two dimensional arrays of data. Conventional transmission of data by fibers requires many fibers with array of laser diodes and photodetectors.

In practice, fiber bundles are also used for transmission of images. Image is formed on the fiber-optic bundle entrance surface and each fiber transmits the incident image to the exit surface. Since the fibers do not preserve phase, only 2D intensity distribution can be transmitted in this way. Each single mode fiber transmit only one pixel of an image. Multimode fibers may be also used, so that each mode represent different pixel element. Direct transmission of image through multimode fiber is hindered by the mode scrambling and phase randomization. To overcome these obstacles wavelength and time-division multiplexing have been used , with each pixel transmitted on a separate wavelength or time interval [1-2]. Phase-conjugate techniques also was tested in [3-5], but only in the unpractical scheme when reconstructed image return back to the fiber input end. Another method of three-dimensional imaging over single mode fibers was demonstrated in [6-9], using laser light of reduced spatial coherence. Coherence encoding, needed for a transmission of images by this methods, was realized with grating interferometer or with the help of an acousto-optic deflector.

We suggest simple practical holographic method of image transmission over single multimode fiber or over fiber bundle with coherent light using filtering by holographic optical elements. Originally this method was successfully tested for the single multimode fiber [10-11]. In this research we have modified holographic method for transmission of laser illuminated images over commercially available fiber bundle (fiber endoscope, or fiberscope).

Principle Of Holographic One-Way Direct Image Transmission

In this section we will describe the basic principle of direct parallel image transmission, using holographic grating recording in photorefractive crystal $LiNbO_3$. doped by Fe.

First we remind basic features of image transmission over single multimode fiber, suggested and demonstrated in the paper [11]. This method was realized with the help of HeNe laser and a multimode fiber with 70 μm diameter, numerical aperture of o.17 and two meter long. After passing the optical fiber, the signal light wave E_s is mixed with another (reference) coherent wave E_r at the photorefractive crystal lithium niobate. The signal wave was also modulated by the amplitude mask(image) with transmission function T(x.y). In this way dynamic hologram of the image and fiber wave was recorded in the crystal by photogalvanic mechanism of recording [11]. Retrieval of this hologram by by the plane wave R (counterpropagating to the reference wave) lead to appearance of the diffracted wave D, that is phase conjugate to the signal wave. This phase conjugated wave propagate in the reverse direction via the fiber, speckle pattern is corrected and output wave reproduce input image.

The image formation may be explained in the following way: The probe signal beam excites N modes in the fiber, which form the resolution elements of the future image. Each of this n modes has its own propagation constant k_n and for this reason the beam has a speckle pattern at the fiber output. Then this beam is mixed in the crystal with the reference (pump) wave, modulated by the mask transmission. In our case diffracted, phase conjugated wave will be proportional to the transmission function T(x,y) and to the photogalvanic coefficient, that determine diffraction efficiency. Diffracted wave after propagating through the fiber into reverse direction is emitted from the fiber output end as a sum N eigen-modes with information about the image. This concept was confirmed by experimental demonstration of image transmission via commercial multimode fiber.

In this paper we use the same principle of holographic filtering with phase conjugated wave with more simple two wave sceme and using semi-permanent hologram. First we have recorded hologram of a fiber transmitting signal beam through the fiber and mixing it with the plane wave in the recording media: photorefractive crystal lithium niobate. Hologram recorded in the crystal may stay at room temperature at least several hours, so we may consider it as a fixed one. During retrieval, without changing optical scheme we introduce an image to the input end of the fiber bundle and block the reference beam.

In this case diffracted wave should be plane reference wave, modulated by the image. In other words, we have reconstructed image using hologram as a complex holographic filter, using simple two –wave mixing scheme.

Experimental Results With The Coherent Fiber Bundle

In our experiments we have used commercial semi-rigid imaging fiber bundle (fiberscope) from Edmund Industrial Optics. This bundle incorporate six thousands of tightly packed individual fibers that are aligned coherently – both input and output ends retain position exactly opposite the other. Fiberscope length was about 10 cm, diameter 0.5mm with 25X eyepiece that offer a possibility of focusing of wide-angle image.

This fiberscope was placed in the signal wave leg of the traditional two scheme of hologram recording. Laser light from the diode-pumped solid-state CW laser (wavelength 532 nm, power up to 100 mW) was splitted in two beams, one was transmitted through fiberscope and thus forming a signal wave. Another, reference wave propagated in the free space and both beams recombine on the recording media : photorefractive crystal lithium niobate, doped with Fe. Variable beam-splitter was used to adjust optimal ratio of intensities for signal and reference waves. In our experiments we have used natural, unexpanded and unfocused laser beam (approximately 3mm in diameter). Eyepiece attached to fiberscope allow us to focus output signal beam on the crystal.

At the first reading stage hologram of fiberscope was recorded in the photorefractive crystal. On the reading-transmitting stage, reference wave was blocked and image (Air-force resolution chart) was placed before input end of the fiberscope.

Diffracted beam in this scheme contain information about tested image. We have realized transmission of images with spatial frequencies of 2l /mm that was captured by the CCD camera attached to a beam profiler.

These preliminary experimental results demonstrate feasibility of the proposed concept of the holographic two-wave method of image transmission via fiberscope with coherent illumination.

Discussions and Conclusion

Three-dimensional data transmission (like 3D-images) now is possible only with inevitable delay by in-series methods. Recently conceived method of parallel image transmission through multimode fiber is based on real-time holography using phase-conjugation principles. In this method image-bearing beam, aberrated by multimode fiber may be corrected by holographic complex filter. Holographic complex filter, working in real time, may be recorded in the photorefractive material with high diffraction efficiency.

First proof-of-principle experiment in 1991 (done in our group in the Institute of Physics, Kiev, Ukraine), proved feasibility of this idea for image transmission via multimode commercial fiber [1]. These encouraging experimental results allow us to be optimistic about possibility of development practical design for parallel information transmission.

There are several options based on the real-time holographic filtering, that are waiting for experimental testing and theoretical and computational

These encouraging experimental results allow us to be optimistic about possibility of development practical design for parallel information transmission.

Acknowledgement

I wish to acknowledge encouraging support and help from my NASA colleagues Ruth Jones and Joseph Grant

References

1.A.M.Tai, Appl.Opt.22, 3826 (1983)
2.L.Akopov,G.Voevodkin,E.Dianov, A.Kuznetsov, and S.Nefedov, Sov.J.Opt.Tecnnol. 56, 474 (1990).

3.S.Volkov,A.Volyar,N.Kukhtarev,L.Kuchikyan and V.Savchenko,

Phase conjugation of multimpode lightguide radiation in photorefractive crystals, opt.Spectrosc.(USSR)64 (4), 553 (1988).

4. A.Yariv, “3D pictorial transmission in optical fibers” Appl.Phys.Lett,. vol.29,n0.2,pp 88-89,1976.

5. G.Dunning and R.Lind,”Demonstration of image transmission through fibers by optical phase conjugation”, Opt.Lett.,vol.7,no.11, pp.558-560,1982.

6. P.Naulleau and E.Leith, “Imaging through optical fibers by spatial coherence encoding methods”, J.Opt.Soc.Am.A. Vol.13, No.10, 2096, 1996.

7.P.Naulleau,M.Brown,C.Chen, and E.Leith, “Direct 3D image gransmission through single mode fibers with monochromatic light”, Opt Lett. 21, 36-38 (1996)

8.P.Naulleau, C.Chen, and ED.Leith,”Analysis of direct 3D image transmission through optical; fibers by the use of coherence methods”, Appl.Opt.35, 3953-3962 (1996).

9. P.Naulleau,D.Dilworth,B.Hoover,J.Lopez and E.Leith, “Holography under adverse conditions” Proc.SPIE Vol.3358,p380 (1998).

10. A. Volyar, A.Gnatovskii, N.Kukhtarev, and S.Lapaeva, “Image Transmission via multimode fiber assisted by polarization preserving phase conjugation in the photorefractive crystals”, Appl.Phys.B.,Vol. B52, No.6, 400-401, (1991)

11 N.Kukhtarev. A.Volyar, A.Gnatovskii, “Polarized phase conjugation and some principles of parallel information transmission by a fiber/crystal system”, International Journal of Nonlinear Optical Physics”, Vol.2, No.3 (1993) 447-464, World Scientific Publishing Company.

2002

NASA FACULTY FELLOWSHIP PROGRAM

MARSHALL SPACE FLIGHT CENTER
THE UNIVERSITY OF ALABAMA

THE LAND USE AND LAND COVER DICHOTOMY: A COMPARISON OF TWO LAND CLASSIFICATION SYSTEMS IN SUPPORT OF URBAN EARTH SCIENCE APPLICATIONS

Prepared by:	William K. McAllister, Ph.D.
Academic Rank:	Assistant Professor
Institution and Department:	Alabama A & M University Department of Community Planning and Urban Studies
NASA/MSFC Directorate:	Earth Science
MSFC Colleague:	Dale Quattrochi, Ph.D.

Introduction

One is likely to read the terms "land use" and "land cover" in the same sentence, yet these concepts have different origins and different applications. Land cover is typically analyzed by earth scientists working with remotely sensed images. Land use is typically studied by urban planners who must prescribe solutions that could prevent future problems. This apparent dichotomy has led to different classification systems for land-based data. The works of earth scientists and urban planning practitioners are beginning to come together in the field of spatial analysis and in their common use of new spatial analysis technology. In this context, the technology can stimulate a common "language" that allows a broader sharing of ideas.

The increasing amount of land use and land cover change challenges the various efforts to classify in ways that are efficient, effective, and agreeable to all groups of users. If land cover and land uses can be identified by remote methods using aerial photography and satellites, then these ways are more efficient than field surveys of the same area. New technology, such as high-resolution satellite sensors, and new methods, such as more refined algorithms for image interpretation, are providing refined data to better identify the actual cover and apparent use of land, thus effectiveness is improved. However, the closer together and the more vertical the land uses are, the more difficult the task of identification is, and the greater is the need to supplement remotely sensed data with field study (in situ). Thus, a number of land classification methods were developed in order to organize the greatly expanding volume of data on land characteristics in ways useful to different groups. This paper distinguishes two land based classification systems, one developed primarily for remotely sensed data, and the other, a more comprehensive system requiring in situ collection methods. The intent is to look at how the two systems developed and how they can work together so that land based information can be shared among different users and compared over time.

Modern Land-Based Classification Lineage

Two streams of land-based classification systems have separate histories based on either an urban or a rural emphasis. The urban stream begins with the Standard Land Use Classification Manual (SLUCM) developed in 1965 through support from the U. S. Urban Renewal Administration, since absorbed into Housing and Urban Development (HUD); and the Bureau of Public Roads, now the Federal Highway Administration (FHwA). It was designed for land use analysis, typically done by urban planners. A direct descendent of SLUCM is the Land Based Classification System (LBCS) designed by the American Planning Association (APA) under research supported by six federal agencies.

The rural stream begins in 1971 with Anderson and others [2], working for the U. S. Geological Survey (USGS). Other agencies supporting this system were the National Aeronautics and Space Administration (NASA), the Soil Conservation Service (SCS), and two professional organizations, the Association of American Geographers (AAG) and the International Geographical Union (IGU). Anderson observed that SLUCM contained eight of its nine classes for urban land types, while only five per cent of the country's land at that

time was urban [2]. To study rural lands, the Anderson team developed a new system where Level I (most generalized scale) contained one urban class and eight rural classes. This effort in the 1970s established a land use and land cover (LULC) classification system for remotely sensed data at a time when the digitizing of spatial data was just emerging. The Anderson system was initially designed for land cover analysis for a new nationwide digital mapping of LULC based on high altitude photography at a scale of 1:250,000. A survey of users of land use and land cover data by the USGS in 1992 found that the Anderson system was the most commonly used classification (approximately 25 per cent of the respondents) [1].

Figure 1 gives some insight into the derivation of the major national land-based classification systems and their federal agency involvement. Not surprisingly, urban oriented agencies seem to favor the LBCS and its derivative systems. Joining FHwA and HUD are the Federal Aviation Administration (FAA), the Bureau of Transportation Statistics (BTS), Federal Emergency Management Agency (FEMA), and the Air Force. In addition, national classification systems have mostly evolved, indicated by lines, rather than developed anew. The North American Industry Classification System (NAICS), used by the Census Bureau to organize data collected by its economic censuses every five years, is a specialized classification system. NAICS is also used to monitor the North American Free Trade Agreement. Nevertheless, both the Anderson system and LBCS, the completely redesigned version of SLUCM, should dominate their respective areas of emphasis because of their comprehensive design.

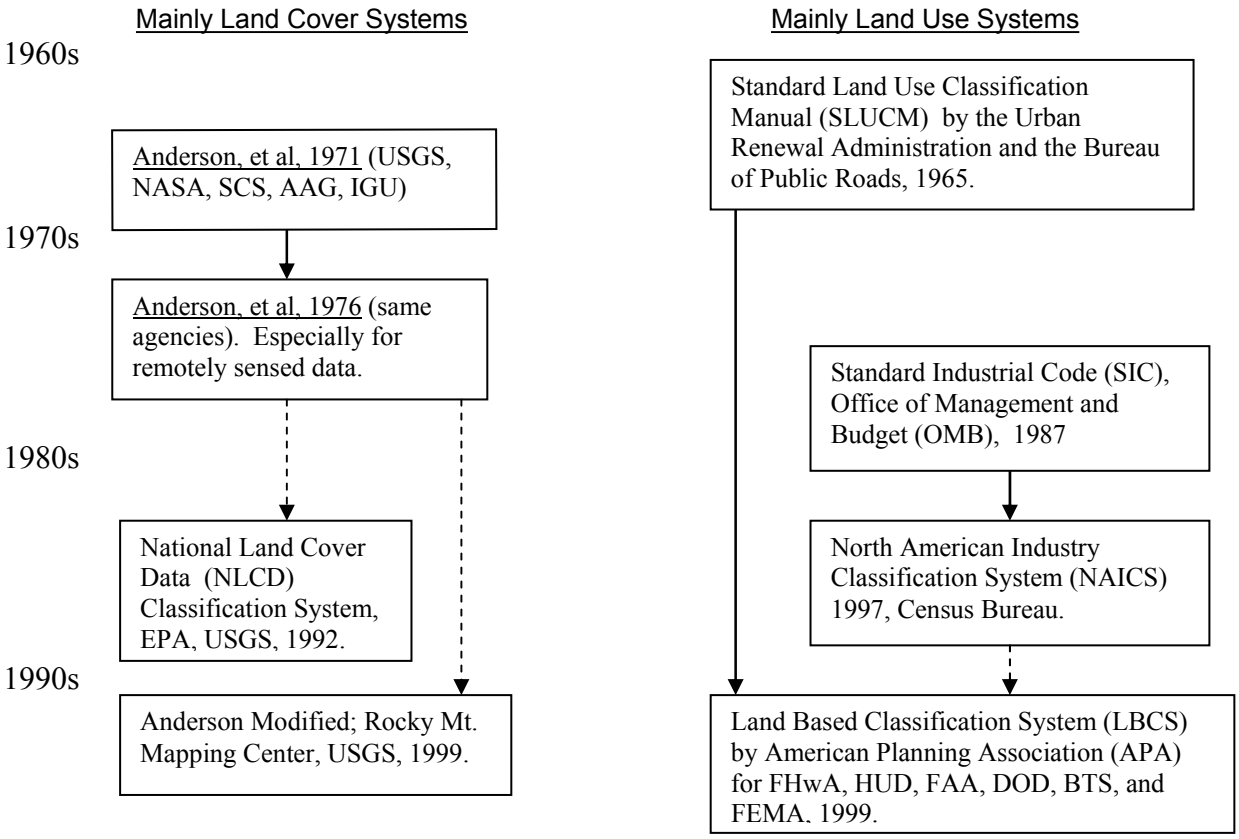

Figure 1. National Land Based Classification Systems and Their Derivations

The advances in remote sensing technology have led to at least two refinements of the Anderson classification. The National Land Cover Data (NLCD) Classification System modifies Anderson Level II, both by combining and subdividing Anderson's original 37 classes, resulting in 21 classes suitable for remotely sensed data collected by the Landsat Thematic Mapper at a 30-meter resolution. The NLCD began in 1992 and was completed in 2000. For high-resolution imagery, a second refinement of Anderson was developed at the Rocky Mountain Mapping Center of USGS for the USGS national 1:24,000 scale mapping program using NLCD. Technology advances notwithstanding, aerial photography and some field confirmation might need to supplement even the latest high-resolution satellite data, especially in urban areas.

Land Cover and Land Use Distinctions

Land cover refers to the biophysical materials observable on the land, while land use refers to how the land is being used by humans [5]. For example, a state park may be used for recreation, but it can appear to have a forest cover from the air. The concepts are closely related, and sometimes intermingled. Remotely sensed data from airplanes and satellites record responses from the earth's surface, both natural and artificial. However, remote sensing image-forming technology does not record land use activities directly. These activities, as well as other dimensions of land use, are distinctions that conceptually set land use apart from land cover. In practice, the collection of land cover data, including an increasing amount of land use data, is ongoing through programs emanating from NASA's Earth Science Enterprise, as well as from many privately owned satellites. By varying the remote sensing devices to include certain non-visible and thermal wave lengths, additional indicators can help extract even more information about land cover and land use activities and their environmental impacts over time.

Anderson, et al and LBCS Distinctions

Even though the Anderson and LBCS schemes are both hierarchical in structure, thus offering flexibility for simple to complex applications, their distinctions are more notable. These comprehensive systems of classification are distinguishable in several important ways, including the dimensionality of the system of classifying; the spatial building blocks, e.g. pixels versus polygons; rural versus urban applications; and descriptive versus prescriptive purposes of the analysis. Each is addressed here. >The most fundamental distinction between these two classification systems appears to be their range of dimensionality. The Anderson system was designed for classifying remotely sensed data in dimensions available from current technology. [2] Guttenberg argues that urban planners will need several additional dimensions of land use information [3]. Largely due to Guttenberg's rational approach, the LBCS received sub classifications for dimensions representing activities, economic land use functions, structural uses, the status of site development, and the nature of land ownership [4]. Each of these dimensions is recorded as a separate field in a land use database. >The digital files of remotely sensed data are in the form of cells or pixels. These spatial building blocks are also useful to the spatial analysis done by planners, but in conjunction with other digital forms. Streams and their watersheds, for example, can be analyzed using geometry of points, lines, and areas, rather than adding together pixels. Areas are often called polygons,

and these are useful for representing not only watersheds, but also a variety of oddly shaped pieces of real property in the form of land parcels. Parcels are one of the most important digital building blocks for planners. >Remotely sensed data seems to be more applicable for assessing change in rural areas and along the rural-urban fringe. Urban applications demand more information than remote sensing can currently provide, but the gap is shrinking. >One reason that urban planners need a large amount of information is because they prescribe change. Prescriptive practices might require knowledge of actual uses and even patterns of ownership [3]. Detailed classifications also can introduce errors during manipulation. [6].

The Confluence of Land Use and Land Cover Analysis

The merging of images from remotely sensed sources with other land-based data can be processed by geographic information systems (GIS). GIS are computerized spatial analysis tools used by planners and others to answer important land-based questions involving commonality of data, and to show this overlaid data on maps in various useful combinations. The resulting visual images can help analysts, administrators and elected officials make better decisions. Modern GIS can join both pixel (raster data) and polygon (vector data) files. Using GIS, earth scientists and urban planners can collaborate on analyzing a range of quality-of-life problems existing along the urban-rural continuum over time. To accomplish this, the "languages" of earth science and urban planning will need to communicate.

Conclusion

Classification is a form of abstraction of raw data. Carefully done it can lead to good science. And science results based on data and information that are organized under themes that are compatible with other classification systems can be shared amongst a broader audience. Sharing also can help contain costs, as well as improve the quality of research.

References

[1] American Planning Association. 1999. Land Based Classification System. Accessed on Internet: http://**www.planning.org/lbcs** June 5, 2002.

[2] Anderson, J., E. Hardy, J. Roach and R. Witmer, (1976), *A Land Use and Land Cover Classification System for Use with Remote Sensor Data,* Government Printing Office, pp 28.

[3] Guttenberg, A. (1993), The Language of Planning: Essays on the Origins and Ends of American Planning Thought. University of Illinois Press, pp. 21-48.

[4] Jeer, Sanjay, (1997), *LBCS Discussion Issues*. American Planning Association. Accessed on Internet: http://**www.planning.org/lbcs** June 5, 2002.

[5] Jensen, J., (2000), Remote Sensing of the Environment: An Earth Resource Perspective. Prentice Hall, pp. 407-470.

[6] Kaiser, E., D. Godschalk and S. Chapin, (1996), *Urban Land Use Planning*, University of Illinois Press.

2002

NASA FACULTY FELLOWSHIP PROGRAM

MARSHALL SPACE FLIGHT CENTER
THE UNIVERSITY OF ALABAMA

CONCENTRATION AND VELOCITY GRADIENTS IN FLUIDIZED BEDS

Prepared By:	James P. McClymer
Academic Rank:	Associate Professor
Institution and Department:	University of Maine Department of Physics and Astronomy
NASA/MSFC Directorate:	SD-46
MSFC Colleague:	Dr. Phil Segre

Introduction

Sedimenting and fluidized beds are widely used in industry for separation process and enhanced heat transfer. As is commonly the case, widespread use does not mean there are no interesting, fundamental questions. Detailed understanding of these beds requires complete understanding of multi-particle, long-range hydrodynamic interactions as a function of concentration. Such problems are still minimally tractable.

It was recently recognized [5] that the stability of fluidized beds cannot be explained by the standard "classical" model. It was commonly accepted that sedementing and fluidized beds have uniform concentration profiles. Recent experiments show that concentration and velocities vary significantly on multi-particle length scales [1,2,3,6,7]. Another experiment [8] explicitly showed that an initially uniform concentration profile in a sedementing bed is unstable. This instability can be understood in light of two facts. It is empirically known that sedimentation velocity decreases with increasing particle concentration,

$$(1)\ V_{SED} = V_0 (1-\phi)^k, k > 0 .$$

The value of k depends on the interparticle potential [4] and is typically between 5 to 6. Creating a stable bed would then seem to require maintaining the exactly appropriate flow velocity for a given concentration. Correlated fluctuations in particle number, and hence density, were recently discovered [6]. These denser regions sink faster than the surrounding particles while the less dense regions rise. Since there are more particles in the sinking regions than the rising regions, the bed collapses, unless another mechanism exists to counter the collapse. Segre [5] recently made detailed measurements on a stable bed. His measurements indicate that both the concentration and the sedimentation velocity is height dependent. This height dependence provides the mechanism to stabilize the bed.

Procedure

In this work we focus on the height dependence of particle concentration, average velocity components, fluctuations in these velocities and, with the flow turned off, the sedimentation velocity. The latter quantities are measured using Particle Imaging Velocimetry (PIV). The PIV technique uses a 1-megapixel camera to capture two time-displaced images of particles in the bed. The depth of field of the imaging system is approximately 0.5 cm. The camera images a region with characteristic length of 2.6 cm for the small particles and 4.7 cm. for the large particles. The local direction of particle flow is determined by calculating the correlation function for sub-regions of 32 X 32 pixels. The velocity vector map is created from this correlation function using the time between images (we use 15 to 30 ms). The software is sensitive variations of $1/64^{th}$ of a pixel. We produce velocity maps at various heights, each consisting of 3844 velocities. We break this map into three vertical zones for increased height information.

The concentration profile is measured using an expanded (1 cm diameter) linearly polarized HeNe Laser incident on the fluidized bed. A COHU camera (gamma=1, AGC off) with a lens and a polarizer images the transmitted linearly polarized light to minimize

the effects of multiply scattered light. The intensity profile (640 X 480 pixels) is well described by a Gaussian fit and the height of the Gaussian is used to characterize the concentration. This value is compared to the heights found for known concentrations. The sedimentation velocity is estimated using by imaging a region near the bottom of the bed and using PIV to measure the velocity as a function of time. With a nearly uniform concentration profile, the time can be converted to height information.

The stable fluidized beds are made from large pseudo-monodisperse particles (silica spheres with radii (250-300) microns and (425-500) microns) dispersed in a glycerin/water mix. The Peclet number is sufficiently large that Brownian motion of the particles can be ignored and the Reynolds number sufficiently small that particle inertia is negligible. A packed particle bed is used to randomize and disperse the flowing fluid introduced by a peristaltic pump. The bed itself is a rectangular glass cell 8 cm wide (x), 0.8 cm deep and a height of 30.5 cm (z). The depth of field of the camera is approximately 0.5 cm so depth information is averaged. Over flow fluid is returned to the reservoir making a closed loop system. In these experiments the particles form a sediment approximately 5.7 cm high with the pump off and expand to 22 cm with the pump on. For the smaller particles the pump velocity is .5 mm/s and 1.1 mm/s for the large particles. At this concentration the bed has a very well defined "top" where particle concentration rapidly drops to zero.

Results

Figure 1 A and B show the average velocity in the x and z direction and their RMS fluctuations ($\mathbf{F}_{vx}$ and $\mathbf{F}_{vy}$) for a stable bed for the two particle sizes. The two beds have the same average particle concentration. The stability of the bed is clearly shown by the near zero average velocities. The velocity fluctuations are largest near the bottom of the bed (which results in a larger uncertainty for the velocity values) and vanish near the top. The particles at the top of the bed are stationary. The RMS velocity fluctuations are well fit by a power law.

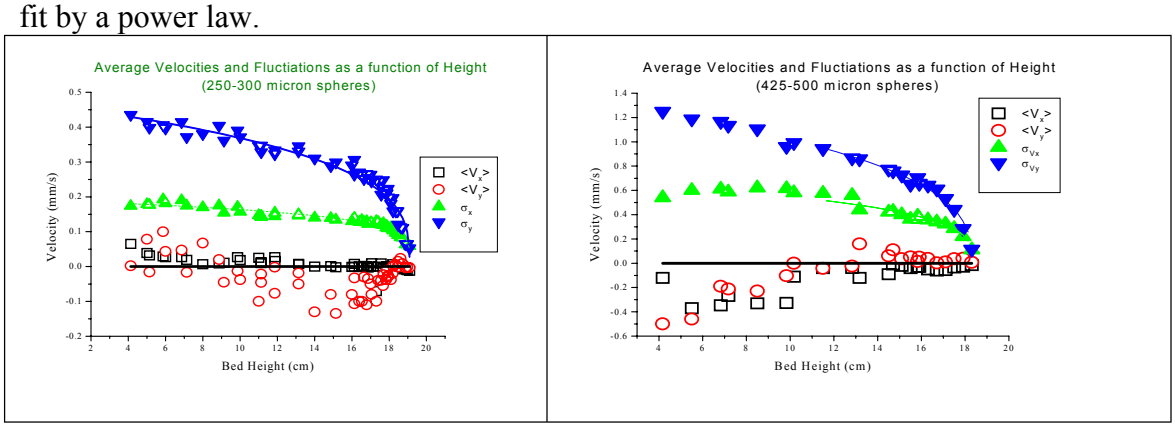

Figure 1. Average Velocity (open red circles $<V_z>$, open black boxes $<V_x>$) and RMS values of velocity fluctuations (filled green up triangles RMS(V_x), filled blue down triangles RMS(V_z). Fluctuations are well fit by a power law with an exponent near 1/3.

Figure 2 shows the sedimentation velocity for the two beds. The sedimentation velocity is less than the pump velocity at all heights (except at the top of the column). An "excess"

velocity is defined as $V_{ex} = V_{pump} - V_{sed}$. Figure 3 shows the concentration profile for the two beds (Figure 4). The correlation length is determined from the velocity maps and the height dependence shown in Figure 4.

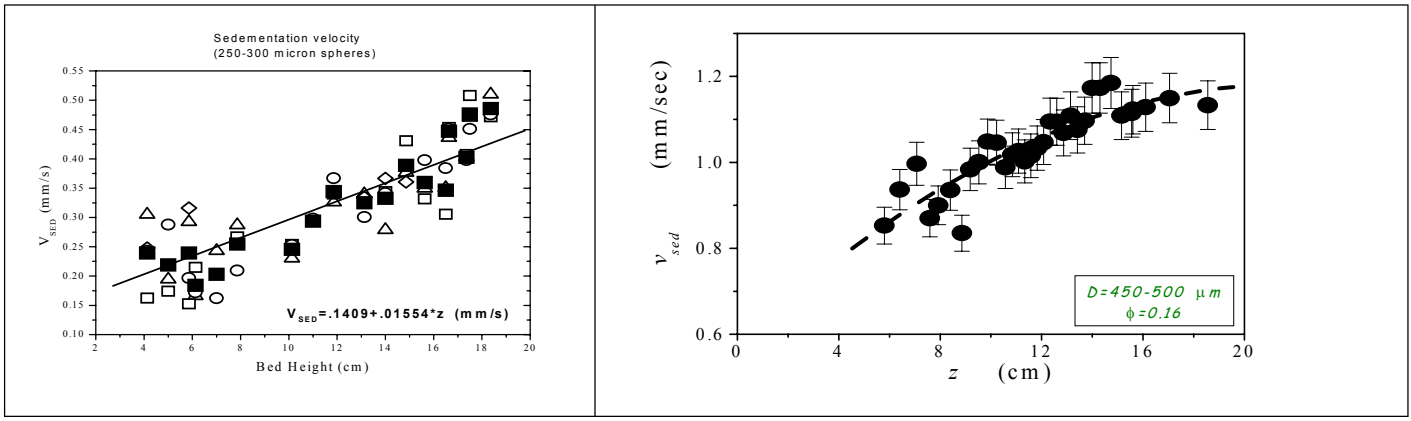

Figure 2. Sedimentation velocity as a function of height.

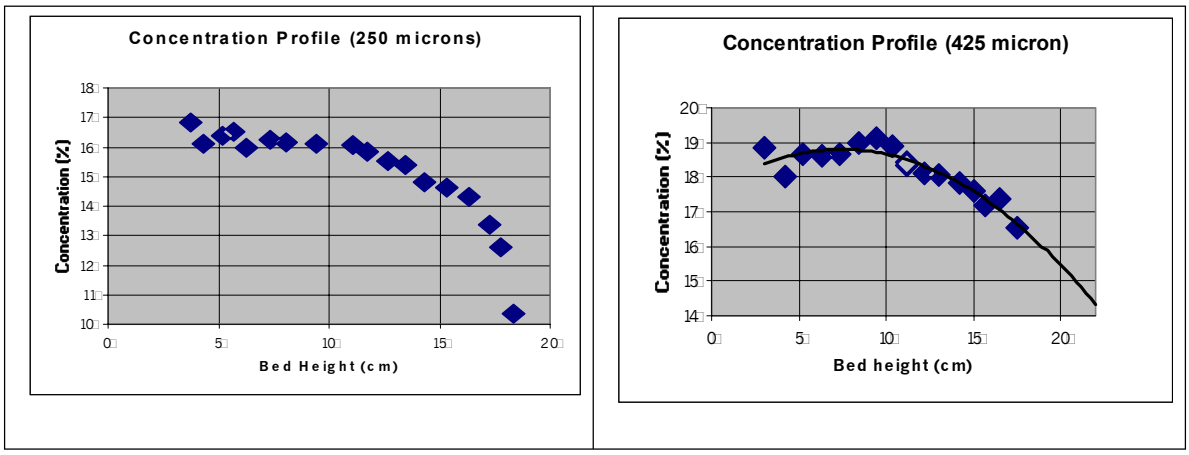

Figure 3.Concentration as a function of height for the two particle sizes.

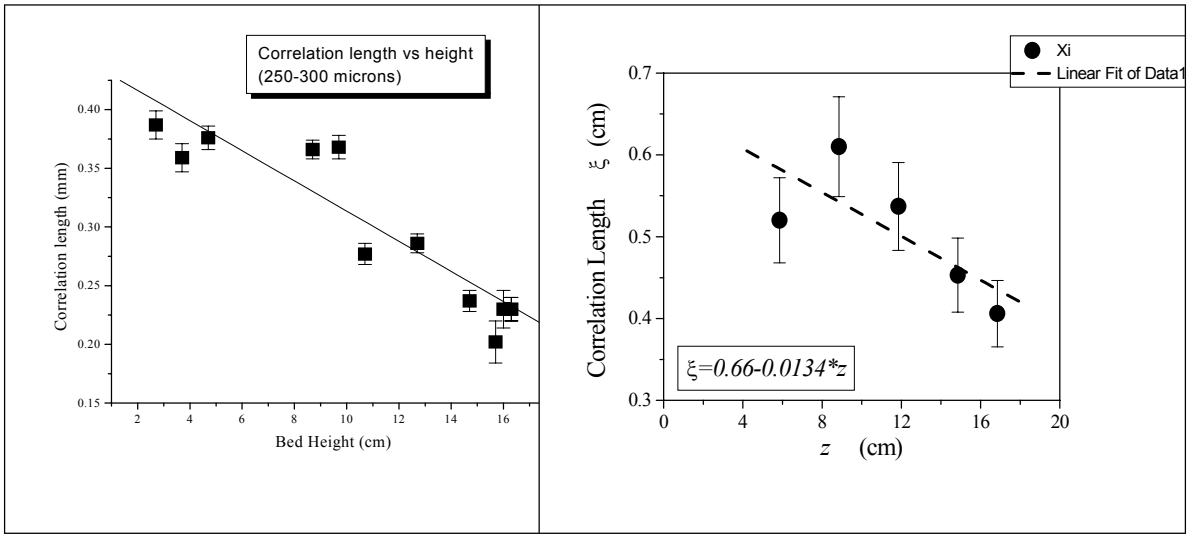

Figure 4. Correlation Lengths for two particle sizes.

Conclusion

Segre [5] developed a flux balance equation

2. $$\partial(\phi\, v_{ex})/\partial z = -0.8\sigma_{vz}\sqrt{S(\phi)\phi\, a^3/\xi^5}$$

where a, ξ,ϕ are the particle radius, correlation length, and concentration respectively. $S(\phi)$ corrects for excluded volume effects using the Carnahan-Starling equation for hard spheres [4]. Integrating EQ (2) gives the result in Figure 5 in which the integral of the two terms (flux) and their sum is shown. As predicted the sum is near zero.

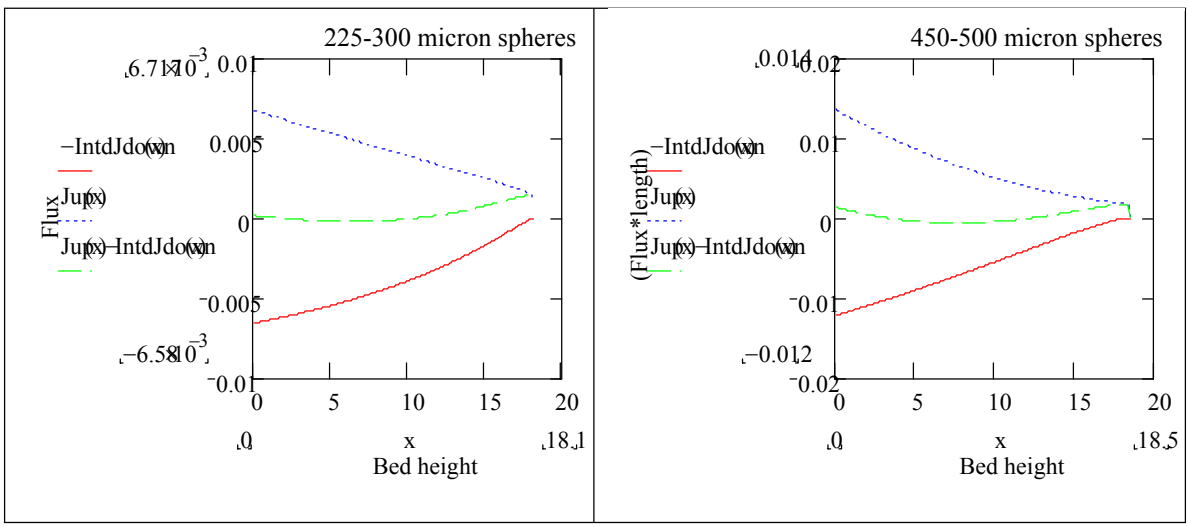

Figure 5. The blue curves are the upward flux due to the excess velocity. The red curve is the downward flux due to concentration fluctuations. The green curve is the sum of the two curves and is near zero over the entire bed height.

Acknowledgements

The author thanks Phil Segre for sharing his laboratory and scientific knowledge with me as well as his hospitality. Space precludes thanking all the other MSFC people I enjoyed working with.

References

[1] Ladd, A.J.C., (2002) Phys. Rev. Lett. **76**, 1392 (1996) and **88**, 48301.
[2] Lei, X., B.J. Ackerson, and P. Tong, (2001) Phys. Rev. Lett. **86**, 3300.
[3] Nicolai, H. and E. Guazzelli, (1985) Phys. Fluids **7**, 3.
[4] Russell, W.B., D.A. Seville and W.R. Schowalter,(1989) *Colloidal Dispersions*, Cambridge Univ. Press, Cambridge.
[5] Segre, P.N. Private Communication/Preprint.
[6] Segre, P.N., E. Herbolzheimer and P.N. Chaiken, (1997) Phys. Rev. Lett. **79**, 2574.
[7] Segre, P.N., F. Liu, P. Umbanhower, and D.A. Weitz, (2001) Nature **409**, 594.

[8] Tee,S.Y., P.J. Mucha, L. Cipelletti, S. Manly, M.P. Brenner, P.N. Segre and D.A. Weitz, (2002) Phys. Rev. Lett., in press

2002

NASA FACULTY FELLOWSHIP PROGRAM

MARSHALL SPACE FLIGHT CENTER
THE UNIVERSITY OF ALABAMA

Development of Processing Parameters for Organic Binders Using Selective Laser Sintering

Prepared By:	Amir A. Mobasher
Academic Rank:	Assistant Professor
Institution and Department:	Alabama A&M University Department of Mechanical Engineering
NASA/MSFC Directorate:	Engineering
MSFC Colleague:	Mr. Ken Cooper

Introduction

What is rapid prototyping? Why is it important in the design process? Before we address these two crucial questions and have appreciation for rapid prototyping, we shall address and understand the design process. That is what are the steps required to be taken by the designer to bring his/her idea to reality and consequently to profitability? Although the process from design-to-manufacture varies from business to business, a general pass involves (1) The concept, (2) Preliminary Design, (3) Preliminary Prototype Fabrication, (4) Short-run Production and (5) Final Production. Any new product or an improvement to an existing product starts with a concept. The motivation for the concept is generally based on a need or a gap that may exist in our current life style, technology, etc. Once it is established that the need for a particular product exists, the idea might be carried into the next phase of preliminary design. In this step, the designer may prepare a two dimensional drawings or even a Computer Aided Design (CAD) solid model of the part to be built. In this phase the design may go through several iterations as the designer determines the feasibility of the product through discussions with colleagues and co-workers and presenting it to management. Once the design has been given the "go", a prototype must be fabricated to check out the design. Traditionally (Before Rapid Prototyping), this phase of the design was carried out either by hand working or machining the part. Both of these techniques require tremendous amount of man power and labor hours. The next stage of the process involves Short-run Production. This phase may be necessary to further proof a part before entering into final production. In this phase, from tens to hundred parts maybe produced and distributed for testing before entering the final production. Final step in the design involves the Final production. In this step, the parts are typically machined, injection molded or cast in large numbers depending on the design criteria and costs.

Traditionally the process of design-to-manufacture took several months or even years to fully mature. That is due to the overhead associated with iterations in steps (2) and (3). In that, the designer gave the preliminary design to the machine shop. Depending on the complexity of the part, this may take several days or even weeks to build the part. Then the part may go back to the designer for approval and verification. Then there may be additional modifications to the design which much be corrected in the prototyping phase. Rapid prototyping therefore is the process of replacing this time consuming process with a much more efficient and faster process.
Rapid Prototyping (RP), referes to the layer-by-layer fabrication of three-dimensional physical models directly from a computer aided design (CAD). This additive manufacturing process provides designers and engineers to literally print out their ideas in three dimensions. The RP processes provide a fast and inexpensive alternative for producing prototypes and functional models as compared to the traditional routs for part production. The advantage of building parts in layers is that it allows you to build complex shapes that would be virtually impossible to machine, in addition to the more simple designs. RP can can build intricate internal structures, parts inside parts, and very thin-wall features just as easily as building a simple cube. All of the RP processes construct objects by producing very thin cross sections of the part, one on top of the other, until the solid physical part is completed. This simplifies the three dimensional construction process in that the essentially two dimensional slices are being created and stacked together. For example, instead of of trying to cut out a sphere with a detailed machining process, stacks of various sized "circles" are build consecutively in the RP machine to create a sphere with ease.

History of Rapid Prototyping

RP stems from the ever-growing CAD industry, more specifically, the solid modeling side of the CAD. Solid modeling is the branch of CAD that produces true three dimensional objects in electronic format. A solid model has volume and is fully enclosed. Before solid modeling was introduced in the late 80's, three dimensional models were created with wire frames and surfaces. A wire frame is an approximate presentation of a three dimensional object. Not until the development of true solid modeling could innovative processes such as RP be developed. the first RP system was developed by Charles Hall in 1986, who also helped found 3D systems. This process, called sterolithography, builds objects by curing thin consecutive slices of certain ultraviolet light sensitive liquid resins with a low power laser. There are now many national and international companies manufacturing and selling RP processes. Among these machines are:

(1) JP-Sytem 5 (JP5), By Schroff Development- This process builds models from CAD Data using label paper and a knife plotter. JP5 is a simple and inexpensive modler for creating rough 3D models.
(2) Balistic Particle Manufacturing (BPM)- This process involves firing droplets of molten vax from a moving jet onto a stationary platform.
(3) The Model Maker (MM), and Rapid Tool Maker (RTM) by Sanders Prototype: This process produces highly accurate wax patterns using ink-jet printing technology with molten wax.
(4) Multi-Jet Modeling (MJM) used by 3D Systems, Inc.: This process uses inkjet printing technology with many jets enclosed into a single print head to produce concept modles.
(5) Direct Shell Production by Soligen Inc.: Uses Binder printing technology developed by MIT. The binder is printed by layers of ceramic powder to produce investment shells directly from CAD.
(6) The Z402 System by Z-Corp: Also uses MIT 3D printing technology to build very fast concept models from a starch like material
(7) Fused Deposition Modeling (FDM), by Strasys, Inc. Produces models from wax or ABS Plastic using motion control and extrusion technology similar to a hot glue gun.
(8) Laminated Object Manufacturing by Helisys, Inc. Builds physical models by stalking sheets of paper or plastic material and cutting away excess material with laser.
(9) Stereolithography, by 3D Systems, Corp. Is the oldest RP system and builds models by curing epoxy resins with a low power laser.
(10) Selective Laser Sintering, by DTM can build with a variety of materials and works by selective melting together powder with laser into a desired shape.
(11) Laser Engineered Net Shaping, by Optomec Design Co., builds parts directly by metal powders by fusing the powder together with a laser beam.

In the course of past few years some of these machines have gained considerable speed and accuracy such as Selective Laser Sintering (SLS). The NASA Marshall's National Center for Advanced Manufacturing RP center has variety of these machines available. A considerable amount of research is directed towards this area at this center. Among the goals of this center is to produce actual functional parts from metallic materials using current technologies such SLS machines. Potentially there exists a strong market for this technology. Among many

applications of this technology is to build actual parts on demand on space for space vehicles rather than transporting the spare parts with the space vehicle.

The process of Selective Laser Sintering involves the acquisition of a layer of a part from a cad drawing and fusing a powder with laser beam only in the regions where solid is present. This is a highly accurate process and the parts generated in this manner are extremely durable. The objective of this research effort is to establish parameters for the SLS Machine for producing functional parts from Titanium Alloys.

Methodology Adopted for the Laser Sintering Technique

There are primarily three parameters that dictate the quality of the part generated via SLS processing. These parameters are: (1) Laser Power, (2) Part Bed Temperature at which the part is built, and the (3) Layer Thickness for the part to be formed. At the first step of this process we formulated a test matrix which spanned the laser power from 5 to 40 watts, layer thickness from 0.003 to 0.012 and the part bed temperature from 40 to 100 C. This was necessary to zero in on the three parameters.

Results

As a result of this research effort, the following parameters were selected:

(1) part Bed temperature was to be maintained around 100
(2) Laser power was to be set around 30 Watts
(3) Powder layer thickness was to be set to minimum of 0.003 However since no satisfactory results were obtained here it was decided -to allow two passes of the roller on the powder before adding the powder to the part bed. At first the samples were tested -using the binder alone. Once the parameters for the binder was selected it was applied to the actual titanium alloy. A summary of the results is given in the following table (1).

Table 1. Summary of Results for the binder material

No.	Observations made	Photo
	The sample was built to the height of 0.125 inches. Sample was run once with the thickness of 0.006. Shifting was present in the part. This is perhaps de to the shear force of roller on the powder. Part appeared to be very brittle and unstable.	
	The sample was built to the height of 0.125 inches. The bed temperature was increased to 100 C. Sample was run twice with the thickness of 0.003. Shifting was still present in the part. Part appeared to be very brittle and unstable; however, the integrity of the part appeared to be a slightly better than the previous runs.	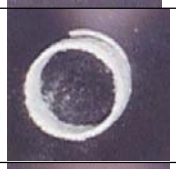
	It is observed that the quality of the parts appears to be highly dependent on the part bed temperature. The par appeared to be more stable by increasing the temperature to 100 C. The parts still appear to be sheared off, so in the next run the powder will be added on top of the part instead of front of it. The temperature will be raised to 110 C.	

	The sample was built to the height of 0.25 inches. The bed temperature was set to 100C. Sample was run once with the thickness of 0.003. In this run we sprayed a layer of powder on top of the part area so that shear force was minimized. Shifting was still present in the part but was corrected after several layers. Part appeared to be more stable than the previous runs. This might be attributed to the increase in surface contact area or binding area due to elimination of shifting.	
	The sample was built to the height of 0.20 inches. The bed temperature was set to 100 C. Sample was run once with the thickness of 0.003. In this run we sprayed a layer of powder on top of the part area so that shear force was minimized. Shifting was eliminated entirely. Part appeared to be more brittle than the case where laser power was set to 40 Watts.	

Resources

The machine used for this project was the Selective Laser Sintering Machine (SLS2000) located in the RP laboratory of the NCAM at NASA Marshall. Material used in the research is the Titanium alloy. There are two software that drive the SLS process: Build Software and Sinter. The build prepares the stl files and gives a visual representation of the location of each part in the Part bed. The Sinter software is the driver software for the SLS machine, in which all the operations and control such as piston movement, loading and unloading the powder, movement of the roller, and latching and unlatching the doors for the machine are performed via this software.

Conclusion

1. The parameters established for this process are Part Bed Temperature of 100 C, Laser power of 25 to 30 and layer thickness of 0.003 or lower if possible.

2. Due to rarity of sample all cases were conducted in the presence of Oxygen. This might contribute to "vaporizing" The binder material before it is sintered.

3. It is essential to eliminate or at least minimize shifting. Shifting of layers causes decrease in the binding surface area and hence adds to instability of the part.

Acknowledgements

The author would like to thank the entire team of engineers and scientists in the Rapid Prototyping Research area of the Marshall Space Flight Center's NCAM. The author wishes to extend his thanks to Mrs. Gail Gordon for providing this opportunity to work at the NASA Center. Special thanks goes to Mr. Ken Cooper for his patience and guidance for helping the author in performing this research. His selflessness and availability through out the course of this research made this research effort a truly pleasant experience.

References

1. *Rapid Prototyping Technology, Selectiona and Application. Kenneth G. Cooper, Marcel Dekker, 2001*
2. *Producing Metal Parts with Selective Laser Sintering/Hot Isostatic Pressing, Suman Das, Martin Wohlert, Joseph J. Beaman and David L. Bourell, JOM, pp17-20, 1998*

2002

NASA FACULTY FELLOWSHIP PROGRAM

MARSHALL SPACE FLIGHT CENTER

THE UNIVERSITY OF ALABAMA IN HUNTSVILLE

FATIGUE AND FRACTURE ANALYSES OF CRACKS IN DUCTILE MATERIALS

REPORT NOT AVAILABLE

Prepared By:	James C. Newman, Jr.
Academic Rank:	Professor
Institution and Department:	Mississippi State University Department of Aerospace Engineering
NASA/MSFC Directorate:	Engineering
MSFC Colleague:	Wayne Gregg

2002

NASA FACULTY FELLOWSHIP PROGRAM

MARSHALL SPACE FLIGHT CENTER
THE UNIVERSITY OF ALABAMA

SELF-CONSISTENT LARGE-SCALE MAGNETOSPHERE-IONOSPHERE COUPLING: COMPUTATIONAL ASPECTS AND EXPERIMENTS

Prepared By:	Timothy S. Newman
Academic Rank:	Associate Professor
Institution and Department:	University of Alabama in Huntsville Department of Computer Science
NASA/MSFC Directorate:	SD50
MSFC Colleagues:	Dr. George Khazanov, Dr. Dennis Gallagher

Introduction

Both external and internal phenomena impact the terrestrial magnetosphere. For example, solar wind and particle precipitation effect the distribution of hot plasma in the magnetosphere. Numerous models exist to describe different aspects of magnetosphere characteristics. For example, Tsyganenko has developed a series of models (e.g., [TSYG89]) that describe the magnetic field, and Stern [STER75] and Volland [VOLL73] have developed an analytical model that describes the convection electric field. Over the past several years, NASA colleague Khazanov, working with Fok and others, has developed a large-scale coupled model that tracks particle flow to determine hot ion and electron phase space densities in the magnetosphere. This model utilizes external data such as solar wind densities and velocities and geomagnetic indices (e.g., Kp) to drive computational processes that evaluate magnetic, electric field, and plasma sheet models at any time point. These models are coupled such that energetic ion and electron fluxes are produced, with those fluxes capable of interacting with the electric field model. A diagrammatic representation of the coupled model is shown in Figure 1.

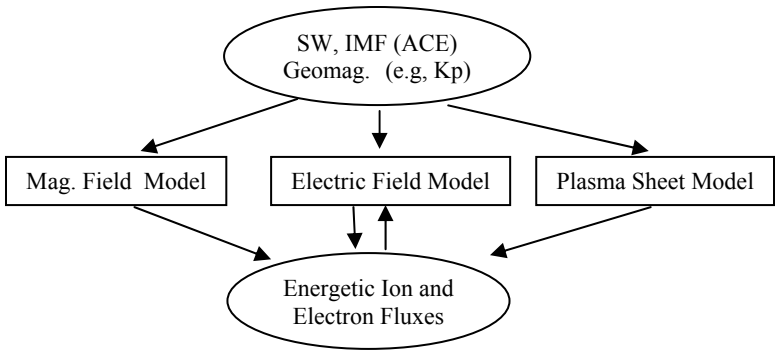

Figure 1: Coupled Model

In this coupled model, the two magnetic field models that have been used to date are the dipole and the Tsyganenko (1996) magnetic field models. The electric field models that have been used to date are the Volland-Stern convection, Weimer, Rice Convection Model (RCM), and AMIE models.

In this report, some of the experiments we have performed (during the NASA Fellowship program) using this model are described. The experiments that were performed involved extending the model and building variations on the model. We have also considered computational aspects of the model, and some of our work in this area is also described.

Contributions

The new model combinations that have been utilized in our work include incorporation (into the coupled model) of time-dependent cross-tail potential within the Volland-Stern convection model, addition of a heavy proton (oxygen) in the Rice Convection Model, and incorporation of the AMIE potential model.

The Coupled Model

The coupled model solves for the hot plasma kinetic energy using a bounce-averaging approach that incorporates effects such as diffusion and charge exchange (decay). Equation 1 expresses the model's kinetic energy solution for each particle species:

$$\frac{\partial Q}{\partial t} + \frac{1}{R_o^2}\frac{\partial}{\partial R_o}\left(R_o^2\left\langle\frac{dR_o}{dt}\right\rangle Q\right) + \frac{\partial}{\partial \varphi}\left(\left\langle\frac{d\varphi}{dt}\right\rangle Q\right) + \frac{1}{\sqrt{E}}\frac{\partial}{\partial E}\left(\sqrt{E}\left\langle\frac{dE}{dt}\right\rangle Q\right) + \frac{1}{f(\mu_o)\mu_o}\frac{\partial}{\partial \mu_o}\left(f(\mu_o)\mu_o\left\langle\frac{d\mu_o}{dt}\right\rangle Q\right) = \left\langle\frac{\delta Q}{\delta t}\right\rangle_{collis} \quad \text{(Eqn. 1)}$$

The coupled model solves for potential using the specified electric field model. In the case of the Rice Convection Model, NASA colleague Khazanov has suggested an extension that allows the cross-field potential to be determined in a self-consistent way through solution of the Poisson's Equation (Eqn. 2):

$$\nabla \cdot \left(-\overleftrightarrow{\Sigma} \cdot \nabla \Phi\right) = \sum_{\alpha} J_{\|\alpha} \sin I \qquad \text{(Eqn. 2)}$$

The coupled, self-consistent RCM-based model involves solution, at each time step, of the Equations 1 and 2. Details of the computational flow of the coupled RCM-based model are omitted from this report. However, we have developed a coarse-grained parallel method to solve Equation 1 and 2 for the coupled RCM-based model. Our solution dedicates one CPU to solution of Equation 1 for each particle species. One CPU is also dedicated to solve the Equation 2. At a high level, the parallel method can be said to operate as follows:

For each time T_i:
- For each CPU C_a:
  - Solve Eqn. 1 for species a
  - Assemble right-hand side (RHS) of Eqn. 2
- Master CPU:
  - Solve Eqn. 2
  - Communicate Result

Some Experiments

Next, some of the experiments that have been performed are described. Most of the experiments have been performed on the May 2, 1986 storm, which is particularly interesting because it has a long main phase. A comparison of the potentials computed by the model near the start, middle, and end of this storm are shown in Figure 1. The figure compares the potentials that were computed from the use of a dipole magnetic field model and three potential models. In the top of the figure, the coupled, self-consistent Rice Convection Model's output is shown. This model calculates an electric field that is more compressed, reflecting a higher potential drop over a smaller region. (In addition, our studies indicate that the coupled, self-consistent RCM enables penetration of plasma sheet particles to low L-shells. Those results are omitted here due to space constraints.) The middle portion of the figure shows the limited self-consistent model (i.e., RCM

without the joint potential solution; RCM based on only the hydrogen species). The bottom portion of the figure uses the Volland-Stern electric field model.

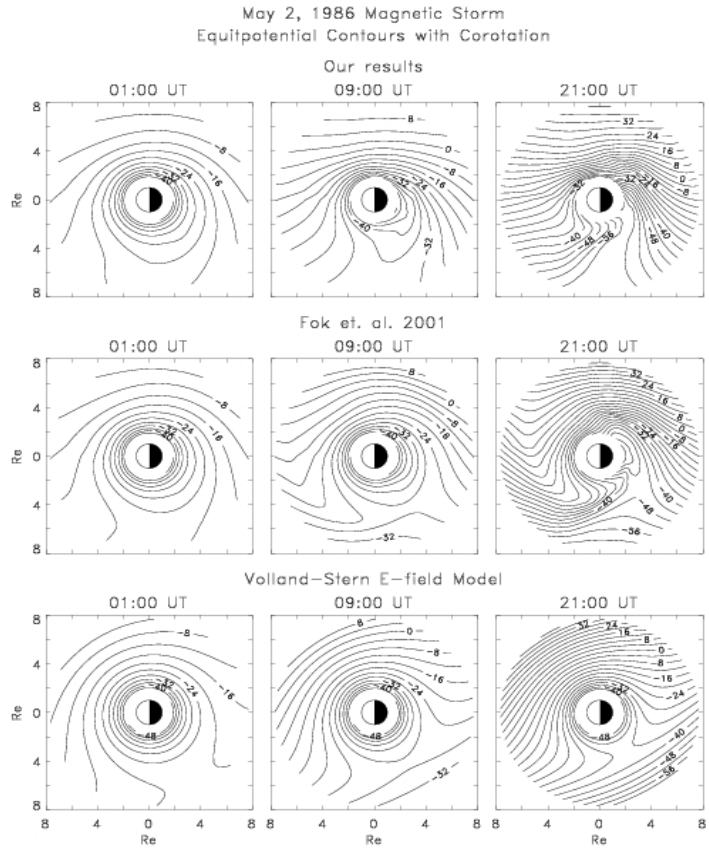

Figure 1. Experimental Results, May 2, 1986 Storm

We have also explored the impact of incorporating a heavy ion species into the coupled, self-consistent RCM model. Our experiments indicate that the impact of adding a heavy ion species is not significant.

Another experiment that was performed explored the impact of incorporating time-dependent cross-tail potential drops (i.e., substorms), such as those suggested by Chen et al. [CHEN93], into the Volland-Stern model. A series of experiments were conducted using Chen et al.'s model substorm, shown in Figure 2. Chen's sub-storm has 9 "spikes" over a 3 hour period.

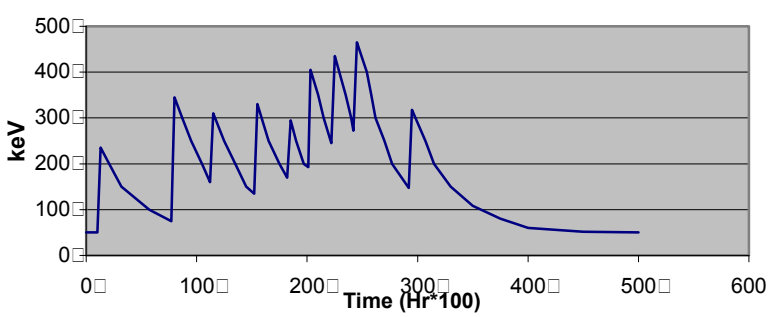

Figure 2. Chen et al. [CHEN93] Model Sub-storm

Computational Considerations

A number of computational improvements have been explored for the large scale model. In the fellowship effort, focus has been on coarse-grained parallel processing of the model. To achieve this parallelism, we have made use of the popular, portable Message-Passing Interface (MPI) on SGI Origin and Linux cluster computers. MPI allows tasks operating on networked CPUs to communicate data and to synchronize operation. The two most basic constructs in the MPI are a synchronized send and synchronized receive operation. Our approach to parallelizing non-self-consistent runs of the model (e.g., using the Weimer or Volland-Stern electric field models) is to simultaneously spawn separate species-specific executables on each CPU in the parallel environment. (Each executable applies the large-scale model to a single particle species.) This very brute-force approach achieves approximately 95% efficiency for a 168 hour simulation run on the May 1-7, 1998 storm. (The large scale model can be computed, with 15 second time steps, in approximately 86 hours on a cluster of two Pentium III/1000 MHz CPUs. Therefore, as long as the time steps are at least 10 seconds, the model can be executed in faster than real-time.) For the coupled, self-consistent version of the RCM, the approach is slightly different; as mentioned above, at each time step, the executables must communicate the RHS of Equation 2 to the Master CPU. This communication takes place using MPI's synchronized send/receive operations. The Master CPU also uses MPI's synchronized send/receive operations to communicate the solved LHS potentials back to the species-specific executables. The large scale model, when used with the coupled, self-consistent version of the RCM, can be computed in approximately the same time as the brute-force parallelization of the non self-consistent runs (e.g., about 72.5 hours to complete a 168 hour simulation with 15 second time steps).

Conclusion

We have demonstrated that self-consistent incorporation of electrons in a hot plasma phase space density solver can allow more sophisticated modeling of magnetosphere-ionosphere coupling. In addition, we have demonstrated that coarse-grained parallel approaches to model computation can allow efficient, real-time calculation of the model.

References

[CHEN93] M.W. Chen, M. Schulz, L. R. Lyons, and D. J. Gorney, "Stormtime Transport of Ring Current and Radiation Belt Ions," *J. Geophysical Research*, 98(A3): 3835-3849, 1993.

[STER75] D. P. Stern, "The Motion of a Proton in the Equatorial Magnetosphere," *J. Geophysical Research*, 80: 595-599, 1975.

[TSYG89] N. A. Tsyganenko, "A Magnetospheric Magnetic Field Model with a Warped Tail Current Sheet," *Planet. Space Sci*,. 37: 5-20, 1989.

[VOLL73] H. Volland, "A Semiempirical Model of Large-Scale Mangetospheric Electric Fields," *J. Geophysical Research*, 78: 171-180, 1973.

2002

NASA FACULTY FELLOWSHIP PROGRAM

MARSHALL SPACE FLIGHT CENTER
THE UNIVERSITY OF ALABAMA

INVESTIGATION OF STRUCTURAL PROPERTIES OF CARBON-EPOXY COMPOSITES USING EMBEDDED FIBER-OPTIC BRAGG GRATINGS

Prepared By:	Albert J. Osei
Academic Rank:	Associate Professor
Institution and Department:	Oakwood College Mathematics and Physics Department
NASA/MSFC Directorate:	Science
MSFC Colleague:	Joseph Grant

Introduction

Real time monitoring of the mechanical integrity and stresses on key aerospace composite structures like aircraft wings, walls of pressure vessels and fuel tanks or any other structurally extended components and panels as in space telescopes is very important to NASA. Future military and commercial aircraft as well as NASA space systems such as Space Based Radar and International Space Station will incorporate a monitoring system to sense any degradation to the structure. In the extreme flight conditions of an aerospace vehicle it might be desirable to measure the strain every ten centimeters and thus fully map out the strain field of a composite component. A series of missions and vehicle health management requirements call for these measurements. At the moment thousands of people support a few vehicle launches per year. This number can be significantly reduced by implementing intelligent vehicles with integral nervous systems (smart structures). This would require maintenance to be performed only as needed. Military and commercial aircrafts have an equally compelling case. Annual maintenance costs are currently reaching astronomical heights. Monitoring techniques are therefore required that allow for maintenance to be performed only when needed. This would allow improved safety by insuring that necessary tasks are performed while reducing costs by eliminating procedures that are costly and not needed.

The advantages fiber optical sensors have over conventional electro-mechanical systems like strain gauges have been widely extolled in the research literature. These advantages include their small size, low weight, immunity to electrical resistance, corrosion resistance, compatibility with composite materials and process conditions, and multiplexing capabilities. One fiber optic device which is suitable for distributed sensing is the fiber Bragg grating (FBG). This is a periodic perturbation in the refractive index of the fiber core. When a broadband light is coupled into the optical fiber sensor, a reflection peak will be obtained centered around a wavelength called Bragg-wavelength. The Bragg-wavelength depends on the refractive index and the period of the grating, which both change due to mechanical and thermal strain applied to the sensor. The shift in the Bragg-wavelength is directly proportional to the strain.

Researchers at NASA MSFC are currently developing techniques for using FBGs for monitoring the integrity of advanced structural materials expected to become the mainstay of the current and future generation space structures. Since carbon-epoxy composites are the materials of choice for the current space structures, the initial study is concentrated on this type of composite. The goals of this activity are to use embedded FBG sensors for measuring strain and temperature of composite structures, and to investigate the effects of various parameters such as composite fiber orientation with respect to the optical sensor, unidirectional fiber composite, fabrication process etc., on the optical performance of the sensor.

This paper describes an experiment to demonstrate the use of an embedded FBG for measuring strain in a composite material. The performance of the fiber optic sensor is determined by direct comparison with results from more conventional instrumentation.

Optical Fiber Selection and Fabrication of Bragg Gratings

Two fiber buffer materials (Acrylic and Polyimide) were selected for the study, which met the fabrication process, temperature, and strain requirements of the proposed composite. High reflectivity Bragg gratings were produced into the core of the single mode, Germanium doped optical fibers using the phase mask method (Hill et al. 1993). The optical fibers were hydrogen loaded (Lemaire et al.) under high pressure to increase photosensitivity prior to writing the grating. A continuous wave argon ion laser operating at 244 nm (second harmonic of the blue line) was used as the source for writing the gratings at Bragg wavelengths around 1300 nm and a bandwidth of around 0.5 nm. Real-time monitoring of grating growth was carried out during the writing process by illuminating the grating with broadband source (a laser diode) covering the grating reflection spectrum. Transmission and reflection spectra were measured with the aid of a monochromator and a recorder.

Embedded Optical Fibers

Carbon /epoxy composite panels, with embedded optical fiber sensors were fabricated using the NASA-MSFC composite fabrication facilities. The carbon/epoxy prepreg used for the panel fabrication was provided by NASA. The fabrication technique focused on the hand lay-up and autoclave cure. Three prominent lay-up orientations (0, 90, and 45 degree) of the fibers (uni-tape and fabric) in the composite lay-up were selected for the study. The optical fiber was arranged to lie parallel, at 45° angle, and perpendicular to the carbon fibers.

Test Set—Up

Shown in Figure 1 is a schematic of the set-up used for performing physical tests on the composite panels fabricated with the embedded Bragg gratings [2,3,5]. The composite was tested under axial tension. It was gripped on either end in a special hydraulic wedge grips. Approximately one inch of the composite was gripped by each of the two wedge grips. A compact tunable diode laser was used to couple light into the optical fiber. The transmission spectrum of the grating was recorded with the aid of a detector and a lock-in amplifier. The tensile loading was increased continuously from zero to maximum at any desired rate. Shift in the Bragg wavelength was obtained from the transmission spectrum. The software developed in house converts this shift into longitudinal strain and plots the load strain data. Longitudinal as well as transverse strains were measured simultaneously and used to determine Poisson's ratio for the composites.

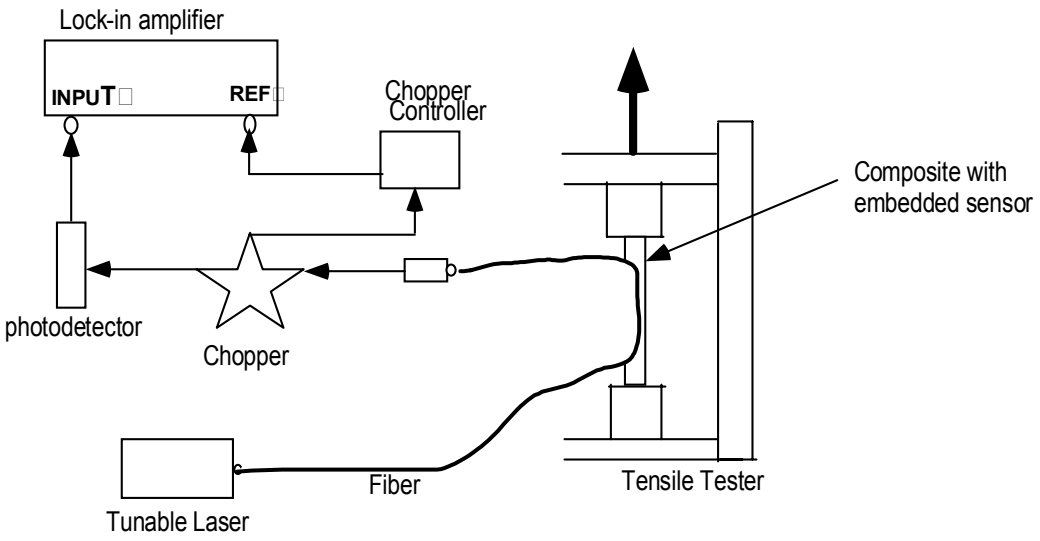

Figure 2: The Experimental Set-Up

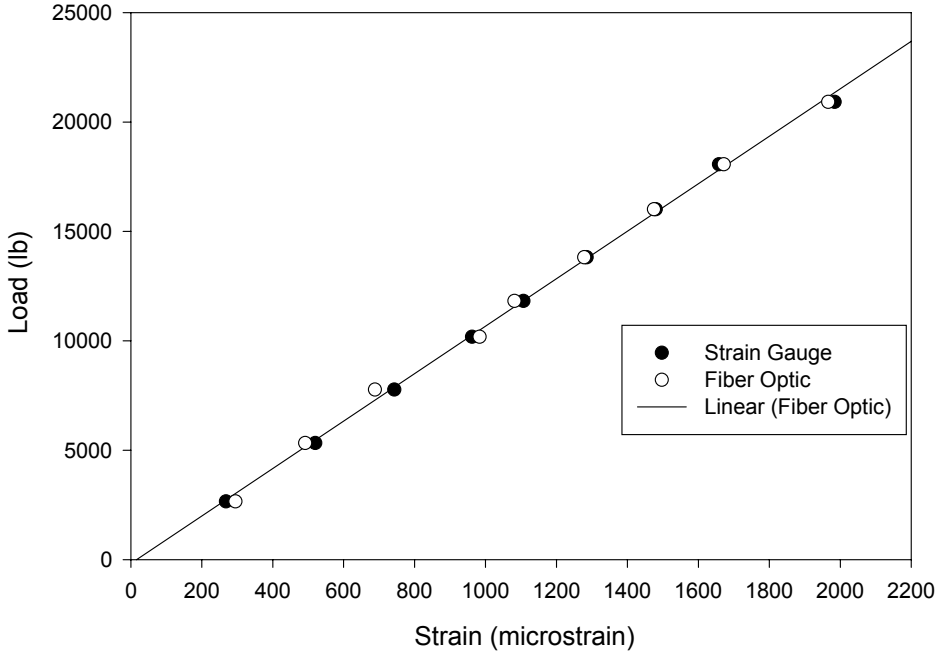

Figure 2. Load versus Strain

Results and Discussions

A plot of load versus strain is shown in Figure 2. The actual strain values were obtained from the fiber optic strain by dividing fiber optic strain measurements by 0.78 as discussed in the literature. Excellent agreement between the strain gauge measured strain and that of the fiber optic sensor is evident. A linear regression of the fiber optic data was performed and the equation is displayed in the figure.

More sets of data were taken and the plots described above were done for each set. Plots of only one data set are shown for convenience. Results show a good repeatability for the experiment.

Concluding Remarks

Optical fibers with Bragg sensors have been embedded into carbon-epoxy composite to measure the tensile strain in the composite material. Excellent agreement between strain measurements from a more conventional instrumentation and the Bragg sensors has been verified. The experimental results of this preliminary study indicate that fiber optic Bragg grating sensors, integrated with composites, have potential applications for monitoring the structural integrity of composite structures.

Acknowledgements

The author is very grateful to Mr. Joseph Grant for his technical support and encouragement Thanks are also due to Dr. Raj Kaul of the Engineering directorate and Scott Taylor for making it possible for the composite panels with the embedded optical fiber Bragg gratings to be fabricated. Helpful discussions with Dr. A. Sharma of Alabama A&M University were very much appreciated. Finally, the author would like to acknowledge the support of NASA.

References

[1] Hill K.O., Malo B., Bilodeau F., Johnson. D.C., Albert J., (1993), "Bragg gratings fabricated in photosensitive monomode optical fiber by UV exposure through a phase mask". Appl. Phy. Lett Vol 62, p. 1035.

[2] Kersey A.D., (1991), "Multiplexing options for quasi-distributed sensing in smart structures using fiber interferometry". Proc. Conf. Optical fiber sensor-based smart structures, VA

[3] LeBlanc M. et al (1996), "Distributed strain measurement based on a fiber Bragg grating and its reflection spectrum analysis". Opt. Lett. 21, 1405.

[4] Lemaire P.J., Atkins R.M., Mizrahi V., Reed W.A., (1993) Electron. Lett. Vol. 29 p1191.

[5] Rao, Y.J. et al; "Strain sensing of modern composite materials with a spatial/wavelength division multiplexed fiber grating network."

2002

NASA/ASEE SUMMER FACULTY FELLOWSHIP PROGRAM

MARSHALL SPACE FLIGHT CENTER
THE UNIVERSITY OF ALABAMA

LOW-ENERGY STUDY OF GAMMA-RAY BURSTS HAVING SPECTRAL LINE FEATURES

Prepared By:	Michael J. Pangia
Academic Rank:	Associate Professor
Institution and Department:	Georgia College & State University Department of Chemistry & Physics
NASA/MSFC Directorate:	Science
MSFC Colleagues:	Gerald J. Fishman Robert D. Preece (UAH)

Introduction

Gamma-ray bursts (GRBs) are energetic, short-duration emissions of gamma-rays. The Burst and Transient Source Experiment (BATSE) that was onboard NASA's Compton Gamma-Ray Observatory has done much to advance our understanding of GRBs. Perhaps foremost is to establish that GRBs originate from astronomical sources that exist well beyond our galaxy. Another area in which BATSE has been instrumental is to provide high-resolution data that can be used in spectral studies. Before BATSE, there were many reports of GRB spectra containing what appeared to be spectral absorption lines, whereas Briggs, after an extensive computer search of 117 bright BATSE GRBs, reported finding only one case that might be an absorption line and ten cases that might be emission lines [1]. None of the eleven BATSE cases were definitively identified as spectral lines, and Briggs indicated reasons as to why the pre-BATSE reports should not be taken as conclusive.

It remains an open question as to what these spectral-like features are, or if they are even real. The purpose of this work is, for the subset of the eleven BATSE GRBs for which low-energy data are available from two BATSE's Spectroscopy Detectors (SDs), to include these data in the spectral analysis. Such a study will provide additional constraints on the model spectral functions to better ascertain the reality of the line features. The spectral analysis program used was RMFIT. Of the six GRBs that met the selection criteria, the analysis was performed on only three of them due to a lack of time.

Spectral Models

The continuum portion of the GRB's spectra is fit using Band's GRB model, a product power-law and exponential function with four parameters and a break point [3]. The secondary models used in this study are a Gaussian, Optically Thin Thermal Bremsstrahlung (OTTB) model, and a Multiplicative Broken Power Law (MBPL); the first two being additive models. The Gaussian is used to model a spectral line. The OTTB model has the following form

$$f_{OTTB} = A \frac{E_P}{E} e^{-(E-E_P)/kT} \qquad (1)$$

where A is an amplitude parameter, T is a temperature parameter, and E_P is known as the pivot energy. For this study E_P is constrained to 10 keV. The MBPL is unity for energies above its break point E_B. Otherwise it is given by

$$f_{MBPL} = \left(\frac{E}{E_B} \right)^b \qquad \text{for } E \le E_B, \qquad (2)$$

where b is known as the low-energy index. Note that both b and E_B are free parameters.

The means by which a secondary model will be judged for improving a fit, and thus assessing the credibility of the data, is known as the Maximum Likelihood Ratio Test (MLRT). The MLRT judges the fit by considering the amount by which the χ^2 value for the fit is improved as a result of the secondary model. For example, for Briggs' study, an improvement in χ^2 of $\Delta\chi^2 = 20$ resulting from a two-parameter, secondary model corresponds to a chance occurrence of 1 in 20,000. For this study we assume that $\Delta\chi^2 = 20$ will have the same order of probability.

Results and Conclusions

Only some results and the highlights of the study will be presented here. Figure 1 shows the background-subtracted data from SD#'s 0 & 5 along with the resulting model fits (shown as solid, unmarked lines) for BATSE Trigger 3245 using just Band's GRB model. Two data types are being used, high-resolution (SHER) type and the low-energy, low-resolution (DISCSP) type. The time interval for the spectra is 7.9 to 22.5 s, which approximates the interval during which Briggs discovered the spectral feature.

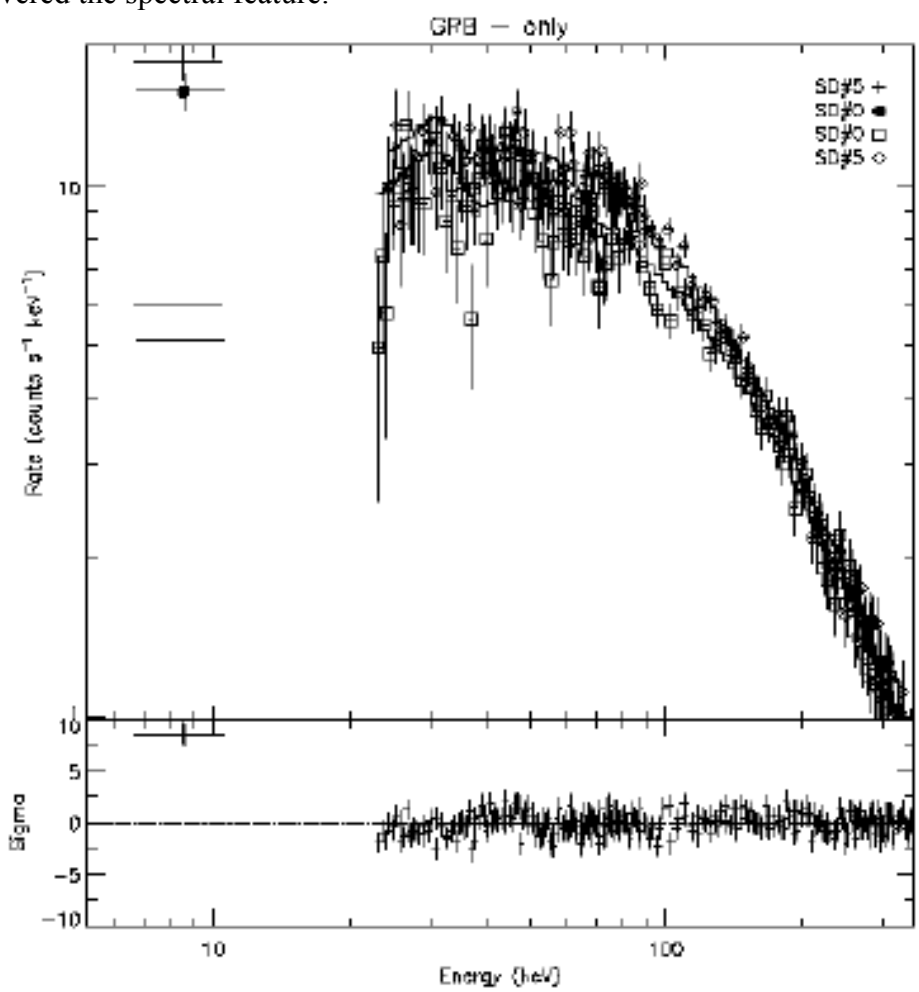

Figure 1: Joint fit of Trig 3245 from 7.9 to 22.5 s.

The lower panel in Figure 1 is a plot of the difference between the measured and model count rates expressed in units of σ. It is evident that there is a significant discrepancy ($\sim 9\sigma$) at the low energy. Preece et al. [2] have studied low-energy (x-ray) discrepancies and have found significant discrepancies are present in fewer than 20% of bright GRBs.

Table 1 gives a summary of the various fitting attempts for Trig 3245. In each case, the continuum was fit with Band's GRB model. The secondary model and its fixed parameter are listed, and, in the last case, a third model (Gaussian) was also used. The number of degrees of freedom (DOF), the resulting χ^2, and the improvements on χ^2 ($\Delta\chi^2$) for each fit are also listed. Most noteworthy is that by far the greatest improvement in the fit resulted from using the OTTB model as the secondary ($\Delta\chi^2 = 170.$); however, adding in a Gaussian as a third component still yields a significant improvement ($\Delta\chi^2 = 21$). This suggests, although is not conclusive, that the feature associated with the Gaussian fit may be real. (The fit determined the energy centroid of the Gaussian to be 43.5 ± 1.3 keV.)

Table 1 Summary of Fit Results for Trig 3245

Trig: 3245	(X-Ray: Excess)				Full Resolution	
				DOF	χ^2	$\Delta\chi^2$
Main Model:	Band's GRB			390	553.47	
Secondary Model	Fixed Param.	w. Third Model	Fixed Param.			
Gaussian	Width			388	535.98	17.49
Gaussian	--			387	535.93	17.54
OTTB	E-Pivot			388	383.30	170.17
		Gaussian	Width	386	361.94	21.36

The type of low-energy discrepancy in Trig 3245 case is known as an "X-Ray Excess." The other two GRBs studied were found to have significant "X-Ray Deficits" (data count rates being lower than the model count rates). Therefore, there may be a connection between the existence of a spectral-line feature and an x-ray discrepancy.

Time histories of the fit parameters of the three GRBs were examined to look for commonalities or correlations. Examination of Trig 3245 shows that there are two peaks in the Gaussian feature that seem to precede two corresponding peaks in the x-ray component; however, the uncertainties in the parameters are too large to make a convincing case for the entire GRB duration. The third case studied (referred to as Case C) was exceptional in two ways. One was that a Gaussian is significant is only about 0.5 s out of 20 s of significant activity. The other exceptional point to make regarding Case C is illustrated in Figure 2, which is the time history of the low-energy MBPL index (holding E_B fixed to 18.1 keV) plotted along with the corresponding reduced χ^2 value for each time interval. (Note that there is one interval for which χ^2 did not converge. This interval is indicated by a negative value for χ^2.) From Figure 2, it is

seen that MBPL low-energy index is notably close to zero in the same narrow interval that the Gaussian line is most prominent.

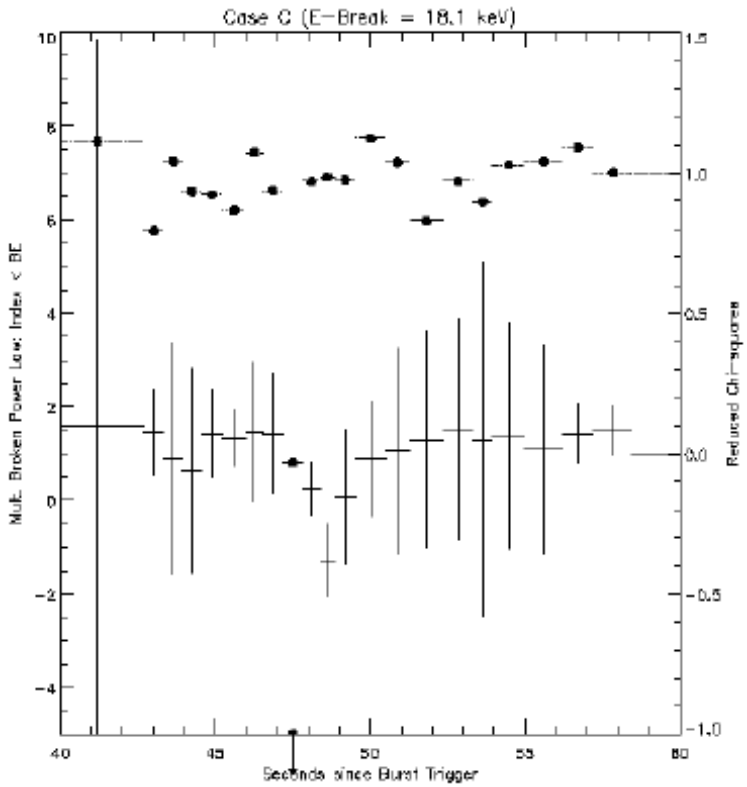

Figure 2 Time History of the MBPL Low Energy Index and Reduced Chi-Squared for Case C.

In conclusion, three of eleven GRBs from Briggs' spectral-line study were analyzed including low-energy SD data from two detectors. The major finding is that these cases were found to have significant x-ray discrepancies. Trig 3245, even after considerably improving the fit using the OTTB model, still had a spectral feature that might be significant ($\Delta\chi^2 = 21$). Case C showed a possible anti-correlation between its x-ray deficit and its spectral feature.

References

[1] Briggs, M. S. (1999) "Low-Energy Spectral Features in GRBs," *ASP Conference Series,* v. 190, pp. 133-149.

[2] Preece, R. D., et al. (1996), "BATSE Observations of Gamma-Ray Burst Spectra. III. Low-Energy Behavior of Time-Averaged Spectra," *The Astrophysical Journal*, v. 473, p. 310-321.

[3] Preece, R. D., et al. (2000), "The BATSE Gamma-Ray Burst Spectral Catalog. I. High Time Resolution Spectroscopy of Bright Burst using High Energy Resolution Data," *The Astrophysical Journal Supplement Series*, v.126, pp. 19-36.

2002

NASA FACULTY FELLOWSHIP PROGRAM

MARSHALL SPACE FLIGHT CENTER
THE UNIVERSITY OF ALABAMA

METAL CUTTING THEORY AND FRICTION STIR WELDING TOOL DESIGN

Prepared By:	Lewis N. Payton
Academic Rank:	PhD
Institution and Department:	Auburn University College of Engineering Lewis.Payton@eng.auburn.edu
NASA/MSFC Directorate:	Engineering (ED-33)
MSFC Colleague:	Dr. Arthur C. Nunes, Jr.

Introduction

Friction Stir Welding (FSW) is a relatively new industrial process that was invented at The Weld Institute (TWI, United Kingdom) and patented in 1992 [12] under research funded by in part by the National Aeronautics and Space Administration (NASA). Often quoted advantages of the process include good strength and ductility along with minimization of residual stress and distortion. Less well advertised are the beneficial effects of this solid state welding process in the field of occupational and environmental safety. It produces superior weld products in difficult to weld materials without producing any toxic fumes or solid waste that must be controlled as hazardous waste. In fact, it reduces noise pollution in the workspace as well.

In the early days of FSW, most welding was performed on modified machine tools, in particular on milling machines with modified milling cutters. In spite of the obvious milling heritage of the process, the techniques and lessons learned from almost 250 years of successful metalworking with milling machines have not been applied in the field of modern Friction Stir Welding. The goal of the current research was to study currently successful FSW tools and parameterize the process in such a way that the design of new tools for new materials could be accelerated. Along the way, several successful new tooling designs were developed for current issues at the Marshall Space Flight Center with accompanying patent disclosures

Survey of the Literature and Process

In order to visualize the process, consider Figure 1. The two materials to be welded are placed in contact via either an overlapping or in this case butt joint fashion. A broad tool with a narrower pin on the end is fabricated. The tool is then inserted while rotating at a high speed into the material until the wider "shoulder" of the tool makes contact with the material being welded. At this point, the tool begins a traverse of the weld seam, deforming the material in its passage, leaving behind a formed weld. The material does not melt during this solid-state deformation. Personnel with shop experience will recognize similarities with a type of end-milling referred to as slot-milling. Many rotary machines can be adapted to this process.

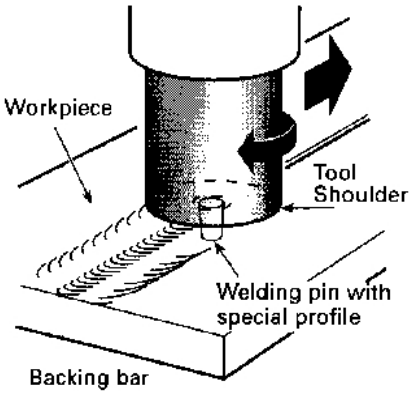

Figure 1. Basic FSW Process

Figure 1 details only the most basic concept of what can be a much more complex system of tooling. A comprehensive literature review of conference papers, referred papers, United States and international patents was performed. Copies of all the papers were provided to key NASA personnel along with an up to date listing of patents. A detailed bibliography and a copy of the patent listing (some 600 plus items) is prohibited in this summary article.

The review process indicated a general lack of standardization, documentation and systematic evaluation in the area of friction stir welding. This is due in part to the proprietary nature of TWI's patents, the relative newness of the process and a lack of instrumentation in the early

development stages. The level of instrumentation available was often minimal leading to a great deal of speculative operator changes based upon tradition and/or lore. The driving motive in such changes was the correlation of a perceived change with an improvement in final weld, as judged by "faster" process time, greater tensile or bending strength. These are at best indirect correlations with the true physical processes. Additionally, many of the papers are in non-refereed conference proceedings, which slows academic research in the field.

The best attempts to quantify the mechanics of the process to date have been conducted at the University of South Carolina [8, 9] and NASA. The most detailed paper of the flow patterns is a "seminal" paper by Kevin Colligan [2]. Efforts to document and characterize material properties of the weld at University of Texas El-Paso have been most notable [5, 6]. Numerous models have been proposed ([7]) . The best tool studies to date are proprietary by The Welding Institute, although none of the modelers take into account the eccentric tool path. Classic milling theory offers simple solutions for the FSW tool designer.

An Application of Milling Theory

Figure 2a depicts what machining theory in general refers to as up milling and down milling. Figure 2b shows the FSW terminology for these as Leading (up-milling against the tool) and Trailing (down-milling with the tool). On the leading (up-milling side), as the tool enters the work, tool tip velocity V assumes a maximum value, which decreases as the tool progresses along the tool path. On the trailing side, V has a minimum value when the tooth leaves the work and a somewhat higher value when the tool enters the work. The tool edge traces out a looped tracheiod path through the material, as well explained by Martellotti [3, 4].

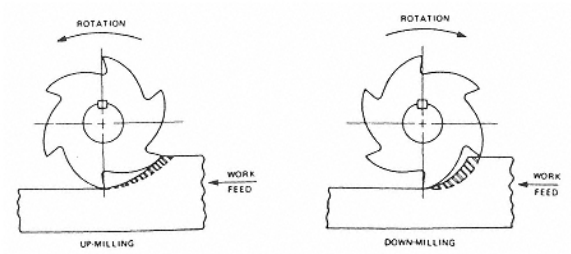

Figure 2A. Up-milling and Down-milling

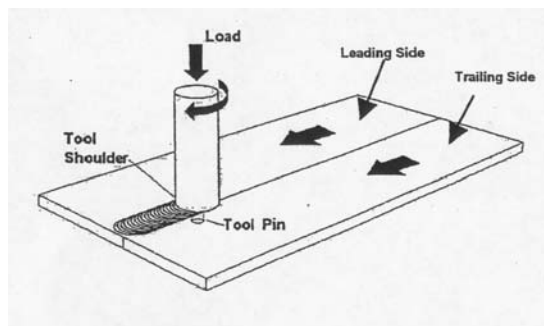

Figure 2B. Leading and Trailing Sides

Silin [1, 11] introduced the use of similarity numbers for use in metal cutting research. His methodology provided a means to accurately calculate the temperature at a milling tool tip. This has since been duplicated through a dimensional analysis approach [10]. Incorporating the eccentric geometry and travel features of Figures 2A and 2B, and generating the proper coefficients to use the data in ASM Handbook of Metals (9th Edition) available at the Marshall Space Flight Center generates the following useful expressions for the FSW tool designer:

$$T_{cutting_edge} = [16{,}148.58]\, HP_s \sqrt{\frac{V * t}{k * (pc)}} \qquad (1)$$

HP_s is the specific horsepower for the alloy or workpiece, k is the coefficient of thermal conductivity for the workpiece, (pc) is the volume specific heat of the work material, V is the cutting speed at the tip of the tool (a geometric consideration) and t is the *undeformed-uncut* chip thickness, generally given by [3]:

$$t_{avg} = \frac{F_t * d}{R\cos^{-1}\left(1 - \frac{d}{R}\right) + \frac{F_t * n}{\pi * D}\sqrt{D * d - d^2}} \qquad (2)$$

where R is the Radius of the cutting edge (specific to shoulder or pin in this application), d is the depth of the cut (specific to the design of tool), D is the diameter of the cutter, n is the number of teeth, and F_t is the feed per tooth. These equations reproduce the results of thermocouple measurements in the laboratory very exactly (e.g. McClure et al [5]). When applied to a very well known material (6061-T6), and overlaid onto a generic process map for a similar aluminum alloy, Figure 3 emerges.

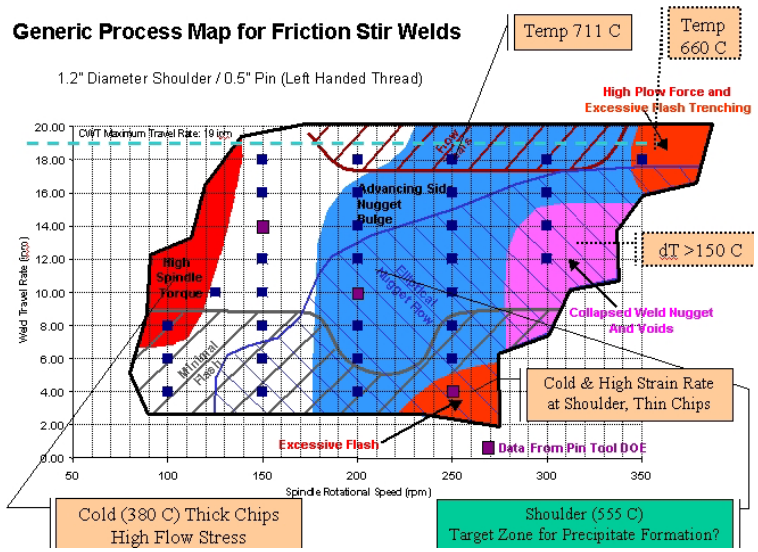

Figure 3. Generic Process Map showing empirical results and metal cutting predictions

This figure, restricted in size as it is, is highly significant. It details the empirical results of a large FSW designed experiment to determine the optimum cutting conditions in the material with callouts to show the predicted values of Equation (1). By examining the callouts and the associated problem, the underlying temperature, strain or strain rate which creates the empirically documented problem becomes apparent. More importantly, in the "sweet spot" identified by the experiment (lowest right callout), the temperature under the shoulder exceeds that required for precipitation hardening, which suggests a possible design target using these criteria and Equation (1), tailored to that specific material. Additionally, Equation (1) details the true benefit of increasing the number of scrolls in a design. The addition of a second scroll under the shoulder greatly reduces the extreme temperature effect of the shoulder, while promoting better rotation of the shear wall plug in the Nunes model of FSW [7].

Recommendations

NASA Marshall Space Flight Center should continue to investigate the use of Equation (1) and other metal cutting methodologies to assist in tool design. Metal cutting theory suggests optimization criteria and precludes the need for the complex empirical experiments, which produced the underlying process chart of Figure 3. This requires additional material data (specific horsepower of the workpiece) but this data can easily be obtained in-house with slight modifications to existing machinery. Instrumentation of horsepower at the spindle and cutting edge is critical. Additional recommendations have been provided through patent disclosures.

Acknowledgements

The author would like to thank the entire team of engineers and scientists in the Process Development Team (ED-33) of the Marshall Space Flight Center's Engineering Directorate for allowing me to work with them this summer. In particular, I appreciate the patience shown by Dr Arthur C. Nunes, Jr., during my many hours of investigation into this process, as well as Kirby Lawless, Jeff Ding, Bob Carter, Dr. Judy Schneider, Carolyn Russell, and Mandy Lazar.

References

1. Astakhov, V.P., *Metal Cutting Mechanics*. 1998, Boca Raton: CRC Press. 297.
2. Colligan, K., *Material flow behavior during friction stir welding of aluminum.* Welding Journal, 1999. 78 (7): p. 229S.
3. Martellotti, M.E., *An Analysis of the Milling Process.* Transactions of the American Society of Mechanical Engineers, 1941: p. 677.
4. Martellotti, M.E., *An Analysis of the Milling Process, Part II-Down Milling.* Transactions of the American Society of Mechanical Engineers, 1945: p. 233.
5. McClure, J.C., et al. *A Thermal Model of Friction Stir Welding*. in *5th International Conference on Trends in Welding Research*. 2001.
6. Murr, L.E., et al., *Microstructures in friction-stir welded metals.* Journal of Materials Processing & Manufacturing Science, 1999. **7**(2): p. 145.
7. Nunes, A.C. *Wiping Metal Transfer in Friction Stir Welding*. in *Proceedings of the 2001 TMS Annual Automotive Alloys and Joining Aluminum Symposia*. 2001. New Orleans, LA: The Minerals, Metals and Materials Society.
8. Reynolds, A.P., W.D. Lockwood, and T.U. Seidel, *Processing-property correlation in friction stir welds*, in *Aluminum Alloys: Their Physical and Mechanical Properties, Pts 1-3*. 2000. p. 1719.
9. Reynolds, A.P. and W. Tang. *Alloy, Tool Geometry, and Process Parameter Effects of Friction Stir Welding Energies and Resultant FSW Joint Properties*. in *Friction Stir Welding and Processing*. 2001. Indianapolis, Indiana: TMS.
10. Shaw, M.C., *Metal Cutting Principles*. 1984, Oxford: Clarendon Press.
11. Silin, S.S., *Similarity Methods in Metal Cutting (in Russian)*. 1979, Moscow: Mashinostroenie.
12. Thomas, W.M., Dolby, R.E. *Friction Stir Welding Developments,* in *6th International Conference on Trends in Welding Research*. 2002. Pin Mountain, Georgia.

2002
NASA FACULTY FELLOWSHIP PROGRAM

MARSHALL SPACE FLIGHT CENTER
THE UNIVERSITY OF ALABAMA

USING CASE TO EXPLOIT PROCESS MODELING IN TECHNOLOGY TRANSFER

Prepared By:	Cheryl Renz-Olar
Academic Rank:	Accompanying Student
Institution and Department:	University of Alabama in Huntsville Department of Accounting and Information Systems
NASA/MSFC Directorate:	Customer and Employee Relations
MSFC Colleague:	Jim Dowdy

USING CASE TO EXPLOIT PROCESS MODELING IN TECHNOLOGY TRANSFER

A successful business will be one that has processes in place to run that business. Creating processes, reengineering processes, and continually improving processes can be accomplished through extensive modeling. Casewise® Corporate Modeler™ CASE is a computer aided software engineering tool that will enable the Technology Transfer Department (TT) at NASA Marshall Space Flight Center (MSFC) to capture these abilities. After successful implementation of CASE, it could then go on to be applied in other departments at MSFC and other centers at NASA.

The success of a business process is dependent upon the players working as a team and continuously improving the process. A good process fosters customer satisfaction as well as internal satisfaction in the organizational infrastructure. CASE provides a method for business process success through functions consisting of systems and processes business models; specialized diagrams; matrix management; simulation; report generation and publishing; and, linking, importing, and exporting documents and files. The software has an underlying repository or database to support these functions. The Casewise® manual informs us that dynamics modeling is a technique used in business design and analysis. Feedback is used as a tool for the end users and generates different ways of dealing with the process.

Feedback on this project resulted from collection of issues through a systems analyst interface approach of interviews with process coordinators and Technical Points of Contact (TPOCs). These interviews were part of the following project schedule:

Project Schedule

- Set a plan for process intervention.
- Get a list of Space Act Agreement (SAA) Process participants.
- Obtain the series of documents associated with the SAA Process.
- Gain knowledge of the process through meetings with process support staff.
- Obtain initial copy of Casewise®.
- Pursue a learning curve of the CASE tool.
- Model NASA, MSFC, and TT enterprises using organizational hierarchy models.
- Create a data flow diagram of the SAA Process.
- Interview process coordinators and TPOCs to collect issues.
- Diagram a new business dynamics model of the SAA Process with issues attached and descriptions populated.
- Generate an issues report and publish it for end users.
- Do preview presentation on CASE for the TT Department.
- Produce interview reports for the SAA process owner.
- Write project report.
- Train CASE administrator.

- Give final presentation.

In addition to the project schedule, goals were set for the project initiative as follows:

Project Goals

- Analyze the process looking for obvious holes, glitches, or issues.
- Provide help on executing the process by determining whom the players are, what the steps are, and how it is implemented.
- Interview the coordinators and TPOCs.
- Build models of the process based on the actual formal process and the interview feedback.
- Explore the possibility of collecting metrics on the process and the sub processes.
- Create the ongoing ability to change the process as needed to ensure continuous process improvement.
- Collect information that will help to generate training documentation.
- Work toward automation of the process.

In order to analyze the SAA Process by collecting issues, interview questions for the process coordinators and TPOCs were spawned as follows:

Coordinator Interview Questions

- What issues do you have with the Space Act Agreement (SAA) Process?
- What suggestions do have for improving the process?

TPOC Interview Questions

- What is your understanding of CAITS and CAITS form?
- What are your expectations of flow time for the whole process?
- Are you aware, in the concurrence cycle, where the longest waiting time for signature resides? Does this concern you?
- How many outside companies do you work with per year that might produce Space Act Agreements (SAAs)?
- Why do want to do SAAs, what do get from them, and what do you need from them?
- What issues do you have with the process?
- Do you have any suggestions for improving the SAA process?

For the SAA Process, I created process dynamics diagrams, which show an overview of the process, the functions of the process, and how the process works. A function dynamics diagram provides the explosion of one elementary systems process into its individual transaction steps. Sub process diagrams can then be produced to further break down the steps within different process parts. When a process diagram is exploded or decomposed into sub process diagrams, this allows for the advantage of keeping the sub processes internal to the organization, while publishing only the main process. Issues generated from the above interview questions were then attached to the appropriate diagram objects and the descriptions populated.

An issue report was published for the end users to generate ideas for process improvement. Interview reports were also produced for the same purpose. Issue collection is inline with CaER's personal vision for processes and systems to include listening to feedback from customers and implementing changes as needed.

In addition to populating the object descriptions for the various process steps, the appropriate SAA documents were linked to the correlating process steps. These documents can be exploded and opened in the application that they were created in. Linking documentation provides for deeper analysis of the process steps.

Completed documentation for each individual Space Act Agreement (SAA) could also be attached to duplicate process models to track the actual individual SAAs, both with documentation and metrics. Metrics such as service time and costs have input areas in the properties boxes for each process object. The metrics can be tracked and reports generated through simulation. The business process simulations are a powerful means of performing statistical breakdown of business processes in relation to the metrics that are entered.

Another means of analysis in Casewise® is matrix management. According to the CASE manual, matrix diagrams show associations between data and objects in models such as applications and technologies, or processes and organizations. This is a useful way to analyze impacts of any process redesign, and also to record the activity between business objects. A matrix diagram can aid in examining and planning a business area and can be used to:

- Show the interactions between objects.
- Report on the interactions between objects.
- Identify intersection patterns.
- Perform impact analysis.
- Record and define the interactions between objects as an aid in scoping and planning.

Casewise® has some additional capabilities. The published report information can be completed in Microsoft Word or Excel, as well as in HTML for posting on a web site or company intranet. A diagram can be exported via the Web for external/internal controlled changes and imported back into the original diagram. The software can also be linked to third party software to import and export data back and forth.

In conclusion, CASE can promote successful business processes while furthering the goal of Technology Transfer, which is to encourage broad use of MSFC-developed technologies by American private enterprise. The importance of good processes is evident by Art Stephenson's (MSFC Center Director) statement, "Our processes are far from perfect. We need to continually look at ways to improve them. We need to use "out of the box" thinking to find new and better ways of doing our business." Finally, I want to impart that CASE can help to continue the vision of the Space Act Agreement Process at NASA/MSFC to meet the needs of customers and move at the speed of business. This will be accomplished by continuous process improvement.

2002

NASA FACULTY FELLOWSHIP PROGRAM

MARSHALL SPACE FLIGHT CENTER
UNIVERSITY OF ALABAMA

INDEPENDENT REVIEW OF THE FAILURE MODES OF F-1 ENGINE AND PROPELLANTS SYSTEM

Prepared By:	Paul Ray
Academic Rank:	Associate Professor
Institution and Department:	The University of Alabama Department of Industrial Engineering
NASA/MSFC Directorate:	Space Transportation, TD 30
NASA Colleagues:	Hugh Brady & Alberto Duarte

Introduction

The F-1 is the powerful engine, that hurdled the Saturn V launch vehicle from the Earth to the moon on July 16,1969. The force that lifted the rocket overcoming the gravitational force during the first stage of the flight was provided by a cluster of five F-1 rocket engines, each of them developing over 1.5 million pounds of thrust (MSFC-MAN-507). The F-1 Rocket engine used RP-1 (Rocket Propellant-1, commercially known as Kerosene), as fuel with lox (liquid Oxygen) as oxidizer. NASA terminated Saturn V activity and has focused on Space Shuttle since 1972. The interest in rocket system has been revived to meet the National Launch System (NLS) program and a directive from the President to return to the Moon and exploration of the space including Mars. The new program Space Launch Initiative (SLI) is directed to drastically reduce the cost of flight for payloads, and adopt a reusable launch vehicle (RLV). To achieve this goal it is essential to have the ability of lifting huge payloads into low earth orbit. Probably requiring powerful boosters as strap-ons to a core vehicle, as was done for the Saturn launch vehicle. The logic in favor of adopting Saturn system, a proven technology, to meet the SLI challenge is very strong. The F-1 engine was the largest and most powerful liquid rocket engine ever built, and had exceptional performance. This study reviews the failure modes of the F-1 engine and propellant system.

F-1 Rocket Engine Features

The Engine features include a bell-shaped thrust chamber with a 10:1 expansion ratio, with a detachable, conical nozzle extension, which increases the thrust chamber expansion ratio to 16:1. The thrust chamber is cooled regeneratively by fuel. Gas generator exhaust gases cool the nozzle extension. Liquid oxygen and RP-1 fuel are supplied to the thrust chamber by a single turbo pump powered by a gas generator. RP-1 fuel is also used as the turbo pump lubricant and as the working fluid for the engine fluid power system. There are provisions for supply and return of RP-1 fuel as the working fluid for a thrust vector control system. The engine contains a heat exchanger system to condition engine supplied liquid oxygen and externally supplied helium for stage propellant tank pressurization. An instrumentation system monitors engine performance and operation. External thermal insulation provides an allowable engine environment during operation (MSFC - MAN-507).

Functional Breakdown Of F-1 Engine (Saturn V- Ic Stage)

Function of F-1 Engine: The main function of the F-1 engine has been to provide initial thrust to lift the vehicle from the earth. This is the maximum thrust required for the rocket to overcome the gravitational pull of the earth. The S-IC stage provided the first boost of the Saturn V launch vehicle to an altitude of about 200,000 feet and provided acceleration to increase the vehicle inertial velocity to 9,029 feet per second. Engines similar to the F-1 will most likely be deployed at the first stage of launch vehicle in future. This study was focused to consider the F-1 engine as it was used at the first stage of Saturn-V vehicle.

Functional Breakdown: Eight functional subsystems of the F-1 engine identified were: fuel feed, oxidizer feed, igniter fuel, Gas generator, vehicle pressurization, hydraulic control, electrical, and

flight instrumentation (Rocketdyne, RAR 3181-1503). The Saturn V, S-IC stage propulsion had four outboard systems and one inboard system. Outboard and inboard systems were identical, except Gimbal device provisions, which were required on outboard subsystem only.

Figure1. Shows the subsystems with Saturn code numbers (RAR 3181-1503).

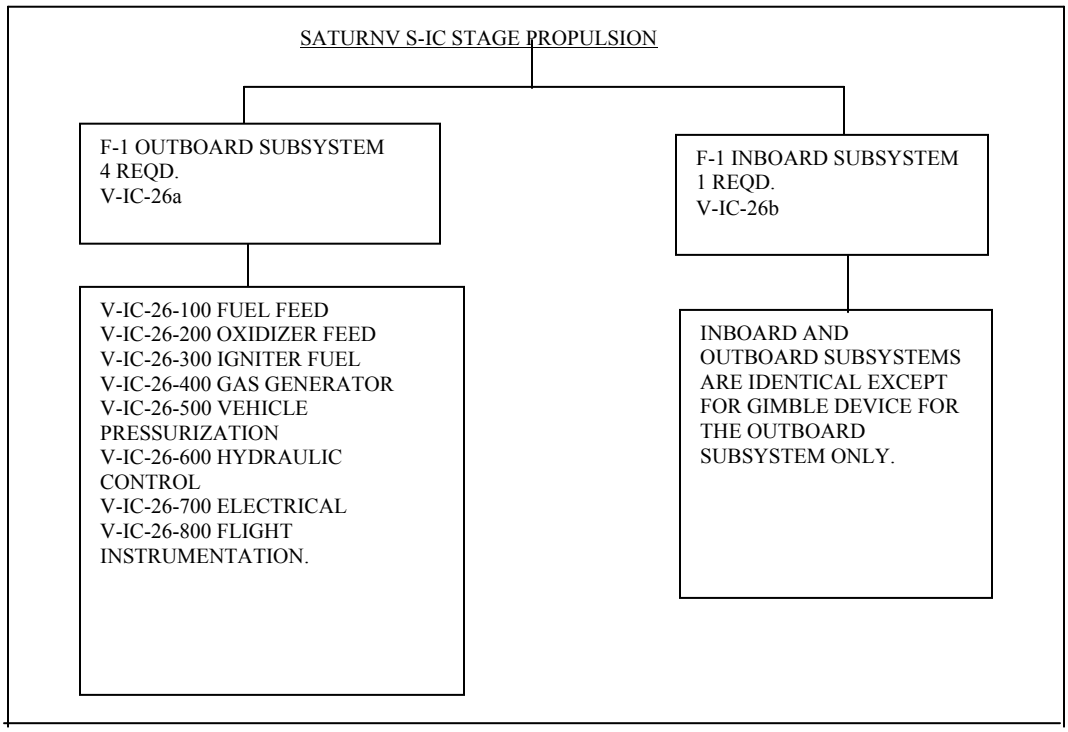

Figure 1. Functional Breakdown of the F-1 Subsystem

Failure Modes Of The F-1 Engine

These data have been adopted from the Rocketdyne report, RAR 3182-1503, for Saturn V, S-IC stage consisting of F-1.The detailed report has been provided to the Transportation Directorate as attachment No.3. Because of the restricted size, only the significant information has been included in this report.

Failure Modes of Fuel feed subsystem (V-IC-26-100): Twenty-five components of the fuel feed subsystem have been identified for failure modes analysis.

Ducting and Connections (26-101) and Tubing and Fittings (26-102): Failure during operation is leakage. The effects of failure are delay in launch. The critical effect is Fire hazard in propulsion section. The severity is dependent on the amount, location, and altitude. Main Fuel Valve (26-107) failure due to poppet seal leakage will displace inert pre-fill fluid by RP-1 and cause thrust chamber rough combustion. This may result in some engine damage and launch delay. Thrust Chamber (26-109a) failure will cause combustion instability and leakage of igniter fuel manifold or tubes between manifolds and injector orifices. This failure will cause severe engine damage

and propulsion loss. Thrust Chamber Drain Plug Leakage will also cause fire hazard and engine damage. Thrust Chamber external tube leakage can result in combustion instability and fire hazard. Thrust Chamber internal tube leakage above or below throat can result in loss of inert pre-fill and combustion instability leading to engine damage. Inert Fill Check Valve (26-110) may fail to open or close and will be detected and corrected. Redundancy will also be provided. This failure will cause launch delay.

Oxidizer Feed (V-IC-26-200): The Oxidizer feed subsystem has eight components.
Ducting, and Connections, (26-201): Minor leakage during operation will cause launch delay for correction. Possible loss due to freezing of hydraulic lines or operating valves may preclude start of the engine. The effects are Launch delay and/or launch abort. Main Oxidizer Valve Purge Check Valve (26-207): The failure may be either failure to open or to close the valve. Failure to open will cause delay for correction and failure to close will allow extra lox to flow to thrust Chamber and may result in engine damage by burning the turbine blades.

Igniter Fuel (V-IC-26-300): The subsystem consists of five components. Tubing and Fittings for Igniter Fuel (26-301): Failure may be leakage, causing launching delay or fire hazard. Hypergolic Cartridge (26-302b): may fail to rupture or lack of hypergolic flow to the Thrust Chamber. This will cause failure to start S-IC stage propulsion and Launch. Abort.

Gas Generator (V-IC-26-400): The subsystem consists of twelve components. Tubing and Fittings (bootstrap assemblies and coolant fittings – 26-401): Lox and Fuel leakage may cause Launch delay or abort. Leakage may also cause fire hazard in S-IC stage propulsion section. The G.G Control Valve leakage below ball seal may hard start and cause damage to G.G. assembly. Hot Gas Duct and Turbine Exhaust Manifold (26- 408): Hot gas leakage during operation will cause fire hazard in lower altitude and engine performance degradation.

Vehicle Pressurization (V-IC-26-500): There are four components of this subsystem. Tubing and Fittings (26-501): Oxidizer leakage may freeze the engine hydraulic control system; result in failure of S-IC stage, and cause launch abort. Heat Exchanger Lox (260502b): Leakage of liquid or gaseous oxygen may cause fire hazard in exhaust ducts, possible damage by burning through. Increased temperature and backpressure may affect turbine operation and stage propulsion.

Hydraulic Control (V-IC-26-600): The subsystem has seven components. Tubing & Fittings and Orifices (26-601): Failure during operation by leakage will cause fire hazard in lower altitude and cutoff may abnormally sequenced or not occur at all. Check Valves (26-603b): Failure may prevent flow of ground supplied hydraulic fuel to high pressure fuel duct and may cause lack of sufficient fuel pressure to 4-way valve start sequence. Engine damage may occur due to hard start and cutoff of S-IC stage propulsion subsystem.

Electrical (V-IC-26-700): This subsystem has three components. Start Solenoid (26-701): Fails to operate at prescribed time. Engine will not start. Expiration of the ignition stage limit timer will initiate safe cutoff. Actual loss may be launch abort.

Flight Instrumentation (V-IC-26-800): The subsystem has two components. Primary Flight Instrumentation (26-801): Fuel and hot gas leakage at pressure connections will cause fire hazard

at lower altitude. Lox leakage at pressure connections may cause freezing of hydraulic control lines and preclude engine start.

F-1 Significant Engine Failure Modes Per Expert Inputs

Interviews were arranged from July 1, to 26,2002 to collect data from the memory of work experience of the engineers who were associated with the Saturn projects. A total of twenty-four engineers were contacted and relevant data were obtained from eight engineers who were actively connected with the operation and testing of F-1 engines. These inputs were of qualitative nature and indicated the risk associated with significant failure modes experienced by them. The following functions and/or components were experienced as of significant risk. The outcome of the survey is given in Table 1 below:

Table 1. Risk Ranking from the Experts

Failure Modes	Gross	Pearson	Galuska	Tepool	Goetz	Hyde	Cornelius	Total
Combustion Instability	5	5	5	5	5	5	5	35
Fuel-Mix at injection Face	3	3	3	4	4	1	1	19
Propellant Leakage	2	3	3	2	1	2	2	15
Structural failures	4	2	2	2	2	3	3	18
Ignition at Start	4	2	2	2	4	3	3	20
Nozzle Tubes	3	2	2	2	3	2	2	16

Legend: The scale of risk ranking is from 1 to 5. 5 indicate the highest risk.

From the survey it is evident that the experts evaluated, combustion instability as the worst risk followed by fuel-mix at injector face, and ignition at start. The risks of Propellant leakage, Combustion chamber nozzle tube failure, and Structural failures represented the risk of the next level.

Conclusion

Though individual data sources vary in identifying failure modes, some common modes appear in some form in all data sources. These Failure Modes are: Combustion instability, Fuel-mix at injection face, Nozzle tubes, Propellant leakage, Hydraulic Valves, and Structural failures. The likelihood of leakage is high as there are so many joints in fuel and Oxidizer lines, but severity in

most cases is not likely to be serious. The mitigation steps are simple and enhanced design may be adequate to remove the risks. Hydraulic Valve and Structural failures can be removed by enhancing the design. Nozzle tube problems may be eliminated by replacing the tubes design by channel design as used in the RD180 engine (Russian design). The Channel-nozzle design takes significantly less time and cost to fabricate (D. Smith, NFFP Seminar July 2002). The operation of a rocket engine with channel nozzles is expected to take significantly less maintenance effort, and be trouble-free compared to that with tube-nozzles (Gautney). However, combustion instability appears to be a major problem, as the current knowledge in this phenomenon is still not adequate (K.Gross), and it will require substantial research and experimentation to comprehend the principles that control the phenomenon. The effect of combustion instability is very severe and may cause loss of engine. The problem with fuel-mix also requires research and trial to formulate the principles guiding the operational efficiency. Rocketdyne report No. R-8099 cited Turbo-machinery is a failure area and likely to be vulnerable to failure as the components are subjected to extreme temperature difference between compressor and turbine sides isolated by bearings.

Acknowledgement

I express my gratitude to Dr. Freeman, Dr. Karr, Dr. Bland and the administrators in the Marshall Space Flight Center for offering me the opportunity to participate in the 2002 NASA/ASEE Faculty Fellowship Program. I would like to express my gratitude to Mr. Denny Kross, Mr. Hugh Brady, Mr. Douglas L. Blackwell and Mr. Alberto Duarte for selecting me as the 2002 NASA Faculty Fellowship Program. I am grateful to all the engineers for spontaneously helping me whenever approached. My appreciation to Mr. Reggie Alexander and Mr. Justin, who helped me in developing the FMEA table. I am particularly grateful to Ms. Sandra Holland and Ms. Ann W. Pigg for their patience and cheerful help during the summer. This acknowledgement would not be complete without expressing my sincere appreciation to the librarians at the Redstone Scientific Information Center (RSIC).

References

1. Biggs, Bob, “F-1, the No-Frills Giant, ”Threshold Engineering Journal of Power Technology, No. 8. Pp. 20-31. Rockwell International, Los Angeles Basin Data Services Center, spring 1992.
2. Failure Effect Analysis Saturn V, S- IC Stage, F – 1 Engine Subsystem -PFRT configuration, – (RAR 3181-1503). Prepared by M. J. Rudzinski of Reliability Analysis Unit, Rocketdyne, and June 25, 1963.
3. NASA Technical Memorandum No. NASA TM – 82424. George C. Marshall Space Flight Center, Alabama. May 1981.
4. Saturn V Flight Manual – SA 509, National Aeronautics and Space Administration, August 15,1969.
5. Stages To Saturn, A Technological History of the Apollo/Saturn Launch Vehicles, Roger E. Bilstein, The NASA History Series. Scientific and Technological Information Branch, 1980. National Aeronautics and Space Administration, Washing, DC.

2002

NASA FACULTY FELLOWSHIP PROGRAM

MARSHALL SPACE FLIGHT CENTER

THE UNIVERSITY OF ALABAMA

NASA'S BIOREACTOR: GROWING CELLS IN A SIMULATED MICROGRAVITY ENVIRONMENT

Prepared By:	Denise Richardson
Academic Rank:	Adjunct Professor
Institution and Department:	Mississippi State University
	Department of Curriculum and Instruction
NASA/MSFC Directorate:	Science Directorate, SD13
MSFC Colleague:	Mr. Dan Woodard

Introduction

National Science Education Standards (NSES), Science for All Americans, the Secretary's Commission on Achieving Necessary Skills (SCANS) as well as the National Aeronautics and Space Administration (NASA) are all making an effort to promote scientific literacy in America. Unfortunately, major evaluation programs such as the National Assessment of Educational Progress (NAEP) and the Third International Mathematics and Science Study (TIMSS) have provided information that suggested our students are not able to compete with peers from comparable countries. Although results indicated that American students are recalling memorized, factual knowledge well enough, the real problem is the ability to *apply* what they know.

Concerned with these reports, the National Science Teacher's Association (NSTA) has developed a mission to support innovation and high quality in science teaching and learning for every student. NSTA recommends less emphasis on factual knowledge (memorization) and information and more *understanding* of the concepts. Science process skills are considered imperative to prepare America's students for the 21st century. The National Aeronautics and Space Administration (NASA) supports this mission and adds that NASA strives to help prepare and encourage the next generation of researchers and explorers.

One method that NASA supports educators and its mission is to publish educational briefs. NASA describes a brief as a publication that ranges from one-to-thirty pages. The focus is on mission discoveries and results. The brief provides curriculum to educators that supports their objectives and NASA's interest. Educational Briefs are specific to the grade level and course so that educators may have choices that fit their methods and students' level. Sometimes, the brief includes lessons and activities teachers may use. For example, NASA's Microgravity Division has designed a student bioreactor. Consequently, an Educational Brief is being written that focuses on how to build a student bioreactor and experiments that can be conducted in it. These experiments mimic the experiments done by NASA and other researchers in the real world of work.

Educational Brief for Student Bioreactor

The Educational Brief is officially titled, *NASA's Bioreactor: Growing Cells in a Simulated Microgravity Environment.* Targeted to secondary students, particularly 10-12, this brief explains why it is important to conduct experiments in microgravity conditions. It focuses on NASA's Cell Science program.

Cells have been cultured for years in petri dishes, producing two-dimensional, monolayered, flat cells. However, when cells grow in the body, they grow three-dimensionally into tissue that structures itself to perform a certain body function. This discrepancy limits research. Therefore, NASA invented the Bioreactor, also called the rotating wall vessel bioreactor. The Bioreactor was developed so experiments could be performed in a weightless environment similar to space. Cells are put in a growth medium and allowed to constantly rotate. This creates free-fall conditions.

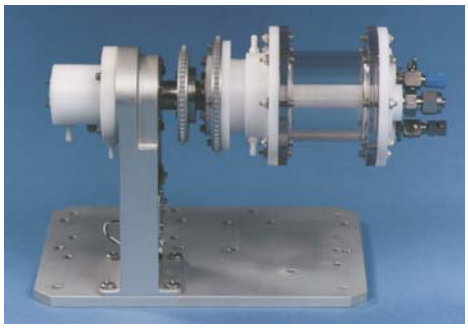

Figure 1: Bioreactor

The Student Bioreactor

The student bioreactor was designed by Dr. Greg Vogt, nationally recognized space educator and author of more than 50 children's books on space. Using a motor extracted from a toy rock tumbler, and common products that can be purchased at local stores, Dr. Bob Richmond, Mr. Dan Woodard, and Miss Denise Richardson built the bioreactor.

Figure 2: Toy Rock Tumbler

Figure 3: Toy Rock Tumbler Motor

Upon having built the bioreactor, the team proceeded to brainstorm about how to make the rock tumbler easier to build. The motor, shown above, proved to be more difficult than anticipated and many tools were needed to remove it safely. Thus, other motors sources are being considered for trial two of this project.

Despite the difficulty in building the bioreactor, research went forward. The third step, the experiment with Mung beans is described in the brief. The research team allowed the beans to rotate in the student bioreactor for five days. The speed was controlled by a variac. The control group stayed in a vial of water for the same amount of time. Upon the fifth day, the team removed the beans from both groups and weighed them. Also, the length and width were measured. Germination was observed and noted for both groups and data was recorded in a data table. Sample beans from both groups were then planted in potting soil in a plastic cup and placed in the Richardson's office where ample sunlight could reach the beans.

Seven milliliters of water was added every other day. As of two weeks after planting, the beans were not above the soil. The research is continuing.

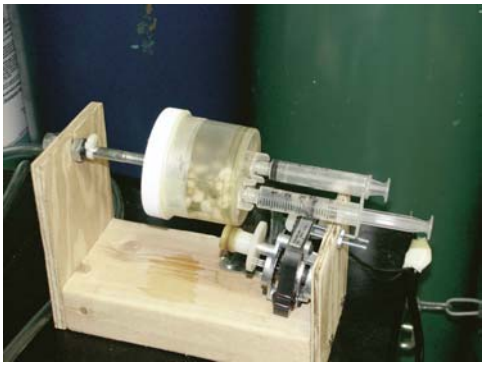

Figure 4: Bioreactor rotates Mung beans.

Results

The beans germinated in the vial of water showed significantly less growth than the beans in the bioreactor.

Future Plans for the Educational Brief

The research team plans to continue revising the Educational Brief until it is no longer in draft form and can be published on the NASA website. Further, the bioreactor is also in trial form and the team will continue to revise until it is as feasibly made as possible. Further activities for students that educators can use are also planned. For example, using the student bioreactor to grow green fluorescent protein and using chemiluminescence as well. This is similar to the experiments in cancer research that involve genes of fireflies and mice.

Resources

The researchers utilized a motor removed from a toy rock tumbler at a local hobby store. The cost was approximately $30. Additionally, two by four wood seven inches long and 1/4" plywood was purchased from a local home improvement store. At that same store, wood screws, a small caster with a fixed base, machine screws with nuts, lock nuts, hex bolts with matching nuts and washers were also purchased. Finally, tee nuts, marine glue, Nalgene plastic jar and Luerlock valves were purchased from an educational company and pharmacy respectfully. The variac used was available in Richmond's laboratory.

Conclusion

The student bioreactor is a good tool for educators to use to teach science process skills as well as work skills recommended by the SCANS competencies. The National Science Education standards stress inquiry learning and having students *do* science as opposed to just listening to science. The student bioreactor can easily be adapted into the curriculum by educators who wish to follow the various learning cycles.

Acknowledgements

The author would like to thank Infiniti Technology, in particular Ms. Twila Schneider. The author also wishes to thank Dr. Robert Richmond, of Marshall Space Flight Centers' Cell and Radiation Biology Laboratory, Dr. Vimla Chopra of the University of Galveston and Dr. Gregrory Vogt for the design of the experiment and student bioreactor respectfully. Special thanks goes to Mr. Dan Woodard for the opportunity to work with NASA's Educational Brief and for a really fun and useful summer job.

References

[1] The National Aeronautics and Space Administration (August 5, 2002). Marshall Space Flight Center (2002). Available online: http://inside.msfc.nasa.gov/index.html/

[2] National Center for Education Statistics (2002, August 5). National Assessment of Educational Progress: The Nation's Report Card (2001). Available online: http://nces.ed.gov/nationsreportcard/

[3] National Center for Education Statistics (2002, August 5). The third international math and science study (1995). Available online: [http://nces.ed.gov/timss/]

[4] National Science Teachers Association (2002). Available online: [http://www.nsta.org/]

[5] Science Teacher (1999). Glow-in-the-dark mice. Science Teacher, 66, (9), 12-13.

[6] Science for All Americans (2002). Available online: [http://www.project2061.org/tools/sfaa/default.htm]

[7] U. S. Department of Labor (2002 August 5). The Secretaries Commission on Achieving Necessary Skills. Available online: [http://wdr.doleta.gov/SCANS/whatwork/].

2002

NASA FACULTY FELLOWSHIP PROGRAM

MARSHALL SPACE FLIGHT CENTER
THE UNIVERSITY OF ALABAMA

MEMBRANE-BASED GAS TRAPS FOR AMMONIA, FREON-21, AND WATER SYSTEMS TO SIMPLIFY GROUND PROCESSING

Prepared By:	Stephen M.C. Ritchie
Academic Rank:	Assistant Professor
Institution and Department:	University of Alabama Department of Chemical Engineering
NASA/MSFC Directorate:	Flight Projects
MSFC Colleagues:	Jon Holladay Allen Shariett

Introduction

Gas traps are critical for the smooth operation of coolant loops because gas bubbles can cause loss of centrifugal pump prime, interference with sensor readings, inhibition of heat transfer, and blockage of passages to remote systems. Coolant loops are ubiquitous in space flight hardware, and thus there is a great need for this technology. Conventional gas traps will not function in micro-gravity due to the absence of buoyancy forces. Therefore, clever designs that make use of adhesion and momentum are required for adequate separation, preferable in a single pass.

The gas traps currently used in water coolant loops on the International Space Station are composed of membrane tube sets in a shell. Each tube set is composed of a hydrophilic membrane (used for water transport and capture of bubbles) and a hydrophobic membrane (used for venting of air bubbles). For the hydrophilic membrane, there are two critical pressures, the pressure drop and the bubble pressure. The pressure drop is the decrease in system pressure across the gas trap. The bubble pressure is the pressure required for air bubbles to pass across the water filled membrane. A significant difference between these pressures is needed to ensure complete capture of air bubbles in a single pass. Bubbles trapped by the device adsorb on the hydrophobic membrane in the interior of the hydrophilic membrane tube. After adsorption, the air is vented due to a pressure drop of approximately 1 atmosphere across the membrane. For water systems, the air is vented to the ambient (cabin). Because water vapor can also transport across the hydrophobic membrane, it is critical that a minimum surface area is used to avoid excessive water loss (would like to have a closed loop for the coolant).

The currently used gas traps only provide a difference in pressure drop and bubble pressure of 3-4 psid. This makes the gas traps susceptible to failure at high bubble loading and if gas venting is impaired. One mechanism for the latter is when particles adhere to the hydrophobic membrane, promoting formation of a water layer about it that can blind the membrane for gas transport (Figure 1). This mechanism is the most probable cause for observed failures with the existing design. The objective of this project was to devise a strategy for choosing new membrane materials (database development and procedure), redesign of the gas trap to mitigate blinding effects, and to develop a design that can be used in ammonia and Freon-21 coolant loops.

Material Selection Rational and Database

Material selection is critical for the success of these gas traps. For example, if the membrane is more hydrophilic then a smaller pore size membrane may be used with the same pressure drop. However, the corresponding bubble pressure will be much higher. The currently used hydrophilic membrane is composed of nylon-11. The permeability (pressure normalized flux) of this membrane is such that a 3.6 μm pore size is required to obtain a design pressure drop of 2 psid. This pore size results in a bubble pressure of 6-7 psid. Therefore, a small increase in pressure drop of only 4-5 psid will result in failure of the gas trap.

The new material chosen for the hydrophilic membrane is polyethersulfone (PES). Its Hansen solubility parameter is 25.3 $MPa^{1/2}$ (vs. ~ 22 $MPa^{1/2}$ for nylon-11). A higher solubility parameter is indicative of more polarity and hydrogen bonding capability, both of which are hydrophilic characteristics. For this membrane, a pore size of 0.22 □m will permit a pressure drop of 5 psid and a bubble pressure of 50 psid. Clearly this results in a much higher tolerance for pressure increases. Since the system pressure is 27 psia, 100% capture of bubbles using this material will be possible in a single pass gas trap.

Additional aspects of the materials database that lead to the choice of PES for the hydrophilic membrane include extensive empirical data from manufacturer compatibility tables, surface tension and contact angle data, predictive correlations for flux (Hagen-Poiseuille) and bubble pressure, and industrial availability. This last aspect is the most critical, since spares for the existing design have failed due to oxidation during storage. A reliable industrial supplier should have other customers so that a consistent product is available should replacements be needed in the future. The current membranes were custom-made and have not been reproducible.

Predictive Correlations for Design

A few simple correlations for design variables are given below. For each, these should be approached as guides only, with at least some pilot testing for variation in membrane properties. The first correlation is the Hagen-Poiseuille Equation. This relationship is effective for the membranes used here due to their open structure and relative large pores (convective flow under pressure gradient). In this equation,

$$J = \frac{\varepsilon d_p^2 \Delta P}{32 z \mu} \qquad (1)$$

J is the volumetric flux (liters/m^2 hr), □ is the porosity (unitless), d_p is the pore diameter (□m), □P is the pressure drop (psid), z is the membrane thickness (□m), and □ is the coolant viscosity (cP). Because J, □, z, and □ are fixed, this equation serves as an excellent predictive tool for the relationship between pore size and pressure drop. Another useful predictive equation is for the bubble pressure,

$$P = \frac{4k\cos\theta}{d}\sigma \qquad (2)$$

where P is the bubble pressure (psid), k is a shape factor (unitless), □ is the contact angle (degrees), d is the pore diameter (□m), and □ is the liquid surface tension (mN/m). Once again, the true value of this equation is the relationship between P and d, since the other parameters are constant. Finally, the pressure normalized flux, or permeability, is defined as,

$$Permeability = \frac{(volume)}{(time)(area)(pressure)} \qquad (3)$$

The volumetric flow rate is set and the permeability is a constant based on the membrane and the fluid. When the gas trap captures air bubbles, they will tend to collect at the end away from the entrance. If bubbles are not vented rapidly, they will coalesce and begin to fill out the volume inside the trap. Since this effectively decreases the hydrophilic membrane area for water transport, the pressure drop in the gas trap must increase. Therefore, it should be possible to predict what volume of air (not rapidly vented) will cause failure of the gas trap.

Recommended Materials and New Design

Since the current design is still working on the Space Station, it was determined that particles are not fatal to the performance of the hydrophobic membrane. Therefore, no material change was made on the hydrophobic membrane (Celguard, Inc.). The hydrophilic membrane will be composed of PES instead of nylon-11. PES tubular or capillary membranes are widely available in industry. Some potential sources are Membrana, Hydranautics, and PCI Membrane Systems among others. In addition, a smaller pore size material may be used with comparable pressure drop, but much greater bubble pressure.

Because air bubbles collect at one end of the gas trap, the new design will incorporate a bundle of five (5) hydrophobic membranes for gas venting. To prevent excessive water loss, 80% of the fiber length (near the entrance) will be coated with an impermeable layer. This will permit the same previous design area for gas venting, but all of the area will be located where the bubbles collect. Previous experience shows that gravity is sufficient to drain water from the surface of a particle fouled hydrophobic membrane, and thus it should be a reasonable assumption that a coalesced air bubble will have the same effect, and that all of this area will be available for gas venting. A diagram of the proposed design is given in Figure 2.

Designs for Ammonia and Freon-21

Ammonia and Freon-21 have vapor pressures 1000 and 100 times greater than water, respectively. Therefore, any continuous venting system will probably result in an unacceptable loss of coolant. Therefore, besides the exterior tube membrane made of perfluoroethylene (PTFE), the interior venting membranes will be replaced by a solenoid valve and accumulator at the end of the gas trap away from the fluid entrance. Since captured gas bubbles cause an increase in pressure drop, this can be monitored to trigger the solenoid valve after a significant amount of air is captured in the gas trap. Use of an evacuated accumulator will provide sufficient driving force to displace the air from the trap before closure of the valve.

Conclusions and Future Directions

A sound diagnosis of previous gas traps failures has resulted in a rational approach for future material selection. The new design should permit minimal resistance to coolant flow with 100% capture of NCG. Gas venting will be performed continuously for water systems and periodically for ammonia and Freon-21 systems due to differences in

vapor pressures. A Center Director's Discretionary Fund proposal has been put forth as a result of the work herein, with collaboration between various groups in the Flight Projects Directorate and the Engineering Directorate.

Acknowledgements

The author would like to thank the entire MPLM team and FD24 for making this summer so intellectually stimulating and for making him feel welcome and involved in the group. Thanks go to Randy McClendon/FD24 and Lanny Upton/FD23 for their support and encouragement. Thanks to Monsi Roman, Paul Wieland, and Don Holder of FD21, Mike Holt from ED25, Darryl Edwards of Qualis Corp., and Dallas Clark for valuable discussions and input. Acknowledgements to the NASA Summer Faculty Fellowship Program at MSFC for supporting this work. Finally, a special thank you to Jon Holladay/FD23 and Allen Shariett/FD24 for their guidance as colleagues on this project.

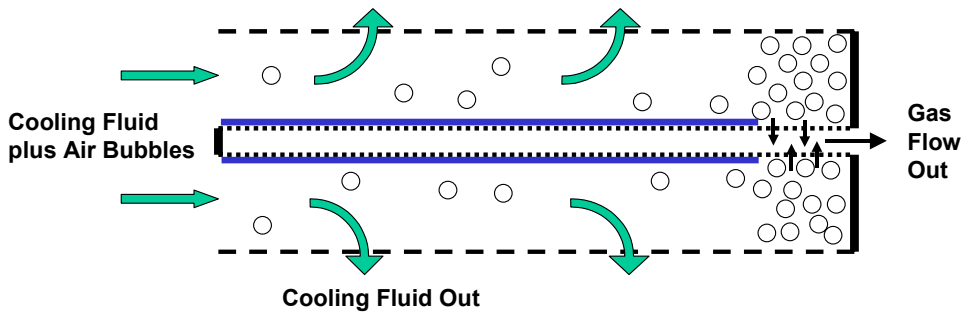

Figure 1: Failure mechanism for current water coolant loop gas trap.

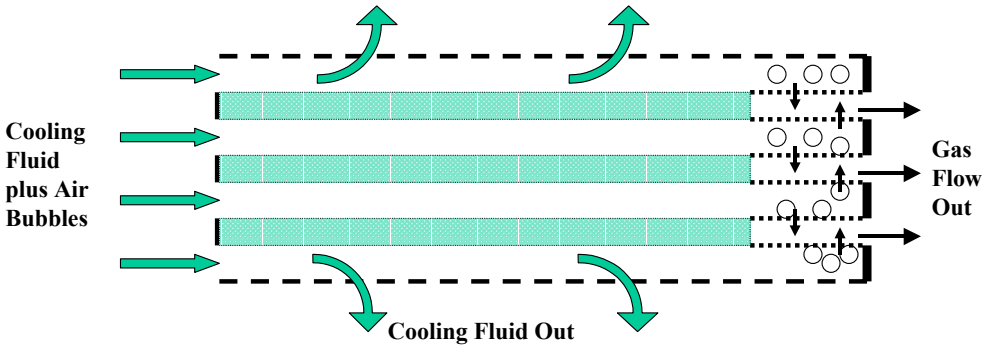

Figure 2: Proposed design for water coolant loop gas trap.

2002

NASA/ASEE SUMMER FACULTY FELLOWSHIP PROGRAM

MARSHALL SPACE FLIGHT CENTER
THE UNIVERSITY OF ALABAMA

MEASURING ORGANIZATIONAL COMMUNICATION HEALTH

Prepared by:	Edward W. Rogers
Academic Rank:	Assistant Professor
Institution and Department:	The University of Alabama in Huntsville Department of Management and Marketing
NASA/Directorate:	Transportation Directorate (TD-60)
MSFC Colleague:	Jim Turner

Organizational Communication

Communication in organizations can be looked at as a solution to the problem posed by inherent tensions between the specialization tendencies toward efficiency and integration needs of production. As organizations attempt to produce in a more efficient manner than what the open labor market could produce, they inevitably face organizing costs. Structuring communication is one of those costs that is necessary to take advantage of the efficiencies gained by specialization.

The introduction of electronic means of communication has offered organizations ways to greatly improve the efficiency of internal communications and potentially generate added surplus value by reducing overall organizing costs. However, the research has not always shown that more efficient transactions of communication necessarily improve overall communication. Sarbaugh-Thompson and Feldman (1998) actually report a decline in overall communication with an increased use of electronic mail. Other approaches look at organizational pathologies as a study in how organizations fail because of communication dysfunctionalities. Tompkins (1992) and Vaughan (1996) both use this sociological approach to analyze why things don't work the way they should.

> We cooperate, communicate openly and share ideas with each other for the common good.
>
> ***Marshall Values***, 2002

It is important to consider the approach to studying communications within knowledge organizations because the nature of the work and the type of coordination is different than traditional organizations. The cooperation needed for knowledge work is much more intimate than that required for physical production. Building on each other's ideas requires a deeper level of communication than building on each other's assembly line parts. This makes communications in knowledge organization both much more salient to the production process and more difficult to accurately identify points of failure or critical success factors. A robust communication system is one that delivers both the technical ***content*** and ***credibility*** of that content in the same message. This view of communication is useful I believe because it shifts the concept of efficiency from a pure transaction speed to include content and usability of the message. For example, a usability criterion of knowledge may explain in part the preference for face-to-face exchanges at Marshall that most of the interviewees expressed.

> "Cooperation cannot be commanded." "No machine, no method, no management technique can substitute for a warm personal touch in dealing with human beings."
>
> *Werner Von Braun, 1962*

Communication research in organizations has struggled to delineate clear constructs for bridging the conceptual gap between action and structure. What actually occurs in the form of communication and what structures are in place are somehow linked with the performance of the organization. The nature, directionality and strength of these linkages has been the subject of much debate within the communications research field (Conrad & Haynes, 2000). The most widely used measure is that of communication satisfaction. This construct was incorporated into this survey instrument specifically to connect the findings here to the broader field of communications study and to establish a baseline of communications performance within the population of NASA employees.

Studying Communications in TD-60

Over the course of twelve weeks, I had the opportunity to interview over 35 people in and connected with TD-60. This list included department managers, group leads, team leads, task engineers, and internal customers of TD-60 in other Marshall organization lines. The interviews were open-ended without a lot of specific probing. The goal was to gather a fairly unbiased view of communications rather than focus on a particular problem. Most of the conversations centered on how communication works, what has changed recently and sometimes what doesn't work. The material gathered from the interviews guided the formation of a survey instrument for use in assessing the communication health of the organization. The survey will be administered at the end of the summer fellowship so the data from it is not available for this report.

Interview Data on Communications in TD-60

Much about communications at Marshall seem to work extremely well. People were amazed at how much gets done, with so much information and so many competing schedules. However, the interview data suggest some general communications issues in TD-60. Often communication is viewed as a activity which takes time from other important work. Meetings are an especially maligned target in this regard. The second biggest communication consumer is email. The response to both of these can be simple to ignore them. For example in a worst case possibility you may have a meeting led by a representative of the boss attended by representatives of the team leaders. Little of substance may take place as a result. The use of email can be particularly intriguing when people use automatic lists to mass invite and inform people some of whom use automatic filters to delete those emails. This situation can result in an apparent increase in communication (more messages sent) but actual less communication (eliminated face-to-face and deleted emails). This presents a risk of decreasing system stability. Expected outcomes might be more crisis communication or more back-door channels for safety or redundancy in channels since the formal channels are untrustworthy (people don't come to meetings or read their email).

Another observation from the interview data is the separation of vertical and horizontal communication. Two problems emerge regarding this separation. First, channels that mix uses are not viewed as effective as single focus channels. Second, channels that are primarily vertical are designed for managerial efficiency and so are often inefficient for the providers (engineers and task leads) of that information. Since communication within Marshall is primarily a voluntary activity (the sender has to decide which pieces of information to provide) there must be clear conceptual transparency for the reason and efficacy of investing time and effort in communication. Based on these comments, items to measure communication satisfaction, conceptual transparency and fairness of the employment game were included in the communication health survey instrument. These are all communication health issues that the survey is intended to address.

Customer Perceptions of TD-60

To understand customer perceptions of communications with TD-60 I interviewed several internal (NASA) customers of TD-60. One perspective expressed was the need for TD-60 to appreciate program schedule pressures when performing for these organizations. The internal communication issue seems to be one of effectively and consistently setting priorities for the workloads of people at the task level. Group Leads seem to use their own methods and personalities to accomplish this. Considering this is a critical communication point for achieving customer satisfaction, it should perhaps receive more formal focus, training and accountability.

Designing the Study for TD-60

The Marshall Value of cooperation, open communication and sharing of ideas was taken as a desirable outcome highly associated with success. These behavioral outcomes were adopted as the dependent variable for this study and embedded in the term 'organizational health.' The focus of my summer task then became to identify the organizational antecedents of these behaviors. What makes people cooperate, communicate openly and share ideas freely? If significant antecedents are identified then at least communication health could be predicted and hopefully improved by appropriate and meaningful management intervention. This study, like many others, was prompted in part by the desire to withhold recommendations for intervention based on qualitative data until some quantitative data could demonstrate that intended interventions had an acceptable likelihood of actually increasing the communication health of the organization.

The Communication Health Survey

The study proposes capturing variance across three independent variable constructs that are theoretically linked to the dependent variable. Other measures are included in the survey for correlation with existing studies in the field. A minimal set of demographics is collected as control variables not expected to influence the DV.

Open-Sharing Environment

The dependent variable for this study is "Open Sharing Environment" or Communication Health. This measure is derived from the Marshall Core Values under Teamwork which states that: "We cooperate, communicate openly and share ideas with each other for the common good." Achievement of that value indicates the organization is 'healthy' and has an 'open sharing environment.

The DV is measured by a number of items designed to capture whether that is in fact the environment at Marshall. Sample item: "We value cooperation and sharing at MSFC." This is an untested scale that will have to be validated as part of this project.

Organizational Depth Perception

The construct captures the perception by employees of whether they can see the big picture about their organization. This is deemed important for communications because people will be more apt to communicate (make the effort) if they perceive a positive consequence as a result of their effort i.e. they see that it matters. Two aspects of organizational depth perception are measured here: the overall grasp of the conceptual view of the organization and the confidence that they are hearing everything of importance from the top. This leads me to suggest hypothesis one as:

H_1: If people have a good grasp of what the organization is all about and confidence in the information from the top they will be more likely to openly share and communicate with each other.

Communication Satisfaction

Communication satisfaction is a well established construct best represented by the work of Downs & Hazen (1977) and later work by Gregson (1991) who used a modified version of the Downs & Hazen instrument. Gregson's analysis revealed three factors of communication satisfaction which he termed 1) firmwide, 2) dyadic and 3) feedback. I have adopted these same

three for use in the instrument for Marshall because all three were shown to be positively related to job satisfaction. The results of Gregson's study suggest that factors of communication satisfaction might be related to job satisfaction and turnover. The implication is that monitoring (and improving) communication satisfaction could have a positive (reduction) effect on turnover. These observations lead to hypothesis two as follows:

H_2: If people are satisfied with the communication systems and processes in place they will be more likely to openly share and communicate with each other.

Perceptions of the Employment Game

I coupled the insights of game theory and how interactive games are played with the economic structure of the firm to model what I have termed the 'employment game.' Game theory informs us that people play games according to how they perceive them. In my recent work, I proposed four measures based on game theory for determining how people perceive the employment game (Rogers, 2000). Together these four measures make up what I call the employment game score. Based on this previous work I suggest the following third hypothesis as:

H_3: If people perceive the organizational employment game to be fair and winnable they will be more likely to openly share and communicate with each other.

The survey is intentionally designed to be organizationally neutral so it may be used with minimal changes by other organizations. This will allow testing and validation of the measures outside of Marshall as well as future comparisons on communication health and the hypothesized contributing independent variables. The intent is to administer this survey in TD-60 first and to validate the measures. Then it could be used for the entire Space Transportation Directorate and possible adapted for use across the Center or even the Agency by the summer of 2003.

References

Conrad, C. & Haynes, J. (2000). Development of key constructs. In *The New Handbook of Organizational Communication,* (Eds.) Jablin, F. & Putnam, L., Thousand Oaks: SAGE.

Downs, C. W. & Hazen, M.D. (1977). A factor analytic study of communication satisfaction. *The Journal of Business Communication,* 14(3): 63-73.

Gregson, T. (1991). The separate constructs of communication satisfaction and job satisfaction. *Educational & Psychological Measurement,* 51(1): 39-48.

Rogers, E. W. (2000). *Cooperative knowledge behavior in high tech organizations*. Unpublished doctoral dissertation, Ithaca: Cornell University.

Sarbaugh-Thompson, M. & Feldman, M. (1998). Electronic mail and organizational communication: Does saying "Hi" really matter? *Organizational Science,* 9(6): 685-698.

Tompkins, P. (1992). *Organizational Communication Imperatives: Lessons of the Space Program*, Los Angeles: Roxbury Publishing.

Vaughan, D. (1996). *The Challenger Launch Decision,* Chicago: University of Chicago Press.

Von Braun, W. (1962). Unpublished text of speech given at The Sixteenth National Conference on the Management of Research, French Lick, Indiana.

2002

NASA FACULTY FELLOWSHIP PROGRAM

MARSHALL SPACE FLIGHT CENTER

THE UNIVERSITY OF ALABAMA

MANUFACTURING DEVELOPMENT FOR 100Kw THERMONUCLEAR SIMULATOR

REPORT NOT AVAILABLE

Prepared By:	Russell L. Rosmait
Academic Rank:	Professor
Institution and Department:	Pittsburg State University Department of Engineering Technology
NASA/MSFC Directorate:	Engineering Directorate ED33
MSFC Colleague:	Dr. Wayne R. Gamwell

2002

NASA FACULTY FELLOWSHIP PROGRAM

MARSHALL SPACE FLIGHT CENTER
THE UNVERSITY OF ALABAMA

THERMO-MECHANICAL PROCESSING IN FRICTION STIR WELDS

Prepared by:	Judy Schneider, Ph.D.
Academic Rank:	Assistant Professor
Institution and Department:	Mississippi State University Department of Mechanical Engineering
NASA/MSFC Directorate:	Engineering Materials, Processes and Manufacturing (ED 30)
MSFC Colleague:	Arthur C. Nunes, Jr., Ph.D.

Abstract

Friction stir welding is a solid-phase joining, or welding process that was invented in 1991 at The Welding Institute (TWI) [1]. The process is potentially capable of joining a wide variety of aluminum alloys that are traditionally difficult to fusion weld. The friction stir welding (FSW) process produces welds by moving a non-consumable rotating pin tool along a seam between work pieces that are firmly clamped to an anvil. At the start of the process, the rotating pin is plunged into the material to a pre-determined load. The required heat is produced by a combination of frictional and deformation heating. The shape of the tool shoulder and supporting anvil promotes a high hydrostatic pressure along the joint line as the tool shears and literally stirs the metal together. To produce a defect free weld, process variables (RPM, transverse speed, and downward force) and tool pin design must be chosen carefully. An accurate model of the material flow during the process is necessary to guide process variable selection.

At MSFC a plastic slip line model [2] of the process has been synthesized based on macroscopic images of the resulting weld material. Although this model appears to have captured the main features of the process, material specific interactions are not understood. The objective of the present research was to develop a basic understanding of the evolution of the microstructure to be able to relate it to the deformation process variables of strain, strain rate, and temperature.

Background

A striking feature of the FSW microstructure is a central nugget, shown in Figure 1. The macroscopic features are typically described as an outer heat affected zone (HAZ), an inner thermo-mechanically affected zone (TMAZ), and a central nugget of fine, equiaxed grains. Under a light microscope, this central nugget displays layers of varying thickness, like onion rings [3]. The variations and spiral development are reported to vary with the ratio of weld velocity (V) to pin rotation [3], and can also be observed in the transverse section of the weld shown in Figure 2.

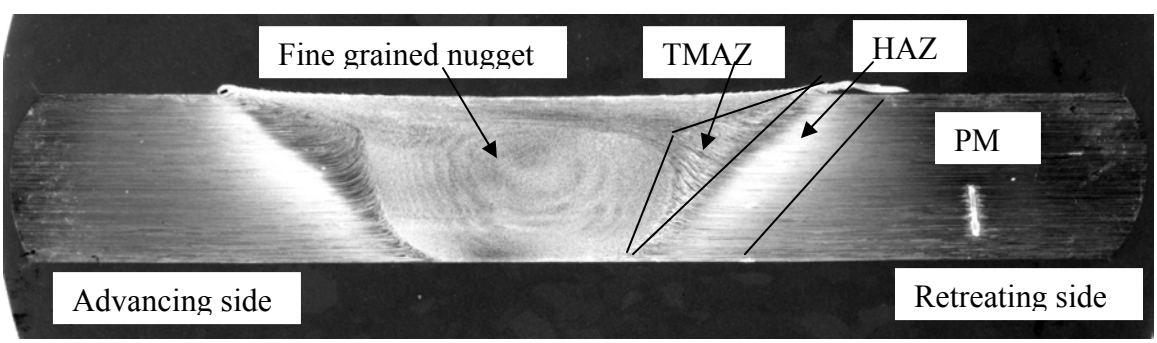

Fig. 1. Optical image of FSW cross-section.

Microscopically the grain morphology shows a transition from the elongated, rolled grains of the parent material (PM) (80 to 100 μm dia. in plane view), to an equiaxed grain of 0.5-10 μm within the nugget. Figure 3 shows this delineation between the TMAZ nugget to be quite sharp. The deformation of the base metal in the TMAZ manifests itself as bending of the grains in the plane of the metallographic section.

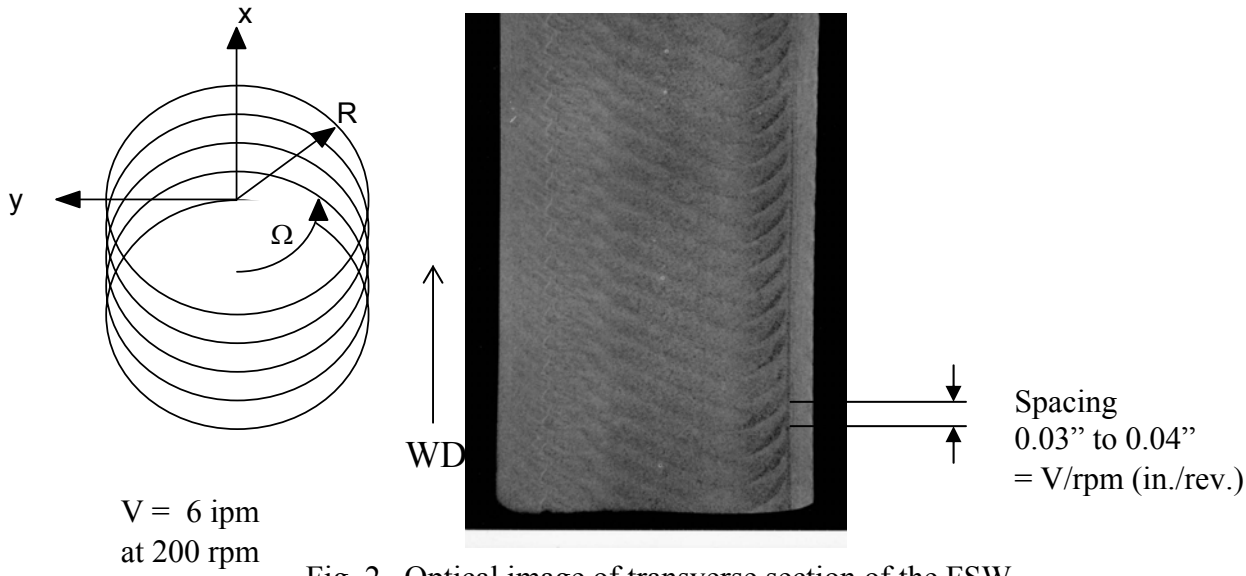

Fig. 2. Optical image of transverse section of the FSW.

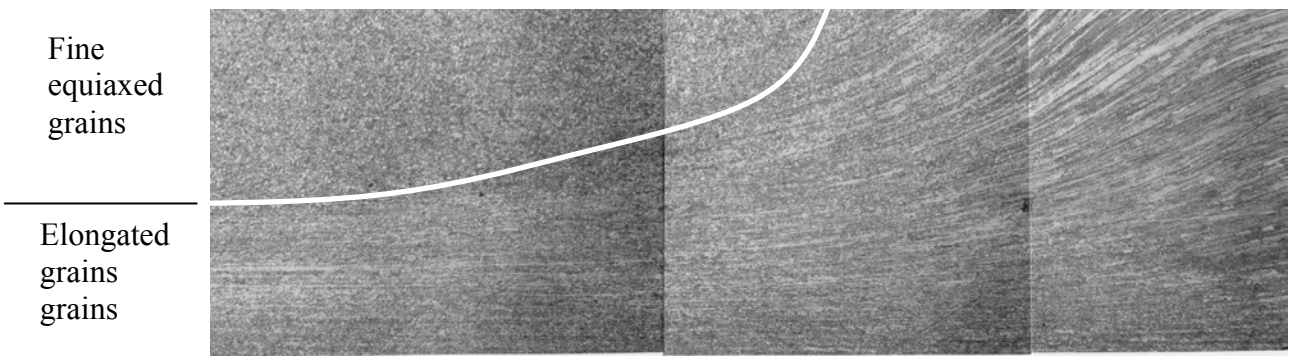

Fig. 3. Optical image of transition from elongated grains (right) into the fine grained, retreating side of the nugget (shoulder side on bottom).

Several FSW flow visualization studies have been reported in the literature using either dissimilar materials or tracer techniques. Li et. al., [4, 5] described patterns observed on metallographic cross sections in FWS made between dissimilar Al alloys and between Al alloys and Cu. Differential etching of the dissimilar materials revealed material flow patterns, described as a chaotic-dynamic mixing.

Colligan [6] studied the material flow using embedded steel spheres placed along the weld centerline prior to welding. This approach allowed single points to be followed in the weld process as interpreted by post weld xray inspection. Colligan reported that material is stirred only in the upper portion of the weld and that in the rest of the weld materials is simply extruded around the pin. However, a concern has been whether the 0.015" dia. steel tracer spheres used in his study, would flow in the same way as the Al alloy during welding. Also, no information on shear zone behavior can be obtained.

Seidel and Reynolds [7] utilized a marker insertion technique to investigate the shearing around the tool pin. The flow path was reconstructed using a serial sectioning technique to produce three-dimensional plots of the deformed marker. The flow visualization studies all indicate the flow path or deformation process in a FSW is complicated and may even consist of several paths. It is possible that the confinement of the shoulder and anvil set up flow at the plate surfaces different from the flow established by the weld pin geometry.

To explain the results of the flow visualization studies, a wiping model of the material flow in FWS has been proposed that is similar to an orthogonal metal cutting model [2]. In this

model a rapidly rotating cylinder is super positioned within a slowly rotating ring vortex, and a uniform translation flow generates a 'wiping' flow that appears to model the plastic flow around the pin-tool. This model predicts almost instantaneous strain increments. A marker experiment was conducted to investigate the magnitude of the shear zone. Tungsten was selected as a marker due to its high melting temperature, and brittle mechanical behavior. Temperature measurements in Al alloys [8] along with analytical predictions indicate a temperature of 450° C in the welding of Al alloys. This corresponds to 0.2 times the absolute melting temperature of tungsten, at which no appreciate change in mechanical properties is expected. Reported shear strength of drawn tungsten wire is 58 ksi [9].

Experimental procedure

The material used in this study was an Al-Li-Cu alloy. The plate had a thickness of 8.2 mm (0.323") and was welded along the plate rolling direction. A thin 0.0025' diameter wire was placed transversely along the center of the plates. The plates were then tack welded together prior to clamping in the vertical welding tool (VWT). An initial pass was made to join the plates at the surface prior to the full penetration FSW. Tungsten wire placement was verified prior to the start of the full penetration FSW process. After welding the plates were x-ray inspected in the transverse (Figure 5) and normal (Figure 6) directions to the FSW. Serial sectioning was used to verify wire segment spacing. Keller's regent was used to reveal the grain structure in metallographic samples. The wire marker tends to agree with Colligan's research [6], but illustrates the severe shearing zone the material enters during FSW.

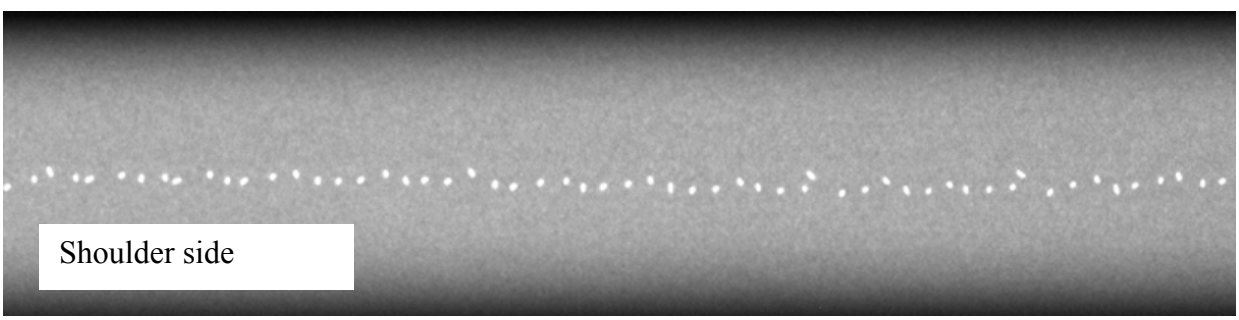

Fig. 5. Transverse x-ray of FSW

Fig. 6. Normal x-ray of FSW. Tungsten wire segments are 0.025" in length and are spaced 0.020 to 0.028" apart.

Discussion

The material being welded is sheared under a compressive load to large strains associated with plastic flow. The shear zone is confined, or hydrostatically loaded, by the surrounding parent material, the anvil and the tool shoulder. Conservation of volume in this process means that there will be local changes in displacement and velocity, which result in gradients of strain and strain rate. The effects of pressure can alter the rate controlling mechanisms for deformation since at elevated temperatures; diffusion will be slowed due to limited vacancies, making the glide of dislocations more favorable.

The range of distinct grain morphology and sizes observed in the FSW zones is an indication of the strain, strain rate, and temperature conditions the material has undergone in the TMAZ. The parent material is characterized by pancake shaped grains, typical of that resulting from cold rolling. The initial grains are in the range of 60 to 80 microns in diameter and 0.5 to 10 microns in thickness. In the weld nugget fine, equiaxed, high grain boundary angles of 15-20° are observed [10-13].

Most commonly, the mechanism of the grain size variations is reported to be recrystallization with subsequent grain growth. One researcher reported the refined grain size to be stable and unaffected by subsequent heat treatments up to 65 h at 150 °C under static conditions [12]. Another researcher compared the grain boundary orientation of the nugget before and after a post weld heat treatment at 500 C for 10 s and concluded that the orientation in the nugget reflected that of a dynamically, not statically, recrystallized grain boundary angle [13]. Murr [14] has reported seeing spiral dislocations present in TEM studies, indicative of dislocation climb, and suggestive of a continuous recrystallization process.

The constant hardness profile reported for pure Al alloy (1100) [14] can be explained by self-compensating strengthening mechanisms and used to determine a dislocation density profile corresponding to the grain morphology. Plates of Al alloys are usually cold rolled which strengthens the plate by increasing dislocation density (ρ) or strain hardening (eqn. 1). As the grains undergo recrystallization, the annihilation of strain induced dislocations result in the formation of smaller, equiaxed grains. An increase in strengthening is noted as the grain size (d) decreases (eqn. 2). The material threshold stress is given as σ_o, flow stress is given as σ_{ys} and k values are the material constants.

$$\sigma_{ys} = \sigma_o + k_1 (\rho^{0.5}) \qquad \text{eqn. 1}$$

$$\sigma_{ys} = \sigma_o + k_2 / (d^{0.5}) \qquad \text{eqn. 2}$$

Using material constants from the literature [15], a constant hardness can be maintained assuming a dislocation density of 10^{12} in the 100 μm parent material to a dislocation density of 10^8 in the recrystallized grains of 10 nm. A dislocation density of 10^{12} was selected as representative of a strained microstructure, while 10^8 was selected as representative of a unstrained microstructure.

Conclusions

Very fine, recrystallized grains are observed in the weld nugget toward the anvil side of the weld, on the retreating side as shown in Figure 7. This suggests that TMAZ processing associated with the FSW results in an appropriate level of strain for the temperature profile that results in a high level of grain refinement. The effects of the heat input may subsequently cause the grains to grow. Conversely, this distribution of fine grains may suggest that different flow paths are subjected to different strain accumulations which may affect the final recrystallized

grain size under the imposed temperature. Data shown in Figure 8 illustrate the tradeoffs in total strain vs recrystallization temperatures [16].

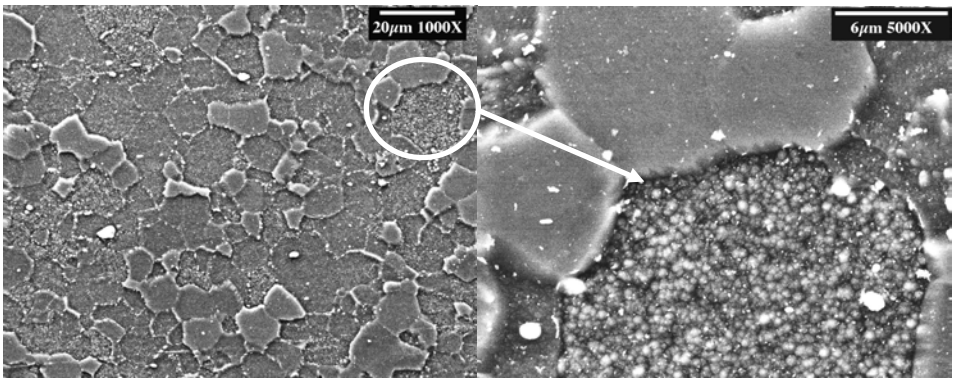

(a) (b)

Fig. 7. a) SEM-SE image of recrystallized region of FWS,
b) Closeup image of recrystallized region in Figure 7a.

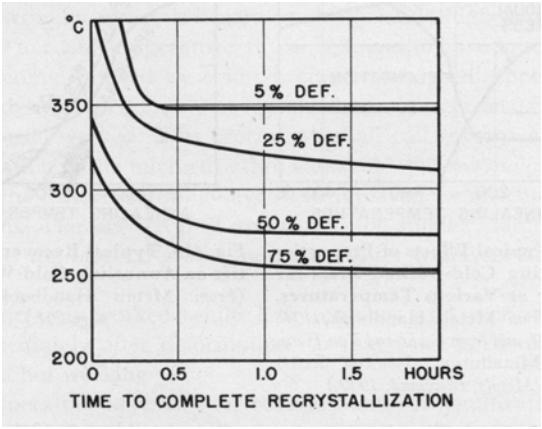

Fig. 8. Effect of strain on recrystallization temperature [16].

References

1 Thomas, W.M., et. al., 1991. *Friction Stir Butt Welding*, U.S. Patent No. 5,460,317.
2 Nunes, A.C., Jr., "Wiping Metal Transfer in Friction Stir Welding", TMS Annual Meeting, New Orleans, LA, 2001.
3 Krishnan, K.N., Mat. Sci. & Engr. A, 327 (2002), 246-251.
4 Li, Y., Murr, L.E., McClure, J.C., Scripta Mater., Vol. 40, No. 9, (1999) 1041-1046.
5 Li, Y., Murr, L.E., McClure, J.C., Mat. Sci. & Engr., A271 (1999) 213-223.
6 Colligan, K., Welding Research (1999) 229s-237s.
7 Seidel, T.U., Reynolds, A.P., Met. & Mat. Trans. A, 32A (2001), p. 2879-2884.
8 Tang, W., Guo X., McClure, J.C., Murr, L.E., J. Mat. Proc. & Mfgt. Sci., (1998), p. 163-172.
9 Materials Information Website, http:\\www.matweb.com.
10 Mishra, R.S., Mahoney, M.W., McFadden, S.X., Mara, N.A., Mukherjee, A.K., Script mater., 42 (2000) 13-168.
11 Murr, L.E., Liu, G., McClure, J.C., J. Mat. Sci. Letters, 16 (1997) 1801-1803.
12 Jata, K.V., Semiatin, S.LScripta mater., 43, (2000) 743-740.
13 Sato, Y.S., Kokawa, H., Ikeda, K., Enomoto, M., Jogan, S., Hashimoto, T., Met. & Mat. Trans. A., 32A, (2001) 941-948.
14 Murr, L.E., Li, G., McClure, J.C., J. Mat. Sc. Letters, 16 (1997) p. 1801-1803.
15 Barlow, et. al., Act. metal., 2002.
16 Hultgren, R., Fundamentals of Physical Metallurgy, 1952, p. 158.

2002

NASA FACULTY FELLOWSHIP PROGRAM

MARSHALL SPACE FLIGHT CENTER
THE UNIVERSITY OF ALABAMA

POTENTIAL OF SINTERED REGOLITH MATERIALS FOR DERIVATION OF *IN-SITU* RESOURCE UTILIZATION

Prepared By:	Lois G. Schwarz
Academic Rank:	Assistant Professor
Institution and Department:	University of Alabama in Huntsville Department of Civil and Environmental Engineering
NASA/MSFC Directorate:	SD46 - Biological and Physical Research
MSFC Colleague:	Dr. Sandor Lehoczky

Introduction

Practical interplanetary exploration leading to sustained human habitation on Mars will need to rely on *in-situ* resource utilization (ISRU). Material processing and fabrication using indigenous resources to produce metal alloys and ceramics would be economically beneficial rather than transporting necessary materials from Earth. ISRU is constrained, however, by resource availability, mining, and processing methods. Desirable materials will be dependent on manufacturing and construction processes, as well as, performance in uniquely hostile environments. A specifically developed Martian soil simulant, JSC Mars-1, that is spectrally similar to the ubiquitous Martian regolith, is used in research since only a limited amount of Martian soil has been retrieved from the planet [1].

Sintering involves shrinkage of a body as particles pull closer together and porosity decreases. Dominant in the sintering process is atomic motion, governed by diffusion mechanics, occurring at a rate that increases as temperature increases as described by the Arrhenius equation [2]. Distinct stages of densification are defined by solid state atomic diffusion, the formation of a liquid (oftentimes glassy) phase between the particles, and by reactions at the grain boundaries. The transport of thermal energy by sintering can be categorized into the mechanisms of conduction, convection, and radiation; the latter is usually dominant from the furnace heating elements [2]. The most influential parameter in sintering is temperature, other variables include time held at peak temperature or soak period, rates of heating and cooling, atmosphere type, particle surface area, compaction or density, and additives to increase particle bonding, softening, and flexibility.

Objectives

Investigate the potential of using a sintering process method on JSC Mars-1 to (a) isolate raw metals and/or compounds and (b) develop a material suitable for structural products that may manifest enhanced engineering properties. These materials could be used for construction purposes of storage facilities, habitat facilities, launch platforms, shielding, etc.

Sample Preparation and Sintering Process

Soil samples of 1.500 g (± 0.005 g) were heated in crucibles made of boron nitride or alumina with caps having a small weep hole to allow any volatiles generated during heating to escape. Several samples were heated in an air atmosphere; most samples underwent argon replacement whereby the air was purged. Replacing air with an inert gas would reduce potential oxidation, however, each constituent of the soil has a different sensitivity to the sintering atmosphere [2].

The sintering program involved initially heating the sample to about 400° C and holding this temperature for 30 minutes. Then the temperature was increased to a selected maximum ranging from 860° to 1425° C, maintained for 30 minutes, and subsequently cooled by incrementally reducing the temperature (each stage was nominally 300° to 400° C) and maintained for 10 minutes. This range of peak temperature was selected based on melting points, Curie temperatures, and phase transition temperatures of the oxides and elements present in the soil.

Differential thermal analysis (DTA) was planned to trace and map the temperatures at which phase transitions of the different constituents would occur and provide insight into nucleation and growth processes that can exhibit temperature dependence [3], however, significant

electrical noise was generated by the furnace and masked distinguishable variations in the thermocouple response of the different oxide components. This difficulty will need to be addressed in future work.

Results

Most of the experiments were conducted in argon atmosphere and an alumina crucible. It was found that as the peak temperature increased, sintering increased (based on observed particle bonding) and color darkened accompanied by phase transformations, metallic sparkle, and metalloid deposition. Depending on sintering temperature, different materials formed from JSC Mars-1 depending on the melting point of each oxide and chemical reactions that may occur between the reactants and products. Samples heated to 1160° C evidenced spherical deposits within the semi-bonded granular matrix. Soil heated to 1225° C evidenced significant shrinkage and a glassy metallic type structure. When the furnace temperature was higher than 1300° C, soil became molten and appeared to have a relatively low viscosity that allowed permeation into the crucible microstructure, the cooled material manifested a glassy appearance with phase transition relics. From the range of temperatures investigated, it can be ascertained that the melting point of the composite is near 1250° C. Of particular interest is the distinct non-wetting behavior exhibited by soil heated in a boron nitride crucible and air environment. Several specimens were heated to either 860° or 1160° C in CO_2 atmosphere for comparison purposes with those in argon. Reaction onsets can occur at lower temperatures in different environments due to the influence of lingering gases released by reaction and remaining in proximity of the reaction zone to suppress further transformation [2]. For the method used, no significant effect was found; this may be attributed in part to (a) the purging process used, (b) the amount of air entrapped in the pore structure, and (c) the amount of oxygen emitted from the oxides during heating.

When the peak sintering temperature was less than 1225° C, the integrity of the alumina crucible was maintained, however, at higher temperature the structure was compromised. Thermal cracking was significant and molten material permeated and/or diffused into the microstructure of the crucible at an invasion rate of about 2 mm/hour. It is not certain whether cracking generally occurred prior to reaching the peak temperature, during the soak period, or during the cooling stages. This phenomenon occurred for both types of crucibles and regardless of preheat treatment before use. Another problem noted with the alumina crucible was the inability to remove the sample; the sample may have (a) reacted chemically and bonded to the crucible, (b) impregnated the pore structure of the crucible, and/or (c) undergone a combination of bonding and permeation. To address this problem, an alumina crucible consisting of 18 sample chambers was machined. Each chamber contained a soil sample with (a) adjacent layer(s) of fine powder material (alumina, boron nitride, or carbon) placed on the bottom or on the top and bottom of the soil, (b) a percentage of carbon powder (2%, 6%, or 10%) mixed with the soil, or (c) no powder layer or additive. Designated chambers were exposed to either air or argon atmosphere while simultaneously undergoing the thermal process. It was found that each soil sample liquefied and the wetting front migrated into the surrounding crucible material, regardless of cracking that occurred in the crucible. In those cases where alumina powder was placed on either the bottom or on the bottom and top of the sample, the alumina powder formed a disc that was discolored but not necessarily permeated by the liquid soil. When boron nitride powder was used, the powder floated to the top of the liquid soil and the perimeter of the powder disc appeared to be

bonded to the crucible wall. When the soil was "sandwiched" between layers of boron nitride in air atmosphere, glassy product formed at the bottom of the chamber and also wicked up the wall. In addition, when boron nitride powder was adjacent to the lower boundary of soil, the liquid soil migrated to a noticeably lesser extent into the crucible microstructure. It is uncertain whether the liquid soil actually permeated the pore structure of the crucible due to pore size and interconnectivity and/or if the liquid soil diffused into the crucible due to mechanisms of chemical concentrations and thermal gradients. The additions of graphite to the soil or as base layers appeared to have no benefit for containing molten soil and decreasing diffusional mass transport into the crucible. It was also found that the migration of molten soil into the crucible microstructure caused the crucible to become extremely difficult to cut using conventional methods and a diamond blade saw.

Characterization of Sintered Martian Soil Simulant

A limited number of sintered specimens underwent microcharacterization using electron microprobe analysis to identify and quantify the various constituents present in the sintered matrix and map the microstructure accordingly. Analysis conducted on a specimen sintered at 1160° C in an argon atmosphere and alumina crucible showed areas of relatively pure Fe presence and formations of Fe-Mg and Fe-Ti spinels. Evidence of phase material formations was indicative of iron being oxidized internally and ejected from olivine (Fe_2SiO_4) present prior to sintering. Microprobe analysis was also conducted on a specimen that underwent melting at a peak temperature of 1300° C in an argon atmosphere and alumina crucible. Significant glassy areas lacking crystalline structure were observed throughout the structure. This was one of the specimens that could not be removed from the crucible and analysis of the interface provided evidence of a Fe-Ti reaction product phase growing along the soil-crucible interface.

Illustrated in Figure 1 is a cross-section from the soil specimen that melted and formed a droplet at 1300° C in air while contained in a boron nitride crucible and the analysis of one of the many spherical metallic deposits that were dispersed in the melted soil structure and that also collected on the bottom. These spheres are seen as bright spots in the secondary backscattered image on the right-hand side in Figure 1(a). Element analysis determined iron in a low oxidation state (heavy metal) formed in areas evidencing a low level of P. Illustrated in Figure 1(b) is a backscattered image of a single metallic sphere and four distinct phases can be seen. Analysis of the metallic composition of this sphere is shown in Figure 1(c). About 2 mm of melted glassy material grows into about 20 Fe spheres with 10 μm diameter.

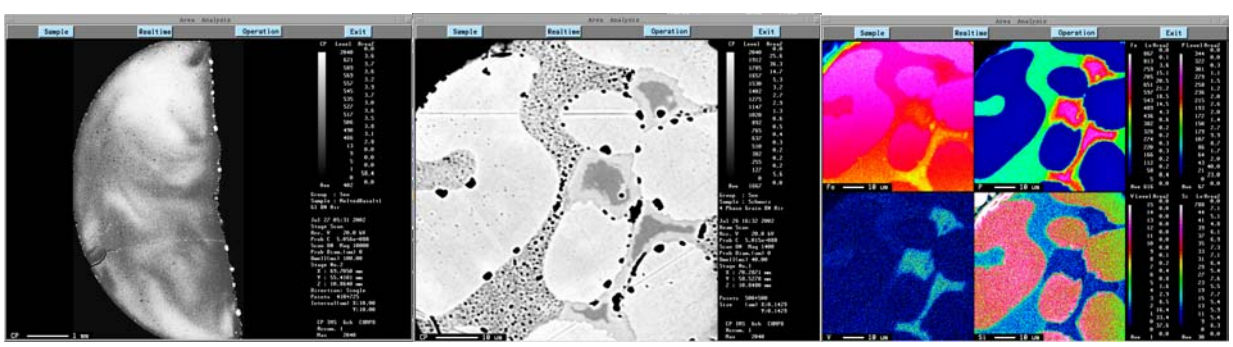

(a) (b) (c)

Figure 1: Melted Specimen at 1300° C in Air Atmosphere and Boron Nitride Crucible

Notwithstanding the exploratory nature of this experimental study, work of this nature will need to continue to assess the microstructure of other products formed by various sintering temperatures and protocols. Future studies may include (a) thermal analysis involving differential thermal analysis to quantify temperatures, thermodynamics, and kinetics of reactions to map phase transitions, (b) dilatometry to quantify solid state transformations, shrinkage during sintering, and glass transformation temperature, (c) thermogravimetric analysis to determine weight changes for transformations involving the absorption or evolution of gases from a sample consisting of a condensed phase, (d) identification and quantification of effluent volatiles by gas chromatography and mass spectroscopy, (e) addition of sintering aids such as binders, plasticizers, and dispersants, and (f) assessment of engineering properties addressing such as compressive, tensile, and bending strength, porosity, density, shrinkage, fatigue life, and shielding capabilities.

Conclusions

Based on the results of the sintering process conducted on JSC Mars-1, the following conclusions can be advanced.

- An Fe-rich metallic phase material is produced at sintering temperatures near or above 1160° C, coalesces, and gravitationally settles at sintering temperatures of about 1300° C.
- Spherical metal deposits form and a low level of P may necessitate precipitation.
- Soil is transformed into a molten material near 1250° C and manifests a low viscosity as evidenced by permeation/diffusion into the microstructure of the crucible.
- Crucibles made of alumina evidence reaction and product formation with molten soil, crucibles made of boron nitride evidenced the least reactivity.
- Future research may focus on enhancing nucleation and migration of metallic spheres by introducing additives, exploring sintering protocols, and investigating separation techniques involving sedimentation, applications of magnetic field theory, or centrifuge methodology.

Acknowledgements

The author would like to extend grateful appreciation to the scientists in the ISRU research area in SD46 at Marshall Space Flight Center for their support this summer: Peter Curreri, Sandor Lehoczky, Ben Penn; USRA scientists Paul Carpenter, Laurent Sibille, Subhayu Sen; the furnace laboratory assistance provided by Curtis Bahr, Don Lovell, Jeff Quick; and microscopy sample preparation by Sheryl Gallop.

References

[1] Allen, C.C., Morris, R.V., Jager, K.M., Golden, D.C., Lindstrom, D.J., Lindstrom, M.M., and Lockwood, J.P. (1998), "Martian Regolith Simulant JSC Mars-1," *Lunar and Planetary Science XXIX*.

[2] German, R.M. (1998), Powder Metallurgy of Iron and Steel, John Wiley and Sons, Inc., New York, pp. 181-275.

[3] Speyer, R.F. (1994), Thermal Analysis of Materials, Marcel Dekker, Inc., New York, pp. 35-90.

2002

NASA FACULTY FELLOWSHIP PROGRAM

MARSHALL SPACE FLIGHT CENTER
THE UNIVERSITY OF ALABAMA

PRELIMINARY DESIGN, FEASIBILITY AND COST EVALUATION OF 1 TO 15-KILOMETER HEIGHT STEEL TOWERS

Prepared By:	Ajay Shanker
Academic Rank:	Associate Professor
Institution and Department:	University of Florida School of Building Construction
NASA/MSFC Directorate:	Flight Projects
MSFC Colleague:	David Smitherman

Introduction

Design and construction of tall towers is an on-going research program of NASA. The agency has already done preliminary review in this area and has determined that multi-kilometer height towers are technically and economically feasible. The proposed towers will provide high altitude launch platforms reaching above eighty percent of Earth's atmosphere and provide tremendous gains in the potential energy as well as substantial reduction in aerodynamic drag. NASA has also determined that a 15-KM tower will have many useful applications in: (i)Meteorology,(ii)Oceanography, (iii)Astronomy, (iv)High Altitude Launch, (v)Physics Drop Tower, (vi) Biosphere Research, (vii) Nanotechnology, (viii) Energy/Power, (ix)Broadband Wireless Technology, (x)Space Transportation and (xi)Space Tourism.

Research Plan and Findings

In order to determine structural feasibility of constructing a 15-Km tall tower, it was decided to use the following twelve-step design process: (i) select appropriate software, (ii)develop trial model, select materials, (iii)preliminary design and weight calculations for all members, (iv)revise member sizes, if needed, (v)check structural stability for self weight, (vi)revise model, if needed, (vii)check stability for self weight, (viii)detailed design of each component, (ix)check for wind loads, (x)check for earthquake loads, (xi)check for equipment vibrations and (xii)check for temperature variations.

This process first starts with a design that is just sufficient to support its own weight. The process allows for revision of design for all natural hazards and other loads in a sequential order. It may be noted that response of a tower to wind, earthquake, equipment thrust etc., can only be calculated if all individual components of tower are completely designed. This approach for designing a tower first for own self weight and subsequently strengthening for all external loads allows for a least weight design that can be accomplished using structural design software. SAP2000 structural design software was used for constructing the model. SAP 2000 has been used for designing many important structures, e.g., Petronas Towers, Malaysia, Eiffel Tower-II, Nevada, Las Vegas and Safeco field, Seattle, Washington and many other structures throughout the world. This software can generate extremely large structures having millions of members.

A 50mx50mx200m module (Figure1) was used to develop a 15-KM tall steel tower. The module is comprised of eight beams each 50m long, four columns each 200m long, four horizontal braces each 31m long and twelve diagonal braces each 61m long. Structural members of such lengths are not uncommon and can be easily constructed in the form of a 2D or 3D truss using existing steel sections produced by the steel industry. The module has an internal spatial node that connects twelve braces to four 200m long columns (Figure1). This 3D bracing allows for increased shear strength in all three axes and also braces 200m long columns at every 50m. In order to reduce steel weight of beams and braces, it is recommended that trusses be used for construction. Calculations were made to find number of modules needed in each kilometer and then module was replicated in fifteen different files; one for each kilometer of tower. The replication process allows tall 200m meter sides of the module to be supported by four braces at 90 degrees to each other at every 50 meters (Figure 2). Such a bracing system for columns will substantially reduce buckling effects.

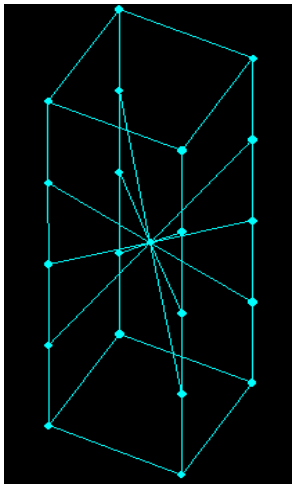

Figure 1

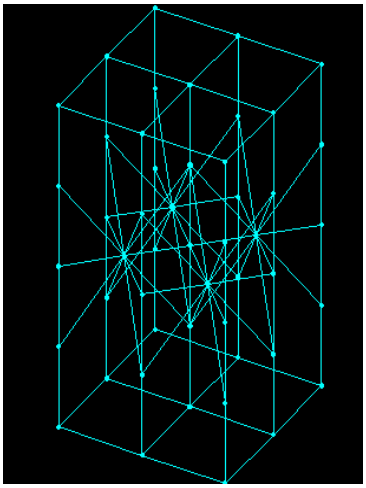

Figure 2

All fifteen files were then combined and a 3D view of the resulting tower is shown in Figure 3. Figures 4-6 show 3D views of particular parts of tower for visual comparison. It was noted that lowest kilometer has same amount of steel that is used in top eleven kilometers combined. This tower has 147,899 joints and 505,984 members.

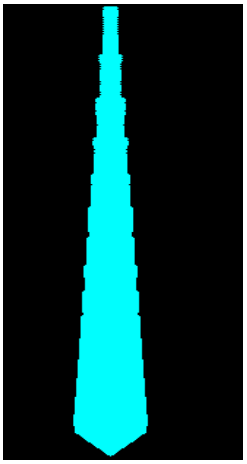

KM1-15
Figure 3

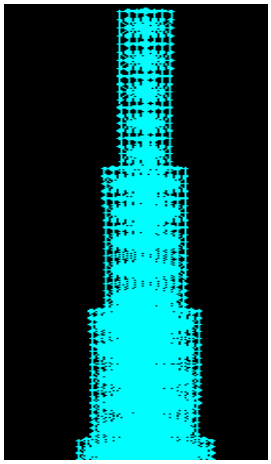

KM1-4
Figure 4

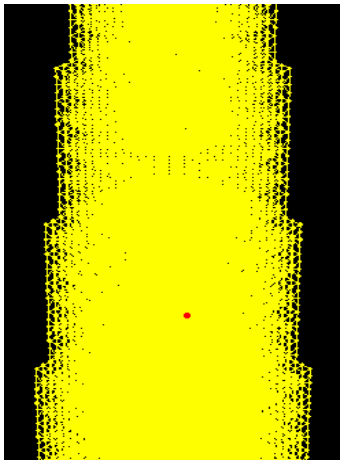

KM 7-10
Figure 5

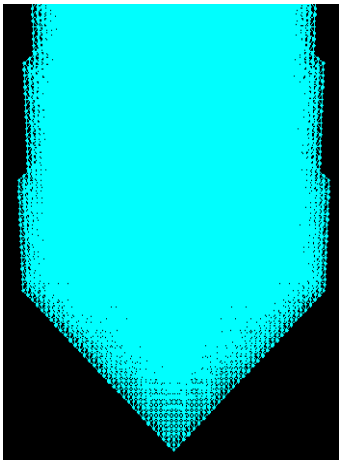

KM13-15
Figure 6

The structural data from the software was included in the basic analysis of the tower (Table 1). Self weight of Individual braces and beam elements were assumed as follows: 50kg/m for a 50-long beam, 30kg/m for a 31m long horizontal brace, and 60 kg/m for a 61m long diagonal brace. These self weights are quite comparable to self weights of similar trusses used in the steel industry for 2D or 3D trusses as per Steel Joist Institute data.

No	Km	Col. Grid Size	No. of Cols.	Total Col. Length ms	No. of Beams	Total Beam Length ms.	No. of Bracing Nodes	Total Beam wt. kg.	No. of Hoz. Braces	No. of Diag. Braces	Total Hoz. Brace Length(ms.)	Total Diag. Brace Length	Total Wt. of Hoz. Braces
1	14-15	4x4	16	16,000	120	6,000	45	300,000	180	360	6,363	22,043	190,890
2	13-14	6x6	36	36,000	300	15,000	125	750,000	500	1,000	17,675	61,230	530,250
3	12-13	8x8	64	64,000	560	28,000	245	1,400,000	980	1,960	34,643	120,011	1,039,290
4	11-12	10x10	100	100,000	900	45,000	405	2,250,000	1,620	3,240	57,267	198,385	1,718,010
5	10-11	12x12	144	144,000	1,320	66,000	605	3,300,000	2,420	4,840	85,547	296,353	2,566,410
6	9-10	14x14	196	196,000	1,820	91,000	845	4,550,000	3,380	6,760	119,483	413,915	3,584,490
7	8-9	16x16	256	256,000	2,400	120,000	1,125	6,000,000	4,500	9,000	159,075	551,070	4,772,250
8	7-8	18x18	324	324,000	3,060	153,000	1,445	7,650,000	5,780	11,560	204,323	707,819	6,129,690
9	6-7	20x20	400	400,000	3,800	190,000	1,805	9,500,000	7,220	14,440	255,227	884,161	7,656,810
10	5-6	22x22	484	484,000	4,620	231,000	2,205	11,550,000	8,820	17,640	311,787	1,080,097	9,353,610
11	4-5	24x24	576	576,000	5,520	276,000	2,645	13,800,000	10,580	21,160	374,003	1,295,627	11,220,090
12	3-4	26x26	676	676,000	6,500	325,000	3,125	16,250,000	12,500	25,000	441,875	1,530,750	13,256,250
13	2-3	28x28	784	784,000	7,560	378,000	3,645	18,900,000	14,580	29,160	515,403	1,785,467	15,462,090
14	1-2	30x30	900	900,000	8,700	435,000	4,205	21,750,000	16,820	33,640	594,587	2,059,777	17,837,610
15	0-1	32x32	1,024	1,024,000	9,920	496,000	4,805	24,800,000	19,220	38,440	679,427	2,353,681	20,382,810

Table 1

No	Total Wt. Of Diag. Braces	Total Col. Wt. Prov.	Total Steel Wt/ Km.	Cum. Total Steel Wt.	Factored Total Steel Wt./ Km.	Cost of Structural Steel ($)	Col. X-Area Needed m2	Col. Wt. Needed Kg.	Col. X-area Needed in2	X-Area per Col. in2
1	1,322,568	635,401	2,448,859	2,448,859	3,428,403	1,346,872	0.08	643,201	126.92	7.93
2	3,673,800	2,715,808	7,669,858	10,118,717	14,166,204	5,565,294	0.34	2,657,715	524.42	14.57
3	7,200,648	7,103,114	16,743,052	26,861,769	37,606,477	14,773,973	0.90	7,055,334	1,392.16	21.75
4	11,903,112	15,875,104	31,746,226	58,607,995	82,051,193	32,234,397	1.96	15,393,588	3,037.47	30.37
5	17,781,192	29,667,569	53,315,171	111,923,166	156,692,432	61,557,741	3.74	29,396,997	5,800.63	40.28
6	24,834,888	52,356,071	85,325,449	197,248,615	276,148,061	108,486,738	6.59	51,808,015	10,222.78	52.16
7	33,064,200	86,170,096	130,006,546	327,255,161	458,157,225	179,990,339	10.94	85,954,673	16,960.62	66.25
8	42,469,128	138,132,347	194,381,165	521,636,326	730,290,856	286,899,979	17.44	137,009,542	27,034.79	83.44
9	53,049,672	211,472,644	281,679,126	803,315,452	1,124,641,633	441,823,499	26.86	210,993,516	41,633.35	104.08
10	64,805,832	318,554,080	404,263,522	1,207,578,974	1,690,610,564	664,168,436	40.37	317,174,694	62,585.08	129.31
11	77,737,608	468,987,896	571,745,594	1,779,324,568	2,491,054,395	978,628,512	59.49	467,345,605	92,216.88	160.10
12	91,845,000	680,804,567	802,155,817	2,581,480,385	3,614,072,539	1,419,814,212	86.31	678,034,538	133,790.13	197.91
13	107,128,008	970,488,900	1,111,978,998	3,693,459,383	5,170,843,136	2,031,402,661	123.49	970,099,576	191,420.55	244.16
14	123,586,632	1,392,213,960	1,555,388,202	5,248,847,585	7,348,386,619	2,886,866,172	175.49	1,378,627,539	272,031.50	302.26
15	141,220,872	1,942,258,987	2,128,662,669	7,377,510,254	10,328,514,356	4,057,630,640	246.66	1,937,727,975	382,353.49	373.39

Table 2

The data presented in Table1 and Table2 is based on use of A913 high strength low alloy steel with a density of 7856kg/m^3, Load Factor of 1.4 and Resistance Factor of 0.85. It may be noted that most of the steel columns will need special fabrication and therefore can be designed and built for slenderness ratio of less than 20. AISC permits 85% of yield stress as critical failure stress for columns with slenderness ration of less than 20. Therefore buckling of columns was excluded in this preliminary analysis. The analysis indicates that for a 15-KM tower we need 7,377,510,254 KG of steel. This amount of steel would cost $4,057,630,640 at the current market rate of $0.55 per KG. It may also be noted that steel requirement increase exponentially and the requirements for a 5-KM Tower are substantially lower (Figure 7 and 8).

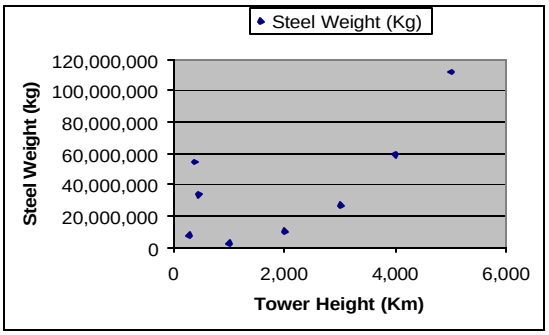

Figure 7

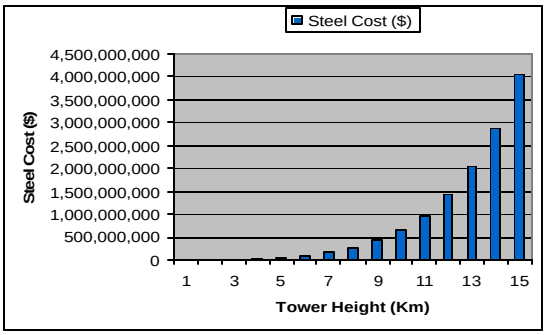

Figure 8

Conclusions

Based on the tower geometry and other assumptions, it is concluded that construction of a 15-KM self supporting steel tower is possible. The material costs, however, may exceed four billion dollars. The cost of substructure and labor involved are extremely difficult to estimate but will definitely add additional 4 billion dollars. These calculations indicate that a 15-KM tower may be cost prohibitive. As columns in lower stories become extremely large special design and fabrication techniques may have to be explored. However, a 4 to 5-KM tall tower appears to be cost effective and can be built using existing material sizes with little or no need for specialized design and fabrication. The design considered in this analysis did not increase the number of columns for subsequent lower stories and it is suggested that alternate designs with a higher rate of increase of column should be explored. NASA may want to limit future research on tall towers to be preferably within 1-5 KM range and definitely not more than 10-Kilometers.
Please send your input to author at shankerajay@hotmail.com.

Recommendation for Future Research

This research is the first attempt to approximately quantify the steel requirements of 1-15KM tall steel towers. Future research should address labor and installation costs that include advanced robotic construction techniques. Materials, e.g., composites, aluminum and concrete should also be explored for reducing cost. A triangulated form of construction should also be explored as it may reduce steel requirements. As the tower files become extremely large (54MB for this example) a faster computer with 3-4MB of RAM should be used to do analysis. Number of columns should be increased as a faster rate as we approach lower parts of the tower. Effects of wind, earthquake, temperature changes and equipment thrust and vibrations should be included to modify the structure. Carbon nanotube materials and other forms of construction, e.g., inflatable structures should also be explored

Acknowledgements

The author wishes to extend sincere appreciation to Mr. David Smitherman for reviewing and providing valuable input continuously throughout the project duration. The author would also like to thank Ms. Eileen Velez, Mr. Wayne Parks and Mr. Joe Howell all of Flight Projects Directorate, at Marshall Space Flight Center, Huntsville, Alabama, for their help in completing the work.

2002

NASA FACULTY FELLOWSHIP PROGRAM

MARSHALL SPACE FLIGHT CENTER
THE UNIVERSITY OF ALABAMA

ACTIVE AND PASSIVE CONTROL OF ISS RACK SHELF VIBRATIONS

Prepared By:	W. Steve Shepard Jr.
Academic Rank:	Assistant Professor
Institution and Department:	The University of Alabama Mechanical Engineering
NASA/MSFC Directorate:	Engineering
MSFC Colleague:	Christy B. Gattis

Introduction

One of the main goals of the International Space Station (ISS) is to provide a platform for performing laboratory experiments in a microgravity environment. These experiments are typically housed in experiment racks that may contain multiple experiments occurring simultaneously. System functions as well as experiments can produce both vibratory and transient disturbances than can be transmitted through the rack shelf, into the rack, and subsequently into the Station. Of course, Station vibrations can also be transmitted into the experiment rack and subsequently into a shelf-based experiment. The experiments on ISS rely on the calm microgravity environment that can potentially be provided. Consequently, the vibrations mentioned above can have an adverse on impact these experiments. Therefore, methods are needed for preventing these vibrations from impacting experiments.

In controlling the vibrations that can impact experiments, there are two vibratory transmission paths that must be considered. One path is between each rack and the ISS structure. Some experiment racks use the Active Rack Isolation System (ARIS) [1], a control system designed to mitigate these vibrations. However, internal vibrations must still be limited to the levels required by ARIS. For example, a motor automating an experiment on the same shelf could produce vibrations that enter other components requiring a calm environment. Of course, this issue is important with regard to vibration transmission between multiple shelves, multiple racks, and the Station. Some vibration isolators have been developed for use in a microgravity environment. One approach uses a electromagnetic voice coil to provide active vibration control [2] while another approach uses an arced piezoelectric film beam to provide passive and active vibration control [3]. While these arced beams can potentially provide a large degree of passive isolation, they require a relatively large clearance between the two structures. In a space-limited rack, this can be a major concern. The goal of this research is to examine new methods for using adaptive structure technologies to provide active vibration control and enhanced passive vibration control of ISS rack shelf vibrations.

Active and Passive Vibration Control Approaches Considered

The first vibration control approach considered in this research involves the application of piezoelectric patches directly onto the surface of a rack shelf. When driven by a voltage, these thin piezoelectric patches induce a bending moment into the plate [4-7]. By driving these actuators with an appropriate signal, usually derived from a feedback control system, the apparent structural impedance of the structure can be modified in the frequency range of interest. This impedance modification is accomplished via the superposition of waves within the structure. For this effort, the frequency range up to 300 Hz was of primary interest. By appropriately positioning multiple actuators on the shelf, this method can be used to potentially suppress vibrations of all three flexural shelf modes in this frequency range. By demonstrating the ability to selectively control each of these modes, any type of excitation in the plate structure can be controlled. A schematic of this control system on a simulated rack shelf is shown in Figure 1. Results of this effort are described below.

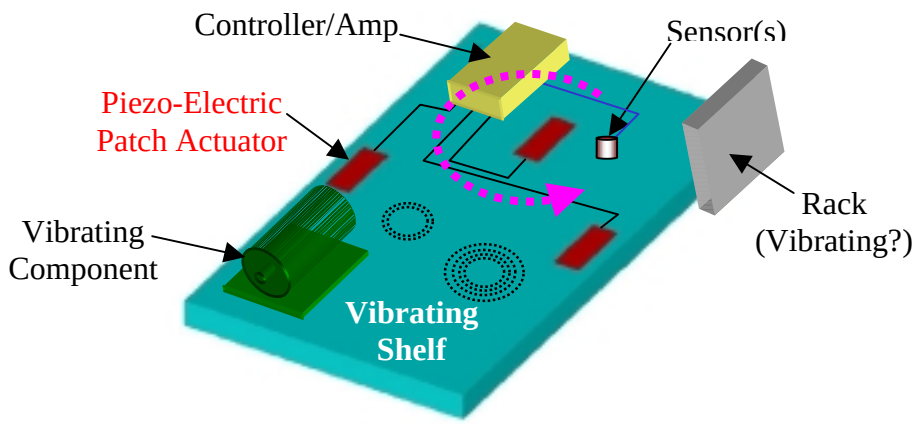

Figure 1: Shelf-Level Active Vibration Control

The second control approach involves using an active or semi-active vibration isolator to prevent vibratory forces from being transmitted between the shelf and the isolated component, as shown in Figure 2. This approach is inherently different from that described above. Here, some form of passive vibration isolation may be needed in addition to an active component [8, 9, 3, 10] due to the very high natural frequency of the component. By using an active component, the vibratory force levels transmitted into the rack shelf can be drastically reduced. As a result, the vibration levels in the shelf, and thus other components on the shelf, can be reduced. The various actuators and isolators considered in this effort along with some preliminary performance characteristics are discussed below.

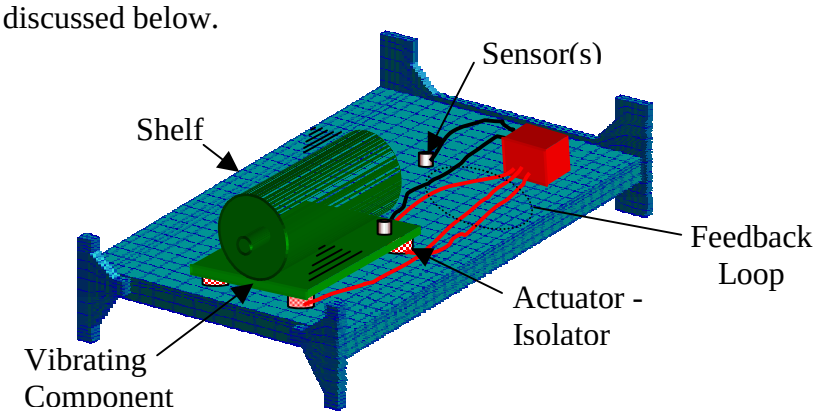

Figure 2: Component-Level Active Vibration Control

Results

To ensure that the patches effectively couple to the rack shelf mode shapes for maximum controllability, the patches should be located where the second derivative of mode displacement is greatest [4]. The patch locations that will enable control of the first three flexural modes below 300 Hz were shown in Figure 1. How the patches excite each of these modes is shown in Figure 3. Note that these mode shapes are approximate and only used to estimate the patch locations. The actual mode shapes for the simulated rack shelf will need to be experimentally verified in the appropriate test fixture before the exact patch locations are determined. Nevertheless, these locations provide individual coupling to the first three modes. The numbers in the figure indicate the relative excitation levels for each of the patches to independently

control a particular mode. These values were determined finding the modal participation factors via FEA for each of the modes due to the forces induced by the patches. Only two patches are needed for the first two modes. By using two centrally located patches, the spillover from the third off-center patch to Mode 1 can be reduced for Mode 3 control. Provided the mode shapes are not drastically impacted by supported components, this arrangement provides complete control of the structure up to 300 Hz.

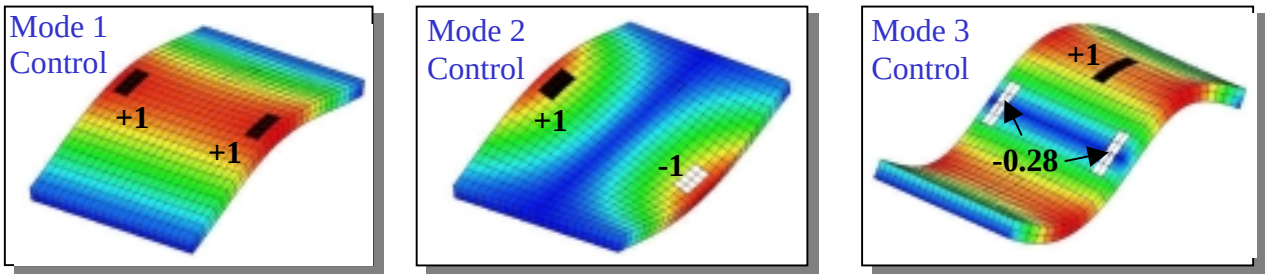

Figure 3: Control of Modes 1-3 with Piezo-Electric Patches

To examine active control at the component level, various forms of active and semi-active isolators were considered. The concepts included piezoelectric disks, PVDF films, and piezoelectric patches. When using this approach, some form of passive isolation is often needed. Consequently, PVDF films can be arranged in a stacked or scrolled configuration to decrease the dynamic stiffness and thereby increase the degree of passive isolation. A concept that provides improved passive isolation above 2 Hz as well as the capability for active vibration isolation and position keeping is the Beam Overhang Simple Support Isolator (BOSS) shown in Figure 4(a). This isolator relies on an overhanging beam to provide a low dynamic stiffness and a piezoelectric patch in the central region to provide low frequency and static control. A performance curve for this concept is shown in Figure 4(b). The dynamic stiffness of the BOSS was experimentally measured and found to be within 10% of the predicted value. The first flexural mode that degrades isolation performance does not occur until about 360 Hz. The large and small beams in the figure represent the shelf and component connections.

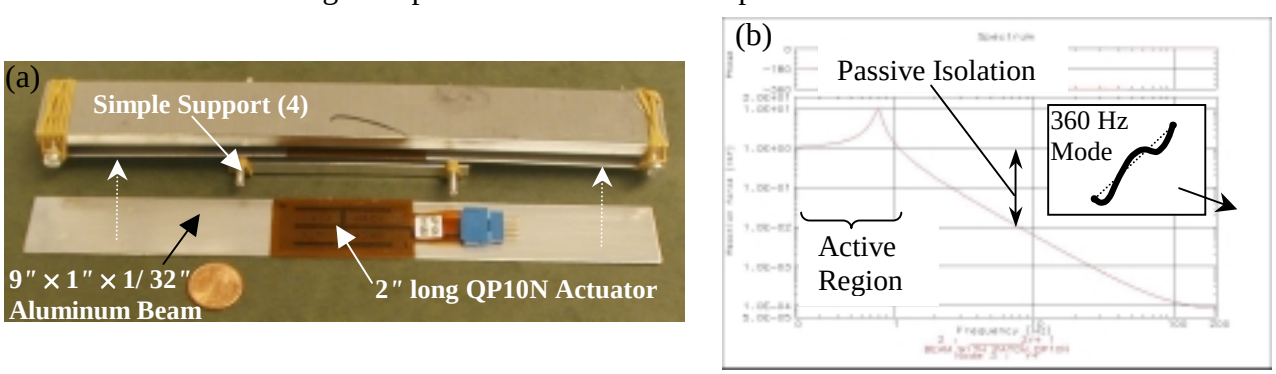

Figure 4: (a) BOSS Isolator, (b) Predicted BOSS Performance Curve

Resources

All FEA modeling for patch placement selection was performed using IDEAS Master Series. Some of the isolator performance predictions were conducted using IDEAS Master Series as well as MatLab. Other computations were performed using MS Excel.

Conclusion

Various active and passive control methods were examined for use in controlling rack shelf vibrations for the International Space Station. The locations of piezoelectric patches on a shelf simulator were determined to provide independent control of the first three modes. Various forms of active and semi-active isolators were developed for providing vibration control at the component level. In future work, some of these devices will be constructed and tested to evaluate their performance characteristics.

Acknowledgements

The author would like to thank the engineers in the Structural Dynamics and Loads Group at Marshall Space Flight Center's Engineering Directorate. Special appreciation is expressed to Christy Gattis for guiding this effort and providing valuable input.

References

[1] Bushnell, G. S., and Becraft, M. D. (1999), "Flight test of an International Space Station active rack isolation prototype system," *Smart Mater. Struct.*, Vol. 8, No. 6, pp. 791-797.

[2] Jones, D. I., Owens, A. R., and Owen, R. G. (1987), "A microgravity isolation mount," *Acta Astronautica*, Vol. 15, No. 6/7, pp. 441-448.

[3] Stampleman, D. S., and von Flotow, A. H. (November 25-30, 1990), "Microgravity isolation mounts based upon piezoelectric film," in *Proceedings of Winter Annual Meeting, ASME*, Vol. 90-WA/NCA-8, pp. 57-65.

[4] Bayer, J. I., Varadan, V. V., and Varadan, V. K. (1991), "Discrete piezoelectric sensors and actuators for active control of two-dimensional spacecraft components," in *Proceedings of SPIE, Sensors and Sensor Integration*, Vol. 1480, pp. 102-114.

[5] Guigou, C., Fuller, C. R., and Wagstaff, P. R. (1994), "Active isolation of vibration with adaptive structures," *J. Acoust. Soc. Am.*, Vol. 96, No. 1, pp. 294-299.

[6] Kim, S. J., and Jones, J. D. (1995), "Influence of piezo-actuator thickness on the active vibration control of a cantilever beam," *Journal of Intelligent Material Systems and Structures*, Vol. 6, No. 5, pp. 610-623.

[7] Song, G., Schmidt, S. P., and Agrawal, B. N. (1998), "Experimental study of active vibration suppression of flexible structure using modular control patch," in *Proceedings of Proceedings of the 1998 IEEE Aerospace Conference*, Vol. Part 1 of 5, pp. 189-201.

[8] Cobb, R. G., Sullivan, J. M., Das, A., Davis, L. P., Hyde, T. T., Davis, T., Rahman, Z. H., and Spanos, J. T. (1999), "Vibration isolation and suppression system for precision payloads in space," *Smart Mater. Struct.*, Vol. 8, No. 6, pp. 798-812.

[9] Kim, S.-M., Elliott, S. J., and Brennan, M. J. (2001), "Decentralized control for multichannel active vibration isolation," *IEEE Transactions on Control Systems Technology*, Vol. 9, No. 1, pp. 93-100.

[10] Tzou, H. S., and Gadre, M. (1988), "Active vibration isolation by Polymeric Piezoelectret with variable feedback gains," *AIAA J.*, Vol. 26, No. 8, pp. 1014-1017.

2002

NASA FACULTY FELLOWSHIP PROGRAM

MARSHALL SPACE FLIGHT CENTER

THE UNIVERSITY OF ALABAMA

COMPARATIVE STUDY OF TWO KINEMATICS AND DYNAMICS ANALYSIS TOOLS FOR MULTI-BODY SYSTEMS

REPORT NOT AVAILABLE

Prepared By:	Yeu-Sheng Paul Shiue
Academic Rank:	Associate Professor
Institution and Department:	Christian Brothers University Mechanical Engineering Department
NASA/MSFC Directorate:	Engineering
MSFC Colleague:	Mr. Geoffrey Beech

2002

NASA FACULTY FELLOWSHIP PROGRAM

MARSHALL SPACE FLIGHT CENTER
THE UNIVERSITY OF ALABAMA

PROBABLE DISASTEROUS CONSEQUENCES OF COLLISION BETWEEN UNKNOWN SMALL (100M) ASTEROIDS AND KNOWN (~1 KM) NEAR EARTH ORBITING (NEOS) ASTEROIDS

Prepared By:	Larry Smalley
Academic Rank	Professor
Institution and Department	University of Alabama in Huntsville Physics
NASA/MSFC Directorate:	Advanced Projects
MSFC Colleague	Dr. Jonathan Campbell

The long-term stability of the Solar System is not well understood. Ironically its stability is taken for granted even though our knowledge of **all** the constituents [comets, asteroids. (The Asteroid Belt between Mars and Jupiter, Trojan Asteroids, Kuiper belt, Ort Cloud), planetoids, planets, moons, etc], and its long-term dynamics cannot be easily computed. At best one might say that the solar system is chaotic, but much of the time it seems to exists near a quasi-stationary state. An asteroid that passes near the Earth regularly returns with clock-like precision. Taking into account every *known* detail of its path through the solar system, its orbit is calculated forward thousands of years with no untoward calamity on the horizon. And then one day, this passive visitor slams into the Earth during a sunny afternoon picnic! Can this happen? Unfortunately, this is a real possibility in the ordinary history of the solar system. In fact our knowledge of the solar system in the small is sketchy, as will be pointed out. Events, which lie outside our awareness, can precipitate disasters that we **may** perceive when it's too late to launch effective counter measures. In this work, one such scenario is discribed and the direct consequences for the Earth are calculated.

It is estimated that The Asteroid Belt--the vast region of debris between Jupiter and Mars-- contains a million or so asteroids larger than 1 km, and it is suggested that with Earth Based Telescopes we might be able to "see" 100,000. More important are two groups of asteroids known as Near Earth Object (NEO) Asteroids (or NEOs for short) that are in nearly the same orbit as the Earth. The NEOs can be further classified as Earth Crossing (ECR) Asteroids that tend to have orbits *slightly* out of the plane of the ecliptic. These in turn can be described as (a) Earth Passing asteroid in which the Earth or the asteroid passes one another, and (b) Horseshoe orbits in which the Earth and the asteroid periodically draws "near" to one another and the separates and draws closer in the opposite direction. These latter Horseshoe orbits are well known in the Saturn rings in which a large moon shepherds smaller moonlets. It appears that around 1700 NEOs are known--estimates suggest that there may be 1800 of them; however, the faint albedo of asteroids makes it very difficult for Telescopes to see them without constant, full sky surveillance. Many have been discovered long after their closes approach to the Earth, a time which would be too late for protective efforts if it had been a threatening encounter. There should be a real fear! These ~1-km sized asteroids (or larger) are known as **Earth Busters** and are capable of destroying civilization, as we know it.

JPL maintains an orbital simulation for most of these known asteroids using an Orbit View applet [1]. The Ephemeras and the "Risk" pages for some NEOs are also found on the NEO pages. A sample is given for the recently *rediscovered* asteroid 1950DA [2], which **may** miss the Earth in 2880. The reacquisition of asteroids is extremely important since after leaving the vicinity of the Earth, the faintness of the asteroid makes it difficult to continue tracking. During this dark period, it is possible that the asteroid might encounter perturbations. This why it is now thought that 1950DA is now listed as a potential threat to the Earth in 2880. For amateur astronomers, there is a complete orbital package called Orbit Fit [3] that can accurately calculate the orbits. The orbital elements given at the NEODys Website are in a form that can be entered directly into the Orbit Fit. Package. [4]

NASA's Near-Earth Object Program Office announced, March 12, 2002, an Automatic, Near-Earth Asteroid Collision Monitoring System, called SENTRY. The arrival of the SENTRY (in development for nearly two years) is a highly automated, accurate, and robust system for continually updating the orbits, future close Earth approaches, and Earth impact probabilities for all Near-Earth Asteroids. The system includes data from amateur astronomers, major telescope, and radar observations,

There is a limitation to the SENTRY Program: It cannot readily discover the smaller (and lower albedo) ≈ 100-m asteroids that could seriously damage the Earth. This blind spot in SENTRY was very evident when the "small," 100-m sized asteroid 2002 MN passed within 0.3 lunar distances of the Earth on June 14, 2002, **some three days prior** to its discovery. It is estimated that there are upwards to 200,000 of these ≈100-m class asteroids that visit the environs the Earth!

Although 100-meter-sized asteroids would pose direct, serious damage upon collision with the Earth, in this work, it is shown that their greatest potential threat to the Earth is instead due to the risk from colliding with the relatively stable NEOs. In this work, simulations of these orbital collisions are obtained using the package, Orbital Explorer [5]. Since this is an astronomical, simulation package, one needs only a simplified set of orbital elements for the 1-km asteroid to obtain the relevant stability information {mass, radius, x, y, z, v_x, v_y, v_z}. The data for the planets and the sun, plus the starting positions of the "bodies," are part of the simulation package. One can determine the parameter for an asteroid by iterating a "trial set" until the NEO's orbit is *stable*. On a PC, the calculation to determine stability to 100,000y takes about 12 hours. The task to find a wide range of stable orbits is straightforward but tedious. However, the result of these calculations shows that the stable orbits straddle **dense** bands of unstable orbits. Although it is not *obvious*, what this means is that if a stability calculations goes to ≈ 5000y, in all cases investigated, it will be stable to 100,000y, *assuming that there are no subsequent perturbations*—therein lies the danger!

In our calculations, the average composition (and thereby their density) of asteroids is assumed to be a mixture of iron and stone. This fixes, for simplicity, the mass-density of all the asteroids in our simulations and thus the total mass of a 100-m asteroid. It is then easily shown that the collision between a 100-m and a 1-km asteroid could easily impart velocity increments up to 2 km/s to the 1-km asteroid. *But this is overkill!* Calculations show that relatively long-term, stable orbits of a NEOs are **easily** destabilized by a glancing collision with a 100-m asteroid that departs only a relatively small velocity increment of 0.25 km/s. It seems counter intuitive that such a small incremental nudge to an asteroid already moving 25-40 km/s would make much difference. In fact, orbital simulations show that the stability of the NEO's orbit rapidly degenerates and invariably **the NEO subsequently collides with the Earth within the timescale of human lifetimes**. The Orbital Explorer program has the useful feature that allows one to stop an orbital calculation in midstream and insert parameter changes, such as decreasing the velocity v_x of the NEO by 0.25 km/s. This is the mathematical equivalent of an impulse due to the collision of a 100-m asteroid with the 1-km NEO. [As an aside, it doesn't make much difference if the increment is positive or negative since the NEOs straddle bands of unstable orbits.] In the examples given below, the NEOs are described only by their

velocity components, and the "impulse" is applied to the v_x component of NEO. Orbital diagram for the NEOs s are described by the reduced set of parameters: NEO{30326, 4595,1100}.The first figure below shows the relative orbital positions of the inner planets and the asteroid (red) at 8892y86d. Assuming that the orbit is stable, at this time v_x is decremented by -0.25 km/s to simulate a collision. The last second shows that the NEO collides with the Earth at 8943y358d for an elapsed time of 48y93d!

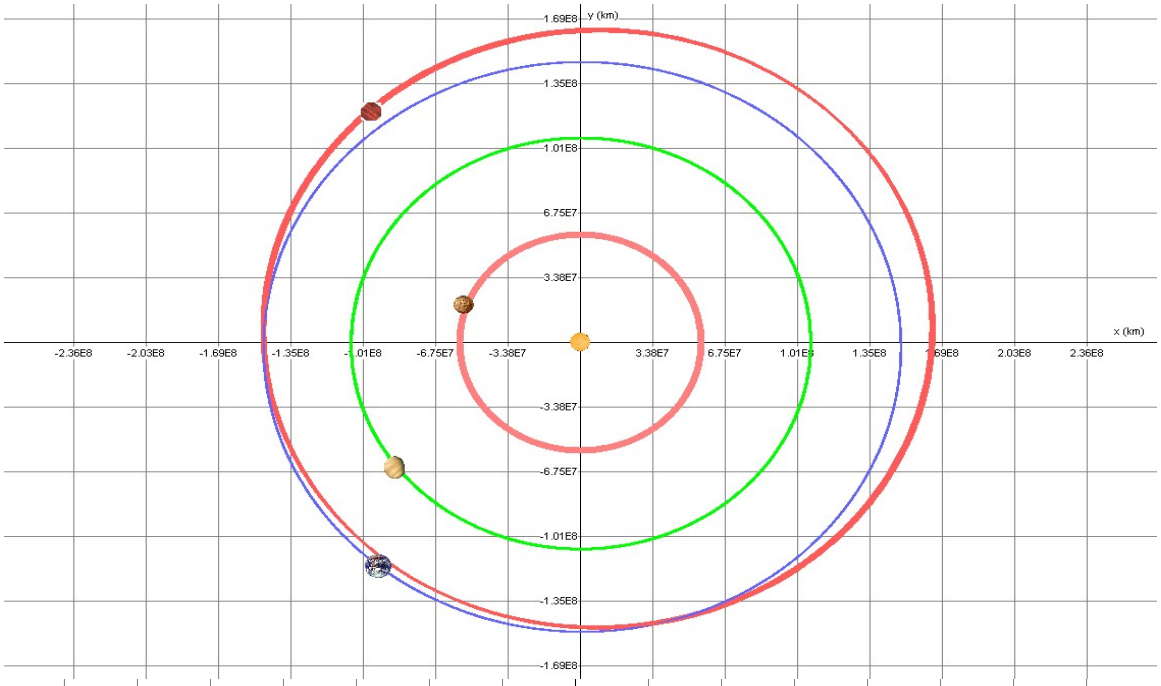

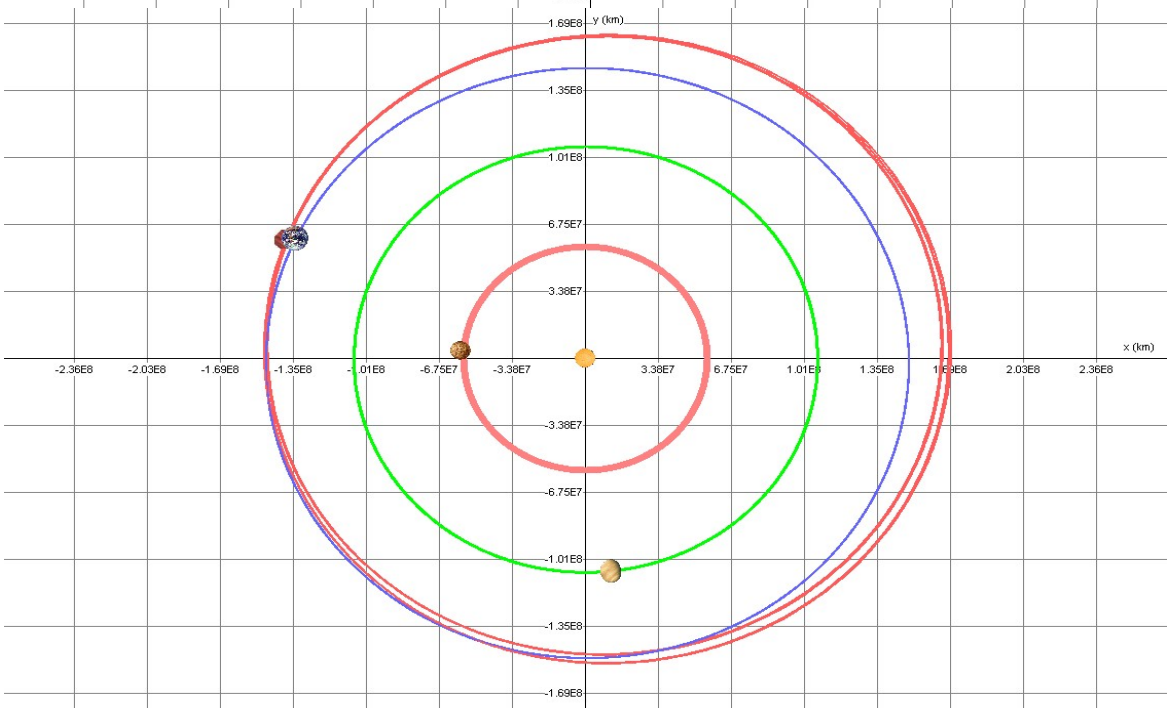

An interesting example is the NEO{30326,495, 1300}. The first figure shows the

simulation stopped at 50109y74d and v_x is decremented by 0.25 km/s and runs until 56501y239d, at which time v_x is decremented by 0.25 km/s. and then runs until the NEO collides with the Earth at 56,542y159d shown in the second figure. One might conclude that an overall decrement of v_x of 0.5 km/s would have caused the asteroid to collide. To test this premise, the v_x parameter was changed to 29826. The asteroid collided with the Earth in 29y8d!

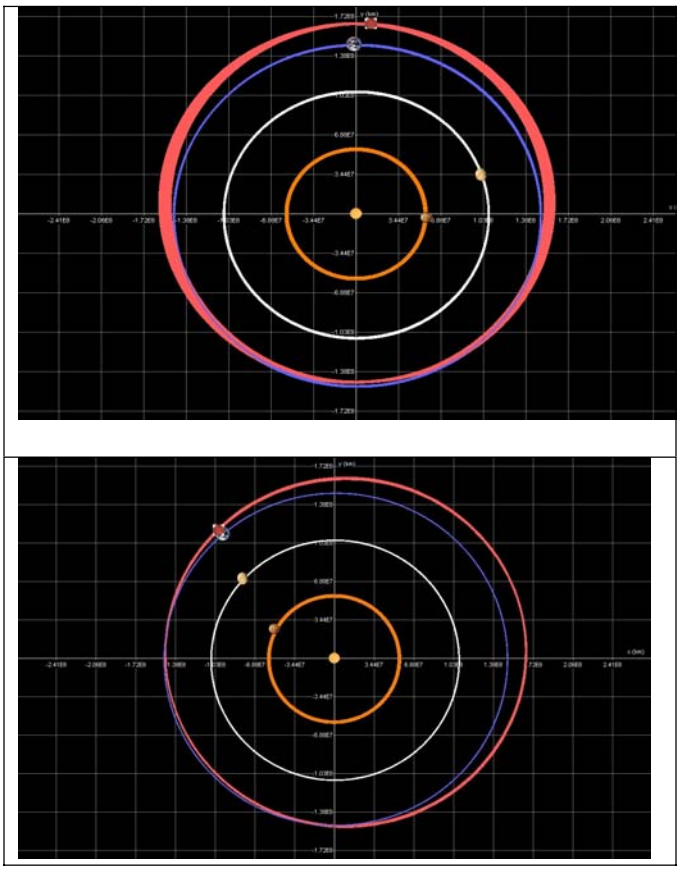

Taking into account all the close encounters of NEOs with planets and the known asteroids, the best calculations may predict that the Earth is safe from collision. But from our poor knowledge of the shear number and whereabouts of the small 100-m asteroids, it truly becomes impossible to calculate with certainty that we are safe from the collision with the NEOs. Thus it is important to develop advanced monitoring system and options for rapid defense. Options could be the use of space based lasers for ablative thrust, parasitic spacecraft that attach to the asteroid and use the engines in an ablative mode, etc. But if they fail as well, there is always nuclear energy to break up the NEO.

References

1. Orbit Viewer applet were originally written and kindly provided by Osamu Ajiki (AstroArts),and further modified by Ron Baalke (JPL).
2. http://neo.jpl.nasa.gov/news/news127.html .
3. NEODys Near-Earth Objects .
4. The ObFit package is also found on the NeoDys site: OrbFit .
5. Orbital Explorer shareware http://www.ottisoft.com/orbit_x.htm

2002

NASA FACULTY FELLOWSHIP PROGRAM

MARSHALL SPACE FLIGHT CENTER
THE UNIVERSITY OF ALABAMA

LIGHTNING LOCATION

Prepared by:	Richard Solakiewicz
Academic Rank:	Professor
Institution and Department:	Chicago State University Department of Mathematics and Computer Science
NASA/MSFC Directorate:	National Space Science and Technology Center, SD60
NASA Colleague:	Dr. William Koshak

Lightning Location

The Lightning Mapping Array (LMA) is a collection of radio wave Time of Arrival (TOA) sensors. With knowledge of the sensors' positions and TOA's from a source, it is possible to locate the source and find its time of occurrence. The n sensors' locations are specified by (h_j, V_j, λ_j), $j = 1, 2, \ldots, n$, where h denotes altitude above the Earth's surface, V is the geodetic latitude, and λ is the longitude. We will also use spherical coordinates (R,φ, λ), with R being the distance from the center of the Earth and φ denoting spherical latitude. Oblate spheroidal coordinates are given by (ξ, η, λ), where ξ = constant represents an oblate spheroid and η is the spheroidal latitude. The longitudes in all 3 systems are the same. Latitudes are related through

$$\tan V = \frac{a}{b}\tan\eta = \frac{a^2}{b^2}\tan\varphi, \tag{1}$$

where a = 6378137 m and b = 6356752.3142 m are the mean equatorial and polar radii of the Earth respectively [3].

Let $\hat{\mathbf{w}}$ and $\hat{\mathbf{u}}$ be vectors pointing from the center of the Earth to the North Pole and to the intersection of the equator and prime meridian respectively. Define $\hat{\mathbf{v}}$ by $\hat{\mathbf{w}} \times \hat{\mathbf{u}}$. Clearly,

$$u = A\cosh\xi\cos\eta\cos\lambda, \quad v = A\cosh\xi\cos\eta\sin\lambda, \quad w = A\sinh\xi\sin\eta. \tag{2}$$

Here, $A = \sqrt{a^2 - b^2} \approx 521854$ m.

Sensor locations may be written in terms of Cartesian coordinates by using

$$(a\cos\eta + h\cos V)\cos\lambda = u, \quad (a\cos\eta + h\cos V)\sin\lambda = v, \quad b\sin\eta + h\sin V = w, \tag{3}$$

where η is obtained in terms of V by (1). Another transformation is used to place the origin of a new coordinate system at the location of sensor 1. We use

$$\begin{pmatrix} x \\ y \\ z \end{pmatrix} = \begin{pmatrix} -\sin\lambda_1 & \cos\lambda_1 & 0 \\ -\sin\varphi_1\cos\lambda_1 & -\sin\varphi_1\sin\lambda_1 & \cos\varphi_1 \\ \cos\varphi_1\cos\lambda_1 & \cos\varphi_1\sin\lambda_1 & \sin\varphi_1 \end{pmatrix} \cdot \begin{pmatrix} u - u_1 \\ v - v_1 \\ w - w_1 \end{pmatrix}. \tag{4}$$

In the xyz system, the sensors' z coordinates are not very different compared to other distances in the problem. This may account for more difficulty in retrieving results in this direction, particularly for sources that are distant from the network of sensors. Retrievals of x, y, and t are generally better. A method is suggested to improve the retrieval of the z coordinate of the source.

If we let the position vector $\mathbf{r} = x\hat{\mathbf{x}} + y\hat{\mathbf{y}} + z\hat{\mathbf{z}}$ denote the source location and $\mathbf{r}_j$ be the locations of the sensors, then

$$\left|\mathbf{r}_j - \mathbf{r}\right| = c\left(t_j - t\right), \tag{5}$$

where c is the speed of light, t is the time of occurrence of the lightning event, and t_j denotes the TOA recorded at sensor j. More sensors are used than are necessary to solve the system of eqs. in (5). The effects of timing errors may be decreased by solving the system in a least squares sense; i.e.,

$$E = \sum_{j=1}^{n} \left[\mathbf{r}_j - \mathbf{r} - c\left(t_j - t\right)\right]^2 \tag{6}$$

is to be minimized. Apparently, numerical algorithms must be employed to solve the nonlinear problem. Computer time may be reduced by starting with a good estimate of the solution.

Reasonable estimates of the minimum of E might be obtained by working with

$$E = \sum_{j=1}^{n} \left[\mathbf{r}_j - \mathbf{r}^{\,2} - c^2\left(t_j - t\right)^2\right] \tag{7}$$

instead. One method available is to write $\mathbf{r}_j - \mathbf{r}^{\,2} = r_j^{\,2} + r^2 - 2\mathbf{r}_j \cdot \mathbf{r}$ and subtract off the nonlinear terms by using $\mathbf{r}_1 - \mathbf{r}^{\,2} = c^2\left(t_1 - t\right)^2$ [5]. This leads to a system of linear eqs.

Instead of subtracting the eq. for TOA at sensor 1, we can follow [4] and subtract a TOA eq. averaged over all of the sensors,

$$\frac{1}{n}\sum_{j=1}^{n} \mathbf{r}_j - \mathbf{r}^{\,2} = \frac{c^2}{n}\sum_{j=1}^{n}\left(t_j - t\right)^2. \tag{8}$$

This leads to the linear system

$$2\left(\mathbf{r}_j - \frac{1}{n}\sum_{k=1}^{n}\mathbf{r}_k\right)\cdot\mathbf{r} - 2c^2\left(t_j - \frac{1}{n}\sum_{k=1}^{n}t_k\right)t = \left(r_j^{\,2} - \frac{1}{n}\sum_{k=1}^{n}r_k^{\,2}\right) - c^2\left(t_j^{\,2} - \frac{1}{n}\sum_{k=1}^{n}t_k^{\,2}\right). \tag{9}$$

It was demonstrated in [4] that the averaging approach yielded results almost as good as those obtained by minimizing E in (6).

Even with this method, the retrieval of the z coordinate might be improved. If the x, y, and t results are reasonably good, we can substitute these results back into (7) and minimize E as a function of z alone. This leads to the cubic eq.

$$\frac{\partial E}{\partial z} = -4\sum_{j=1}^{n}\left[\left(x_j - x\right)^2 + \left(y_j - y\right)^2 + \left(z_j - z\right)^2 - c^2\left(t_j - t\right)^2\right]\left(z_j - z\right) = 0. \tag{10}$$

The solution that yields the smallest value of E is to be used. Define the following sums of sensor coordinates:

$$\begin{gathered}\frac{1}{n}\sum_{j=1}^{n} x_j^{\,p} = A_p,\ \frac{1}{n}\sum_{j=1}^{n} y_j^{\,p} = B_p,\ \frac{1}{n}\sum_{j=1}^{n} z_j^{\,p} = C_p;\ 1 \le p \le 4;\\ \frac{1}{n}\sum_{j=1}^{n} x_j^{\,q} y_j^{\,s} = F_{qs},\ \frac{1}{n}\sum_{j=1}^{n} x_j^{\,q} z_j^{\,s} = G_{qs},\ \frac{1}{n}\sum_{j=1}^{n} y_j^{\,q} z_j^{\,s} = H_{qs};\ 1 \le q,s \le 2.\end{gathered} \tag{11}$$

These sums may be evaluated and stored in memory once the sensors are selected. Certain additional sums will have to be performed after arrival times at the sensors are obtained,

$$\begin{gathered}\frac{1}{n}\sum_{j=1}^{n} \left(ct_j\right)^p = D_p,\ 1 \le p \le 4;\\ \frac{1}{n}\sum_{j=1}^{n} x_j^{\,q}\left(ct_j\right)^s = J_{qs},\ \frac{1}{n}\sum_{j=1}^{n} y_j^{\,q}\left(ct_j\right)^s = K_{qs},\ \frac{1}{n}\sum_{j=1}^{n} z_j^{\,q}\left(ct_j\right)^s = L_{qs};\ 1 \le q,s \le 2.\end{gathered} \tag{12}$$

In terms of the sums defined above, the sum of the squared residuals is given by

$$\begin{aligned}E = {} & z^4\\ & -\{4C_1\}z^3\\ & +\{2[(A_2+B_2+3C_2-D_2)-2(A_1x+B_1y-D_1ct)+(x^2+y^2-c^2t^2)]\}z^2\\ & -\{4[(G_{21}+H_{21}-L_{12}+C_3)-2(G_{11}x+H_{11}y-L_{11}ct)+C_1(x^2+y^2-c^2t^2)]\}z\\ & +\{2(F_{22}+G_{22}+H_{22}-J_{22}-K_{22}-L_{22})+A_4+B_4+C_4+D_4\\ & \quad -4[(A_3+F_{12}+G_{12}-J_{12})x+(B_3+F_{21}+H_{12}-K_{12})y+(D_3-J_{21}-K_{21}-L_{21})ct]\\ & \quad +2[(3A_2+B_2+C_2-D_2)x^2+(A_2+3B_2+C_2-D_2)y^2-(A_2+B_2+C_2-3D_2)c^2t^2]\\ & \quad +8(F_{11}xy-J_{11}xct-K_{11}yct)-4(A_1x^3+B_1y^3+D_1c^3t^3)\\ & \quad -4(B_1x^2y+A_1xy^2-D_1x^2ct-A_1xc^2t^2-D_1y^2ct-B_1yc^2t^2)\\ & \quad +x^4+y^4+c^4t^4+2x^2y^2-2(x^2+y^2)c^2t^2\}\end{aligned} \tag{13}$$

The cubic eq. obtained by setting $\partial E/\partial z = 0$,

$$\begin{gathered}z^3 + a_2z^2 + a_1z + a_0 = 0;\\ a_2 = -3C_1,\\ a_1 = A_2+B_2+3C_2-D_2-2(A_1x+B_1y-D_1ct)+x^2+y^2-c^2t^2,\\ a_0 = -[(G_{21}+H_{21}-L_{12}+C_3)-2(G_{11}x+H_{11}y-L_{11}ct)+C_1(x^2+y^2-c^2t^2)].\end{gathered} \tag{14}$$

may be solved exactly [1]. The coordinates as given by the procedure described may be used as a starting point for a numerical method (e.g., Newton, Marquardt [2]) to minimize E.

Once x, y, z, and t are obtained to sufficient accuracy, the inverse of (4) may be employed to obtain the source location in terms of the Cartesian coordinates u, v, and w. From these, longitude is immediately obtained from $\tan\lambda = v/u$. For the latitude and altitude, we begin with

$$\begin{gathered}\rho\tilde{\mathbf{n}} + w\hat{\mathbf{w}} = \rho_0\tilde{\mathbf{n}} + w_0\hat{\mathbf{w}} + \mu\mathbf{N}, \quad \rho^2 = u^2 + v^2, \quad \mathbf{N} = \frac{\rho_0}{a^2}\tilde{\mathbf{n}} + \frac{w_0}{b^2}\hat{\mathbf{w}}, \\ \rho_0 = \rho/\left(1 + \mu/a^2\right), \quad w_0 = w/\left(1 + \mu/b^2\right),\end{gathered} \tag{15}$$

where ρ_0 and w_0 correspond to a point on the surface of the Earth directly below the source. Substituting into the eq. of the oblate spheroid taken as the Earth's surface yields

$$\begin{gathered}\mu^4 + 2\left(a^2 + b^2\right)\mu^3 + \left[\left(a^2 + b^2\right)^2 + 2a^2b^2 - a^2\rho^2 - b^2w^2\right]\mu^2 \\ + 2a^2b^2\left(a^2 + b^2 - \rho^2 - w^2\right)\mu + a^2b^2\left(a^2b^2 - b^2\rho^2 - a^2w^2\right) = 0.\end{gathered} \tag{16}$$

Once the unknown constant μ is obtained, the associated coordinates ρ_0 and w_0 may be recovered by (15). The geodetic latitude and altitude may be calculated from

$$V = \tan^{-1}\frac{a^2w_0}{b^2\rho_0}, \quad h = \sqrt{\left(\rho - \rho_0\right)^2 + \left(w - w_0\right)^2}. \tag{17}$$

Since spherical and geodetic latitudes are not very different, we may simply perturb;

$$\eta \approx \tan^{-1}\left(\frac{aw}{b\rho}\right) - \frac{\left(a^2 - b^2\right)\rho w\left(\sqrt{a^2w^2 + b^2\rho^2} - ab\right)}{\left(a^2 - b^2\right)\left(a^2w^2 - b^2\rho^2\right) + ab\left(\rho^2 + w^2\right)\sqrt{a^2w^2 + b^2\rho^2}}. \tag{18}$$

The geodetic latitude may then be recovered by (1), and the altitude may be determined from (3).

References

1. Abranowitz, M. and I. Stegun (1970), *Handbook of Mathematical Functions*, 9th Printing, Dover, NY, 17-18.
2. Burden, R. and J. Faires (1993), *Numerical Analysis*, 5th Ed., PWS-Kent, Boston, 553-576.
3. Defense Mapping Agency (DMA) (1991), Department of Defense World Geodetic System 1984, 2nd Ed., Technical Report TR83502, 3-1, 3-10.
4. Hager, W. and D. Wang (1995), "An analysis of errors in the location, current, and velocity of lightning", *J. Geophys. Res.*, 100, 25,721-25,729.
5. Koshak, W. and R. Solakiewicz (2001), "TOA lightning location retrieval on spherical and oblate spheroidal earth geometries", *J. Atmos. Oceanic Technol.*, 18, 187-199.

2002

NASA FACULTY FELLOWSHIP PROGRAM

MARSHALL SPACE FLIGHT CENTER
THE UNIVERSITY OF ALABAMA

A Computational Method for Determining the Equilibrium Composition and Product Temperature in a LH_2/LOX Combustor

Prepared By:	Mehmet Sözen
Academic Rank:	Associate Professor
Institution and Department:	Embry-Riddle Aeronautical University Physical Sciences Department Engineering Physics Program
NASA/MSFC Directorate:	Engineering, ED25
MSFC Colleague:	Dr. Alok Majumdar

Introduction

The Generalized Fluid System Simulation Package [2] (GFSSP) is a general-purpose computer program developed at NASA/MSFC for analyzing steady state and transient flow rates, pressures, temperatures, and concentrations in a complex flow network. The code can handle compressible and incompressible flows as well as phase change and mixture thermodynamics. The program which was developed out of need for an easy to use system level simulation tool for complex flow networks, has been used for the following purposes to name a few: Space Shuttle Main Engine (SSME) High Pressure Oxidizer Turbopump Secondary Flow Circuits, Axial Thrust Balance of the Fastrac Engine Turbopump, Pressurized Propellant Feed System for the Propulsion Test Article at Stennis Space Center, X-34 Main Propulsion System, X-33 Reaction Control System and Thermal Protection System, and International Space Station Environmental Control and Life Support System design. There has been an increasing demand for implementing a combustion simulation capability into GFSSP in order to increase its system level simulation capability of a propulsion system starting from the propellant tanks up to the thruster nozzle for spacecraft as well as launch vehicles.

The present work was undertaken for addressing this need. In what follows, the model used for combustion of liquid hydrogen (LH_2) with liquid oxygen (LOX) using chemical equilibrium assumption, and the novel computational method developed for determining the equilibrium composition and temperature of the combustion products by application of the first and second laws of thermodynamics will be described. The modular FORTRAN code developed as a subroutine that can be incorporated into any flow network code with little effort has been successfully implemented in GFSSP as the preliminary runs indicate. The code provides capability of modeling the heat transfer rate to the coolants for parametric analysis in system design.

Theoretical Model

The current investigation considers the problem of combustion of LH_2 with LOX in a combustor with the assumption of H_2O, H_2, O_2, OH, H, and O constituting the products of combustion. The schematic diagram of the problem is depicted in Figure 1.

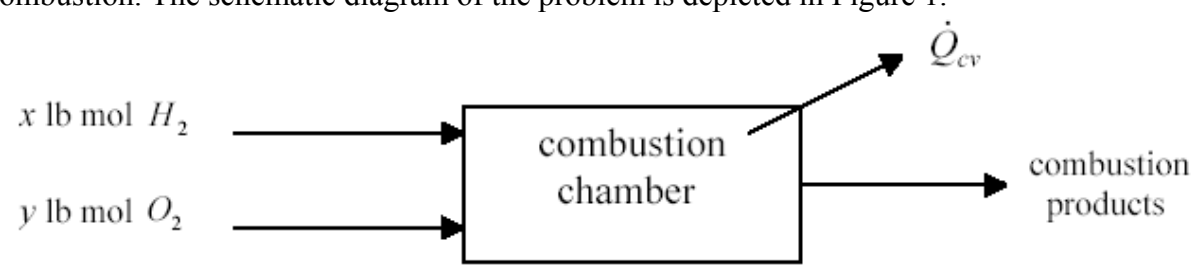

Figure 1: Schematic diagram of the combustion chamber.

The problem is solved by using chemical equilibrium assumption for steady flow case by applying the first and second laws of thermodynamics [4]. An equivalent approach of using chemical equilibrium is the minimization of Gibbs free energy, which has been used in codes like CEA [1,5]. For given inlet conditions and exit pressure, the resulting equations, which turn out to be coupled, non-linear, algebraic equations, are solved simultaneously. Three cases are

considered; (a) stoichiometric case, (b) fuel rich case, and (c) oxygen rich case, for all possible environments.

Stoichiometric Case:

The chemistry mechanism used for this case is given by a set of reactions as follows

$$\begin{array}{ccccc} 2H_2 & + & O_2 & \Leftrightarrow & 2H_2O \\ & & H_2 & \Leftrightarrow & 2H \\ & & O_2 & \Leftrightarrow & 2O \\ 2H_2O & \Leftrightarrow & H_2 & + & 2OH \end{array}$$

and the changes in each specie in the form of fractions a, b, c, and d can be expressed as

$$\begin{array}{ccccc} 2H_2 & + & O_2 & \Leftrightarrow & 2H_2O \\ -2a & & -a & & +2a \\ & & H_2 & \Leftrightarrow & 2H \\ & & -b & & +2b \\ & & O_2 & \Leftrightarrow & 2O \\ & & -c & & +2c \\ 2H_2O & \Leftrightarrow & H_2 & + & 2OH \\ -2d & & +d & & +2d \end{array}$$

which result in the following overall reaction

$$\begin{array}{ccccccccc} 2H_2 & + & O_2 & \rightarrow & (2a-2d)H_2O & + & (2-2a-b+d)H_2 & + & (1-a-c)O_2 \\ & & & & (2d)OH & + & (2b)H & + & (2c)O \end{array}$$

The individual mole fractions of species in the products can be expressed in terms of fractions a, b, c, and d in the following form

$$z_{H_2O} = \frac{2a-2d}{3-a+b+c+d} \qquad z_{H_2} = \frac{2-2a-b+d}{3-a+b+c+d}$$

$$z_{O_2} = \frac{1-a-c}{3-a+b+c+d} \qquad z_{OH} = \frac{2d}{3-a+b+c+d}$$

$$z_H = \frac{2b}{3-a+b+c+d} \qquad z_O = \frac{2c}{3-a+b+c+d}$$

and the application of second law with chemical equilibrium assumption yields

$$K_1 = \frac{z_{H_2O}^2}{z_{H_2}^2 \cdot z_{O_2}} \left(\frac{P}{P_o}\right)^{-1} \qquad K_2 = \frac{z_H^2}{z_{H_2}} \left(\frac{P}{P_o}\right)$$

$$K_3 = \frac{z_O^2}{z_{O_2}}\left(\frac{P}{P_o}\right) \qquad K_4 = \frac{z_{H_2} \cdot z_{OH}^2}{z_{H_2O}^2}\left(\frac{P}{P_o}\right)$$

and the first law of thermodynamics in the absence of work is expressed as

$$\begin{aligned}\dot{Q}_{c.v.} + (\dot{n}_{H_2})_r(\Delta\bar{h}_{H_2})_r + (\dot{n}_{O_2})_r(\Delta\bar{h}_{O_2})_r = {} & (\dot{n}_{H_2O})_p(\bar{h}^o_{f_{H_2O}} + \Delta\bar{h}_{H_2O})_p + (\dot{n}_{H_2})_p(\Delta\bar{h}_{H_2})_p \\ & + (\dot{n}_{O_2})_p(\Delta\bar{h}_{O_2})_p + (\dot{n}_{OH})_p(\bar{h}^o_{f_{OH}} + \Delta\bar{h}_{OH})_p \\ & + (\dot{n}_H)_p(\bar{h}^o_{f_H} + \Delta\bar{h}_H)_p + (\dot{n}_O)_p(\bar{h}^o_{f_O} + \Delta\bar{h}_O)_p\end{aligned}$$

where the number of moles per unit time, $\dot{n}_i$, for any specie i, can also be expressed in terms of the fractions a, b, c, and d can be expressed as

$$(\dot{n}_{H_2O})_p = \frac{(2a-2d)}{3}(\dot{n}_{tot})_r \qquad (\dot{n}_{H_2})_p = \frac{(2-2a-b+d)}{3}(\dot{n}_{tot})_r$$

$$(\dot{n}_{O_2})_p = \frac{(1-a-c)}{3}(\dot{n}_{tot})_r \qquad (\dot{n}_{OH})_p = \frac{2d}{3}(\dot{n}_{tot})_r$$

$$(\dot{n}_H)_p = \frac{2b}{3}(\dot{n}_{tot})_r \qquad (\dot{n}_O)_p = \frac{2c}{3}(\dot{n}_{tot})_r$$

where $(\dot{n}_{tot})_r = (\dot{n}_{H_2})_r + (\dot{n}_{O_2})_r$, $(\dot{n}_{H_2})_r = \dfrac{\dot{m}_{H_2}}{MW_{H_2}}$, $(\dot{n}_{O_2})_r = \dfrac{\dot{m}_{O_2}}{MW_{O_2}}$, and

$$(\dot{n}_{tot})_p = \frac{(3-a+b+c+d)}{3}(\dot{n}_{tot})_r .$$

The five equations to be solved simultaneously can be written in the following form after some manipulations

$$f_1 = \frac{(2a-2d)^2(3-a+b+c+d)}{(2-2a-b+d)^2(1-a-c)}\left(\frac{P}{P_o}\right)^{-1} - K_1 = 0 \tag{1}$$

$$f_2 = \frac{(2b)^2}{(3-a+b+c+d)(2-2a-b+d)}\left(\frac{P}{P_o}\right) - K_2 = 0 \tag{2}$$

$$f_3 = \frac{(2c)^2}{(3-a+b+c+d)(1-a-c)}\left(\frac{P}{P_o}\right) - K_3 = 0 \tag{3}$$

$$f_4 = \frac{(2-2a-b+d)(2d)^2}{(2a-2d)^2(3-a+b+c+d)}\left(\frac{P}{P_o}\right) - K_4 = 0 \tag{4}$$

$$
\begin{aligned}
f_5 = \dot{Q}_{c.v.} &+ (\dot{n}_{H_2})_r (\Delta\bar{h}_{H_2})_r + (\dot{n}_{O_2})_r (\Delta\bar{h}_{O_2})_r - (\dot{n}_{H_2O})_p (\bar{h}^o_{f_{H_2O}} + \Delta\bar{h}_{H_2O})_p \\
&- (\dot{n}_{H_2})_p (\Delta\bar{h}_{H_2})_p - (\dot{n}_{O_2})_p (\Delta\bar{h}_{O_2})_p - (\dot{n}_{OH})_p (\bar{h}^o_{f_{OH}} + \Delta\bar{h}_{OH})_p \\
&- (\dot{n}_H)_p (\bar{h}^o_{f_H} + \Delta\bar{h}_H)_p - (\dot{n}_O)_p (\bar{h}^o_{f_O} + \Delta\bar{h}_O)_p = 0
\end{aligned} \tag{5}
$$

The corresponding equations have been developed for the fuel rich case and oxygen rich case.

<u>*Fuel rich case (FRC)*</u>

The chemistry mechanism for this case uses the following reactions

$$xH_2 \quad + \quad yO_2 \quad \Leftrightarrow \quad 2yH_2O \quad + \quad (x-2y)H_2 \qquad \text{for} \quad x > 2y$$

$$H_2 \quad \Leftrightarrow \quad 2H$$

$$O_2 \quad \Leftrightarrow \quad 2O$$

$$2H_2O \quad \Leftrightarrow \quad H_2 \quad + \quad 2OH$$

and the changes in each specie in the form of fractions a, b, c, and d can be expressed as

$$
\begin{array}{ccccccc}
xH_2 & + & yO_2 & \Leftrightarrow & 2yH_2O & + & (x-2y)H_2 \\
-2ya & & -ya & & +2ya & & +(x-2y)a
\end{array}
$$

$$
\begin{array}{ccc}
H_2 & \Leftrightarrow & 2H \\
-b & & +2b
\end{array}
$$

$$
\begin{array}{ccc}
O_2 & \Leftrightarrow & 2O \\
-c & & +2c
\end{array}
$$

$$
\begin{array}{ccccc}
2H_2O & \Leftrightarrow & H_2 & + & 2OH \\
-2d & & +d & & +2d
\end{array}
$$

The overall reaction is given by

$$
\begin{aligned}
xH_2 \quad + \quad yO_2 \quad \rightarrow \quad & (2ya-2d)H_2O \quad + \quad [x(1+a)-4ya-b+d]H_2 \\
& + \quad (y-ya-c)O_2 \quad + \quad (2d)OH \quad + \quad (2b)H \quad + \quad (2c)O
\end{aligned}
$$

Individual mole fractions are given as

$$z_{H_2O} = \frac{(2ya-2d)}{x(1+a)+y-3ya+b+c+d} \qquad z_{H_2} = \frac{x(1+a)-4ya-b+d}{x(1+a)+y-3ya+b+c+d}$$

$$z_{O_2} = \frac{y-ya-c}{x(1+a)+y-3ya+b+c+d} \qquad z_{OH} = \frac{2d}{x(1+a)+y-3ya+b+c+d}$$

$$z_H = \frac{2b}{x(1+a)+y-3ya+b+c+d} \qquad z_O = \frac{2c}{x(1+a)+y-3ya+b+c+d}$$

With equilibrium constants given in terms of the mole fractions of products

$$K_1 = \frac{z_{H_2O}^{2y}}{z_{H_2}^{2y} \cdot z_{O_2}^{y}} \left(\frac{P}{P_o}\right)^{-y} \qquad K_2 = \frac{z_H^2}{z_{H_2}} \left(\frac{P}{P_o}\right)$$

$$K_3 = \frac{z_O^2}{z_{O_2}} \left(\frac{P}{P_o}\right) \qquad K_4 = \frac{z_{H_2} \cdot z_{OH}^2}{z_{H_2O}^2} \left(\frac{P}{P_o}\right)$$

The five coupled, non-linear algebraic equations for this case become

$$f_1 = \frac{(2ya-2d)^{2y}\left[x(1+a)+y-3ya+b+c+d\right]^y}{\left[x(1+a)-4ya-b+d\right]^{2y}(y-ya-c)^y}\left(\frac{P}{P_o}\right)^{-y} - K_1 = 0 \tag{1*}$$

$$f_2 = \frac{(2b)^2}{\left[x(1+a)+y-3ya+b+c+d\right]\left[x(1+a)-4ya-b+d\right]}\left(\frac{P}{P_o}\right) - K_2 = 0 \tag{2*}$$

$$f_3 = \frac{(2c)^2}{\left[x(1+a)+y-3ya+b+c+d\right](y-ya-c)}\left(\frac{P}{P_o}\right) - K_3 = 0 \tag{3*}$$

$$f_4 = \frac{\left[x(1+a)-4ya-b+d\right](2d)^2}{(2ya-2d)^2\left[x(1+a)+y-3ya+b+c+d\right]}\left(\frac{P}{P_o}\right) - K_4 = 0 \tag{4*}$$

$$\begin{aligned} f_5 = {} & \dot{Q}_{c.v.} + (\dot{n}_{H_2})_r(\Delta\bar{h}_{H_2})_r + (\dot{n}_{O_2})_r(\Delta\bar{h}_{O_2})_r - (\dot{n}_{H_2O})_p(\bar{h}^o_{f_{H_2O}} + \Delta\bar{h}_{H_2O})_p \\ & - (\dot{n}_{H_2})_p(\Delta\bar{h}_{H_2})_p - (\dot{n}_{O_2})_p(\Delta\bar{h}_{O_2})_p - (\dot{n}_{OH})_p(\bar{h}^o_{f_{OH}} + \Delta\bar{h}_{OH})_p \\ & - (\dot{n}_H)_p(\bar{h}^o_{f_H} + \Delta\bar{h}_H)_p - (\dot{n}_O)_p(\bar{h}^o_{f_O} + \Delta\bar{h}_O)_p = 0 \end{aligned} \tag{5*}$$

where the number of moles per unit time, $\dot{n}_i$, for any specie i, are expressed in terms of the fractions a, b, c, and d accordingly.

<u>*Oxygen rich case (ORC)*</u>

The chemistry mechanism for this case uses the following reactions

$$xH_2 \quad + \quad yO_2 \quad \Leftrightarrow \quad xH_2O \quad + \quad (y-\frac{x}{2})O_2 \qquad \text{for } x<2y$$

$$H_2 \quad \Leftrightarrow \quad 2H$$

$$O_2 \quad \Leftrightarrow \quad 2O$$

$$2H_2O \quad \Leftrightarrow \quad H_2 \quad + \quad 2OH$$

and the changes in each specie in the form of fractions a, b, c, and d can be expressed as

$$
\begin{array}{ccccccc}
xH_2 & + & yO_2 & \Leftrightarrow & xH_2O & + & (y-\frac{x}{2})O_2 \\
-xa & & -\frac{x}{2}a & & +xa & & +(y-\frac{x}{2})a
\end{array}
$$

$$
\begin{array}{ccc}
H_2 & \Leftrightarrow & 2H \\
-b & & +2b
\end{array}
$$

$$
\begin{array}{ccc}
O_2 & \Leftrightarrow & 2O \\
-c & & +2c
\end{array}
$$

$$
\begin{array}{ccccc}
2H_2O & \Leftrightarrow & H_2 & + & 2OH \\
-2d & & +d & & +2d
\end{array}
$$

The overall reaction is given by

$$
\begin{aligned}
xH_2 \;+\; yO_2 \;\rightarrow\; & (xa-2d)H_2O \;+\; [x(1-a)-b+d]H_2 \\
& +\; [y-(y-x)a-c]O_2 \;+\; (2d)OH \;+\; (2b)H \;+\; (2c)O
\end{aligned}
$$

Individual mole fractions are given as

$$
z_{H_2O} = \frac{(xa-2d)}{x+y+(y-x)a+b+c+d} \qquad z_{H_2} = \frac{x(1-a)-b+d}{x+y+(y-x)a+b+c+d}
$$

$$
z_{O_2} = \frac{y+(y-x)a-c}{x+y+(y-x)a+b+c+d} \qquad z_{OH} = \frac{2d}{x+y+(y-x)a+b+c+d}
$$

$$
z_H = \frac{2b}{x+y+(y-x)a+b+c+d} \qquad z_O = \frac{2c}{x+y+(y-x)a+b+c+d}
$$

With equilibrium constants given in terms of the mole fractions of products

$$
K_1 = \frac{z_{H_2O}^x}{z_{H_2}^x \cdot z_{O_2}^{x/2}}\left(\frac{P}{P_o}\right)^{-x/2} \qquad K_2 = \frac{z_H^2}{z_{H_2}}\left(\frac{P}{P_o}\right)
$$

$$
K_3 = \frac{z_O^2}{z_{O_2}}\left(\frac{P}{P_o}\right) \qquad K_4 = \frac{z_{H_2} \cdot z_{OH}^2}{z_{H_2O}^2}\left(\frac{P}{P_o}\right)
$$

The five coupled, non-linear algebraic equations for this case become

$$
f_1 = \frac{(xa-2d)^x\,[x+y+(y-x)a+b+c+d]^{x/2}}{[x(1-a)-b+d]^x\,[y+(y-x)a-c]^{x/2}}\left(\frac{P}{P_o}\right)^{-x/2} - K_1 = 0 \qquad (1^{**})
$$

$$
f_2 = \frac{(2b)^2}{[x+y+(y-x)a+b+c+d]x(1-a)-b+d]}\left(\frac{P}{P_o}\right) - K_2 = 0 \qquad (2^{**})
$$

$$f_3 = \frac{(2c)^2}{[x+y+(y-x)a+b+c+d][y+(y-x)a-c]}\left(\frac{P}{P_o}\right) - K_3 = 0 \qquad (3^{**})$$

$$f_4 = \frac{[x(1-a)-b+d](2d)^2}{(xa-2d)^2[x+y+(y-x)a+b+c+d]}\left(\frac{P}{P_o}\right) - K_4 = 0 \qquad (4^{**})$$

$$\begin{aligned} f_5 = {} & \dot{Q}_{c.v.} + (\dot{n}_{H_2})_r(\Delta\bar{h}_{H_2})_r + (\dot{n}_{O_2})_r(\Delta\bar{h}_{O_2})_r - (\dot{n}_{H_2O})_p(\bar{h}^o_{f_{H_2O}} + \Delta\bar{h}_{H_2O})_p \\ & - (\dot{n}_{H_2})_p(\Delta\bar{h}_{H_2})_p - (\dot{n}_{O_2})_p(\Delta\bar{h}_{O_2})_p - (\dot{n}_{OH})_p(\bar{h}^o_{f_{OH}} + \Delta\bar{h}_{OH})_p \\ & - (\dot{n}_H)_p(\bar{h}^o_{f_H} + \Delta\bar{h}_H)_p - (\dot{n}_O)_p(\bar{h}^o_{f_O} + \Delta\bar{h}_O)_p = 0 \end{aligned} \qquad (5^{**})$$

where the number of moles per unit time, $\dot{n}_i$, for any specie i, are expressed in terms of the fractions a, b, c, and d accordingly.

Solution Method

It should be noted that whichever of the three cases is under consideration, the set of equations to be solved will be equations 1-5, or 1*-5*, or 1**-5**. In these equations the chemical equilibrium constants K_1, K_2, K_3, and K_4 as well as all the $\Delta\bar{h}_i$ terms for the reactants and products are all functions of temperature. These functions have been correlated with least squares method with third or fourth order polynomials in three ranges of temperature from $0^{\circ}\mathrm{R}$ up to $10000^{\circ}\mathrm{R}$.

Newton-Raphson Solution Scheme:

The application of the Newton-Raphson method involves the following 7 steps [3]:

1. Develop the governing equations. The equations have to be in the following form:

$$f_1(x_1, x_2, x_3, x_4, x_5) = 0 \qquad (6a)$$
$$f_2(x_1, x_2, x_3, x_4, x_5) = 0 \qquad (6b)$$
$$f_3(x_1, x_2, x_3, x_4, x_5) = 0 \qquad (6c)$$
$$f_4(x_1, x_2, x_3, x_4, x_5) = 0 \qquad (6d)$$
$$f_5(x_1, x_2, x_3, x_4, x_5) = 0 \qquad (6e)$$

   Note that equations 1-5, 1*-5*, and 1**-5** are already in this form with a, b, c, d and T corresponding to $x_1, x_2, x_3, x_4,$ and x_5 respectively.

2. Guess a solution for the equations:
   Guess $x_1^*, x_2^*, x_3^*, x_4^*, x_5^*$ as an initial solution for the governing equations.

3. Calculate the residual of each equation.
   When the guessed solutions are substituted into equations (6a-6e), the right hand sides of the equations, which are not zero, are the residuals.

$$f_1(x_1^*, x_2^*, x_3^*, x_4^*, x_5^*) = R_1 \qquad (7a)$$

$$f_2(x_1^*, x_2^*, x_3^*, x_4^*, x_5^*) = R_2 \tag{7b}$$
$$f_3(x_1^*, x_2^*, x_3^*, x_4^*, x_5^*) = R_3 \tag{7c}$$
$$f_4(x_1^*, x_2^*, x_3^*, x_4^*, x_5^*) = R_4 \tag{7d}$$
$$f_5(x_1^*, x_2^*, x_3^*, x_4^*, x_5^*) = R_5 \tag{7e}$$

The intent of the solution scheme is to correct $x_1^*, x_2^*, x_3^*, x_4^*,$ and x_5^* with a set of corrections $x_1'', x_2'', x_3'', x_4'',$ and x_5'' such that $R_1, R_2, R_3, R_4,$ and R_5 are zero.

4. Develop a set of correction equations for all variables.
   First construct the matrix of influence coefficient:

$$\begin{matrix}
\frac{\partial f_1}{\partial x_1} & \frac{\partial f_1}{\partial x_2} & \frac{\partial f_1}{\partial x_3} & \frac{\partial f_1}{\partial x_4} & \frac{\partial f_1}{\partial x_5} \\
\frac{\partial f_2}{\partial x_1} & \frac{\partial f_2}{\partial x_2} & \frac{\partial f_2}{\partial x_3} & \frac{\partial f_2}{\partial x_4} & \frac{\partial f_2}{\partial x_5} \\
\frac{\partial f_3}{\partial x_1} & \frac{\partial f_3}{\partial x_2} & \frac{\partial f_3}{\partial x_3} & \frac{\partial f_3}{\partial x_4} & \frac{\partial f_3}{\partial x_5} \\
\frac{\partial f_4}{\partial x_1} & \frac{\partial f_4}{\partial x_2} & \frac{\partial f_4}{\partial x_3} & \frac{\partial f_4}{\partial x_4} & \frac{\partial f_4}{\partial x_5} \\
\frac{\partial f_5}{\partial x_1} & \frac{\partial f_5}{\partial x_2} & \frac{\partial f_5}{\partial x_3} & \frac{\partial f_5}{\partial x_4} & \frac{\partial f_5}{\partial x_5}
\end{matrix}$$

   Then construct the set of simultaneous equations for corrections:

$$\begin{bmatrix}
\frac{\partial f_1}{\partial x_1} & \frac{\partial f_1}{\partial x_2} & \frac{\partial f_1}{\partial x_3} & \frac{\partial f_1}{\partial x_4} & \frac{\partial f_1}{\partial x_5} \\
\frac{\partial f_2}{\partial x_1} & \frac{\partial f_2}{\partial x_2} & \frac{\partial f_2}{\partial x_3} & \frac{\partial f_2}{\partial x_4} & \frac{\partial f_2}{\partial x_5} \\
\frac{\partial f_3}{\partial x_1} & \frac{\partial f_3}{\partial x_2} & \frac{\partial f_3}{\partial x_3} & \frac{\partial f_3}{\partial x_4} & \frac{\partial f_3}{\partial x_5} \\
\frac{\partial f_4}{\partial x_1} & \frac{\partial f_4}{\partial x_2} & \frac{\partial f_4}{\partial x_3} & \frac{\partial f_4}{\partial x_4} & \frac{\partial f_4}{\partial x_5} \\
\frac{\partial f_5}{\partial x_1} & \frac{\partial f_5}{\partial x_2} & \frac{\partial f_5}{\partial x_3} & \frac{\partial f_5}{\partial x_4} & \frac{\partial f_5}{\partial x_5}
\end{bmatrix}
\begin{Bmatrix} x_1'' \\ x_2'' \\ x_3'' \\ x_4'' \\ x_5'' \end{Bmatrix}
=
\begin{Bmatrix} R_1 \\ R_2 \\ R_3 \\ R_4 \\ R_5 \end{Bmatrix}$$

5. Solve for $x_1'', x_2'', x_3'', x_4'',$ and x_5'' by solving the simultaneous equations.
6. Apply correction to each variable.
7. Iterate until corrections become smaller than a prescribed value.

Subroutines EQNS, SIMUL, PARDIF, and GAUSSY as described in reference [3] were modified for the problem under investigation. EQNS provides the simultaneous equations to be solved; SIMUL performs the Newton-Raphson solution of equations in EQNS with application of PARDIF and GAUSSY appropriately; PARDIF extracts the partial derivatives; and GAUSSY solves the resulting set of linear simultaneous equations by Gauss elimination method.

Conclusion

A modular FORTRAN code was developed for applying the first and second laws of thermodynamics to the combustion of LH_2 with LOX. Chemical equilibrium assumption based on the minimization of Gibbs free energy was employed. Case studies were performed with stoichiometric, fuel-rich and oxygen-rich cases. All these yielded very good results compared with hand calculations. Preliminary runs also indicate successful integration of this modular code with GFSSP. This modular code enhances the capability of GFSSP in performing system level simulation of a complete propulsion system using LH_2/LOX, starting from the propellant tanks up to the thruster nozzle.

Acknowledgements

The author would like to thank Dr. Alok Majumdar for his continuous encouragement and mentorship during the author's NASA Summer Faculty Fellowship appointment at Marshall Space Flight Center.

References

[1] Gordon, S., and McBride, B. (1994), "Computer Program for Calculation of Complex Chemical Equilibrium Composition and Applications: I. Analysis", NASA Reference Publication 1311, October.
[2] Majumdar, A. (1999), "Generalized Fluid System Simulation Program (GFSSP) Version 3.0", Sverdrup Technology Report No. MG-99-290, Contract No. NAS8-40836.
[3] Stoecker, W. F. (1989), *Design of Thermal Systems*, McGraw-Hill Higher Education, pp.50-55.
[4] Van Wylen, G. J, Sonntag, R. E., and Borgnakke, C. (1997), *Fundamentals of Classical Thermodynamics*, Fourth Edition, John Wiley and Sons.
[5] Zeleznik, F. J., and Gordon, S. (1968), "Calculation of Complex Chemical Equilibrium", *Industrial Eng. Chemistry*, Vol. 60, No. 6, pp. 27-57.

2002

NASA/ASEE FACULTY FELLOWSHIP PROGRAM

MARSHALL SPACE FLIGHT CENTER
THE UNIVERSITY OF ALABAMA

PHASE RETRIEVAL USING A GENETIC ALGORITHM ON THE SYSTEMATIC IMAGE-BASED OPTICAL ALIGNMENT TESTBED

Prepared By:	Jaime R. Taylor
Academic Rank:	Professor
Institution and Department:	Austin Peay State University Physics
NASA/MSFC Directorate:	Engineering
MSFC Colleagues:	Dr. Jim Steincamp John Rakoczy

Introduction

NASA's Marshall Space Flight Center's Systematic Image-Based Optical Alignment (SIBOA) Testbed was developed to test phase retrieval algorithms and hardware techniques. Individuals working with the facility developed the idea of implementing phase retrieval by breaking the determination of the tip/tilt of each mirror apart from the piston motion (or translation) of each mirror. Presented in this report is an algorithm that determines the optimal phase correction associated only with the piston motion of the mirrors.

A description of the Phase Retrieval problem is first presented. The Systematic Image-Based Optical Alignment (SIBOA) Testbeb is then described. A Discrete Fourier Transform (DFT) is necessary to transfer the incoming wavefront (or estimate of phase error) into the spatial frequency domain to compare it with the image. A method for reducing the DFT to seven scalar/matrix multiplications is presented. A genetic algorithm is then used to search for the phase error. The results of this new algorithm on a test problem are presented.

What is Phase Retrieval?

Phase retrieval is the process of recovering wavefront error given a measurement of a Point-Spread-Function (PSF). An incoming wavefront has the form $Ae^{i\Phi}$ where A is the amplitude and Φ is the phase. A perfectly focused wavefront has zero phase error. The phase error cannot be measured directly, only the square of the amplitude of the Fourier transform (PSF). Figure 1a shows an uncorrected PSF and Figure 1b is the same PSF corrected.

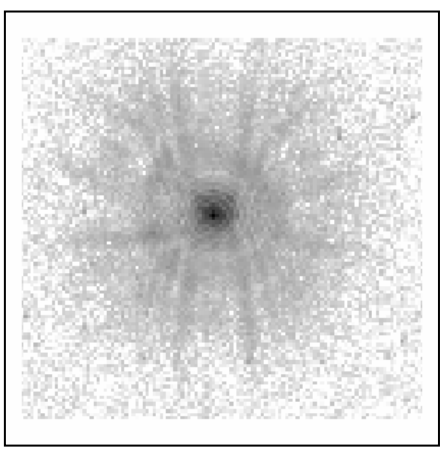

Figure 1a. Uncorrected PSF.

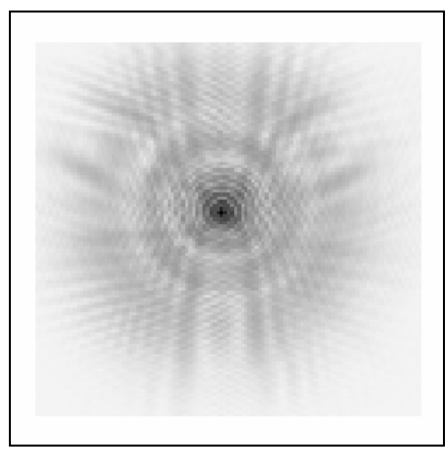

Figure 1b. Corrected PSF.

A known source is put through the optical system, the PSF is measured, and the phase distortion is calculated. Adaptive optics are then used to correct the phase [10]. Phase retrieval is much harder than standard image restoration due to the fact it is non-linear. Many solution techniques have been applied to the phase retrieval problem such as Iterative Fourier Transform Methods [4], optimization methods using simulated annealing [8], neural networks [9], and the simplex method [5], and other techniques such as the application of the wavelet transform [1]. Reference [6] and [7] present the phase retrieval problem with more mathematical rigor.

Major Problems that exist are unpredictability of convergence (iterative Fourier transform methods), converges to local minimum (maximum likelihood approaches tend to get stuck at local minima), and a vast number of necessary FFT calculations. This work addresses all these concerns.

SIBOA Testbed and Problem Statement

The Systematic Image-Based Optical Alignment (SIBOA) Testbed is a seven mirror adaptive optics system, see Figure 2 below. Each mirror has the ability to tip/tilt and to translate under piston motion. The individuals working with this system have implemented sensing hardware that allows the tip/tilt to be corrected independently of the piston motion. An algorithm already exists for the fast reliable solution of the tip/tilt problem [2]. The problem addressed here is finding the phase error to be corrected with the piston motion.

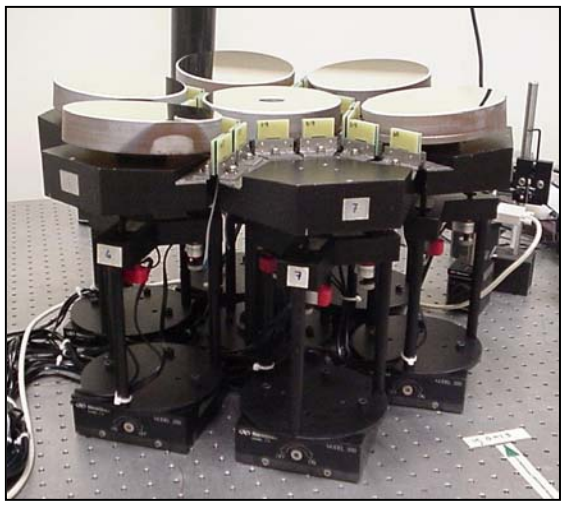

Figure 2. The Systematic Image-Based Optical Alignment Testbed.

Reduced Discrete Fourier Transform

It is possible to reduce the DFT, Equation 1, to seven scalar/matrix multiplications due to the fact the tip/tilt and the piston motion of the mirrors are sensed and corrected with independent hardware. The piston motion results in a uniform phase change across the surface of the mirror.

$$X(k) = \sum_{n=0}^{N-1} x(n)\, e^{-j\left(2\frac{\pi}{N}\right)nk} \tag{1}$$

Due to this fact *x(n)* can be written as $re^{i\Phi}$ where *r,* the amplitude, is one at the mirror locations and zero outside the mirrors, and Φ is a constant value between $-\pi$ and π for each mirror. Since Φ is constant for each mirror the phase term, $e^{i\Phi}$, can be factored out of the calculation and the DFT for each mirror need only be calculated once for a particular correction cycle. Each time a new set of phase parameters is tested, the phase term for each

mirror (a scalar) is multiplied by the DFT term for each mirror (a matrix). These terms are then added to produce the complete DFT.

Genetic Algorithm

A general description of binary GAs is provided in the classic text by David Goldberg [3]. For this application a binary GA was used with uniform crossover with reduced surrogate. After every ten generations the population was "restarted" using a new range, given by the min and max parameter values of the top forty individuals in the population, centered about the average of the top five individuals. Restarting the population did three things, it reintroduced new genetic material that might have been lost, it reduced the search space, and most importantly in increased the resolution within this reduced search space.

Results

The PSF was calculated using a known phase error. The algorithm developed here was applied to the PSF to estimate the known phase error; the estimated error was then compared to the known error. Several tests cases were examined. The GA was able to determine the phase error to whatever accuracy the user wanted up to machine precision. Figure 3 shows an example of the evolution of the populations in the GA.

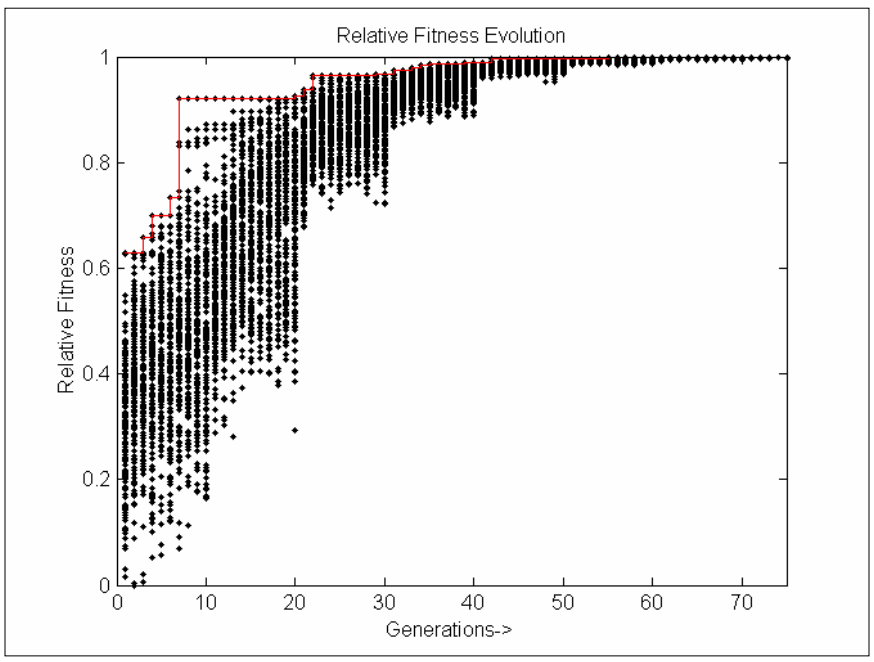

Figure 3. Evolution of the GA populations.

After every ten generations a restart population was randomly determined with a new parameter range. Figure 3 shows how after every ten generations the min and max errors fall within this reduced range. The algorithm user can allow this evolution to continue until their desired parameter precision is found.

Acknowledgements

The author would like to thank Dr. Jim Steincamp for providing the problem and many suggestions for research direction. The author would also like to thank Mr. John Rakoczy for his contribution in understanding the phase retrieval problem and the specific contributions he has made to this field. The author would especially like to thank the MSFC NASA Faculty Fellowship Team for providing this opportunity.

References

[1] Bell, A. (1996), "Phase Retrieval Using the Wavelet Transform," Proceedings ICASSP.

[2] Chiemlowski, M. and Taylor J. (July 1997), "A Real-Time Sunspot Tracking Algorithm," Publications of the Astronomical Society of the Pacific, 109, pp. 837-842.

[3] Goldberg, D. (1989), *Genetic Algorithms in Search, Optimization and Machine Learning,*Reading, MA, Addison Wesley Longman, Inc.

[4] Gonsalves, R. (September 1976), "Phase Retrieval from Modulus Data," Journal of Optical Society of America, Vol. 66, No. 9, pp. 961-964.

[5] Kim, Y. (1997), "Refined Simplex Method for Data Fitting," Astronomical Data Analysis Software and Systems VI ASP Conference Series, Vol. 125, pp. 206-209.

[6] Luke, R. (May 2000), "Fast Algorithms for Phase Retrieval and Deconvolution", in Proceedings of the Workshop on Computational Optics and Imaging for Space Applications NASA/Goddard Space Flight Center.

[7] Luke, R., Burke J. and Lyon, L. (2002), "Optical Wavefront Reconstruction: Theory and Numberical Methods," SIAM Review, **44**, pp.169-224.

[8] Morris, D. (1996), "Simulated Annealing Applied to the Misell Algorithm for Phase Retrieval," IEE Proceedings of Microwave Antennas Propagation, Vol 143, No. 4, pp. 208-303.

[9] Saarinen, B., Kuosmanen, P. and Rusu, C. (2001), "Several Approaches to Signal Reconstruction from Spectrum Magnitudes," Acoustics, Speech, and Signal Processing, Vol. 6, pp. 3921-3924.

[10] Tyson, R. (1998), *Principles of Adaptive Optics,* Academic Press

2002

NASA FACULTY FELLOWSHIP PROGRAM

MARSHALL SPACE FLIGHT CENTER
THE UNIVERSITY OF ALABAMA

USING CASE TO ADOPT ORGANIZATIONAL LEARNING AT NASA

Prepared By:	Gary F. Templeton
Academic Rank:	Assistant Professor
Institution and Department:	University of Alabama in Huntsville Department of Accounting and Information Systems
NASA/MSFC Directorate:	Customer and Employee Relations
MSFC Colleague:	Jim Dowdy

Introduction

The research direction was articulated in a statement of work created in collaboration between two program colleagues, an outside researcher and an internal user. The researcher was to deliver an implemented CASE tool (Casewise™) that was to be used to serve non-traditional (i.e., not software development related) organizational purposes. The explicitly stated functions of the tool were the support of 1) ISO-9000 compliance in the documentation of processes and 2) the management of process improvement. The collaborative team consisted of the researcher (GT), a full-time accompanying student (CRO), and the user (JD). The team originally focused on populating the CASE repository for the purpose of solving the two primary objectives. Consistent with the action research approach, several additional user requirements emerged as the project evolved, needs became apparent in discussions about how the tool would be used to solve organizational problems. These deliverables were contained within the CASE repository:

1) the creation of a 'paradigm diagram'
2) the creation of a context diagram
3) the creation of child diagrams
4) the generation of 73 issues relating to organizational change
5) a compendium of stakeholder interview transcripts

All record keeping was done manually and then keyed into the CASE interface.
An issue is the difference between an organization's current situation (action) and its collective ideals.

Issues were categorized as either 'major' or 'minor,' based on their relevance to change. Major issues relate to radical change, defined as changes to the formal (explicitly stated) organizational memory. Minor issues relate to changes that necessitate modification of the informal (tacitly stated) memory, and not the formal memory. An issues report was generated for the coordinators with the understanding that the information was not to be disseminated outside the group. The collaborative team decided to create an evolutionary prototype exploiting computer aided software engineering (CASE) software. The selected tool was Casewise Modeler 8e™, a product distributed by Casewise Systems.

The colleagues discussed the applicability of embedding organizational learning concepts into the design model to help solve some of the organization's ongoing problems. The discussions about organizational problems were a product of the ongoing collaboration. Three strategic planning elements were used in requirements analysis: the President's Management Agenda (PMA), the Space Act of 1958, and the current myriad of NASA initiatives. The colleagues derived several significant problems from the analysis. The main problem was in controlling the myriad of PMA initiatives as they are incorporated throughout the government agencies. Table 1 summarizes some other significant agency problems: lack of integration, interunit coordination, alignment, and process validity.

Table 1: Systemic Organizational Problems at NASA

Problem	Explanation
Integration	designs are piecemeal; the initiatives are segregated, causing lack of consistency with respect to the achievement of outcomes
Interunit coordination	stepping on toes; operating subunits are segregated and subsequently interpret the initiatives in different ways, operate

	them with different outcomes in mind, do not share resources, and fail to achieve economies of size
Alignment	outcomes are not clear, standardized, nor shared; the initiatives do not achieve a uniform set of outcomes
Process Validity	doing the wrong things; some initiatives are implemented differently from their intended purpose

The problems centered around controlling mandated initiatives as they flowed from the top of the federal bureaucracy to the agency level. At the time of the study, there were five government-wide initiatives (source: President's Management Agenda, 2002) that were being disseminated to the tactical and operational levels:

1. Strategic Management of Human Capital – to retain intellectual capital in the face of government downsizing
2. Competitive Sourcing – capitalizing on competencies readily available in the private sector
3. Improved Financial Performance – improving financial accountability
4. Expanded Electronic Government – achieving greater service at lower cost using electronic delivery of government services
5. Budget Performance Integration – linking 1-4 to performance

The colleagues determined that the use of CASE in implementing an organizational learning paradigm would be a fitting solution to the problems identified. CASE originated in the 1970s to facilitate structure in software development, traditionally an undisciplined process. Recently, CASE tools have accommodated visual programming tools, object-oriented programming, and some organizational development functions (such as quality assurance and ISO 9000 certification). The traditional use of CASE (computer-aided software engineering) is the computer-based support of software development. It is typically used to organize and control large and/or complex projects. While CASE is a tool that supports some activity in the systems development life cycle, I-CASE (integrate CASE) represents a joining of multiple CASE tools in one uniform platform. I-CASE always relies on a specialized database, called a repository, which stores information about the structure (primarily data and processes) of the organization. The repository allows for the ongoing collaboration of a diverse set of project stakeholders (analysts, designers, programmers, testers, users, managers, etc.) using a uniform interface. CASE has the purpose of speeding development, improving quality (by requiring standardization, discipline, and formal problem solving), and lowering costs (especially maintenance) in the software engineering process. The deployment of CASE is based on the premise that including the customer/user early in development, the product is more likely to satisfy requirements, and hence succeed in the marketplace.

Table 2 and the ensuing outline embodies the elements of the design solution.

Change – there are two types of change: radical and incremental:

Radical change – enacted when there is a need to change the explicitly stated FOM

a. Acting Director and Process Owner deliberate issues that might necessitate radical change to the Formal Organizational Memory (a pre-existing example is how processes are explicitly defined in departmental Organizational Work Instructions).

b. Acting Director explicitly and formally states how the FOM Administrator is to change the FOM. The FOM Administrator changes the FOM in one of two ways (either c or d or both)
c. FOM Administrator updates the Process Repository
d. FOM Administrator updates the Logic Repository

Incremental change – enacted within the bounds of the explicitly stated FOM; only the issues repository is updated

a. Process Users *privately* communicate issues to the FOM Administrator
b. FOM Administrator notifies the Process Owner of all updates to the Issues Repository
c. FOM Administrator updates the Issues Repository

Also refer to the NASA-MSFC Continual Improvement website (http://contimp.msfc.nasa.gov/) for other resources. A website depicting the general continuous improvement process at MSFC is available at: http://contimp.msfc.nasa.gov/documents/GeneralContinualImprovementProcessFlow.doc

Social Action – the cognitive and physical behavior intended to achieve organizational outcomes; SA both determines and is determined by one of two types of memory: informal and formal.

Formal Organizational Memory (FOM) – existing descriptions about the organization's structure. The FOM will be captured and managed in the Casewise system by the NAR. An example is the ECA process, which was explicitly defined in the Casewise repository by Cheryl in Summer, 2002. The FOM should describe all organizational processes, such as those that comprise MSFC's Technology Transfer Department:

NTR – New Technology Reporting (Owner: Susan Whitfield)
CA-Commercialization Assistance (Owner: Sammy Nabors)
LP – Licensing of Patents (Owner: Sammy Nabors)
ERNS – External Release of NASA Software (Owner: Caroline Wang)
ECA – External Customer Agreements (Owner: Roger Parisa)

Another FOM resource within MSFC is the *NASA Lessons Learned Database*

Informal Organizational Memory (IOM) – the unstructured and implied knowledge about the process; involves behavioral patterns and knowledge that fits within the guidelines of the FOM; the IOM emerges over time and when captured explicitly (usually in the form of issues), becomes part of the FOM.

Roles – there are four prominent roles during the Action Research Program:

Process user – an individual who operates or interacts with the process as a function of job scope; a common source of issues during incremental change

Process owner – the individual who has the responsibility of maximizing desired process outcomes (such as ROI, efficiency, customer satisfaction, user satisfaction, etc.). This is done through the deliberation of issues intended to improve the process.

Acting Director – manager of several Process Owners in a given organizational subunit (like Technology Transfer).

FOM Administrator – the individual who specializes in populating and maintaining the FOM tool (i.e., Casewise) from which organizational benefits are to be derived. This person should be knowledgeable in the tool and though maintenance, the organization's processes.

A **repository** is a special-purpose database that allows for the graphical manipulation of the data set. The CASE repository does not contain information regarding daily organizational activities (such as transactions). Rather, it represents meta-knowledge about the organization's structure and rarely changes.

Process Repository – representations of formal processes in a centralized, computer-resident location (such as a project file in Casewise™).

Logic Repository – representations of decision logic in a centralized, computer-resident location (such as a project file in Analytica™).

Issues Repository – issues are represented as elements on the process diagrams in Casewise™. An issue is a deviation from the formal system and the informal system. Issues are brought to the attention of the Process Owner when they are discovered. Issues can lead to either incremental or radical system changes.

Cognition skills:

Ideals – the vision, mission, strategies, etc. from which the processes originated. In MSFC-TT, some of the most important ideals are embedded in the Space Act of 1958.

Standards – written performance goals, such as process procedures, structures, and desired outcomes. Standards are set from prior measures of outcomes (VNO and quality). Another MSFC resource on standards is available at: http://standards.nasa.gov/.

Decision Making – deciding between radical or incremental change, and the deliberation within each.

Knowledge Acquisition – acquiring feedback from the operation of processes; see https://msfcsma3.msfc.nasa.gov/dbwebs/apps/qualcomm/nuqualc.taf?function=form for how MSFC uses the Internet for KA on customer satisfaction

Performance criteria:

Resources – any time, money, tool, method, or other investment made in the process(es)

Outcomes – any result that can be attributed to the process(es), such as customer satisfaction (see http://www.theacsi.org/ and https://msfcsma3.msfc.nasa.gov/dbwebs/apps/qualcomm/), user satisfaction (Moore and Benbasat), and return on investment (Phillips).

Process Effectiveness = Outcomes/Resources

Process Efficiency = see Hofer et al.

Balanced scorecard – the balanced scorecard concept implies the use of multiple perspectives in measuring organizational success. It allows management to monitor comprehensive organizational performance over time, as opposed to using a single perspective. See Kaplan and Norton, 1992 and MSFC's balanced scorecard website: http://ntf-2.msfc.nasa.gov/bsc2002.nsf

Table 2: Precursors, Contexts, and Consequences of Organizational Learning
(Source: Templeton and Snyder, 2000)

Factor	**Examples**
Precursors	
Structure	
Structural Stimulants	structural informality, structural simplicity, information technology infusion
Structural Impediments	structural formality, structural complexity, functional specialization, authority relations, quality of internal communication processes, quality of external communication processes, extent of interdisciplinary teamwork, bureaucratization, a procedural culture, appropriateness of reward systems, and management attitude
Culture	shared beliefs, shared norms (Miles and Snow, 1978), and shared assumptions
Cultural Stimulants	cultural complexity, Cognitive norms, behavioral norms (dialogue and management practice)
Cultural Impediments	member homogeneity, barriers to communication
SLL Precursors	need for incremental change, SLL-facilitory conditions, stable task, environment, repetitive channel functions, SLL stimulants, organizational memory performance standards
DLL Precursors	need for radical change, DLL-facilitory conditions (a turbulent environment and nonrepetitive channel functions), DLL stimulants (practicing unskilled learning, striving for failure, achieving collaborative inimitability, organizational memory information system (OMIS)
Contexts	
Internal	the extent of interunit diversity, the presence of proactive strategies, strategy, coordination, incentives to learning, resources devoted to learning, centrality of R&D, diffusion of learning, perceived success
External	environmental turbulence, contradictory information about organizational rules, interfirm trust
Consequences	

Responses to Environmental Turbulence	market-based events, events by competitors
Behavioral Change	implementation of proactive strategies, continuous innovation, seek alternative forms, employee turnover, technology maintenance behaviors, existence of an adaptive component in OMIS
Technological Change	technological complexity, exigencies of speed, global responsiveness, constant innovation
Responses to Competitive Necessity	organizational performance, organizational survival, organizational flexibility, global strategic alliance longevity
Competitive Advantage	technological capability, continuous improvement, price and volume, to quality, to speed, then to mass customization, competent change
New Organizational Technologies	attainment, development, implementation
Enhanced Organizational Knowledge Base	organizational memory, new organizational knowledge, information equivocality
Organizational Effectiveness	planning capabilities, strategic option recognition rates, investment patterns, technology range of choice, facilitation of varying products, product development cycle, integration, economies of scope, employee awareness, energy

2002

NASA FACULTY FELLOWSHIP PROGRAM

MARSHALL SPACE FLIGHT CENTER
THE UNIVERSITY OF ALABAMA

IMPEDANCE-BASED STRUCTURAL HEALTH MONITORING FOR COMPOSITE LAMINATES AT CRYOGENIC ENVIRONMENTS

Prepared By:	Kevin Tseng
Academic Rank:	Assistant Professor
Institution and Department:	Vanderbilt University Department of Civil & Environmental Engineering
NASA/MSFC Directorate:	Engineering
MSFC Colleague:	Dr. Mike Tinker

Introduction

One of the important ways of increasing the payload in a reusable launch vehicle (RLV) is to replace heavy metallic materials by lightweight composite laminates. Engineers and scientists have studied many metallic materials thoroughly, due to the long history of practical usage in many aerospace and aeronautical structures. Compared to metallic materials, composite laminates are a relatively new class of materials and therefore require more attention to ensure the safety and reliability when they are used.

Among various parts and systems of the RLV, this project focuses on tanks containing cryogenic fuel. Historically, aluminum alloys have been used as the materials to construct fuel tanks for launch vehicles. To replace aluminum alloys with composite laminates or honeycomb materials, engineers have to make sure that the composites are free of defects before, during, and after launch. In addition to robust design and manufacturing procedures, the performance of the composite structures needs to be monitored constantly.

In recent years, the impedance-based health monitoring technique has shown its promise in many applications. This technique makes use of the special properties of smart piezoelectric materials to identify the change of material properties due to the nucleation and progression of damage. The piezoceramic patch serves as a sensor and an actuator simultaneously. The electro-mechanical impedance approach using smart piezoelectric ceramic transducers having self-actuating and sensing capabilities has shown potential applications in damage detection in structural systems. Sun et al. [4] and later Ayres et al. [1] reported the use of piezoelectric ceramic patches (PZT) for damage detection and characterization on a laboratory- size truss structure and a prototype truss joint, respectively. The damage detection method is based on the principle of electro-mechanical coupling between the host structure and the bonded PZT patch. The structural impedance modifies the effective electrical impedance of the PZT, and the corresponding change in the driving point impedance is used to identify incipient damage in the structure Giurgiutiu et al. [3]. See Chang [2] for more references.

The piezoelectric patch is bonded onto an existing structure or embedded into a new structure and electrically excited at high frequencies. The signature (impedance or admittance) is extracted as a function of the exciting frequency and is compared with the baseline signature of the healthy state. The damage is quantified using root mean square deviation (RMSD) in the impedance signatures with respect to the baseline signature. A major advantage of this technique is that the procedure is nondestructive in nature and does not perturb the properties and performance of the materials and structures.

This project aims at applying the impedance-based nondestructive testing technique to the damage identification of composite laminates at cryogenic temperature. These materials have potential application for fuel tanks in future RLV's. Regular piezoceramic sensor/actuators are tested to assess their performance under cryogenic temperature. Composite laminates with attached piezoceramic patches are submerged into liquid nitrogen and the impedance signatures are taken. The results show that regular piezoceramic materials are likely not suitable for cryogenic applications. A significant amount of noise can be observed in the impedance signature when the piezoceramic patch is submerged at liquid nitrogen. However, these findings

do not suggest that conventional piezoceramic devices cannot be used for non-cryotank RLV or other applications.

To remedy the deficiency in performance for cryogenic applications, a novel single crystal piezeceramic material, specially designed to function at cryogenic environment, has been identified. This new piezoceramic material appears to be a promising candidate for impedance-based nondestructive testing for composite laminates at cryogenic temperature. More comprehensive tests are planned to assess the performance of the single crystal piezoceramic materials at cryogenic temperature.

Composite Laminates

The composite panels tested in this project are 6-ply woven carbon fiber laminates. Figure 1 is the image of the side of a composite panel under microscope. Woven laminates is selected for the test because their flexibility in forming curved surfaces. Curved surfaces are needed in the construction of fuel tanks for RLV's.

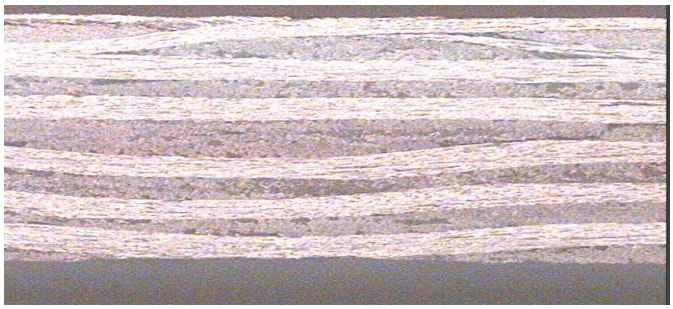

Figure 1: Composite Laminate Ply Count

Impact Damage

Damage in the composite panel is introduced by the impact facility as shown in Figure 2. Various level of damage can be created at the center of the test article by controlling the weight and drop-height of the impact head. The second picture in Figure 2 shows two different levels of impact damage to the composite panel.

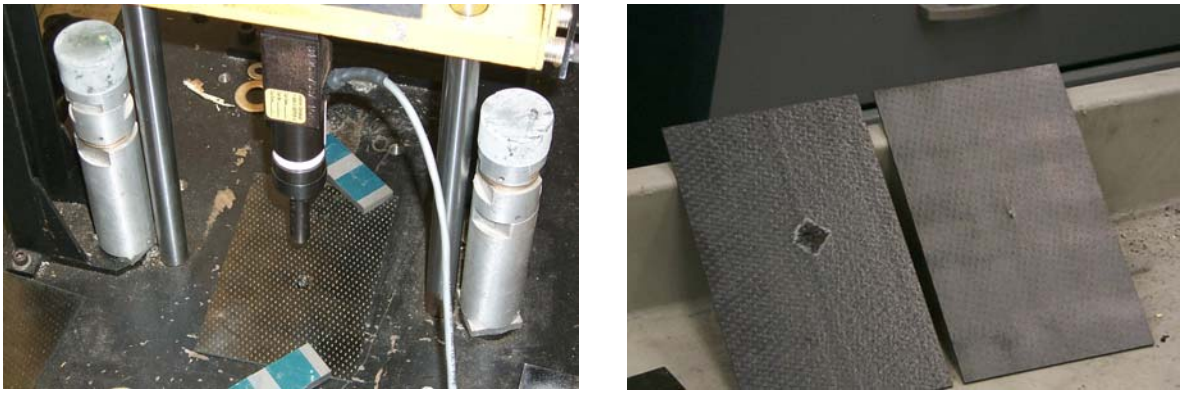

Figure 2: Impact Damage at the Center of the Composite Panel

Cryogenic Environment

To assess the performance of the piezoceramic patch, the test article is placed in a pan and submerged in liquid nitrogen. Liquid nitrogen has a constant temperature of -318ºF. The impedance signatures are taken while the test article is under cryobath.

Figure 3: Test Article Submerged in Liquid Nitrogen

Combined Cryogenic and Impact Damage Tests

In order to evaluate the performance of piezoceramic patches for damage identification at cryogenic temperature, a series of tests combining both impact damage and cryogenic thermal load are conducted. All test articles are configured with regular piezoceramic patches attached.

Results

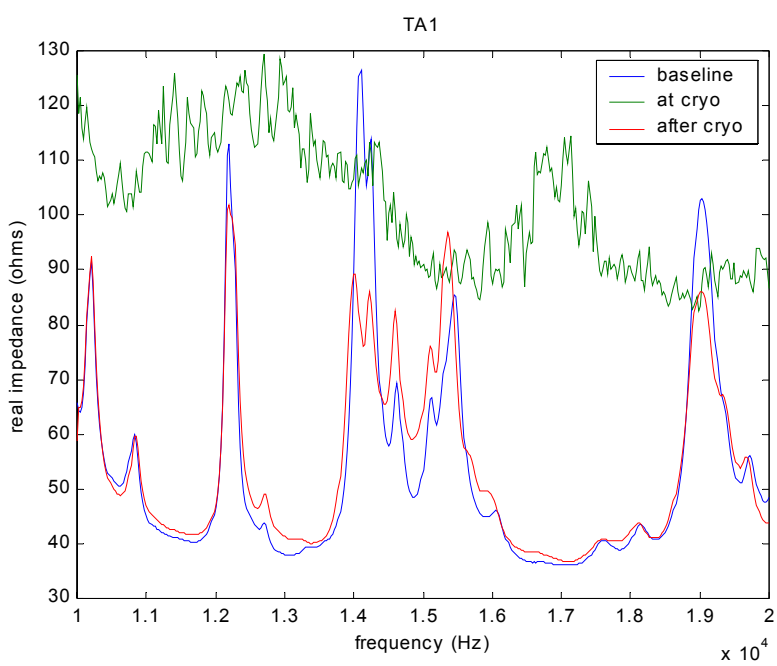

Figure 4: Impedance Signatures Before, During, and After Cryobath

Figure 4 shows a typical impedance signature for the tests conducted in this project. The regular piezoceramic patch functions well before the test article is submerged into liquid nitrogen. During the cryobath, the piezoceramic patch is at the cryogenic temperature of liquid nitrogen. A significant amount of noise can always be observed in the impedance signature for all the test articles. The results also show that after the test articles are removed from the cryobath and returned to room temperature, the performance of piezeoceramic patches seems to recover.

Single-Crystal Piezoceramic Patch

Recently, a single-crystal piezoceramic material has been designed and manufactured by TRS Ceramics Inc. to be used for cryogenic environments. This special piezoceramic material can generate much more energy at cryogenic temperature as compared to the regular piezoceramic materials. More tests with single-crystal piezoceramic patches are planned to verify their performance at the cryogenic temperature of liquid nitrogen.

Conclusions

The test results show that regular piezoceramic patches are not suitable for impedance-based nondestructive damage identification at cryogenic temperature. A significant amount of noise can be observed in the impedance signature when regular piezoceramic patches are submerged into liquid nitrogen. A single-crystal piezoceramic material, specially created for cryogenic applications, has been identified. More tests have been planned to assess the performance of the single-crystal piezoceramic material for damage identification at cryogenic environments.

Acknowledgements

The author would like to thank the entire team of engineers in the Structural Dynamics and Loads Group of the Marshall Space Flight Center's Engineering Directorate. Special thanks go to the author's colleague, Mike Tinker, who has provided the author all the support during the summer. The author is also grateful to John Lassiter, Dan Peairs, Andy Hodge, Erin Richardson, Stephen Herald, Freida Lowery, and John Lowery for their assistance.

References

[1] Ayers J. W., Lalande F., Chaudhry Z., and Rogers C. A. (1998), *Qualitative impedance-based health monitoring of civil infrastructures*, Smat Mater. Struct., vol. 7, pp. 599-605.

[2] Chang, F. K., editor (2001), Proceeding of the 3rd International Workshop on Structural Health Monitoring, Stanford, California, 2001.

[3] Giurgiutiu V., Reynolds A., and Rogers C. A. (1999), *Experimental investigation of E/M impedance health monitoring for spot-welded structural joints*, J. Intell. Mater. Syst. Struct., vol. 10, pp. 802-812.

[4] Sun, F.P., Chaudhry, Z., Rogers, C.A., Majmundar, M., and Liang, C. (1995), *Automated Real-Time Structure Health Monitoring Via Signature Pattern Recognition*, Proceedings of Smart Structures and Materials Conference, San Diego, California, SPIE, vol. 2443, pp. 236-247.

2002

NASA FACULTY FELLOWSHIP PROGRAM

MARSHALL SPACE FLIGHT CENTER
THE UNIVERSITY OF ALABAMA

AN ACCIDENT IN HISTORY: *CHALLENGER* IN PERSPECTIVE

Prepared By:	Stephen P. Waring
Academic Rank:	Associate Professor
Institution and Department:	University of Alabama in Huntsville Department of History
NASA/MSFC Directorate:	Customer and Employee Relations
MSFC Colleague:	Mike Wright

Figure 1: Walking *Enterprise* to Dynamic Test Stand--1978

Introduction

For several years since the publication of a history of Marshall Space Flight Center, I have been studying the origins and meaning of the Space Shuttle *Challenger* accident.[1] My long-term goal is to write a book on the history of the accident, and the 2002 NASA Faculty Fellowship allowed me to make substantial progress toward that goal. This summer I wrote about half the manuscript chapters, filled in numerous gaps in my research, interviewed several Marshall officials, and scanned dozens of photographs and engineering illustrations.

My book will differ in several respects from previous studies. It will cover a longer span of time and events—most books begin with the test phase of the solid rocket motor and end shortly after the accident. Mine will go back to the Apollo Program and discuss the testing and quality control methods used on the Saturn rockets. It will also include considerable coverage of the origins of the shuttle configuration and program management system. In addition, it will also go forward beyond the accident, with almost half the book discussing the post-accident investigations, the redesign of the shuttle and boosters, and the interpretations about the tragedy that appeared in scholarly publications. Its focus will be comprehensive, but will concentrate on the history of solid rocket motor engineering and technology. Most previous studies have made engineering secondary to an examination of communications or bureaucracy.

A Primer on Interpretations of the Accident

The stories about *Challenger* all agree (well, virtually all agree, but that is another story!) that the accident occurred because of a failure in the joint of the steel case of one its solid rocket motors. Beyond this basic fact, interpretations disagree.

Figure 2: Transport of Structural Test Article-1--1977

The orthodox interpretation of the accident is that engineers who worked on the solid rocket motor had understood the technical hazard before the fatal flight on 28 January 1986, but that their managers had failed to communicate that hazard to shuttle program managers and thus had failed to stop shuttle flights and fix the joint problems. This view claims that engineers had understood the dangers and recognized the limitations of the field joints in the motors, and that managers had failed to pass along this information. In other words, the dominant view is that the

engineers knew the hazard and that their managers did not tell; consequently they failed to prevent an accident.

This interpretation was central in the report of the Presidential Commission that investigated the accident.[3] With this report as a starting point, most academic studies have emphasized managerial, communications, and moral failures as the primary causes of the *Challenger* disaster. Often such studies have relied, implicitly or explicitly, on considerable "counter-factual" logic, contending that "if only" historical actors had communicated better, then events would have unfolded differently and the accident would not have happened. If only the managers had listened, if only the managers had reported, if only the managers had not felt pressure to launch, and so on.

At least one explanation departed from this pattern. Most notably, Diane Vaughan, a sociologist, argued that the orthodox interpretation had been shaped by a search for blame after the accident, and so had focused on managerial malfeasance. In a thorough and thoughtful interpretation of the disaster, she turned the bad management thesis on its head, and contended that managers had followed NASA rules and communicated engineering information properly. Rather than rule violations, Vaughan maintained that the accident happened because the engineers and managers followed NASA rules and norms. The structure of the space economy spawned formal rules and cultural patterns that led to engineering "mistakes" that were "socially organized and systematically produced." Accepting imperfect designs was normal for rocket engineers who worked in an organizational environment characterized by limited budgets, tight schedules, and efficiency procedures. Accordingly Vaughan found no malfeasance, but believed that Congress and the White House had created a "bureaupathological" structure in which marginal technology and undue risk-taking was normal. She contended that the accident proved "the inevitability of mistake" in any bureaucracy working with "risky technology."[4]

A Technological History

My approach finds flaws in both types of interpretations and seeks a balance between the extremes that is consistent with all the evidence. The managerial interpretation misinterpreted the engineers' understanding of the joints prior to the accident. The engineers, rather than classifying the joints as hazardous, considered the joints to be safe and reliable. Their managers' reports to shuttle program officials, rather than hiding a hazard, correctly communicated their engineers' consensus that the joints were safe. In other words, the engineers did not know that the joint problems were hazardous, and their managers did tell of the safety and reliability of the joints.

Vaughan also made mistakes. By arguing that there was no wrongdoing and no norms were violated, in effect she made the absurd claim that NASA had no norms for ensuring the safety of launch vehicles and people on them. Her ideas were fatalistic because she called the solid rocket motor "risky technology" that could "never be known" or realistically tested.[4] Accordingly Vaughan, like other interpreters, focused on engineering communications rather than looking at engineering methodology. She mistakenly assumed that bureaucracy made the accident inevitable, and ignored the evidence of successful engineering in bureaucracies, including in the space shuttle program. Engineers working on the space shuttle main engine before the accident,

for example, operated in the same social environment as those working on the solid rocket motor, but the SSME technology did not fail. Moreover after the accident, engineers redesigned the solid rocket motor and it too has operated successfully and safely.

Figure 3: Development Motor 2--1978

Like previous studies, my interpretation recognizes that rules were violated and norms were followed, but emphasizes neither. Rather my approach seeks to understand how the engineers studied the motors and what conclusions they drew. Rather than evidence pointing to malfeasance or "bureaupathology," most of the evidence shows engineers using the state-of-experience methods that seemed to verify the safety of the joints. When they encountered problems with the motor's field joints, they carefully reanalyzed the data, and conducted more tests. But unwittingly, they performed work with flaws that prevented realistic understanding of the limitations of the technology and the risks. Accordingly they believed that the data and tests showed that the joints were safe. Only after the tragedy did the engineers realize that their previous methods had not been rigorous or realistic enough.

After the accident, they had new data that gave them clues about the limitations of their designs. Consequently they recognized the previous mistakes, developed new tests and procedures, and successfully created a new robust design.

Such a technological approach puts engineering at the center, emphasizing design principles, test procedures, and assessment processes. My goal is to write a history that will serve people outside and inside aerospace. A study that focuses on technology will help outsiders see engineering in practice, and explore the social and political context in which engineers work on the daily activities of design, development, testing, analysis, and review. A history of the shuttle's solid rocket motor project will be useful for insiders, especially in describing how engineers inadvertently made mistakes, but quickly learned from them.

Indeed a primary goal of my history will be to ensure that what the engineers experienced and learned is not forgotten. Their lessons remain the greatest memorial to the astronauts who died aboard *Challenger*, the greatest testament to their professionalism as engineers, and the most important legacy of the accident. A year before the accident, Henri Petroski, an engineer,

humanist, and author of *To Engineer is Human*, reflected on the role of failure in engineering design, and explained that

> colossal disasters that do occur are ultimately failures of design, but the lessons learned from those disasters can do more to advance engineering knowledge than all the successful machines and structures in the world. Indeed, failures appear to be inevitable in the wake of prolonged success, which encourages lower margins of safety. Failures in turn lead to greater safety margins and, hence, new periods of success. To understand what engineering is and what engineers do is to understand how failures can happen and how they contribute more than successes to advance technology.[2]

By relating the *Challenger* story of failure and learning, I hope to contribute in some modest way to readers' understanding of engineering and space exploration.

Resources

In conducting my research and writing during the fellowship, I mainly worked from the Marshall Space Flight Center's History Archives. The archive has various historical records, including files from past Center Directors, technical reports, photos, videotapes, and news articles. The collection is outstanding and has a marvelous digital finding aid. I also conducted several oral history interviews.

Acknowledgements

I would not have progressed as well on my project without the assistance of several people. Mike Wright, my NASA colleague, paved the way with helpful advice about sources and interview subjects; he even loaned his computer. Bob Jaques helped me locate information everyday. Ron Tepool, Amanda Goodson, Mike Leberman, Garry Lyles, and Mark Fisher answered questions. Mike Leberman not only answered questions, but also took me on tours of the back spaces of Marshall. Also deserving thanks are Susan Eason, Mike Herston, Jonathan Baggs, and Steve Durham.

References

[1] Dunar, A. J. and Waring, S. P. (1999) *Power to Explore: A History of Marshall Space Flight Center 1960-1990*, NASA SP-4313.

[2] Petroski, H. (1985) *To Engineer is Human: The Role of Failure in Successful Design*, St. Martins Press, p. xii.

[3] Presidential Commission, (1986) *Report on the Space Shuttle Challenger Accident*, U.S. Government Printing Office.

[4] Vaughan, D. (1996) *The Challenger Launch Decision: Risky Technology, Culture, and Deviance at NASA*, University of Chicago Press.

2002

NASA FACULTY FELLOWSHIP PROGRAM

MARSHALL SPACE FLIGHT CENTER
THE UNIVERSITY OF ALABAMA

EVALUATION OF ADVANCED COMPUTING TECHNIQUES AND TECHNOLOGIES: RECONFIGURABLE COMPUTING

Prepared By:	B. Earl Wells
Academic Rank:	Associate Professor
Institution and Department:	University of Alabama in Huntsville Electrical and Computer Engineering
NASA/MSFC Directorate:	Engineering
MSFC Colleague:	David Gwaltney

Background

It is common practice to divide a digital system into software and hardware components. The greatest functionality and performance occurs when functions are placed in dedicated system hardware that is highly parallel and is optimized to perform the intended operations. More often than not it is far too expensive in time and money to create such dedicated hardware so the available hardware resources are used to implement a conventional processor which executes programmable instructions in a highly sequential manner. While this is very flexible such conventional processors are inefficient -- a large percentage of hardware resources (up to 99% of the logic gates that make up its hardware) are idle most of the time. Commercially-off-the-Shelf digital and analog hardware now exists that can change the "circuit" that is being implemented long after the device(s) are fabricated. This means that high speed hardware can now share much of the flexibility normally reserved for software-only systems.

Not all applications need the added speed and other possible features of reconfigurable systems such as fault tolerance and power management techniques, but some applications that could greatly benefit from this technology include, Genetic Algorithms, Real time processing, Data encryption/decryption ,RSA cryptography, Data Compression, Image and Video processing, String matching, Heat and Laplace equations, Newton's mechanics, Continuous System Simulation, Evolutionary Computing, Fault Tolerant Computing, Binary 2D convolution, Boltzmann machine, 3D graphic Accelerators, Discrete Cosine Transforms, Irregular Mathematical operations. For this reason, investigation into emerging techniques and technologies in reconfigurable systems is an active area of research which directly supports the goals and objectives of NASA.

Project Goals

The focus of this project was to survey the technology of reconfigurable computing determine its level of maturity and suitability for NASA applications. To better understand and assess the effectiveness of the reconfigurable design paradigm that is utilized within the HAL-15 reconfigurable computer system. This system was made available to NASA MSFC for this purpose, from Star Bridge Systems, Inc. To implement on at least one application that would benefit from the performance levels that are possible with reconfigurable hardware. It was originally proposed that experiments in fault tolerance and dynamically reconfigurability would be perform but time constraints mandated that these be pursued as future research.

Targeted Reconfigurable Computing Platform

The targeted reconfigurable computer system that was used in this research was one that was developed by Star Bridge Systems, Inc. to utilizes devices which are commonly called Field Programmable Gate Arrays, FPGAs. FPGAs were introduced to the hardware design community in the mid 1980s as a means to incorporate so-called random logic into a minimal number of integrated circuits. Since that time these chips have grown drastically in size and function where they have had a major effect in the areas of rapid prototyping of low volume application specific designs, digital logic emulation, and have served greatly to improve the time-to-market for new product designs. Star Bridge Systems and other companies are trying to capitalize not as a rapid prototyping device but as advanced computing devices. It should be noted that current FPGA technology is not optimized for this use.

Targeted Reconfigurable Platform

The reconfigurable system that served in this evaluation was the HAL-15 Hypercomputer system from Star Bridge Systems, Inc. It has a peak performance estimate of 40 billion fixed point 16-bit multiply accumulates per second operations, and 15 billion 32-bit floating point operations per second. It utilizes a total of 10 Xilinx 4062 800 picosecond FPGAs where each 4062 FPGA has 2304 Combinational Logic Blocks which translates into somewhere between 62,000-130,000 logic gate equivalents. It is PC hosted on a PCI 32 bit 33 Mhz daughter board. Systems can contain multiple daughter boards. The FPGAs are interconnected with the PC and each other using a proprietary bus structure. There is a total of 288 Mbytes of SDRAM and a 200 Mhz system clock.

The development environment is the VIVA ™ Graphical User Interface. This environment supports a structural object oriented design philosophy that allows for the incorporation of certain high level behavioral attributes some of which are normally found in textural-based hardware description languages such as VHDL, Verilog and Handle C ™. These include the concept of polymorphism where objects are created to support data types of multiple precession, operator overloading, where object with the same name can be utilized to handle different operations, and recursion where objects are defined in terms of themselves (note method of representation for hardware is novel). The major synchronization technique that is used closely follows the data flow paradigm where objects that are to be processed sequentially are designed in a pipelined manner where they must wait for the objects the precede it in the pipe to complete before it can begin operations. To accomplish this objects have special signals that performs the necessary handshaking protocol. The tool comes with a large library of high-end objects such as floating-point multipliers, dividers, adders, transcendental functions, etc. In many ways this environment falls somewhere between hardware description languages and schematic capture packages in terms of features and function.

Application 1: Implementation of a Genetic Algorithm

The first application that was implemented was a Genetic Algorithm that minimized a simple numeric objective function. Genetic Algorithms represent a set of search techniques, which are modeled after the evolutionary view of biological systems. They incorporate the ideas that an algorithm can be represented as a pattern that can be matted with other patters via the cross-over operations. A fitness function can then be applied to the resulting children to determine which of the children and parents continue over to the next generation. There is also a small probability of that the pattern will mutate thereby changing one or more of its elements.

Figure 1 shows the high-level Viva diagram for the genetic algorithm. The design is hierarchical with this being the top level -- there are a total of 44 user created objects in this design. Here we see the general structure of the design with two main storage elements. The first is the next generation storage where the children elements are stored and the associate memory which performs the combined operations of next generation storage and applying the fitness function. In this case the population size was set at a value of 16 members. Upon receiving the Go pulse the Generate_Init_Population module randomly generates X, Y data and applies the objective function for all members of the population. It then stores the results in the next generation storage. When it is complete it signals the for loop object to begin operations. This object pulses

the next generation fitness controller, which moves the children elements into the population using the objective function as a key. The associative memory only maintains a copy of the best 16 elements presented to it any elements that are worst than its worst element do no get stored and therefore do not make it to the next generation. After this is done the cross over mutate module gets pulsed. This will create 16 new children by randomly mating two elements from the population in the associative memory and then storing them in the next generation storage. When this is complete the outer level controlling for loop is signaled that the iteration is complete. When all iterations are complete the associative memory is signaled to output the best member of the population.

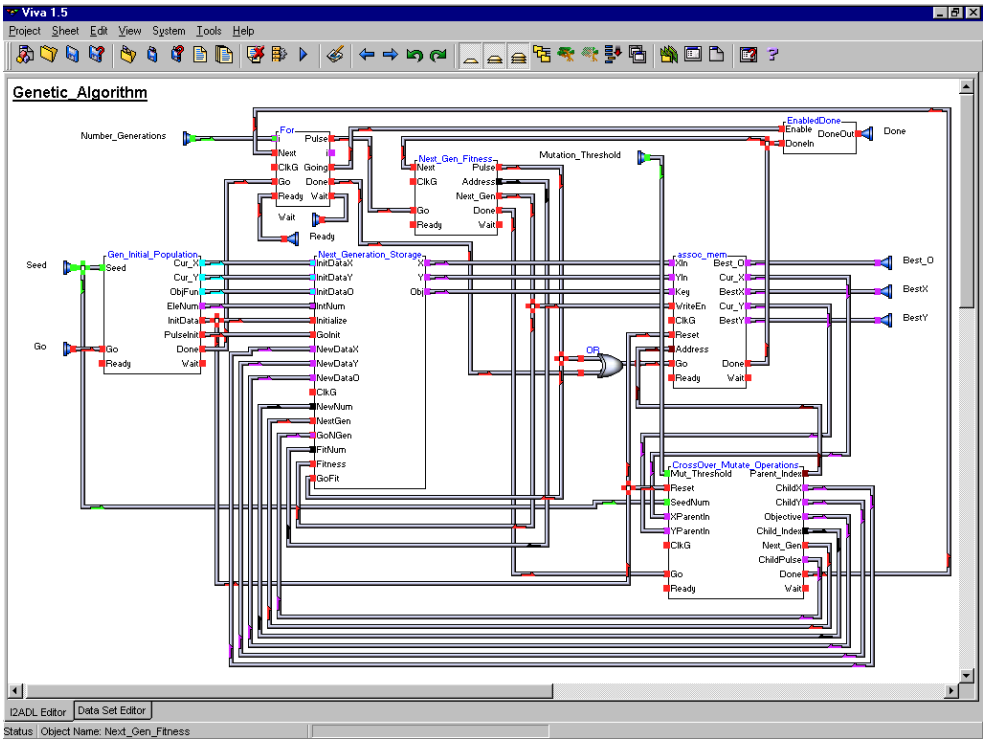

Figure 1: High-Level Viva Representation of the Genetic Algorithm

After the design methodology was fully explored the genetic algorithm was implemented in a couple of weeks. The algorithm occupied less than one of the 10 FPGAs and produced a result, which was an order of magnitude faster than an equivalent software implementation. The implementation utilized only integer arithmetic but an equivalent fixed or floating-point representation could be made by modifying the objective function and a small number of objects.

Application 2: Continuous System Simulation

The second application that was applied was a continuous simulation of a small system of differential equations that form the classical initial value problem. This utilized floating-point arithmetic. A simple Euler integrator module was created that performed the multiply accumulate operation. Figure 2 shows how these were linked to implement the sin function using a simple second order ODE.

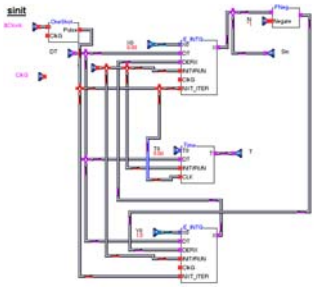

Figure 2: Continuous Simulation of a second order ODE that generates the sin(t)

Continuous simulation seems especially suitable for reconfigurable hardware implementation that has the flexibility to support high-speed operations for arbitrary structured dynamic systems. It directly supports the low level of granularity that is present in most continuous simulations and allows for efficient interpretation communication between object modules --something that is too costly with conventional parallel processing technology. There are still major space time trade-offs need to be considered. How to model nonlinear constructs such as large lookup tables and transcendental are also a major consideration.

Conclusion

This project successfully demonstrated how two types of applications can be implemented on the HAL-15 reconfigurable computer using the Viva design entry language. Viva is competing with schematic capture traditional HDL and other high level languages that are being modified to create hardware. There is a high learning curve associated with these languages. Viva is designed to minimize this learning curve. This investigator is probably biased since he has already learned these tools -- his evaluation is that Viva is closer to schematic capture than HDLs or high-level language derivatives. He also feels that Viva will not replace existing digital design methodologies since they offer a wider amount of control and functionality which is sometime needed. The use of Viva may fill an important need where algorithm developers who are not digital designers can evaluate the effectiveness of their designs or accelerate their calculations without the high learning curve associated with other techniques. This is analogous to the use of specialized graphical object oriented software in domains ranging from discrete event simulation, system architecture description languages to probabilistic analysis. This is just initial research -- more applications will have to be explored before definitive conclusions are reached. Such future research should include more advance Genetic Algorithms, Continuous Simulation, Neural Networks. Also investigations into dynamic reconfiguration techniques, fault tolerance, evolutionary computing and intelligent power management should be explored.

References

[1] Uher, Bill,. (2001), “Computing Faster Than Engineers Can Think” NewsRelease NASA Langley Research Center, Hamption, Virginia, Release No. 01-.

[2] Michell, M. (1998), *An Introduction to Genetic*, MIT Press, ISBN: 0262631857.

[3] Gear, C. W., (1971) *Numerical Initial-Value Problems in Ordinary Differential Equations*, Prentice Hall, Englewood Cliffs, N.J.

2002

NASA FACULTY FELLOWSHIP PROGRAM

MARSHALL SPACE FLIGHT CENTER
THE UNIVERSITY OF ALABAMA

TORQUE LIMIT FOR BOLTED JOINT FOR COMPOSITES
PART A
TTTC PROPERTIES OF LAMINATED COMPOSITES

Prepared By:	Yi Zhao
Academic Rank:	Assistant Professor
Institution and Department:	Embry-Riddle Aeronautical University Department of Aerospace Engineering
NASA/MSFC Directorate:	Engineering
MSFC Colleague(s):	Frank Thomas

Introduction

The existing design code for torque limit of bolted joints for composites at Marshall Space Flight Center is MSFC-STD-486B, which was originally developed in 1960s for metallic materials. The theoretical basis for this code was a simplified mechanics analysis, which takes into account only the bolt, nut and washers, but not the structural members to be connected. The assumption was that metallic materials would not fail due to the bearing stress at the contact area between washer and the mechanical member. This is true for metallic materials; but for composite materials the results could be completely different. Unlike most metallic materials, laminated composite materials have superior mechanical properties (such as modulus and strength) in the in-plane direction, but not in the out-of-plane, or through-the-thickness (TTT) direction. During the torquing, TTT properties (particularly compressive modulus and compressive strength) play a dominant role in composite failure. Because of this concern, structural design engineers at Marshall are currently using a compromised empirical approach: using 50% of the torque value for composite members. Companies like Boeing is using a similar approach.

An initial study was conducted last summer on this topic to develop theoretical model(s) that takes into consideration of composite members. Two simplified models were developed based on stress failure criterion and strain failure criterion, respective. However, these models could not be used to predict the torque limit because of the unavailability of material data, specifically, through-the-thickness compression (TTTC) modulus and strength. Therefore, the task for this summer is to experimentally determine the TTTC properties. Due to the time limitation, only one material has been tested: IM7/8552 with [0°, ±45°, 90°] configuration. This report focuses the test results and their significance, while the experimentation will be described in a separate report by Mr. Kris Kostreva.

Through-the-Thickness Compressive (TTTC) Properties

Two types of joining methods are widely used in aerospace/aircraft structures: adhesive bonding and bolting. Almost all of the primary joints (joints to carry major loads) are bolted joints. But how to determine the torque limit of bolt joint for composites is a big challenge for structural engineers at MSFC and other aerospace/aircraft industry since there is no design standard and/or code for composites. The compromise is to use reduced torque value. This is apparently an empirical approach, and it is material type oriented.

It can be found that all of the composite materials data books contain only in-plane material properties, but not through-the-thickness properties. There could be many reasons behind this fact, but the technical challenge in determining TTT properties experimentally is no doubt one of the major reason. Since the thickness of a composite laminate is fairly small, say 1/8”, it is difficult to either mount a strain gage or other measuring tools. Almost all of the analyses of composite structures are based on laminate theory. According to this theory, TTT properties are assumed to be the same as in-plane 90° tension (ASTM D3039) or compression (ASTM D3410) properties regardless of fiber configuration of the laminates, provided fiber fraction remains the same.

The failure due to bearing stress at the washer area is dominated by material's behavior in the thickness direction, particularly TTTC modulus and TTTC strength. Therefore, design a feasible test fixture and using this fixture to obtain TTTC properties become one of the major parts of this torque limit project. After several trials, an innovative test fixture has been designed that uses linear displacement sensors (LDS). Because of the extremely small displacement in the TTTC tests, a highly accurate measuring device has to be employed. LDS becomes an ideal choice to serve our purpose due to its high accuracy. Table 1 shows the comparison among three measurement tools.

Table 1. Comparison of Various Measuring Tools

Measuring Tools	Features
LDS	≤ 0.1% full scale error No external conditioners 3.5 mV/V output Medium cost
LVDT	0.25% full scale error External conditioners required 4 mV/V output Low cost + conditioners
Extensometer	0.1-0.5% full scale error No external conditioners 3.5 mV/V output High cost

Test Fixture and Specimens

A detailed description of TTTC test fixture can be found in Part B of this report (by Kris Kostreva). The TTTC tests were conducted on an MTS universal testing machine with 220 kips capacity. In order to see the effect of fiber configuration on TTTC properties, coupons with four different fiber configurations were tested:

- Unidirectional [0°]
- Cross ply [0°, 90°]
- Quasi-isotropic [0°, ±45°, 90°]
- Quasi-isotropic [0°, ±30°, ±60°, 90°]

Three different thicknesses were used for IM7/8552 to investigate the thickness effect: 0.132", 0.176" and 0.220".

Test Results

The test results of TTTC modulus and TTTC strength are shown in Fig. 1 and Fig. 2, respectively. Here the relative modulus and relative strength are the test values relative to those from 90º in-plane compressive modulus and strength. These 90º in-plane compressive modulus and strength tests were also conducted by the investigators using the ASTM D3410 fixture, as shown in Fig. 3, following the test procedure specified by the standard.

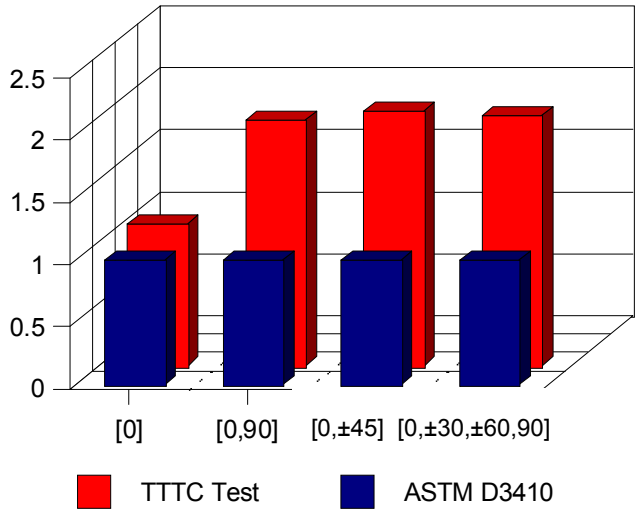

Fig. 1 Comparison of Relative Modulus

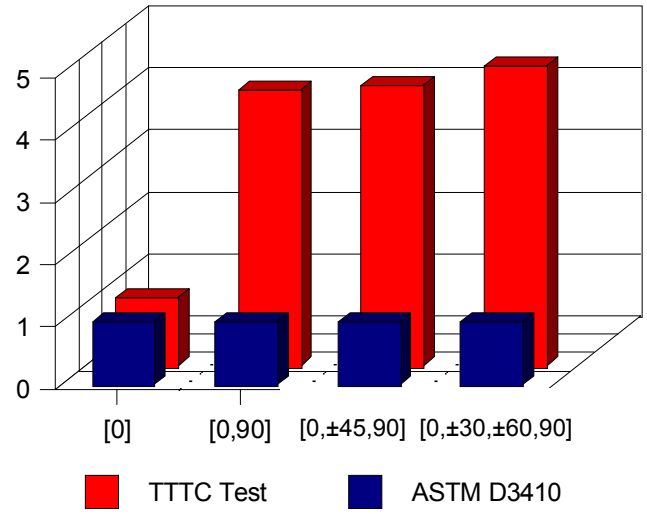

Fig. 2 Comparison of Relative Strength

The results from the TTTC tests are significant, not only to the design and stress analysis engineers in aerospace/aircraft industry, but also to the composites research community. Up to this point, the analysis of composite structures are mainly based on laminate theory. According to this theory, the TTTC modulus obeys the "Rule of Mixture" that applies to modulus in any other direction. This theory also suggests that both TTTC modulus and strength could be approximated by those obtained from 90° tension or compression tests. But the results from this study show that the "Rule of Mixture" is not applicable for TTTC modulus. The four fiber configurations we used in tests have the exact same fiber volume fraction, but have significant different values for TTTC modulus: except for [0°] coupon that is about the same as that from 90° compression test, all three other fiber configurations have a modulus that is at least twice the value as that from 90° compression test. The differences in strength are more notable: the data for three fiber configurations (except for [0°] coupon) are at least four times greater than the strength obtained from 90° compression test.

Fig.3 ASTM D3410 Test Fixture and 90º Specimen

Preliminary Conclusions

While it is premature to conclude that existing theories/methods in determining the TTTC properties for laminated composites are incorrect, this study clearly shows that there is a possibility that TTTC properties have to be determined in a different way other than the existing theories/standards suggest. The preliminary conclusion from this experimental study is summarized in the following:

- For the material tested (IM7/8552), TTTC modulus does not obey "Rule of Mixture."
- For the material tested (IM7/8552), both TTTC modulus and strength vary with fiber configuration.
- For unidirectional laminate, TTTC modulus is about the same as in-plane 90° compression modulus; while the TTTC strength is about 3% higher than in-plane 90° compression strength.
- For cross ply and two other quasi-isotropic materials, the TTTC moduli are at least four times greater than that of in-plane 90° compression strength.

Since there is only material (IM7/8552) tested, it is necessary to test some different fiber/resin composite materials in order to reach some ultimate conclusions.

Acknowledgment

The investigator would like to express his sincere gratitude to NASA/ASEE in general, MSFC and U. Alabama in particular, for providing him a summer faculty fellowship to conduct this research. The investigator would like to thank his NASA colleague Frank Thomas for his collaborations during the course of this study. The investigator would also like to thank the following individuals and group for their support: Karen Stevens and ED03, Paul McConnaughey and ED20, Pete Rodriguez and David Shular of TD20, Wayne Gamwell and ED33, Bill McMahan, Brett Smith, Tom Delay of ED34. A great appreciation will also be extended to Mr. Sidney Rowe for his support.

References

[1] Torque Limits for Standard, Threaded Fasteners, MSFC-STD-486B, November 1992.

[2] "Criteria for Preloaded Bolts," NASA/JSC, NSTS 08307, Revision A, July 1998.

[3] V.S. Avva, H.G. Allen, and K.N. Shivakumar, "Through-the-thickness Tension Strength of 3-D Braided Composites," *J. of Composite Materials,* Vol. 30, No. 1, 1996.

[4] M.L. Benzeggagh, K. Khellil, T. Chotard,"Experimental Determination of Tsai Failure Tension Terms F_{ij} for Unidirectional Composite Materials," *Composites Science and Technology*, Vol. 55, No. 2, 1995.

[5] H.Z. Shan, M.A. Parvizi and T.W. Chou, "Numerical Analysis for Design of Composite Specimens for Through-the-thickness Tensile Measurements," *J. of Composite Materials,* Vol. 28, No. 11, 1994.

[6] H.T. Sun, F.K. Chang and X. Qing, "The Response of Composite Joints with Bolt-Clamping Loads, Part I: Model Development," *J. of Composite Materials*, Vol. 36, No. 1, 2002.

[7] Y. Zhao, D. Ford, and S. Richardson, "Torque Limit for Fasteners in Composites," Technical Report, NASA/MSFC/ED23, August 2001.

REPORT DOCUMENTATION PAGE

Form Approved
OMB No. 0704-0188

Public reporting burden for this collection of information is estimated to average 1 hour per response, including the time for reviewing instructions, searching existing data sources, gathering and maintaining the data needed, and completing and reviewing the collection of information. Send comments regarding this burden estimate or any other aspect of this collection of information, including suggestions for reducing this burden, to Washington Headquarters Services, Directorate for Information Operation and Reports, 1215 Jefferson Davis Highway, Suite 1204, Arlington, VA 22202-4302, and to the Office of Management and Budget, Paperwork Reduction Project (0704-0188), Washington, DC 20503

1. AGENCY USE ONLY *(Leave Blank)*	2. REPORT DATE	3. REPORT TYPE AND DATES COVERED
	April 2003	Contractor Report (Final)

4. TITLE AND SUBTITLE

The 2002 NASA Faculty Fellowship Program Research Reports

5. FUNDING NUMBERS

NAG8–1859

6. AUTHORS

Program Co-Directors: S.K. Nash-Stevenson, C.L. Karr,* L.M. Freeman,* and G. Karr** (Program Co-Directors) J. Bland (Compiler and Editor)

7. PERFORMING ORGANIZATION NAMES(S) AND ADDRESS(ES)

The University of Alabama, Tuscaloosa, AL
The University of Alabama in Huntsville, Huntsville, AL

8. PERFORMING ORGANIZATION REPORT NUMBER

M–1074

9. SPONSORING/MONITORING AGENCY NAME(S) AND ADDRESS(ES)

National Aeronautics and Space Administration
Washington, DC 20546

10. SPONSORING/MONITORING AGENCY REPORT NUMBER

NASA/CR—2003–212397

11. SUPPLEMENTARY NOTES

*The University of Alabama, Tuscaloosa, AL
**The University of Alabama in Huntsville, Huntsville, AL
Prepared for Education Programs Department, Customer and Employee Relations Directorate

12a. DISTRIBUTION/AVAILABILITY STATEMENT

Unclassified-Unlimited
Subject Category 99
Standard Distribution

12b. DISTRIBUTION CODE

13. ABSTRACT *(Maximum 200 words)*

For the 38th consecutive year, a NASA Faculty Fellowship Program was conducted at Marshall Space Flight Center (MSFC). The program was conducted by The University of Alabama and MSFC May 28–August 2, 2002. Operated under the auspices of the American Society for Engineering Education, the MSFC program, as well as those at other NASA Centers, was sponsored by the University Affairs Office, NASA Headquarters, Washington, DC. The basic objectives of the program, which is in its 38th year of operation nationally, are to: (1) Further the professional knowledge of qualified engineering and science faculty members, (2) stimulate an exchange of ideas between participants and NASA, (3) enrich and refresh the research and teaching activities of the participants' institutions, and (4) contribute to the research objectives of the NASA Centers. The Faculty Fellows spent 10 weeks at MSFC engaged in a research project compatible with their interests and background and worked in collaboration with a NASA MSFC colleague. This CD is a compilation of Fellows' reports on their research during the summer of 2002.

14. SUBJECT TERMS

avionics; structures; mechanics; materials, processes, and manufacturing; flight projects; safety, reliability, and quality assurance; space science; optics; propulsion; vehicles development

15. NUMBER OF PAGES

291

16. PRICE CODE

17. SECURITY CLASSIFICATION OF REPORT	18. SECURITY CLASSIFICATION OF THIS PAGE	19. SECURITY CLASSIFICATION OF ABSTRACT	20. LIMITATION OF ABSTRACT
Unclassified	Unclassified	Unclassified	Unlimited